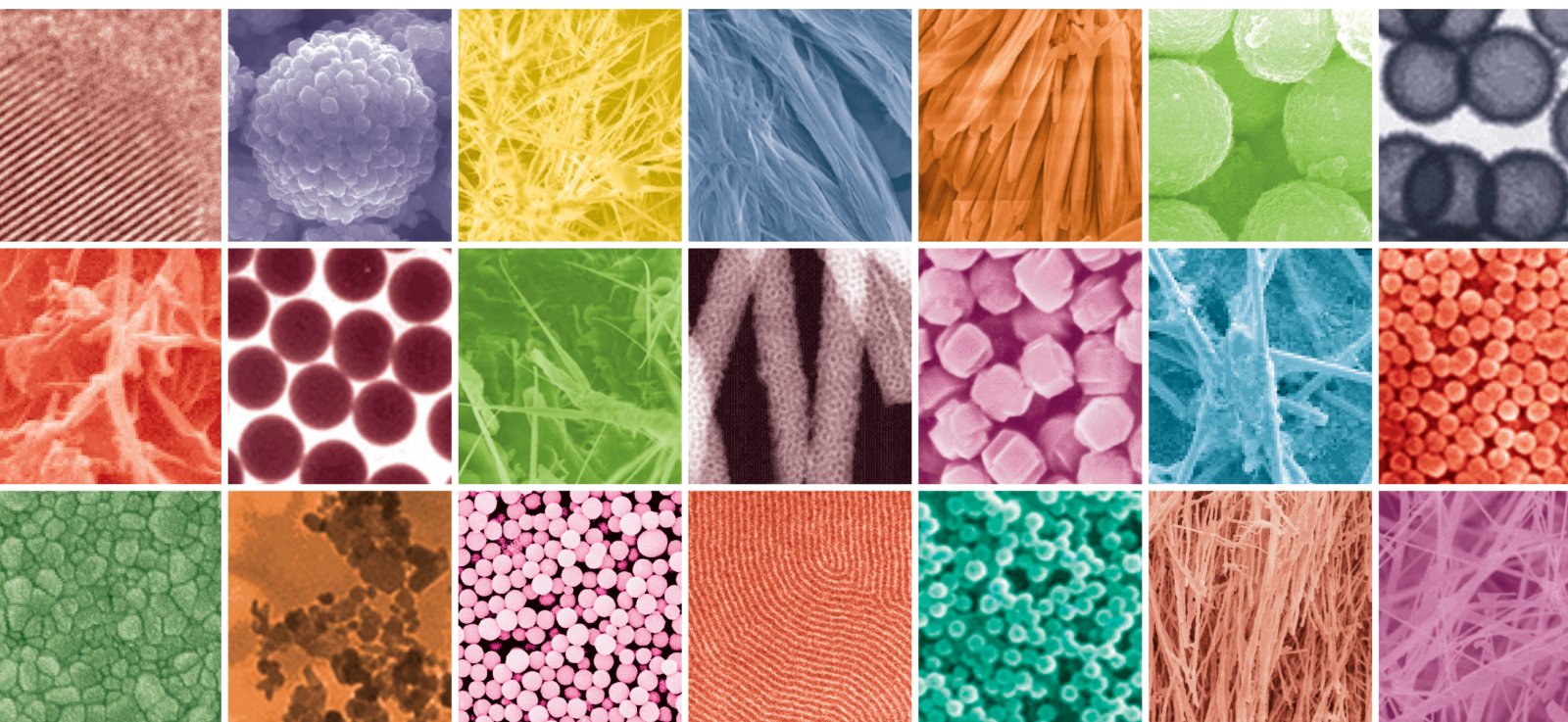


Eco-friendly Waste-based Nanocatalyst Materials in Energy, Environment and Biological Applications

Lead Guest Editor: Balasubramanian Ravindran

Guest Editors: Davidraj Johnravindar and Pounsamy Maharaja





**Eco-friendly Waste-based Nanocatalyst
Materials in Energy, Environment and
Biological Applications**

Journal of Nanomaterials

**Eco-friendly Waste-based Nanocatalyst
Materials in Energy, Environment and
Biological Applications**

Lead Guest Editor: Balasubramanian Ravindran
Guest Editors: Davidraj Johnravindar and
Pounsamy Maharaja





Copyright © 2023 Hindawi Limited. All rights reserved.

This is a special issue published in "Journal of Nanomaterials." All articles are open access articles distributed under the Creative Commons Attribution License, which permits unrestricted use, distribution, and reproduction in any medium, provided the original work is properly cited.




Chief Editor

Stefano Bellucci , Italy

















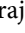
















Associate Editors

Ilaria Armentano, Italy
Stefano Bellucci , Italy
Paulo Cesar Morais , Brazil
William Yu , USA

Academic Editors

Buzuayehu Abebe, Ethiopia
Domenico Acierno , Italy
Sergio-Miguel Acuña-Nelson , Chile
Katerina Aifantis, USA
Omer Alawi , Malaysia
Nageh K. Allam , USA
Muhammad Wahab Amjad , USA
Martin Andersson, Sweden
Hassan Azzazy , Egypt
Ümit Ağbulut , Turkey
Vincenzo Baglio , Italy
Lavinia Balan , France
Nasser Barakat , Egypt
Thierry Baron , France
Carlos Gregorio Barreras-Urbina, Mexico
Andrew R. Barron , USA
Enrico Bergamaschi , Italy
Sergio Bietti , Italy
Raghvendra A. Bohara, India
Mohamed Bououdina , Saudi Arabia
Victor M. Castaño , Mexico
Albano Cavaleiro , Portugal
Kondareddy Cherukula , USA
Shafiul Chowdhury, USA
Yu-Lun Chueh , Taiwan
Elisabetta Comini , Italy
David Cornu, France
Miguel A. Correa-Duarte , Spain
P. Davide Cozzoli , Italy
Anuja Datta , India
Loretta L. Del Mercato, Italy
Yong Ding , USA
Kaliannan Durairaj , Republic of Korea
Ana Espinosa , France
Claude Estournès , France
Giuliana Faggio , Italy
Andrea Falqui , Saudi Arabia

Matteo Ferroni , Italy
Chong Leong Gan , Taiwan
Siddhartha Ghosh, Singapore
Filippo Giubileo , Italy
Iaroslav Gnilitzkiy, Ukraine
Hassanien Gomaa , Egypt
Fabien Grasset , Japan
Jean M. Greneche, France
Kimberly Hamad-Schifferli, USA
Simo-Pekka Hannula, Finland
Michael Harris , USA
Hadi Hashemi Gahruei , Iran
Yasuhiko Hayashi , Japan
Michael Z. Hu , USA
Zhengwei Huang , China
Zafar Iqbal, USA
Balachandran Jeyadevan , Japan
Xin Ju , China
Antonios Kelarakis , United Kingdom
Mohan Kumar Kesarla Kesarla , Mexico
Ali Khorsand Zak , Iran
Avvaru Praveen Kumar , Ethiopia
Prashant Kumar , United Kingdom
Jui-Yang Lai , Taiwan
Saravanan Lakshmanan, India
Meiyong Liao , Japan
Shijun Liao , China
Silvia Licoccia , Italy
Zainovia Lockman, Malaysia
Jim Low , Australia
Rajesh Kumar Manavalan , Russia
Yingji Mao , China
Ivan Marri , Italy
Laura Martinez Maestro , United Kingdom
Sanjay R. Mathur, Germany
Tony McNally, United Kingdom
Pier Gianni Medaglia , Italy
Paul Munroe, Australia
Jae-Min Myoung, Republic of Korea
Rajesh R. Naik, USA
Albert Nasibulin , Russia
Ngoc Thinh Nguyen , Vietnam
Hai Nguyen Tran , Vietnam
Hiromasa Nishikiori , Japan

Sherine Obare , USA
Abdelwahab Omri , Canada
Dillip K. Panda, USA
Sakthivel Pandurengan , India
Dr. Asisa Kumar Panigrahy, India
Mazeyar Parvinzadeh Gashti , Canada
Edward A. Payzant , USA
Alessandro Pegoretti , Italy
Oscar Perales-Pérez, Puerto Rico
Anand Babu Perumal , China
Suresh Perumal , India
Thathan Premkumar , Republic of Korea
Helena Prima-García, Spain
Alexander Pyatenko, Japan
Xiaoliang Qi , China
Haisheng Qian , China
Baskaran Rangasamy , Zambia
Soumyendu Roy , India
Fedlu Kedir Sabir , Ethiopia
Lucien Saviot , France
Shu Seki , Japan
Senthil Kumaran Selvaraj , India
Donglu Shi , USA
Muhammad Hussnain Siddique , Pakistan
Bhanu P. Singh , India
Jagpreet Singh , India
Jagpreet Singh, India
Surinder Singh, USA
Thangjam Ibomcha Singh , Republic of Korea
Korea
Vidya Nand Singh, India
Vladimir Sivakov, Germany
Tushar Sonar, Russia
Pingan Song , Australia
Adolfo Speghini , Italy
Kishore Sridharan , India
Marinella Striccoli , Italy
Andreas Stylianou , Cyprus
Fengqiang Sun , China
Ashok K. Sundramoorthy , India
Bo Tan, Canada
Leander Tapfer , Italy
Dr. T. Sathish Thanikodi , India
Arun Thirumurugan , Chile
Roshan Thotagamuge , Sri Lanka

Valeri P. Tolstoy , Russia
Muhammet S. Toprak , Sweden
Achim Trampert, Germany
Tamer Uyar , USA
Cristian Vacacela Gomez , Ecuador
Luca Valentini, Italy
Viet Van Pham , Vietnam
Antonio Vassallo , Italy
Ester Vazquez , Spain
Ajayan Vinu, Australia
Ruibing Wang , Macau
Magnus Willander , Sweden
Guosong Wu, China
Ping Xiao, United Kingdom
Zhi Li Xiao , USA
Yingchao Yang , USA
Hui Yao , China
Dong Kee Yi , Republic of Korea
Jianbo Yin , China
Hesham MH Zakaly , Russia
Michele Zappalorto , Italy
Mauro Zarrelli , Italy
Osman Ahmed Zeleke, Ethiopia
Wenhui Zeng , USA
Renyun Zhang , Sweden

Contents

Retracted: Utilization of Eco-Friendly Waste Eggshell Catalysts for Enhancing Liquid Product Yields through Pyrolysis of Forestry Residues

Journal of Nanomaterials




Retraction (1 page), Article ID 9848562, Volume 2023 (2023)

Retracted: Copper Oxide Nanoparticles Incorporated in the Metal Mesh Used to Enhance the Heat Transfer Performance of the Catalytic Converter and to Reduce Emission

Journal of Nanomaterials




Retraction (1 page), Article ID 9810313, Volume 2023 (2023)




Tailoring of Ag₃PO₄-Anchored Hydroxyapatite Nanophotocatalyst with Tunable Particle Size by a Facile Ion-Exchange Method for Organic Textile Dyes Photodegradation

Surendran Dhatchayani , Krishnasamy Sankaranarayanan , and K. Kathiresan 

Research Article (15 pages), Article ID 9882964, Volume 2023 (2023)

Mycosynthesis of Zinc Oxide Nanoparticles Coated with Silver using *Ganoderma lucidum* (Curtis) P. Karst and Its Evaluation of *In Vitro* Antidiabetic and Anticancer Potential

D. S. Ranjith Santhosh Kumar , N. Elango, Gayathri Devi Selvaraju , Paul A. Matthew ,

Senthilkumar Palanisamy , Hayoung Cho, Fatimah S. Al Khattaf, Ashraf Atef Hatamleh , and Amit Dutta Roy 

Research Article (9 pages), Article ID 2798532, Volume 2022 (2022)

Mycosynthesis of Noble Metal Nanoparticle Using *Laetiporus versisporus* Mushroom and Analysis of Antioxidant Activity

M. R. Farzana Fathima , A. Usha Raja Nanthini , Fatimah S. Al-Khattaf, Ashraf Atef Hatamleh, and Sadib Bin Kabir 

Research Article (11 pages), Article ID 8086803, Volume 2022 (2022)


Recent Developments on Magnetically Separable Ferrite-Based Nanomaterials for Removal of Environmental Pollutants

Shreyas Pansambal , Arpita Roy , Hamza Elsayed Ahmed Mohamed, Rajeshwari Oza , Canh Minh Vu ,

Abdolrazagh Marzban , Ankush Chauhan , Suresh Ghotekar , and H. C. Ananda Murthy 






Review Article (15 pages), Article ID 8560069, Volume 2022 (2022)

Green Catalytic Pyrolysis: An Eco-Friendly Route for the Production of Fuels and Chemicals by Blending Oil Industry Wastes and Waste Furniture Wood

M. D. Mohan Gift, Savita Verma, Kalapala Prasad, K. Kathiresan, Rohi Prasad, T. Logeswaran, Suresh Ghotekar, D. V. Thao, and J. Isaac JoshuaRamesh Lalvani 




Research Article (9 pages), Article ID 9381646, Volume 2022 (2022)

Enhancing the Production Yield of *Jatropha* and *Pongamia* Oil-Based Biodiesel by Introducing Nanocatalyst






Sathiesh Kumar Nagaraj , Paranthaman Ponnusamy , P. M. Gopal , Huu Tap Van , Lan Huong Nguyen, and Sadib Bin Kabir 

Research Article (6 pages), Article ID 6723296, Volume 2022 (2022)



Properties Evaluation of Electroless Ni-Coated Low-Carbon Steels

M. S. Senthil Saravanan, V. Ananda, S. P. Kumaresh Babu, G. Ramalingam , A. Haiter Lenin , Jemal Mohammed Yimer , J. B. Sajin, and Trijo Tharayil
Research Article (8 pages), Article ID 8497927, Volume 2022 (2022)


[Retracted] Copper Oxide Nanoparticles Incorporated in the Metal Mesh Used to Enhance the Heat Transfer Performance of the Catalytic Converter and to Reduce Emission

M. Prabhakar , S. Prakash , M. Saravana Kumar, S. Sendilvelan , M. V. Sreerag, B. S. Akhil Vishnu, Asif Samad, B. Jansi Rani, Haiter Lenin Allasi , Adisu Haile , and Praveen Kumar Issac
Research Article (9 pages), Article ID 9169713, Volume 2022 (2022)








Synthesis of a Novel Nanoparticle BaCoO_{2.6} through Sol-Gel Method and Elucidation of Its Structure and Electrical Properties

Fareenpoornima Rafiq, Parthipan Govindsamy , and Selvakumar Periyasamy 
Research Article (15 pages), Article ID 3877879, Volume 2022 (2022)




Polymeric Droplets on SiO₂ Nanoparticles through Wastewater Treatment of Carbon-Based Contaminants in Photocatalytic Degradation

Abel Saka , Jule Leta Tesfaye , Lamessa Gudata , S. Karthi, N. Nagaprasad , Suraj Kumar Bhagat , Muhammad Yaqub, and Krishnaraj Ramaswamy 
Research Article (7 pages), Article ID 8464088, Volume 2022 (2022)

Antibacterial Efficacy of Phytosynthesized Multi-Metal Oxide Nanoparticles against Drug-Resistant Foodborne Pathogens

Vijayalakshmi Selvakumar , Karnan Muthusamy, Amitava Mukherjee , Shahana Farheen S., Ramachandran Chelliah , Kaliyan Barathikannan , Deog-Hwan Oh , Ramamoorthy Ayyamperumal , and Shankar Karuppanan 
Research Article (9 pages), Article ID 6506796, Volume 2022 (2022)

[Retracted] Utilization of Eco-Friendly Waste Eggshell Catalysts for Enhancing Liquid Product Yields through Pyrolysis of Forestry Residues

S. Kaliappan, M. Karthick, Pravin P. Patil, P. Madhu , S. Sekar, Ravi Mani, D. Francisca Kalavathi, S. Mohanraj , and Solomon Neway Jida 
Research Article (10 pages), Article ID 3445485, Volume 2022 (2022)

Retraction

Retracted: Utilization of Eco-Friendly Waste Eggshell Catalysts for Enhancing Liquid Product Yields through Pyrolysis of Forestry Residues

Journal of Nanomaterials

Received 20 June 2023; Accepted 20 June 2023; Published 21 June 2023

Copyright © 2023 Journal of Nanomaterials. This is an open access article distributed under the Creative Commons Attribution License, which permits unrestricted use, distribution, and reproduction in any medium, provided the original work is properly cited.

This article has been retracted by Hindawi following an investigation undertaken by the publisher [1]. This investigation has uncovered evidence of one or more of the following indicators of systematic manipulation of the publication process:

1. Discrepancies in scope
2. Discrepancies in the description of the research reported
3. Discrepancies between the availability of data and the research described
4. Inappropriate citations
5. Incoherent, meaningless and/or irrelevant content included in the article
6. Peer-review manipulation

The presence of these indicators undermines our confidence in the integrity of the article's content and we cannot, therefore, vouch for its reliability. Please note that this notice is intended solely to alert readers that the content of this article is unreliable. We have not investigated whether authors were aware of or involved in the systematic manipulation of the publication process.

Wiley and Hindawi regrets that the usual quality checks did not identify these issues before publication and have since put additional measures in place to safeguard research integrity.

We wish to credit our own Research Integrity and Research Publishing teams and anonymous and named external researchers and research integrity experts for contributing to this investigation.

The corresponding author, as the representative of all authors, has been given the opportunity to register their agreement or disagreement to this retraction. We have kept a record of any response received.

References

- [1] S. Kaliappan, M. Karthick, P. P. Patil et al., "Utilization of Eco-Friendly Waste Eggshell Catalysts for Enhancing Liquid Product Yields through Pyrolysis of Forestry Residues," *Journal of Nanomaterials*, vol. 2022, Article ID 3445485, 10 pages, 2022.

Retraction

Retracted: Copper Oxide Nanoparticles Incorporated in the Metal Mesh Used to Enhance the Heat Transfer Performance of the Catalytic Converter and to Reduce Emission

Journal of Nanomaterials

Received 20 June 2023; Accepted 20 June 2023; Published 21 June 2023

Copyright © 2023 Journal of Nanomaterials. This is an open access article distributed under the Creative Commons Attribution License, which permits unrestricted use, distribution, and reproduction in any medium, provided the original work is properly cited.

This article has been retracted by Hindawi following an investigation undertaken by the publisher [1]. This investigation has uncovered evidence of one or more of the following indicators of systematic manipulation of the publication process:

1. Discrepancies in scope
2. Discrepancies in the description of the research reported
3. Discrepancies between the availability of data and the research described
4. Inappropriate citations
5. Incoherent, meaningless and/or irrelevant content included in the article
6. Peer-review manipulation

The presence of these indicators undermines our confidence in the integrity of the article's content and we cannot, therefore, vouch for its reliability. Please note that this notice is intended solely to alert readers that the content of this article is unreliable. We have not investigated whether authors were aware of or involved in the systematic manipulation of the publication process.

Wiley and Hindawi regrets that the usual quality checks did not identify these issues before publication and have since put additional measures in place to safeguard research integrity.

We wish to credit our own Research Integrity and Research Publishing teams and anonymous and named external researchers and research integrity experts for contributing to this investigation.

The corresponding author, as the representative of all authors, has been given the opportunity to register their agreement or disagreement to this retraction. We have kept a record of any response received.

References

- [1] M. Prabhakar, S. Prakash, M. Saravana Kumar et al., "Copper Oxide Nanoparticles Incorporated in the Metal Mesh Used to Enhance the Heat Transfer Performance of the Catalytic Converter and to Reduce Emission," *Journal of Nanomaterials*, vol. 2022, Article ID 9169713, 9 pages, 2022.

Research Article

Tailoring of Ag_3PO_4 -Anchored Hydroxyapatite Nanophotocatalyst with Tunable Particle Size by a Facile Ion-Exchange Method for Organic Textile Dyes Photodegradation

Surendran Dhatchayani ¹, Krishnasamy Sankaranarayanan ¹ and K. Kathiresan ²

¹Functional Materials Laboratory, Department of Physics, Alagappa University, Karaikudi 630003, Tamil Nadu, India

²School of Civil Engineering and Architecture, Adama Science and Technology University, Adama, Ethiopia

Correspondence should be addressed to Krishnasamy Sankaranarayanan; hhrsankar@yahoo.com and K. Kathiresan; kathiresan.karuppanan@astu.edu.et

Received 5 August 2022; Revised 26 September 2022; Accepted 6 October 2022; Published 10 April 2023

Academic Editor: Balasubramani Ravindran

Copyright © 2023 Surendran Dhatchayani et al. This is an open access article distributed under the Creative Commons Attribution License, which permits unrestricted use, distribution, and reproduction in any medium, provided the original work is properly cited.

Silver phosphate (Ag_3PO_4) exhibits excellent photocatalytic performance but has limitation in its stability and reusability. To overcome the issue of reusability, composites of silver phosphate nanostructures are tailored. This paper elucidates the photocatalytic study of silver phosphate-anchored hydroxyapatite (HA) ($\text{Ca}_{10}(\text{PO}_4)_6(\text{OH})_2$) on the degradation of commercial textile dye, Sunfix Red (SR) S3B 150% by changing the experimental parameters such as catalyst concentration, dye concentration, and pH of the dye solution under the sunlight. Silver phosphate-anchored HA ($\text{HA_Ag}_3\text{PO}_4(x)$) was prepared via a two-step process. HA was synthesized by a simple wet chemical precipitation and silver phosphate-anchored HA ($\text{HA_Ag}_3\text{PO}_4(x)$) via *in situ* ion-exchange method. The synthesized photocatalysts were subjected to characterization studies such as X-ray diffraction (XRD), Fourier transform infrared (FTIR) spectroscopy, transmission electron microscopy (TEM), ultraviolet–visible spectroscopy, and X-ray photoelectron spectroscopy (XPS). All the synthesized composites exhibited the bandgap of 2.34 eV and degraded SR in 45 min with the rate constant 0.07168 min^{-1} under sunlight. The trapping tests for radicals were done to study the role of free radicals in the degradation of the dye, SR, and the possible degradation mechanism was proposed. The postphotocatalytic analysis of XRD showed that the structure of Ag_3PO_4 remained intact declaring its structural stability. It was observed that the concentration of AgNO_3 precursor influenced the number of nucleation over the surface of HA and the particle size of Ag_3PO_4 . The applicability of the synthesized material was extended to other organic dyes such as Sunzol Black (SB) DN conc., methylene blue (MB), and rhodamine B (RhB) by the prepared composite and the findings were presented.

1. Introduction

Exploitation of all kinds of natural resources and their replenishment is the major considerations in this age. Among these issues, water pollution and scarcity are making the situation hectic since water is an essential element of social and economic development. Therefore, many efforts have been devoted in order to conserve and sustain water resources. Urbanization and industrialization are not only exploiting the water resources, but also releasing effluents into water to such an extent that it is creating a great threat to the flora and fauna as well as humankind. The water contaminants include a wide range of chemicals, pathogens, and physical

factors such as temperature, etc. [1, 2]. Textile industry is an important water-contaminant source as it consumes huge quantity of water and releases massive effluents. For the past decades, the researchers are paying much attention to the removal of textile organic pollutants by various methods which include biodegradation, electrocoagulation, photodegradation, oxidation, adsorption, and ultrafiltration [3–8]. Among them, photocatalysis has proved to be an excellent method to decompose the organic effluents being highly efficient and cost-effective [9, 10]. Due to photocatalytic efficiency and cost-effectiveness, TiO_2 -based photocatalysts have been of research interest yet their practical application is limited because of their higher bandgap energy which

falls in the UV region [10]. Many researchers focus on other intriguing materials such as $g\text{-C}_3\text{N}_4$, SnO_2 , and ZnO -based heterostructured photocatalysts owing to their tunable bandgaps and photocatalytic efficiency [6, 8, 11].

For recent years, Ag_3PO_4 is being an intriguing candidate for photocatalytic degradation. Ag_3PO_4 possesses high photocatalytic efficiency and its quantum efficiency is nearly 90% [12]. In addition to that, the bandgap of Ag_3PO_4 is 2.34 eV, which makes it suitable for solar-light-driven photocatalysis. In this regard, Ag_3PO_4 can be undoubtedly an interesting candidate to be studied. Nevertheless, its higher solubility and poor stability hinder its vast application [9]. Ag_3PO_4 is vulnerable to photocorrosion. However, Ag_3PO_4 -based heterogeneous composites have been gaining substantial attention due to their enhanced physical and chemical properties, which make them outstanding photocatalysts [13, 14]. Hydroxyapatite (HA) is the inorganic mineral phase of biological hard tissues and is abundant in nature. HA is a remarkable candidate in biomedical as well as environmental applications due to its exceptional biocompatibility, nontoxicity, structural flexibility, facile synthesis, and cost-effectiveness [15, 16]. HA is being tailored with tunable characteristics in a variety of applications owing to (1) the flexibility of the apatite structure that enables HA to host almost half of the elements in the periodic table, (2) an effortless ion-exchange process facilitates the replacement of Ca^{2+} ions in HA by a wide range of ions, and (3) substitution of both anions and cations is possible, i.e., PO_4^{3-} and OH^- functionalities in the apatite structure can be easily replaced by a variety of species like SeO_3^{2-} , VO_4^{3-} , SiO_4^{2-} , CO_3^{2-} , and halides [17–19]. Moreover, HA can be a prominent substrate for a photocatalyst like Ag_3PO_4 for the following features: (1) adsorption capability of the catalyst is very crucial in photocatalysis process and HA can serve this being a well-known adsorbent for inorganic and organic matters, (2) mass transfer limitations can be reduced, (3) hinders the photogenerated electron–hole recombination by effective separation, (4) heterostructures can easily be tailored, and (5) possesses excellent thermal stability, biodegradability, and nontoxicity [9, 15, 20].

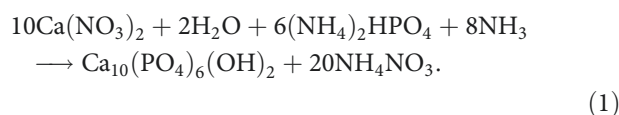
In this work, $\text{HA_Ag}_3\text{PO}_4$ composites were synthesized in two steps in which neat hydroxyapatite was synthesized via chemical precipitation technique and Ag_3PO_4 nanoparticles were anchored on hydroxyapatite via a facile and at the same time very effective postsynthesis process, ion-exchange method [21]. Still, more studies are required in order to explore the behaviors of the photocatalyst for different dyes. In this work, the photocatalytic behavior of Ag_3PO_4 composite in the degradation of the commercial textile dye Sunfix Red (SR) S3B 150% for the first time was studied, and also the degradation under different experimental conditions was investigated. Moreover, the applicability of the prepared composites on other commercial dyes was examined.

2. Experimental

2.1. Materials. All the reagents of analytical grade were purchased and used without further purification. Calcium nitrate tetrahydrate ($\text{Ca}(\text{NO}_3)_2 \cdot 4\text{H}_2\text{O}$), diammonium hydrogen

phosphate ($(\text{NH}_4)_2\text{HPO}_4$), silver nitrate (AgNO_3), and NH_4OH 25% were obtained from Merck, Germany.

2.2. Preparation of Neat HA. The neat HA was prepared by wet chemical precipitation technique reported elsewhere [22] which initially involves the preparation of 0.5 M calcium nitrate solution and 0.3 M diammonium hydrogen phosphate solution. Then, the phosphate solution was added to the calcium precursor at temperature 60°C. The pH of the reaction solution was maintained at 10.5 by adding sufficient amount of ammonium hydroxide and was stirred for 2 hr at 60°C followed by 24 hr aging. Later, the precipitate was filtered and washed many times with deionized water and ethanol. Subsequently, the precipitate was dried at 70°C for 24 hr. The chemical reaction is given as follows:



2.3. Preparation of Ag_3PO_4 -Anchored HA ($\text{HA_Ag}_3\text{PO}_4(x)$). Ag_3PO_4 -anchored HA was synthesized via *in situ* ion-exchange process reported elsewhere [14] and the schematic illustration is given in Figure 1. A hundred milliliters of AgNO_3 solution of appropriate concentration (0.02, 0.05, 0.08 M) was added dropwise into the aqueous dispersion of HA (3 g in 100 mL of deionized water). Subsequently, it was subjected to a vigorous and continuous stirring for 4 hr under dark condition. Then, the composite was separated by centrifugation, washed repeatedly with distilled water, and dried at 60°C in vacuum oven overnight. By this way, the nanocomposites were prepared with different AgNO_3 concentrations of 0.02, 0.05, and 0.08 M and named as $\text{HA_Ag}_3\text{PO}_4(\text{a})$, $\text{HA_Ag}_3\text{PO}_4(\text{b})$, and $\text{HA_Ag}_3\text{PO}_4(\text{c})$, respectively.

2.4. Characterization Techniques. The structural characterization was carried out through X-ray diffraction (XRD) pattern of the sample, which was recorded by a PANalytical X'Pert Pro X-ray diffractometer ($\lambda = 1.5418 \text{ \AA}$) at room temperature. The functional groups of the prepared samples were identified using Fourier transform infrared (FTIR) spectrometer (Perkin Elmer-Spectrum RX I). X-ray photoelectron spectra (XPS) was recorded by a PHI VersaProbe III photoelectron spectrometer and the surface chemical composition and valence state of the prepared samples were studied. The morphologies of samples were examined by JEOL-2100+ high-resolution transmission electron microscope. The optical properties of the samples were analyzed using the UV–vis spectrometer (Thermo Fisher Evolution 220). The concentration of the dye solutions was studied by Electra photometer.

2.5. Analysis of Photocatalytic Performance of the Prepared Composites. The photocatalytic behavior of the prepared samples was investigated through the photodegradation of the commercial organic dyes under sunlight. Initially, the anionic organic dye SR S3B 150% ($\text{C}_{44}\text{H}_{24}\text{N}_{14}\text{Na}_6\text{O}_{20}\text{S}_6$) was taken as a model and the photodegradation was evaluated under different experimental conditions such as Ag_3PO_4 concentration, dosage of photocatalyst, and concentration of

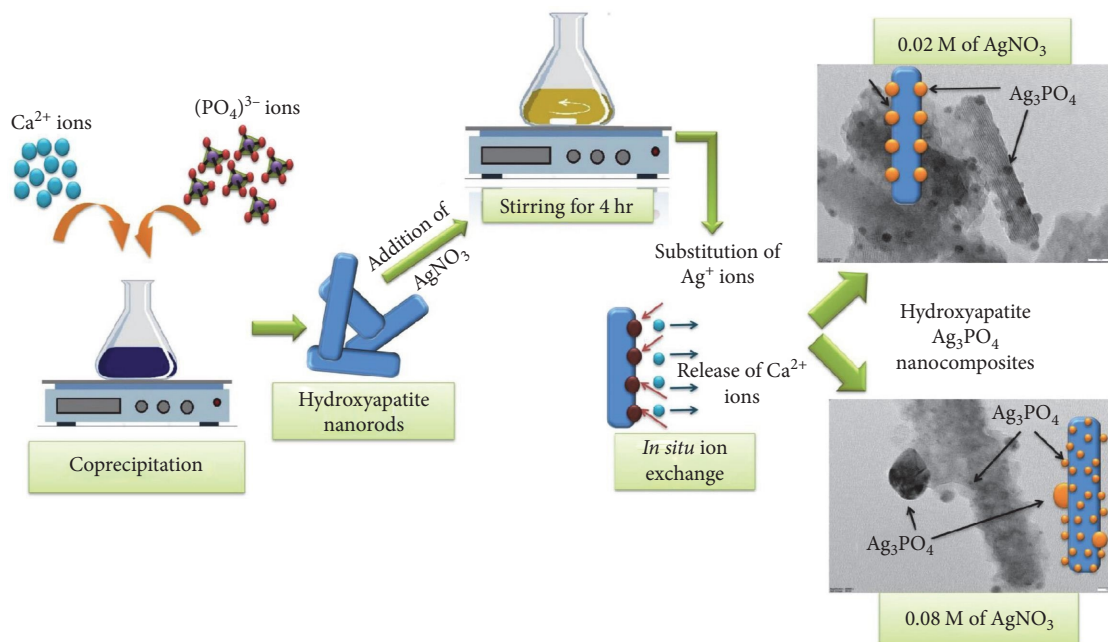


FIGURE 1: Schematic illustration of the experiment for preparing Ag_3PO_4 -anchored HA.

the dye solution. In addition to these, the initial pH of the solution also influences the adsorption and degradation process and, hence, it is very essential for consideration [23]. Therefore, the photodegradation of the dye solution with different initial pH values was also examined. Later, the photocatalytic activity of the selected photocatalyst was also extended to other organic dyes, namely, Sunzol Black (SB) DN conc. (anionic), methylene blue (MB; cationic), rhodamine B (RhB; cationic), and cocktail (CT) of the aforementioned four different dyes. The required concentration of dye solutions was prepared and the initial pH of the dye solutions were adjusted with 2 mol/l NaOH solution or concentrated HNO_3 . The appropriate amounts of catalysts were added to the dye solutions and were magnetically stirred for 1 hr in dark condition to attain adsorption and desorption equilibrium before photocatalytic studies. After irradiation with sunlight, the aliquots were collected in equal intervals and the concentration of the centrifuged aliquots was determined using UV-visible spectrometer. The decolorization rate of the dyes ($D\%$) were calculated by the following equation:

$$D\% = \frac{(C_0 - C)}{C_0} \times 100, \quad (2)$$

where C_0 and C were the initial and instantaneous concentrations of the dye solution, respectively.

The role of active radical species in the photocatalytic degradation process was also examined by applying scavengers. The scavengers such as isopropyl alcohol (IPA), disodium ethylenediaminetetraacetate (EDTA), and ascorbic acid were used to trap the hydroxyl ($\cdot\text{OH}$), photogenerated holes (h^+), and superoxide ($\cdot\text{O}_2^-$) radicals, respectively. The scavengers were added to the organic dye solutions at a concentration of

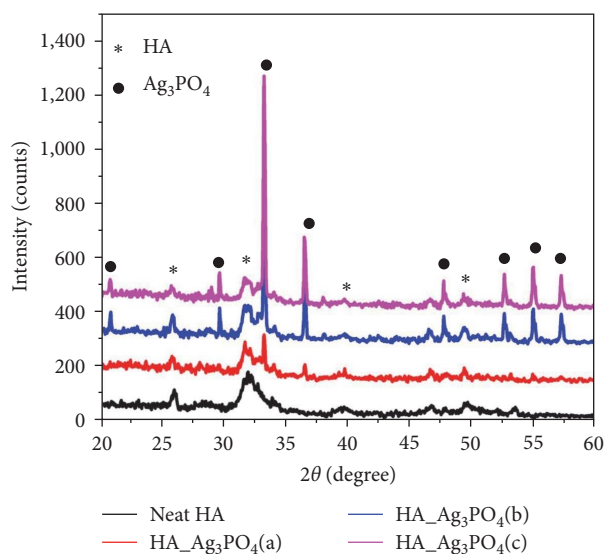


FIGURE 2: XRD patterns of neat HA and the nanocomposites.

1 mmol/L before the addition of photocatalyst and subjected to the photocatalytic degradation as abovementioned.

3. Results and Discussion

3.1. Characterization of the Prepared Composites

3.1.1. XRD Analysis. The XRD patterns of as-prepared neat HA and $\text{HA_Ag}_3\text{PO}_4(x)$ composites were presented in Figure 2. The XRD patterns of all the samples were indexed against HA (JCPDS# 009-0432) and Ag_3PO_4 (JCPDS Card#006-0505). The XRD patterns of $\text{HA_Ag}_3\text{PO}_4(x)$, as shown in Figure 2,

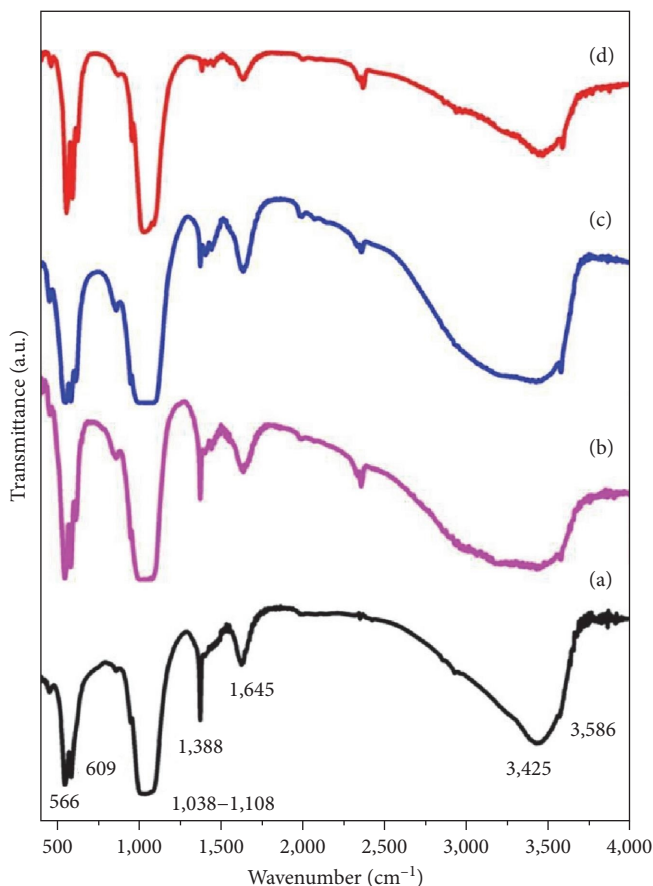


FIGURE 3: FTIR spectra of neat HA (a); HA_{Ag₃PO₄}(a) (b); HA_{Ag₃PO₄}(b) (c); HA_{Ag₃PO₄}(c) (d).

evidence the presence of Ag₃PO₄ in the background of HA. Besides, the intensities of the peaks representing Ag₃PO₄ get increased with the increase in AgNO₃ molar ratio; meanwhile, the characteristic HA peaks remain intact suggesting that the ion-exchange process proceeded by retaining the structure of HA. Further, it ascertains the composite nature of the HA_{Ag₃PO₄}(*x*).

3.1.2. FTIR Analysis. FTIR spectra of the prepared samples are depicted in Figure 3 and are exhibiting the signature bands of hydroxyapatite. The bending vibrational modes of PO₄³⁻ are identified at 566 and 610 cm⁻¹ and the absorption bands corresponding to 1,038–1,108 and 967 cm⁻¹ are ascribed to the stretching vibration modes of PO₄³⁻. The presence of absorption peaks at 1,389 and 1,645 cm⁻¹ approves the incorporation of carbonate ions in HA structure. The presence of hydroxyl group is confirmed by the absorption at 3,586 cm⁻¹ and the broad band around 3,425 cm⁻¹ is due to the absorbed water [24, 25]. The absorption regions (967 and 1,080 cm⁻¹) of asymmetric stretching of P–O–P associated with Ag₃PO₄ coincide with the signature phosphate bands of HA and no metal Ag-related bands in the observed FTIR spectra of the composites (b–d), as shown in Figure 3, were detected [26].

3.1.3. XPS Analysis. Neat HA and HA_{Ag₃PO₄}(c) were subjected to the XPS analysis and Figures 4 and 5 display their

corresponding spectra. The wide range spectra of neat and composite HA exhibit the presence of the elements of hydroxyapatite and additionally Ag in the composite. The characteristic doublet at the binding energies 373.35 and 367.46 eV corresponding to Ag⁺ was evidenced for the sample HA_{Ag₃PO₄}(c) (Figure 5(d)), which strongly suggests the presence of Ag₃PO₄ in the composite [27, 28]. While examining the core level spectra of Ca and P in the samples HA and HA_{Ag₃PO₄}(c), there is no significant shift found as the corresponding binding energies to Ca 2p_{3/2} and Ca 2p_{1/2} were detected around 346.5 and 350 eV, and for P, it was observed around 132.5 eV [29]. The deconvolution of O 1s core spectra of HA_{Ag₃PO₄}(c) discloses three distinct peaks. The binding energy 529.5 eV is ascribed to the lattice oxygen of Ag₃PO₄, which is absent in that of neat HA. The other two peaks are of binding energies 530.9 and 532.6 eV. The earlier is assigned to the oxygen atoms in P=O and the later can be contributed by the oxygen from O–H [29].

In addition, the photoelectron peaks corresponding to C 1s were also identified. It is quite common to get carbonated hydroxyapatite since the synthesis method in open air facilitates the incorporation of atmospheric carbonates in the HA structure. The photoelectron peaks around 284.5 and 286.1 eV are representing to C–C and C–O–C of the absorbed hydrocarbons, whereas 288.2 eV is ascribed to C=O bonds in carbonate [30].

3.1.4. TEM Analysis. The morphological features of the synthesized neat HA and HA-anchored Ag₃PO₄ composites are depicted in Figure 6. The neat HA prepared via simple wet precipitation method exhibited nanorod morphology (Figure 6(a)). While examining the TEM image of composite HA_{Ag₃PO₄}(a), the homogeneous distribution of Ag₃PO₄ spheres of size about 4 nm over the surface of hydroxyapatite is evidenced (Figure 6(d)). The TEM investigation was also extended to the composite HA_{Ag₃PO₄}(c) with the highest Ag⁺ concentration in the present study, which is presented in Figures 6(e) and 6(f). Interestingly, Ag₃PO₄ formations are found to be greater in number than that could be observed in the case of HA_{Ag₃PO₄}(a) (lower Ag⁺ concentration). The higher Ag⁺ concentration (0.08 M) facilitated a larger amount of nucleations over HA surface and also resulted in the reduction of Ag₃PO₄ particle size as indicated by blue arrows in Figure 6(e). Due to the decline in particle size, the surface area to volume ratio was expected to increase, which is a more favorable condition for photocatalysis [27]. Meanwhile, few larger sized Ag₃PO₄ spheres around 5 and 15 nm were also observed on HA as indicated by yellow arrows in Figure 6(e).

3.1.5. UV–Vis Diffuse Reflectance Spectroscopy. The UV–visible diffuse reflectance spectra (DRS) of pure HA and HA_{Ag₃PO₄}(*x*) are shown in Figure 7 and their bandgaps are depicted in Figure 8. Investigation of the bandgaps (Figure 8) gives the essential information about the photocatalytic behavior under visible light. The bandgap of neat HA was found to be 3.4 eV, whereas the composites (HA_{Ag₃PO₄}(*x*)) exhibited bandgap energy of 2.34 eV. The narrowed bandgap (2.34 eV) of the composites is due to the

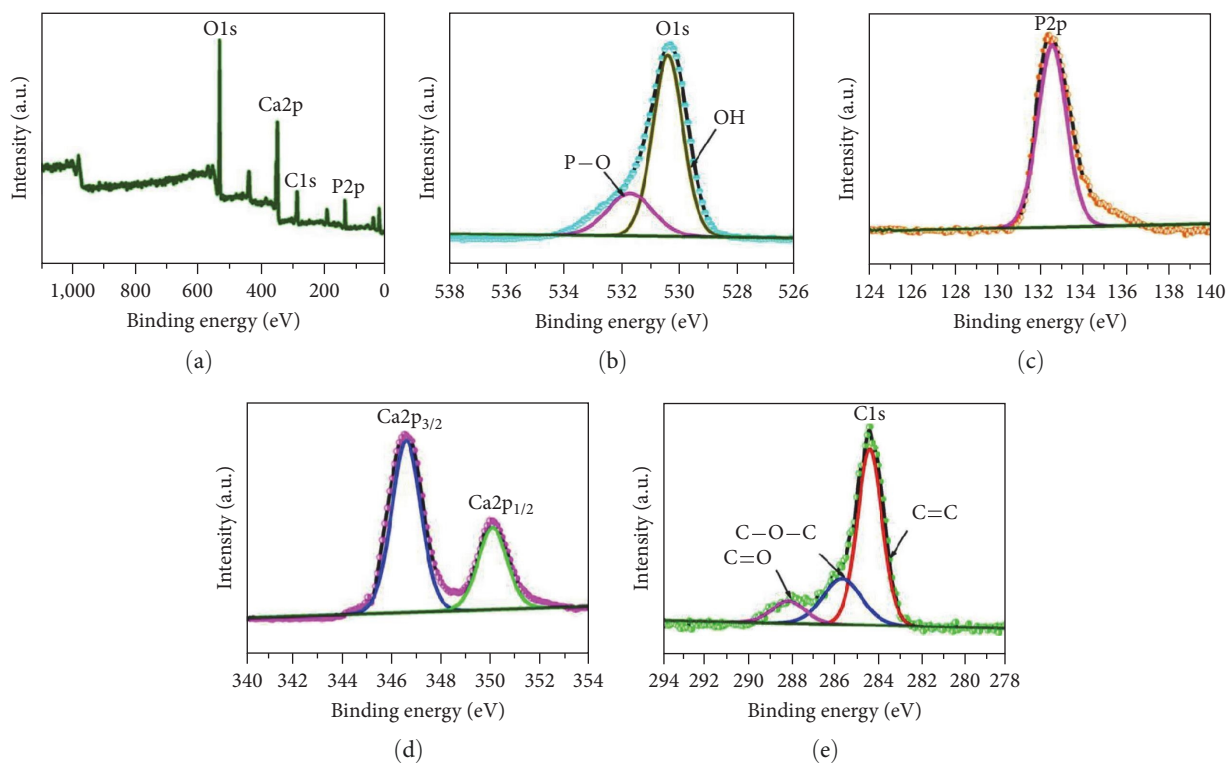


FIGURE 4: XPS spectra of neat HA.

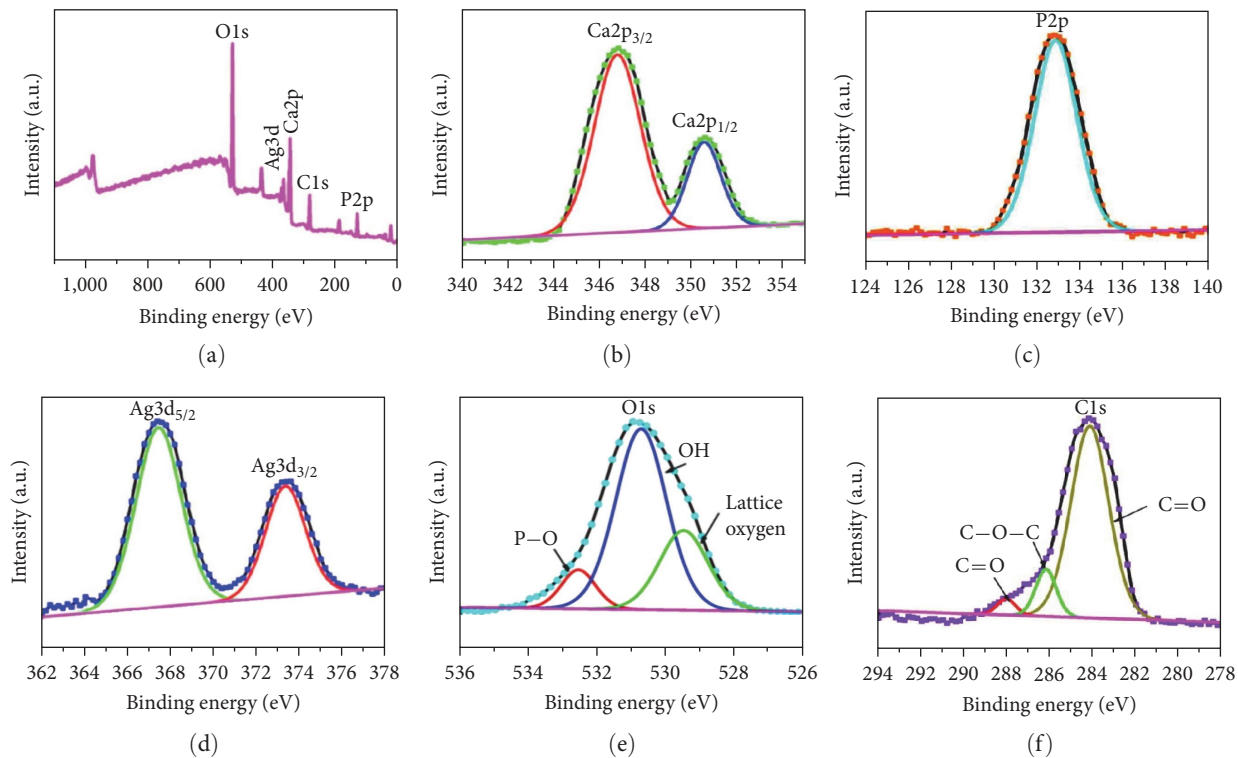


FIGURE 5: XPS spectra of HA_{Ag₃PO₄(c).}

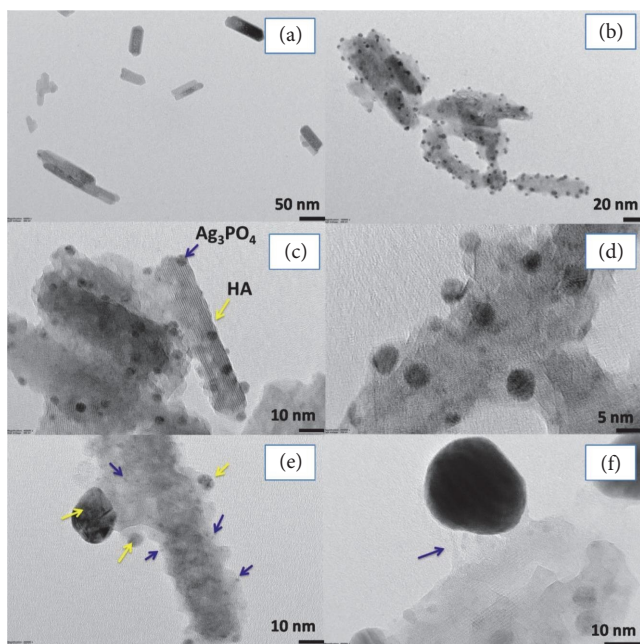


FIGURE 6: TEM images of neat HA (a); HA_Ag₃PO₄(a) at different magnifications (b–d); HA_Ag₃PO₄(c) at different magnifications (e and f).

presence of Ag₃PO₄ which is well matched with the reported values of Ag₃PO₄ [28] and enables the photocatalyst to perform under visible light.

In addition to the bandgap, the valence band and conduction band edge potentials were also estimated by the following empirical formula:

$$E_{VB} = \chi - E^c + 0.5E_g, \quad (3)$$

$$E_{CB} = E_{VB} - E_g, \quad (4)$$

where E_{VB} and E_{CB} are the valence band and conduction band edge potentials, respectively; χ is Mulliken electronegativity of Ag₃PO₄ which is the geometric mean of the electronegativity of the constituent atoms and it was calculated to be 5.96 eV; E^c represents the energy of free electrons on the hydrogen scale (−4.5 eV); and E_g is the bandgap energy of Ag₃PO₄. Thus, calculated VB and CB potentials of Ag₃PO₄ are 2.63 and 0.29 eV, respectively.

3.2. Photocatalytic Degradation of Organic Dyes. The photocatalytic degradation of all the selected organic dyes in the presence of the prepared photocatalysts were analyzed after 60 min adsorption and considered as 0 min for photocatalysis process in sunlight. First, photodegradation of the anionic dye SR S3B 150% was carried out under different conditions such as dye concentration, photocatalyst concentration, and pH of the dye solution, and their influence on the degradation of the dye was investigated. In addition, blank dye solution in the absence of photocatalyst was also examined as a control. For the better investigation of the photocatalytic behavior of the prepared samples, zero-order, first-order,

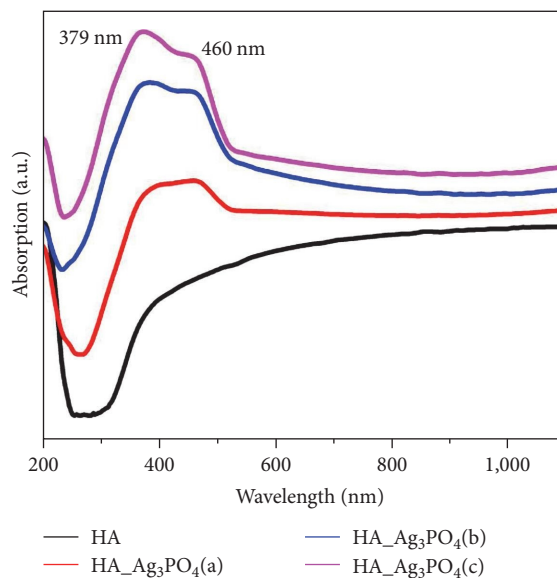


FIGURE 7: UV-visible diffuse reflectance spectra of neat HA and the composites.

and second-order kinetic studies were carried out and the rate constants were determined by the following equations:

zero-order kinetic equation:

$$C_0 - C = k_0 t, \quad (5)$$

first-order kinetic equation:

$$\ln\left(\frac{C_0}{C}\right) = k_1 t, \quad (6)$$

second-order kinetic equation:

$$\frac{1}{C} - \frac{1}{C_0} = k_2 t, \quad (7)$$

where k_0 , k_1 , and k_2 are the rate constants of zero-, first-, and second-order kinetics, respectively; C_0 and C are the concentrations of the dye solution before and after irradiation at time, t .

3.2.1. Effect of Ag₃PO₄ Loading on HA. The adsorption under dark condition and photodegradation of the model dye pollutant SR S3B 150% (20 ppm) under visible light (sunlight) at a fixed dosage concentration of 0.5 g L^{−1} were studied and presented in Figure 9. It is evidenced that the adsorption capacity of the photocatalyst is increased with Ag₃PO₄ concentration. The blank dye solution and with HA did not show a significant degradation under sunlight irradiation, whereas the composites HA_Ag₃PO₄(x) exhibited photocatalytic activity with an increasing trend with increase in Ag₃PO₄ concentration with rate constants 0.00515, 0.02178, and 0.07168 min^{−1}, respectively (Table 1). The composite HA_Ag₃PO₄(c) has the highest rate constant compared with other photocatalysts used in this study and, hence, HA_Ag₃PO₄(c) was selected for further photodegradation investigations. The highest performance of HA_Ag₃PO₄(c)

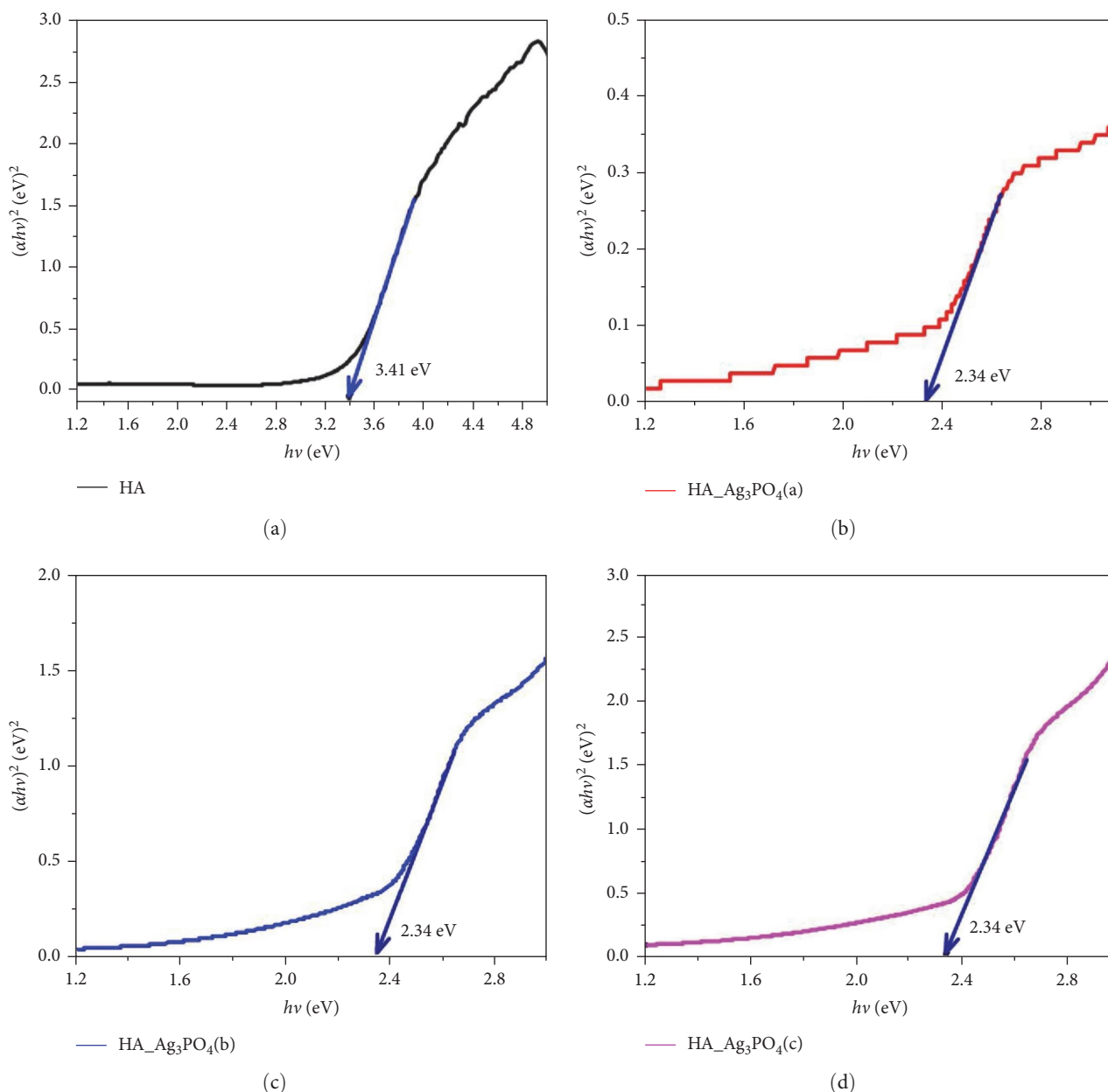


FIGURE 8: Bandgaps of neat HA (a) and prepared composites (c–d).

can be explicitly understood that the higher amount of Ag₃PO₄ gives rise to higher active sites, which leads to higher production of reactive radical species. This is also confirmed by TEM image of HA_Ag₃PO₄(c) (Figure 6(e)), which revealed the larger number of Ag₃PO₄ particles on HA and also it is in agreement with XRD result. Moreover, it is very clear from TEM result that the Ag₃PO₄ particles formed by ion substitution on HA substrate have a declined particle size compared with the lower Ag⁺ concentration, which in turn enhances the active surface area of the material. The surface area of the photocatalytic material is one of the very important parameters to influence photocatalysis [27].

3.2.2. Effect of Dosage of HA_Ag₃PO₄(c). From the above findings, it is evident that the composite HA_Ag₃PO₄(c)

performed an excellent photocatalytic activity and, hence, HA_Ag₃PO₄(c) was taken for further studies. The dependence of HA_Ag₃PO₄(c) on dosage concentration in the photocatalytic degradation of SR S3B 150% was examined. The photocatalyst concentration range was selected from 0.25 to 2 g L⁻¹ at the dye concentration of 20 ppm and their photocatalytic performances were examined for 1 hr, as depicted in Figure 10. As the photocatalyst quantity increased, an increasing trend of degradation of the dyes can be noticed. It is general to have an increasing photodegradation as the number of active sites on the surfaces of the photocatalyst increases. Consequently, it gives rise to large number of reactive radical species. At the end of the photocatalysis (60 min irradiation), the lowest concentration of HA_Ag₃PO₄(c) (0.25 g L⁻¹) degraded the dye to 53%, while the other

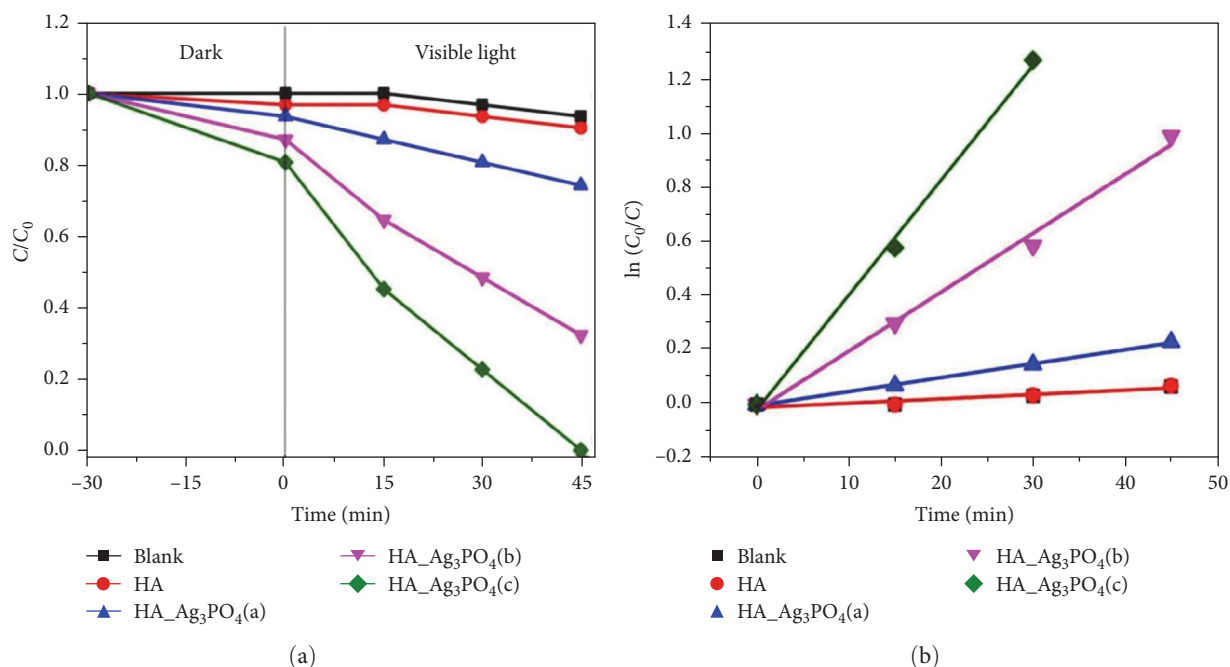


FIGURE 9: Effect of Ag₃PO₄ loading: photocatalytic performance of neat HA and Ag₃PO₄ composites on SR under visible light.

TABLE 1: Kinetics studies of the photocatalytic degradation of SR by the prepared photocatalysts.

Catalysts	Catalyst concentration (g L ⁻¹)	Zero order $C_0 - C = k_0 t$		First order $\ln(C_0/C) = k_1 t$		Second order $(1/C) - (1/C_0) = k_2 t$	
		k_0 (min ⁻¹)	R^2	k_1 (min ⁻¹)	R^2	k_2 (min ⁻¹)	R^2
HA_Ag ₃ PO ₄ (a)	0.5	0.00133	0.99782	0.00515	0.99821	0.03895	0.58407
HA_Ag ₃ PO ₄ (b)	0.5	0.00373	0.98861	0.02178	0.98989	0.0294	0.944
HA_Ag ₃ PO ₄ (c)	0.5	0.0055	0.89646	0.07168	0.98209	0.16905	0.92962

concentrations 0.5, 1 and 1.5 g L⁻¹ degraded the dye completely at 45, 30, and 15 min, respectively. The rate constants obtained from $\ln(C_0/C)$ versus time plot for the concentrations 0.25, 0.5, 1, and 1.5 are 0.009, 0.034, 0.046, and 0.0924, respectively. In the same time, the dye was completely adsorbed at the maximum concentration of 2 g L⁻¹ and the sample dye solution became turbid. Hence, the concentration of HA_Ag₃PO₄(c) is limited to 1.5 g L⁻¹.

3.2.3. Effect of Initial Concentration of the Dye Solution. The impact of initial concentration of the dye solution on photodegradation of SR S3B 150% was studied in the range from 10 to 50 ppm at a fixed photocatalyst concentration 0.5 g L⁻¹, which is presented in Figure 11. It was observed that the percentage of degradation was declined with the increase in dye concentration. The dye solution of concentrations 10 ppm at 30 min were undergone degradation of 100% while the rest of the concentrations 20–50 ppm showed a degradation of 66.6%, 53.8%, 47.2%, and 44%, respectively, at 30 min. A declining trend in the rate constants for the degradation process of increasing concentration was noticed (10, 20, 30, 40, and 50 ppm—0.04621, 0.03662, 0.02613, 0.02246, and 0.01921 min⁻¹, respectively). This can be

clarified by two ways as follows: one reason can be the limitation of the number of active sites on the photocatalyst surface which may be insufficient to degrade the higher concentrations and the other can be explained in terms of amount of adsorption of dyes. As the increase in dye concentration leads to higher amount of dye to be adsorbed on the catalyst surface, it shields the catalyst from the radiation and hinders the photogeneration of the electron–hole pair which is responsible for the degradation of the dye [23, 31, 32].

3.2.4. Effect of Initial pH of the Dye Solution. The initial pH of the polluted solution is a crucial influencing factor in controlling the photodegradation process. The pH affects the surface charge of the catalyst, pollutants adsorption onto the catalyst, and the valence band oxidation potential [33, 34]. The photocatalytic behavior of the selected photocatalyst, in the degradation of SR S3B 150% under a broad range of pH conditions from 2 to 10 with two-step variation, was examined at a fixed irradiation time of 15 min. The results revealed that acidic condition favored the enhanced photodegradation than neutral condition. The maximum photodegradation of the organic dye SR was observed to be 96.8% at pH 4 and also at pH 2 and 6 comparable degradation efficiency (93.5% for

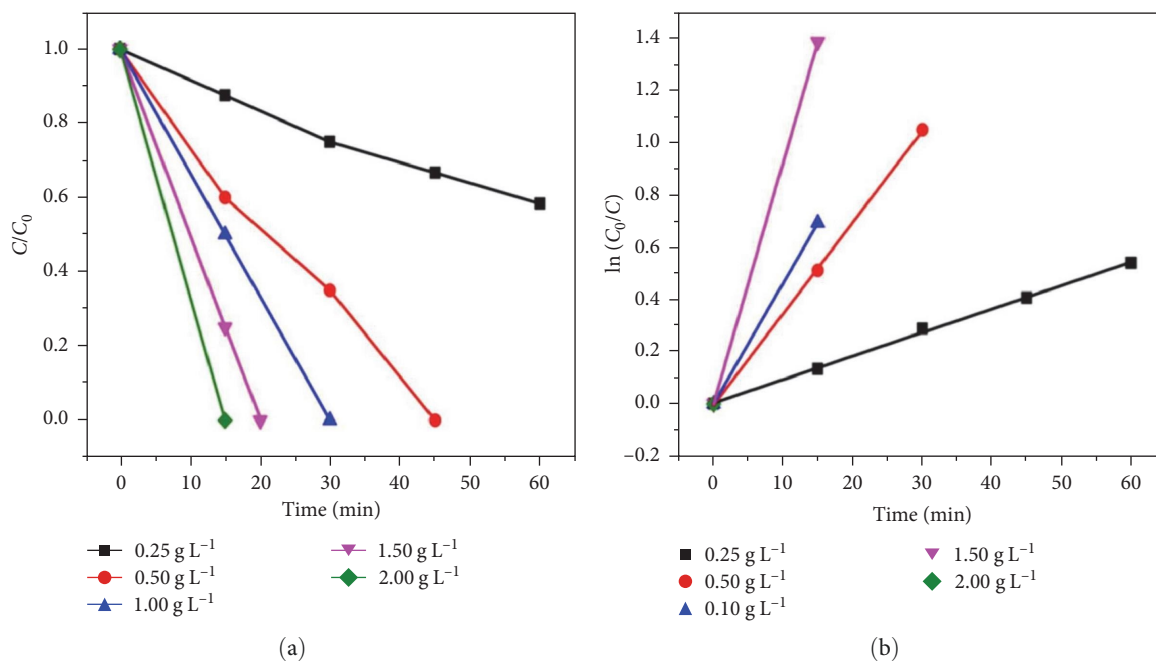


FIGURE 10: Photocatalytic performance of HA_Ag₃PO₄(c) of different dosage concentrations on SR under visible light.

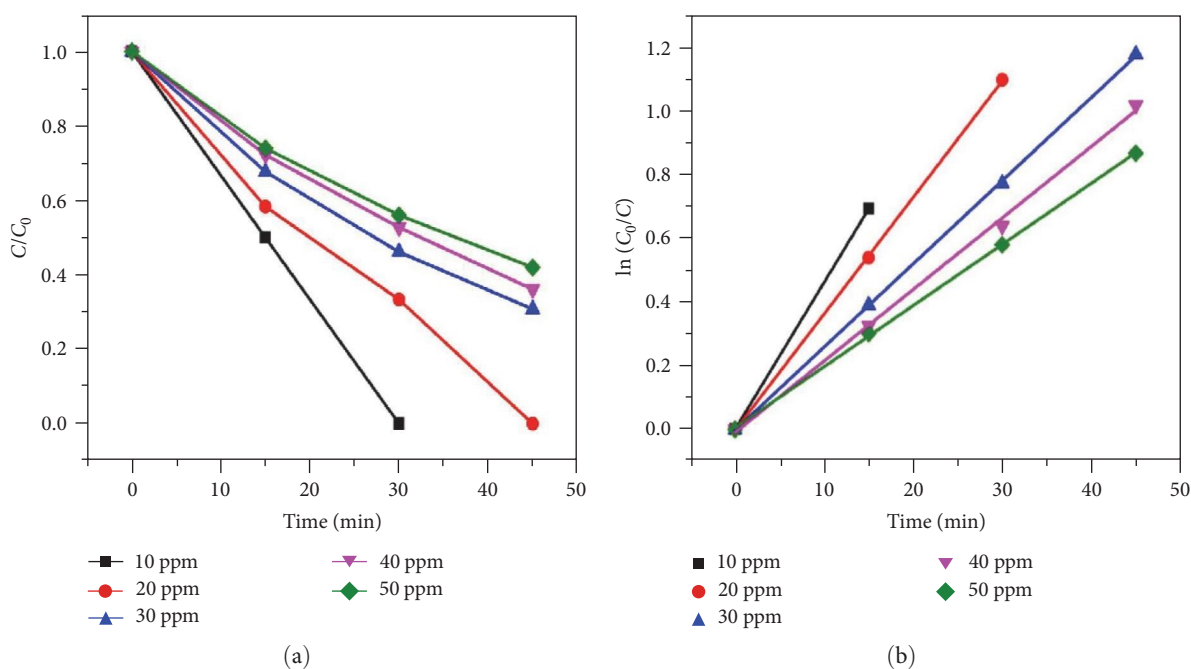


FIGURE 11: Effect of dye concentration on photocatalytic degradation of SR under visible light.

both) were noticed, but very low degradation efficiencies were found at higher pH values. As shown in Figure 12(a), it is evidenced that the higher adsorption facilitated higher photodegradation. At acidic conditions, Ag₃PO₄ becomes positively charged and the higher adsorption of the anionic dye SR occurred due to the electrostatic attraction between the pollutant and catalyst. In the same time, at basic conditions, the deprotonated OH⁻ groups over the catalyst surface hinder the

adsorption of the anionic dye by electrostatic repulsion [35]. Even though the higher pH resulted in lower adsorption, a faster degradation was observed at pH 10. This could be due to the lowering of the oxidation potential of the dye and eventually the dye can be degraded quickly [36].

3.2.5. Quenching Test. The free radicals employed in the photocatalytic process, namely, such as hydroxyl (\cdot OH),

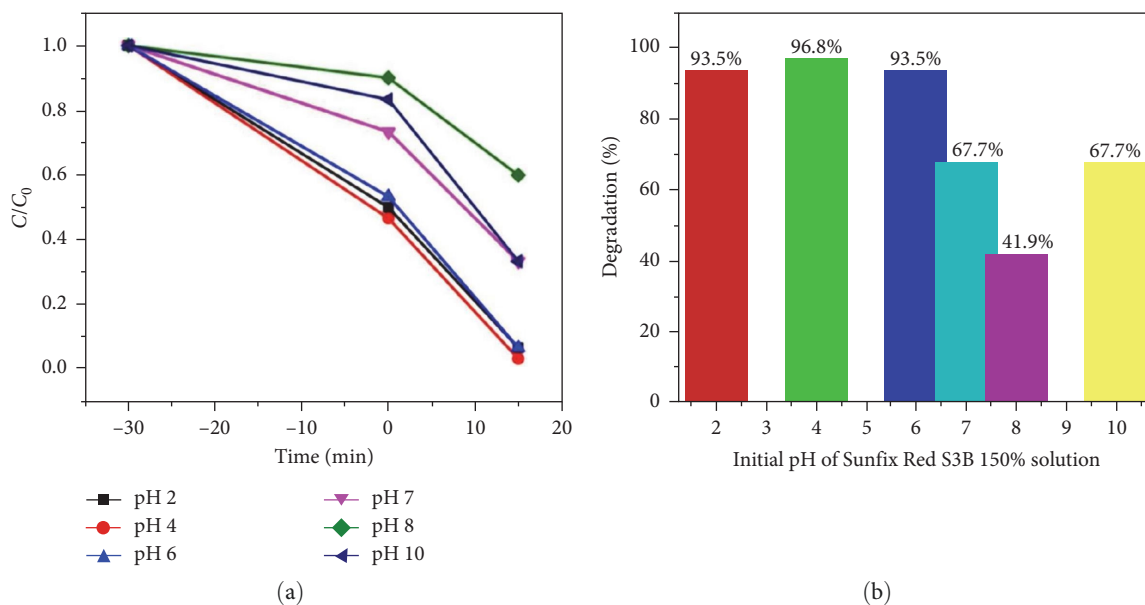


FIGURE 12: Photocatalytic behavior of HA_Ag₃PO₄(c) at different pH (a) and degradation percentage of the dye at different pH (b).

superoxide ($\cdot\text{O}_2^-$), and photogenerated holes (h^+) were trapped by IPA, ascorbic acid, and EDTA, respectively, under similar conditions. The scavengers were taken in the concentration of 1 mmol/L and the concentrations of the dye and the photocatalyst were fixed to 20 ppm and 0.5 g L^{-1} , respectively, and irradiated by direct sunlight for 60 min and the results are given in Figure 13.

From the free radicals trapping test, it can be noted that the photocatalytic degradation was decreased from 100% to 82% with the addition of IPA which reveals that role played by hydroxyl radicals in the degradation of the dye SR is only to a small extent, while the other radical trappers EDTA and ascorbic acid deteriorated the degradation of the dye significantly (46% and 35%, respectively). It is clear that the superoxide radicals and holes took part actively in the photocatalysis process.

3.2.6. Degradation of Other Dyes. The study of photocatalytic behavior of the photocatalyst HA_Ag₃PO₄(c) on some other anionic and cationic dyes was also extended. Anionic dyes such as SR S3B 150% and SB DN conc., the cationic dyes such as MB and RhB, and cocktail of all the four dyes were subjected to photodegradation by HA_Ag₃PO₄(c) under similar conditions and presented in Figure 14. The photocatalytic experiments were carried out for 150 min at 20 ppm dye concentration and photocatalyst concentration of 1 g L^{-1} . All the dyes showed different degradation rate, which is clear from Figure 14. SR and SB were decomposed completely in 30 and 60 min, respectively, while MB and RhB were decolorized to 98.16% and 78.67%, respectively, at the irradiation time 1 hr 45 min. Meanwhile, the degradation of cocktail dye solution was found to be 96.25% in 1 hr 45 min. The rate constants of the degradation of the different dyes are observed in the order $k_{\text{SR}} > k_{\text{SB}} > k_{\text{MB}} > k_{\text{CT}} > k_{\text{RhB}}$ which are depicted in Table 2.

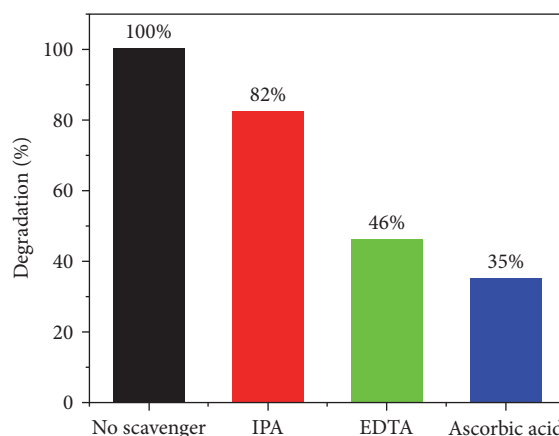
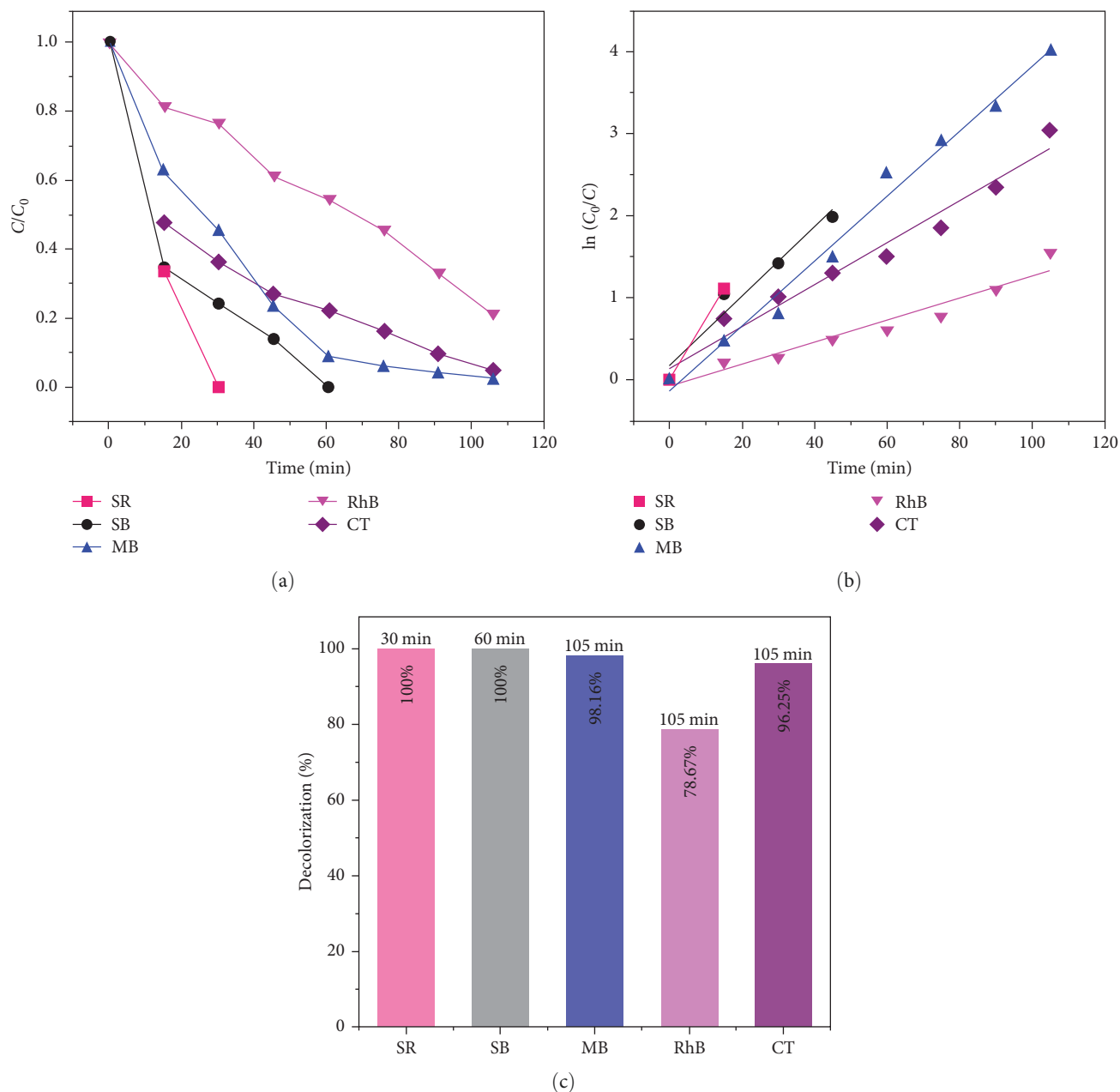


FIGURE 13: Photocatalytic behavior of HA_Ag₃PO₄(c) with scavengers.

4. Possible Photocatalytic Mechanism in the Degradation of Sunfix Red S3B 150%

From the above findings, it can be noted that the concentration of AgNO₃ precursor taken for the formation of HA_Ag₃PO₄ composite influenced the photocatalytic process in two ways. First, as the concentration of AgNO₃ increased from 0.02 to 0.08 M, it showed an increasing order of photocatalysis due to the increased number of active sites available. Meanwhile, it can be seen from the TEM results that the higher concentration of the Ag⁺ precursor also resulted in reduction of particle size which led to enhanced photodegradation of dyes owing to increase in surface-to-volume ratio. In the process of photocatalytic degradation, the photogenerated electron-hole recombination inhibits the photocatalysis [27]. Hence, proper charge separation is required to make them available to carry out the redox process. Many results

FIGURE 14: Degradation of different organic dyes by HA_Ag₃PO₄(c).

reported that heterostructures can inhibit electron-hole recombination through creating a proper transfer channel for the photogenerated charges [27, 37]. In the present work, the adopted synthesis method has resulted in good interfacial bonding between HA and Ag₃PO₄ which has been clearly noticed from the TEM result (Figure 6(f)). This channel may facilitate an easy transfer of photogenerated electrons e_{CB}^- from Ag₃PO₄ to hydroxyapatite being a good electron acceptor [38].

Based on the obtained results, the possible mechanism of photocatalytic degradation is proposed (Figure 15). In the presence of direct sunlight, the photocatalyst is excited and electron-hole pairs are generated. The majority of photogenerated holes (h_{VB}^+) in the valence band directly

involve in the oxidation of the organic dye, while some of them generate some $\cdot OH$, which may contribute a weak photocatalysis, which is confirmed from the quenching test. It is also evident from the estimated value of conduction band potential (0.29 eV) of Ag₃PO₄ that it is more positive than $O_2/\cdot O_2^-$ (-0.33 eV vs. NHE) and hence the photoexcited electrons (e_{CB}^-) could not reduce the dissolved O_2 to superoxide radicals ($\cdot O_2^-$). This may result in the reduction of lattice Ag^+ to Ag metal which may eventually suppress the availability of photogenerated electrons for photocatalytic process [36]. However, hydroxyapatite in the composite captures the photogenerated electrons and makes them available for photocatalysis. Moreover, the transferred photogenerated electrons reduce the adsorbed

TABLE 2: Kinetic studies of HA_Ag₃PO₄(c) of the degradation of different dyes.

Dyes	Catalyst concentration (g L ⁻¹)	Zero order $C_0 - C = k_0 t$		First order $\ln(C_0/C) = k_1 t$		Second order $(1/C) - (1/C_0) = k_2 t$	
		k_0 (min ⁻¹)	R^2	k_1 (min ⁻¹)	R^2	k_2 (min ⁻¹)	R^2
Sunfix Red (SR) S3B 150%	1	0.005	0.92857	0.07324	1	0.88889	1
Sunzol Black (SB) DN conc.	1	0.00427	0.74598	0.042	0.92443	0.45961	0.95049
Methylene blue (MB)	1	0.00989	0.821	0.03927	0.98461	0.40652	0.74271
Rhodamine B (RhB)	1	0.01059	0.98678	0.01343	0.93367	0.01983	0.77052
Cocktail (CT)	1	0.00462	0.74382	0.02544	0.96133	0.24373	0.69454

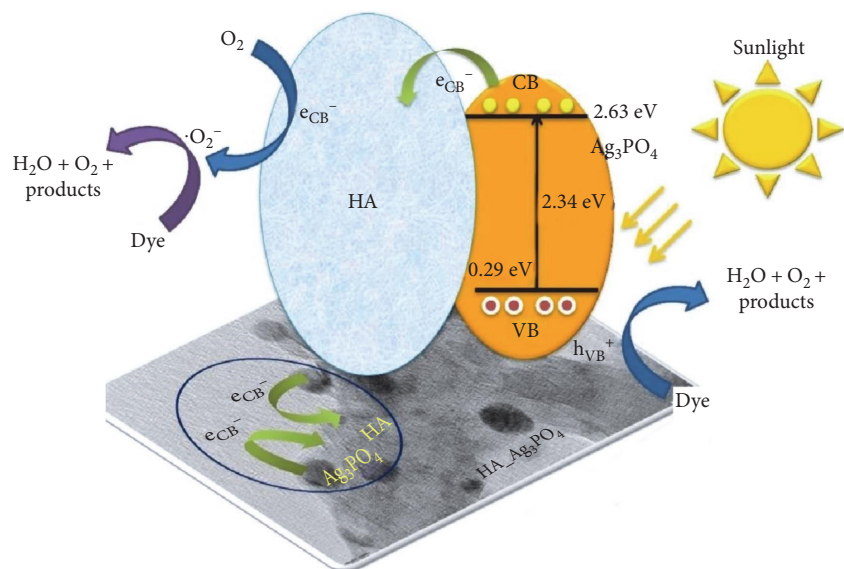
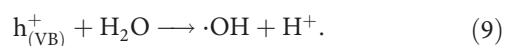
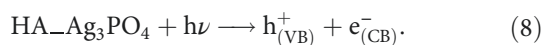
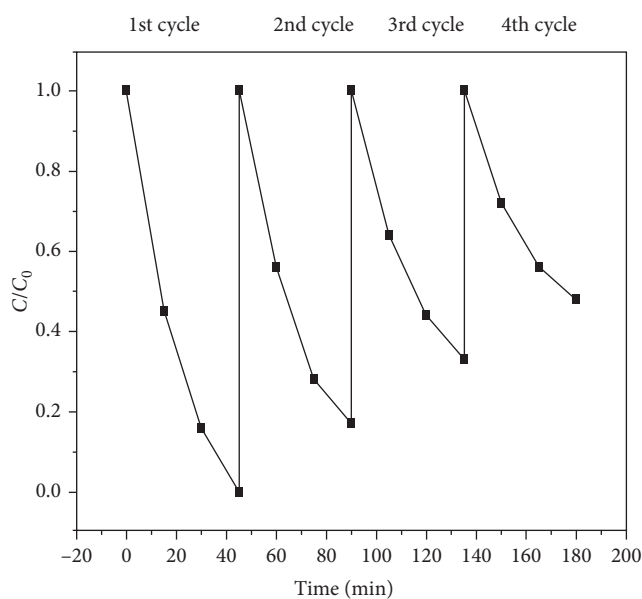


FIGURE 15: Possible photocatalytic mechanism.

O₂ to superoxide radicals ($\cdot\text{O}_2^-$) which actively take part in the photocatalytic degradation of the organic dye under direct sunlight.



4.1. Reusability. The reusability of the prepared composite HA_Ag₃PO₄(c) was examined for four cycles and presented in Figure 16. The sample after every cycle of photocatalytic

FIGURE 16: Recycle test of HA_Ag₃PO₄(c).

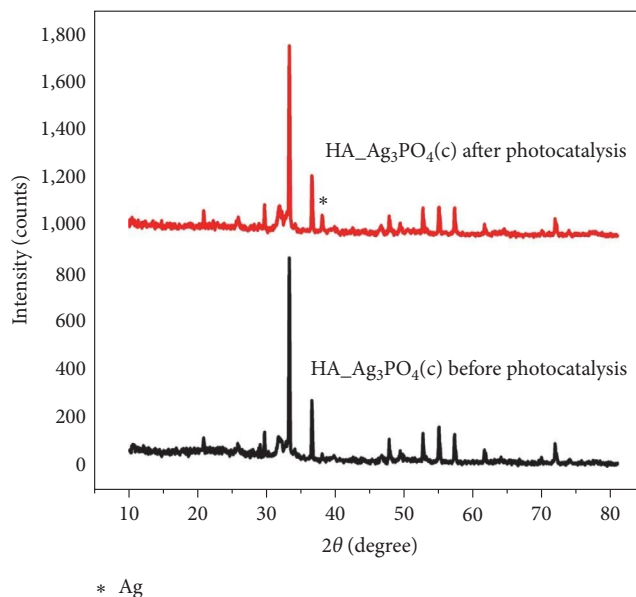


FIGURE 17: XRD pattern of the photocatalyst after four cycles of photodegradation.

TABLE 3: Comparison of removal efficiency of HA_Ag₃PO₄(c).

S. no.	Photocatalysts	Catalyst concentration (g L ⁻¹)	Dyes	Dye concentration (ppm)	Time	Removal efficiency (%)	References
1	Ag ₃ PO ₄ /HAp@γ-Fe ₂ O ₃	1.67	MB	50	4 hr	99	[39]
2	Ag ₃ PO ₄ /HAp	1	RhB	10	30 min	99	[40]
3	Ag ₃ PO ₄ /AgBr/HAp	1.4	MB	10	40 min	100	[6]
4	HA-Ag ₃ PO ₄	0.5	SR	20	45 min	100	Present work

degradation of the dye was regenerated by washing three times with DI water and was dried at 60°C in a vacuum oven and used for the next cycle. The performance of the prepared composite declined gradually after each cycle and the degradation efficiency reduced to 52% from 100% after the fourth cycle of degradation. The photocatalyst after the fourth run was subjected to XRD analysis to investigate the stability and presented in Figure 17. The presence of the peak at 38° is corresponding to pure Ag (111) plane which reveals that the photocatalyst underwent slight photo-corrosion after four cycles. The removal efficiency of the prepared sample was also compared with the previous results and presented in Table 3.

5. Conclusion

Ag₃PO₄-anchored hydroxyapatite was synthesized via a facile in situ ion-exchange method. From the results, it was found that the particle size of Ag₃PO₄ can be tuned by the concentration of AgNO₃ precursor solution. The photocatalytic performance on an anionic dye SR S3B 150% under visible light was carried out at different experimental conditions and found satisfactory results. The photodegradation studies were also extended for other organic dyes such as SB, MB, RhB, and cocktail of all four dyes. The studies revealed

that the synthesized composites can be a proficient photocatalyst for the degradation of studied organic dyes.

Data Availability

All data generated or analyzed during this study are included in the published article.

Conflicts of Interest

The authors declare that they have no conflicts of interest.

Acknowledgments

S. Dhatchayani gratefully acknowledges UGC, New Delhi, for awarding UGC-BSR fellowship (F. No. 25-1/2014-15 (BSR)/7-14/2007(BSR)/13.03.2015) and the authors greatly acknowledge Rusa-Phase 2.0 grant sanctioned vide letter no. F. 24-51/2014-U, Policy (TNMulti-Gen), Department of Education, Government of India, Dt.09.10.2018., UGC-SAP, DST-FIST, and DST-PURSE for financial support to carry out this work. We thank Mr. N. Pandi and Mrs. P. Kanchana for the supply of dyes for the present studies and also extend our gratitude to USIC, Alagappa University for rendering instruments for characterizations.

References

- [1] A. Saravanan, P. Senthil Kumar, S. Jeevanantham et al., "Effective water/wastewater treatment methodologies for toxic pollutants removal: processes and applications towards sustainable development," *Chemosphere*, vol. 280, Article ID 130595, 2021.
- [2] Y. Liu, P. Wang, B. Gojenko et al., "A review of water pollution arising from agriculture and mining activities in central Asia: facts, causes and effects," *Environmental Pollution*, vol. 291, Article ID 118209, 2021.
- [3] A. Shahedi, A. K. Darban, F. Taghipour, and A. Jamshidi-Zanjani, "A review on industrial wastewater treatment via electrocoagulation processes," *Current Opinion in Electrochemistry*, vol. 22, pp. 154–169, 2020.
- [4] I. H. Ali, M. K. Al Mesfer, M. I. Khan, M. Danish, and M. M. Alghamdi, "Exploring adsorption process of lead (II) and chromium (VI) ions from aqueous solutions on acid activated carbon prepared from *Juniperus procera* leaves," *Processes*, vol. 7, no. 4, Article ID 217, 2019.
- [5] C. Amor, L. Marchão, M. S. Lucas, and J. A. Peres, "Application of advanced oxidation processes for the treatment of recalcitrant agro-industrial wastewater: a review," *Water*, vol. 11, no. 2, Article ID 205, 2019.
- [6] N. M. Mahmoodi and M. H. Saffar-Dastgerdi, "Clean laccase immobilized nanobiocatalysts (graphene oxide-zeolite nanocomposites): from production to detailed biocatalytic degradation of organic pollutant," *Applied Catalysis B: Environmental*, vol. 268, Article ID 118443, 2020.
- [7] N. M. Mahmoodi, B. Hayati, and M. Arami, "Textile dye removal from single and ternary systems using date stones: kinetic, isotherm, and thermodynamic studies," *Journal of Chemical and Engineering Data*, vol. 55, no. 11, pp. 4638–4649, 2010.
- [8] N. Nasrollahi, S. Aber, V. Vatanpour, and N. M. Mahmoodi, "The effect of amine functionalization of CuO and ZnO nanoparticles used as additives on the morphology and the permeation properties of polyethersulfone ultrafiltration nanocomposite membranes," *Composites Part B: Engineering*, vol. 154, pp. 388–409, 2018.
- [9] S. Sha, L. Zhang, H. Liu et al., "Synthesis and visible-light photocatalytic degradation of Ag₃PO₄/AgBr/hydroxyapatite ternary nanocomposites prepared from oyster shells," *RSC Advances*, vol. 11, no. 26, pp. 15598–15607, 2021.
- [10] M. Hadei, A. Mesdaghinia, R. Nabizadeh, A. H. Mahvi, S. Rabbani, and K. Naddafi, "A comprehensive systematic review of photocatalytic degradation of pesticides using nano TiO₂," *Environmental Science and Pollution Research*, vol. 28, pp. 13055–13071, 2021.
- [11] N. M. Mahmoodi, B. Hayati, M. Arami, and F. Mazaheri, "Single and binary system dye removal from colored textile wastewater by a dendrimer as a polymeric nanoarchitecture: equilibrium and kinetics," *Journal of Chemical and Engineering Data*, vol. 55, no. 11, pp. 4660–4668, 2010.
- [12] X. Zhu, Y. Shi, Q. Luo et al., "High-efficiency visible-light-driven Ag₃PO₄ photocatalysts modified by conjugated polyvinyl alcohol derivatives," *Materials Research Express*, vol. 6, no. 12, Article ID 125558, 2019.
- [13] P. Huang and J. Luan, "Preparation and characterization of an Ag₃PO₄/GaOOH composite with enhanced photocatalytic performance toward rhodamine B," *New Journal of Chemistry*, vol. 44, no. 6, pp. 2414–2422, 2020.
- [14] N. Tavker, U. K. Gaur, and M. Sharma, "Agro-waste extracted cellulose supported silver phosphate nanostructures as a green photocatalyst for improved photodegradation of RhB dye and industrial fertilizer effluents," *Nanoscale Advances*, vol. 2, no. 7, pp. 2870–2884, 2020.
- [15] M. Du, J. Chen, K. Liu, H. Xing, and C. Song, "Recent advances in biomedical engineering of nano-hydroxyapatite including dentistry, cancer treatment and bone repair," *Composites Part B: Engineering*, vol. 215, Article ID 108790, 2021.
- [16] G. Wang, G. Qian, J. Zan et al., "A co-dispersion nanosystem of graphene oxide @silicon-doped hydroxyapatite to improve scaffold properties," *Materials & Design*, vol. 199, Article ID 109399, 2021.
- [17] N. M. Basfer, S. F. Mansour, and M. K. Ahmed, "Physicochemical properties of hydroxyapatite modified with vanadium ions for degradation of methylene blue," *Journal of Molecular Structure*, vol. 1240, Article ID 130562, 2021.
- [18] S. Dhatchayani, S. Vijayakumar, N. Sarala, B. Vaseeharan, and K. Sankaranarayanan, "Effect of curcumin sorbed selenite substituted hydroxyapatite on osteosarcoma cells: an *in vitro* study," *Journal of Drug Delivery Science and Technology*, vol. 60, Article ID 101963, 2020.
- [19] A. Rout and S. Agrawal, "Structural, morphological and electrical properties of new type Dy doped Ca_{6-x}Na₂Y₂(SiO₄)₆(OH)₂ hydroxyapatite compound synthesized by co-precipitation method," *Journal of Electroceramics*, vol. 48, pp. 74–94, 2022.
- [20] H. Bouyarmane, C. El Bekkali, J. Labrag et al., "Photocatalytic degradation of emerging antibiotic pollutants in waters by TiO₂/Hydroxyapatite nanocomposite materials," *Surfaces and Interfaces*, vol. 24, Article ID 101155, 2021.
- [21] G. Chen, X. Zheng, C. Wang et al., "A postsynthetic ion exchange method for tunable doping of hydroxyapatite nanocrystals," *RSC Advances*, vol. 7, no. 89, pp. 56537–56542, 2017.
- [22] V. Uskoković, M. A. Iyer, and V. M. Wu, "One ion to rule them all: the combined antibacterial, osteoinductive and anticancer properties of selenite-incorporated hydroxyapatite," *Journal of Materials Chemistry B*, vol. 5, no. 7, pp. 1430–1445, 2017.
- [23] A. Aziz, N. Ali, A. Khan et al., "Chitosan-zinc sulfide nanoparticles, characterization and their photocatalytic degradation efficiency for azo dyes," *International Journal of Biological Macromolecules*, vol. 153, pp. 502–512, 2020.
- [24] M. Manoj, D. Mangalaraj, N. Ponpandian, and C. Viswanathan, "Core-shell hydroxyapatite/Mg nanostructures: surfactant free facile synthesis, characterization and their *in vitro* cell viability studies against leukaemia cancer cells (K562)," *RSC Advances*, vol. 5, no. 60, pp. 48705–48711, 2015.
- [25] Y.-G. Zhang, Y.-J. Zhu, and F. Chen, "Novel interconnected nanochannel hydroxyapatite ceramics: synthesis, microstructure, and permeability," *Ceramics International*, vol. 43, no. 7, pp. 5403–5411, 2017.
- [26] R. K. Santos, T. A. Martins, G. N. Silva et al., "Ag₃PO₄/NiO composites with enhanced photocatalytic activity under visible light," *ACS Omega*, vol. 5, no. 34, pp. 21651–21661, 2020.
- [27] Q. Chang, X. Meng, S. L. Hu, F. Zang, and J. L. Yang, "Hydroxyapatite/N-doped carbon dots/Ag₃PO₄ composite for improved visible-light photocatalytic performance," *RSC Advances*, vol. 7, no. 48, pp. 30191–30198, 2017.
- [28] A. N. Martín-Gómez, J. A. Navío, C. Jaramillo-Páez, P. Sánchez-Cid, and M. C. Hidalgo, "Hybrid ZnO/Ag₃PO₄ photocatalysts, with low and high phosphate molar percentages," *Journal of Photochemistry and Photobiology A: Chemistry*, vol. 388, Article ID 112196, 2020.
- [29] G. Bharath, B. Swarna Latha, E. H. Alsharaeh, P. Prakash, and N. Ponpandian, "Enhanced hydroxyapatite nanorods

- formation on graphene oxide nanocomposite as a potential candidate for protein adsorption, pH controlled release and an effective drug delivery platform for cancer therapy,” *Analytical Methods*, vol. 9, no. 2, pp. 240–252, 2017.
- [30] C. C. Negrila, M. V. Predoi, S. L. Iconaru, and D. Predoi, “Development of zinc-doped hydroxyapatite by sol–gel method for medical applications,” *Molecules*, vol. 23, no. 11, Article ID 2986, 2018.
- [31] A. Khan, S. J. Shah, K. Mehmood, Awais, N. Ali, and H. Khan, “Synthesis of potent chitosan beads a suitable alternative for textile dye reduction in sunlight,” *Journal of Materials Science: Materials in Electronics*, vol. 30, pp. 406–414, 2019.
- [32] A. Dargahi, M. R. Samarghandi, Y. Vaziri, G. Ahmadidoost, E. Ghahramani, and A. A. Shekarchi, “Kinetic study of the photocatalytic degradation of the acid blue 113 dye in aqueous solutions using zinc oxide nanoparticles immobilized on synthetic activated carbon,” *Journal of Advances in Environmental Health Research*, vol. 7, no. 2, pp. 75–85, 2019.
- [33] M. F. Hanafi and N. Sapawe, “A review on the water problem associate with organic pollutants derived from phenol, methyl orange, and remazol brilliant blue dyes,” *Materials Today: Proceedings*, vol. 31, Part 1, pp. A141–A150, 2020.
- [34] K. M. Reza, A. S. W. Kurny, and F. Gulshan, “Parameters affecting the photocatalytic degradation of dyes using TiO₂: a review,” *Applied Water Science*, vol. 7, pp. 1569–1578, 2017.
- [35] P. Amornpitoksu, S. Suwanboon, and C. Random, “Photocatalytic dye decolorization under light-emitting-diode irradiation by silver halides prepared from hydrohalic acids,” *Materials Research Express*, vol. 6, no. 11, Article ID 115524, 2019.
- [36] R. Li, X. Song, Y. Huang, Y. Fang, M. Jia, and W. Ma, “Visible-light photocatalytic degradation of azo dyes in water by Ag₃PO₄: an unusual dependency between adsorption and the degradation rate on pH value,” *Journal of Molecular Catalysis A: Chemical*, vol. 421, pp. 57–65, 2016.
- [37] C. Su, L. Liu, M. Zhang, Y. Zhang, and C. Shao, “Fabrication of Ag/TiO₂ nanoheterostructures with visible light photocatalytic function via a solvothermal approach,” *CrystEngComm*, vol. 14, no. 11, pp. 3989–3999, 2012.
- [38] L.-L. Zhang, Q. Tong, X.-Y. Zhang et al., “Preparation and photocatalytic property of alumina doped zinc oxide nanoparticles supported on hydroxyapatite,” *Materials Technology*, vol. 29, no. sup2, pp. A9–A13, 2014.
- [39] X. N. Pham, H.-T. Le, T.-T. Nguyen, and N.-T. Pham, “Ag₃PO₄-supported magnetic hydroxyapatite composite as green photocatalyst for the removal of cationic and anionic dyes from aqueous solution,” *Chemical Engineering & Technology*, vol. 44, no. 10, pp. 1850–1862, 2021.
- [40] U. Sulaeman, S. Suhendar, H. Diastuti, A. Riapanitra, and S. Yin, “Design of Ag₃PO₄ for highly enhanced photocatalyst using hydroxyapatite as a source of phosphate ion,” *Solid State Sciences*, vol. 86, pp. 1–5, 2018.

Research Article

Mycosynthesis of Zinc Oxide Nanoparticles Coated with Silver using *Ganoderma lucidum* (Curtis) P. Karst and Its Evaluation of *In Vitro* Antidiabetic and Anticancer Potential

D. S. Ranjith Santhosh Kumar ¹, N. Elango,¹ Gayathri Devi Selvaraju ², Paul A. Matthew ³, Senthilkumar Palanisamy ⁴, Hayoung Cho,⁵ Fatimah S. Al Khattaf,⁶ Ashraf Atef Hatamleh ⁶, and Amit Dutta Roy ⁷

¹School of Biotechnology, Dr. G.R. Damodaran College of Science, Coimbatore 641014, Tamil Nadu, India

²Department of Biotechnology, Kalaignar Karunanidhi Institute of Technology, Coimbatore 641402, Tamil Nadu, India

³School of Bioscience and Technology, Vellore Institute of Technology, Vellore 632014, Tamil Nadu, India

⁴Nehru Arts and Science College, Coimbatore, Tamil Nadu, India

⁵Department of Environmental Energy and Engineering, Kyonggi University, Yeongtong-Gu, Suwon, Gyeonggi-Do 16227, Republic of Korea

⁶Department of Botany and Microbiology, College of Science, King Saud University, P.O. Box 2455, Riyadh 11451, Saudi Arabia

⁷Department of Biomedical Engineering, Khulna University of Engineering & Technology (KUET), Khulna 9203, Bangladesh

Correspondence should be addressed to D. S. Ranjith Santhosh Kumar; ranjith.deva87@gmail.com and Amit Dutta Roy; amit@bme.kuet.ac.bd

Received 24 July 2022; Revised 2 September 2022; Accepted 12 October 2022; Published 23 December 2022

Academic Editor: Dong Kee Yi

Copyright © 2022 D. S. Ranjith Santhosh Kumar et al. This is an open access article distributed under the Creative Commons Attribution License, which permits unrestricted use, distribution, and reproduction in any medium, provided the original work is properly cited.

Nanotechnology is an evolving interdisciplinary field of research interspersing material science and nanobiotechnology. Nanoparticles are studied extensively for their specific catalytic, magnetic, electronic, optical, antimicrobial, theranostic, diagnosis, wound healing, and anti-inflammatory properties. ZnO nanoparticles (NPs) have many applications owing to their unique characteristics, which include low cost, nontoxicity, abundance in nature, and the ability to prepare compounds with varying morphologies having different properties. The main aim of the study is to biosynthesis of ZnO nanoparticles coated with silver from the aqueous extract of *Ganoderma lucidum* (Curtis) P. Karst and to evaluate its antidiabetic potential by performing alpha-glucosidase inhibition and alpha-amylase inhibition assays and to evaluate the anticancer potential by cytotoxicity (MTT) assay against human breast cancer MDA-MB 231 cell lines. The biosynthesis of ZnO nanoparticles coated with Ag was characterized by UV-vis spectroscopy, Fourier transform infrared spectroscopy, energy dispersive X-ray analysis, scanning electron microscope, and transmission electron microscopy. An increasing concentration in the biosynthesized ZnO nanoparticles coated with Ag produces strong antidiabetic activity through enzyme inhibition effect and anticancer activity through the reduction of cell viability. The present study recommended that the “Biological” method of biological nanoparticle production is a promising approach that allows synthesis in aqueous conditions, with low energy requirements and low costs. In the future, the mycosynthesized nanoparticles might be used in the medical arena to treat and prevent diseases.

1. Introduction

In the sphere of research, nanotechnology has become increasingly essential. Nanotechnology is a field of science and technology that works with tiny molecules and is commonly employed for therapeutic purposes in underdeveloped

nations. Nanoparticles are defined as particles with a diameter of fewer than 100 nm [1].

ZnO, also known as zincite, is a versatile material with a wide range of applications in technology, including electromagnetic shielding, LEDs, and other light-emitting devices [2]. Many research investigations have focused on ZnO NPs,

and they have a wide range of industrial uses, including textiles, cosmetics, water treatment, and UV emitting devices; ZnO NPs play a vital role in therapeutic as well as pharmaceutical areas because of having fewer side effects. ZnO NPs have a huge surface area, which allows them to have an effective target action on cancer cells [3].

The coating is a process in which the metals such as gold, silver, chromium, etc., are doped with the main synthesized nanoparticles to stabilize the particles and also avoid agglomeration. The coating can be used to expand the advantages of any metal nanoparticles [4]. The three most common ways of creating nanoparticles are physical, chemical, and biological. Among all the methods of nanoparticle synthesis, we chose to proceed with the green synthesis because of its rapid, cost-effective, eco-friendly procedures, and avoiding the production of undesirable or harmful byproducts [5].

Ganoderma lucidum (Curtis) P. Karst is a medicinal mushroom belonging to the family of Ganodermataceae. *G. lucidum* is also known as Lingzhi in China, and it has been dubbed the “mushroom of immortality.” In Asian countries, it was traditionally used to enhance the immune power and treat various diseases [6]. There is a huge number of bioactive components including triterpenes, polysaccharides, sterols, and peptides found in the *G. lucidum*. Those identified compounds have numerous health benefits and are also used to treat the diseases, such as cancer, diabetes, asthma, arthritis, etc. [7, 8].

There are no studies on the mycosynthesis of ZnO nanoparticles coated with Ag from *G. lucidum* that we are aware of. Therefore, we aimed to synthesize the silver-coated ZnO nanoparticles and evaluate their antidiabetic and anticancer potential through some respected assays [9].

2. Materials and Methods

2.1. Sample Collection. *G. lucidum* was gathered from the Maruthamalai foothills (11°2'46" N, 76°51'7" E) in the Western Ghats, Coimbatore, Tamil Nadu, India. The Mycology Division of the Indian Forest Genetics and Tree Breeding Institute, Coimbatore, validated *G. lucidum*, and the voucher specimen (RT-25406/9-1-2016) was kept in our laboratory for future reference.

2.2. Preparation of Aqueous Extract. Deionized water was used to completely clean the mushroom sample, removing dirt and other contaminants. It was then air-dried for 5 days in the shade at room temperature. The dried mushroom sample was crushed into a fine powder after being cut into small pieces. In an Erlenmeyer flask, 3 g of mushroom powder was mixed with 300 ml deionized water and heated in a mantle for 2 hr at 80°C, then cooled and filtered using Whatman no. 1 filter paper. As a reducing agent, the filtrate aqueous extract is employed [10].

2.3. Synthesis of Silver-Coated Zinc Oxide Nanoparticles. To make silver-coated zinc oxide nanoparticles (Ag-ZnO NPs), 450 ml of *G. lucidum* aqueous extract was mixed with 45 ml of 1 mM zinc nitrate solution in a 1,000 ml Erlenmeyer flask. The precipitate was separated from the reaction solution by

centrifugation at 10,000 rpm for 15 min and the pellet was collected; the centrifugation process was then done twice more and the remaining pellet was collected. Pellets were dried in a hot air oven until all liquid ingredients were evaporated, then kept in airtight bottles for future research [11].

2.4. Silver Coating. Five milliliters of 10 mM silver nitrate was added drop wisely with the mixture of aqueous extract of *G. lucidum* and 1 mM zinc nitrate solution under constant stirring. The mixture was stirred for 2–3 hr with the use of a magnetic stirrer. Then the mixture of the aqueous solution was placed in the open shaker to improve the synthesis of Ag-ZnO NPs [12, 13].

2.5. Characterization of Biosynthesized Ag-Coated ZnO NPs. The obtained Ag-ZnO NPs from *G. lucidum* were characterized by using UV–vis spectrometry, FTIR analysis, EDX, SEM, and TEM analysis.

UV/VIS 3000+ double beam UV visible ratio-recording scanning spectrophotometer from Lab India (SKU: 174-0020) with dimensions of (WDH)/weight = 540440390 mm/36 kg was used to study the optical absorption spectra of Ag-ZnO NPs. FTIR is a qualitative analysis and it shows the presence of different functional groups, which give rise to the well-known signatures in the IR region of the electromagnetic spectrum. The presence of Ag-coated ZnO nanoparticles was confirmed by an energy-dispersive analysis X-ray (EDX) spectrum using an X-ray microanalyzer (Oxford Instruments, UK). The structural characterization of the ZnO nanoparticles coated with Ag was carried out by SEM (JEOL JEM 2100) and TEM (JEOL JEM 2100). The sample was prepared by air-drying drops of diluted solutions of the preparations on carbon films supported by copper grids.

2.6. Antidiabetic Activity of Silver-Coated Zinc Nanoparticles

2.6.1. In Vitro Alpha-Glucosidase Inhibition Assay. Matsui et al. [14] used an adapted approach to investigate the effect of ZnO NPs coated with Ag on alpha-glucosidase inhibition. The stock solution of alpha-glucosidase (0.5 U/ml) was also prepared in 20 mmol/l sodium phosphate buffer (pH 6.9) in 96 well plates. Alpha-glucosidase has been prepared by varying concentrations of Ag-ZnO NPs and acarbose standard drug (1–5 µg/ml), respectively. The mixture was incubated at 37°C for 15 min, and 100 µl of 4-nitrophenyl-β-D-glucopyranoside (PNPG) was added further. The reaction mixture was incubated for 10 min at 37°C. To stop the reaction, 750 ml of Na₂CO₃ (0.1 M) was added, and the OD values of spectrophotometer (UV-100 Cyber Lab, USA) readings were taken at 405 nm in triplicate. Acarbose alone was used as reference and controls for assay contain only 4-nitrophenyl-β-D-glucopyranoside (PNPG). The percentage of alpha-glucosidase inhibition was measured as follows:

$$\% \text{ Activity of sample} = \frac{A_{405} \text{ of sample} - A_{405} \text{ of controls}}{A_{405} \text{ of control}} \times 100, \quad (1)$$

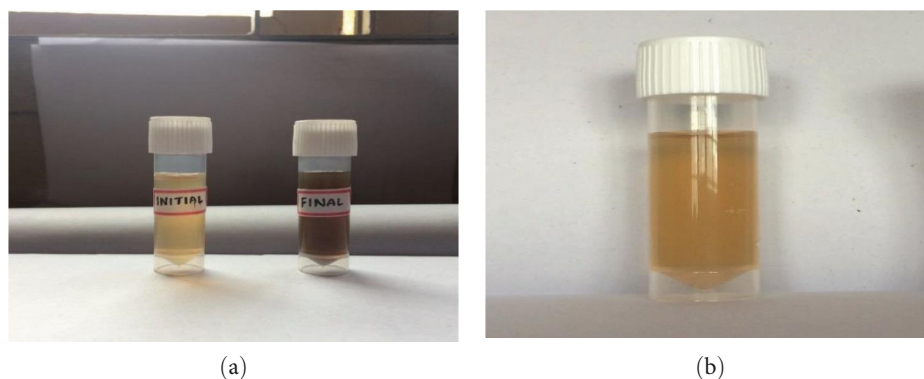


FIGURE 1: Mycosynthesis of Ag-coated ZnO NPs from *G. lucidum*: (a) initial and final color of Ag-coated ZnO NPs; (b) Ag coated with the mixture of *G. lucidum* extract and zinc nitrate solution.

To prevent the action of the alpha-glucosidase by 50% (IC₅₀), the inhibitory concentration of the gold nanoparticles was calculated graphically [10, 14].

2.6.2. In Vitro Alpha-Amylase Enzyme Inhibition Assay. The approach was used to determine the activity of alpha-amylase (Hansawasdi et al. [15]). In each tube, 2 mg of starch azure was suspended in 0.2 ml of 0.5 M Tris-HCl buffer (pH 6.9) and 0.01 M CaCl₂. The tubes holding the substrate solution were boiled for 5 min before being incubated for 5 min at 37°C. Ag-ZnO NPs were taken in each tube containing different concentrations of dimethyl sulfoxide (10, 20, 40, 60, 80, and 100 g/ml) [15].

PPA from the porcine pancreas was dissolved in Tris-HCl buffer to a concentration of 2 units/ml, and 0.1 ml of this enzyme solution was added to each of the tubes stated above. The absorbance of the resulting supernatant was measured at 595 nm using a spectrophotometer (UV-vis spectrophotometer UV-2450, Shimadzu). The alpha-amylase inhibitory activity was calculated as follows:

$$\frac{[(Ac+) - (Ac-)] - [(As - Ab)]}{[(Ac+) - (Ac-)]} \times 100, \quad (2)$$

where Ac+, Ac-, As, and Ab are defined as the absorbance of 100% enzyme activity (only solvent with enzyme), 0% enzyme activity (only solvent without enzyme activity), a test sample (with enzyme), and a blank (a test sample without enzyme), respectively.

2.7. Anticancer Activity of Silver-Coated Zinc Nanoparticles

2.7.1. MTT Assay. The cytotoxic effects of Ag-ZnO NPs against MDA-MB 231 cell lines were determined using the MTT test. The cell lines were seeded in 96-well microtiter plates, which were then filled with the appropriate amounts of Ag-ZnO NPs stock solutions and cultured at 37°C for 48 hr. As a control, cells that had not been treated were utilized. The MTT (3-(4,5-dimethylthiazol-2-yl)-2,5-diphenyl tetrazolium bromide, tetrazole) colorimetric assay was used to test the cultivated cell. MTT (5 mg/ml, 20l) was added to each group of cells, and the plates were incubated

for another 4 hr. The medium was then withdrawn, and DMSO (200L, Sigma-Aldrich, USA) was added to dissolve the formazan crystals formed by metabolically active cells reducing the tetrazolium salt [16].

MTT is reduced into metabolically active cells to yield an insoluble purple formazan product. The cell suspensions were dispensed (100 μl) in triplicate into 96-well culture plates at optimized concentrations of 1 × 10⁵ cells/well for each cell line, after a 24 hr recovery period. Assay plates were read using a spectrophotometer at 560 nm. The absorbance of the samples was measured using a microplate (ELISA) reader [17].

Trypan blue assay was performed to quantify the dead cells following the treatment of cytotoxic stimuli using trypan blue dye.

3. Results and Discussion

3.1. Visual Observation. Analysis of ZnO nanoparticles was made by coating Ag particles, the aqueous solution of *G. lucidum* was then mixed with the solution of zinc nitrate. Later, the silver nitrate slowly started to change its nature which resulted in the color change. This color transition served as evidence for the synthesis completion [18]. The final brownish color change is shown in Figure 1, which exhibited the reduction of zinc nitrate to zinc oxide and it occurs due to the excitation of the surface plasmon resonance effect [11]. The observation was alike to the green synthesis of silver nanoparticles from an aqueous extract of brown seaweed of *Padina boergesenii*, which was completed by Chikkanna et al. [19].

3.2. UV-Visible Spectral Analysis. UV-vis spectroscopy was used to confirm the formation of synthesized nanoparticles in the initial stage. The dark brownish sample of ZnO NPs was coated with Ag nanoparticles, which were synthesized from the extract of *G. lucidum*. The synthesized ZnO NPs were scanned by using UV-vis spectroscopy under the range between 300 and 600 nm [20]. The result obtained from UV-vis spectral analysis showed (Figure 2) a high-absorption peak at 370 nm, which corresponds to synthesized ZnO NPs. Also, this intense response of ZnO NPs could be due to the surface plasmon resonance effect. The synthesized product is

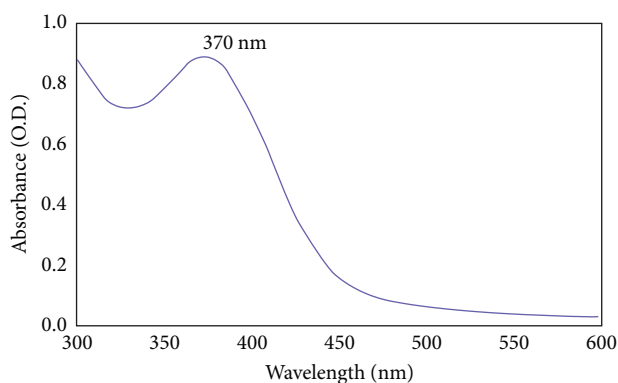


FIGURE 2: UV-vis absorption spectra of Ag-coated ZnO NPs synthesized from *G. lucidum*.

TABLE 1: FTIR analysis of Ag-coated ZnO NPs.

Sr. No.	Wavenumber (cm ⁻¹)	Stretch	Functional groups
1	1,991	NH ₂	Primary amides
2	1,644	N=O	Nitrogen group
3	1,515	CO ₂	Carbonyl group
4	1,392	C=C	Alkenes
5	958	C-S	Alkyl sulfides

confirmed to claim ZnO NPs coated with Ag because no other peaks were observed in the UV spectrum region [21]. A similar observation was also reported earlier by Siva Vijayakumar et al. [22] in the green synthesis of zinc oxide nanoparticles from the extracts of leaf, stem, and *in vitro* grown callus of *Mussaenda frondosa* L.: characterization and their applications.

3.3. Fourier-Transformed Infrared (FTIR) Spectral Analysis. The FTIR absorption spectra of the water-soluble extract before and after reduction of Ag-coated ZnO NPs showed the capping ligand of the silver-coated zinc oxide nanoparticles which may be due to the linkage of an alkenes, alkyl sulfides groups, carboxyl groups, primary amides, and nitro groups as described in Table 1 and Figure 3. FTIR analysis of the synthesized Ag-ZnO NPs exposes strong bands at 1,991, 1,644, 1,515, 1,392, and 958 cm⁻¹. We confirmed that the strong peak was focused at 1,515 cm⁻¹, which corresponds to the carboxyl groups from amino acid residues, and that proteins had the highest ability to bind metals, based on the FTIR results. This intercalation might explain why proteins create metal oxide nanoparticles (i.e., capping of silver-coated zinc nanoparticles) to avoid agglomeration and maintain the medium. It has already been reported in the green synthesis of ZnO nanoparticles using *Solanum nigrum* leaf extract, that the same functional groups of phytochemicals induce the nanoparticles were synthesized using amines, alkanes, and carboxyl ions that are widely seen in secondary metabolites such as terpenoids, flavonoids, and alkaloids.

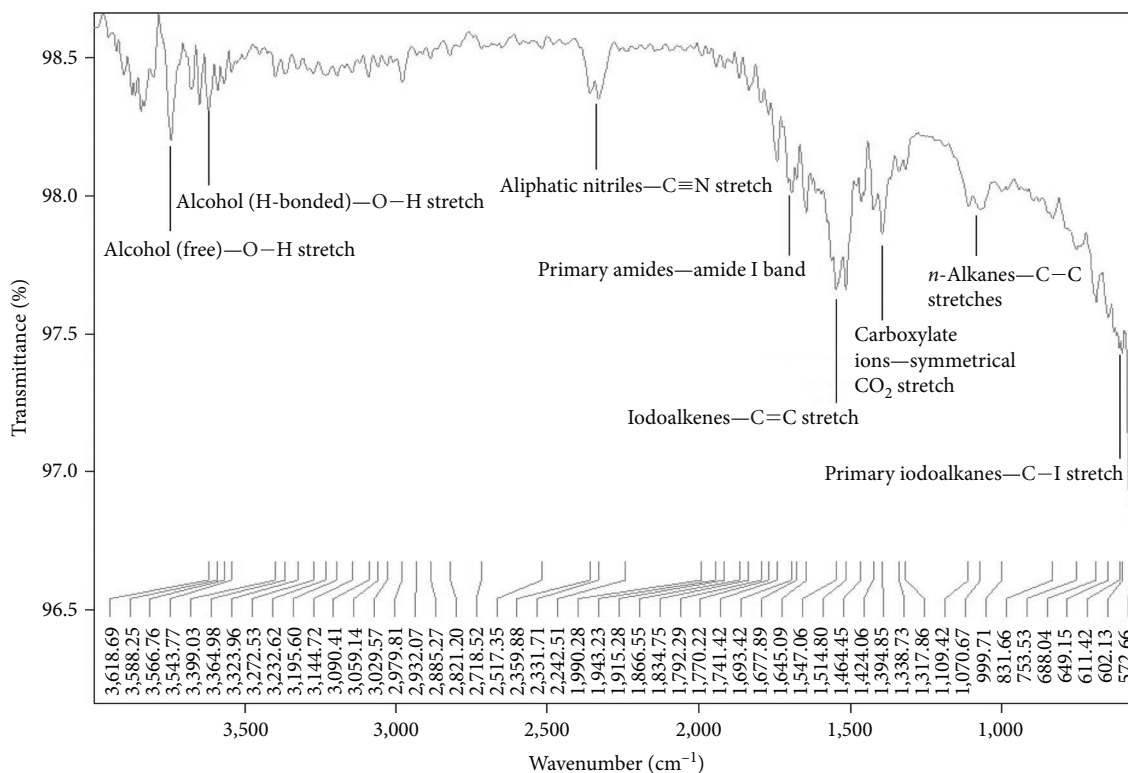
3.4. Scanning Electron Microscope Analysis. The silver-coated zinc nanoparticles synthesized with the aid of *G. lucidum* extract were scanned using SEM in order to determine the

morphology, polydispersed shape, and size of the synthesized nanoparticle. SEM images (Figure 4) showed that the particles formed were spherical, hexagonal, and triangular. The nanoparticles formed were in the range of 20–100 nm in size. The obtained SEM results were similar to the synthesis of ZnO NPs from the leaves of *Passiflora caerulea* L. (*Passifloraceae*), which was reported earlier by Santhoshkumar et al. [23].

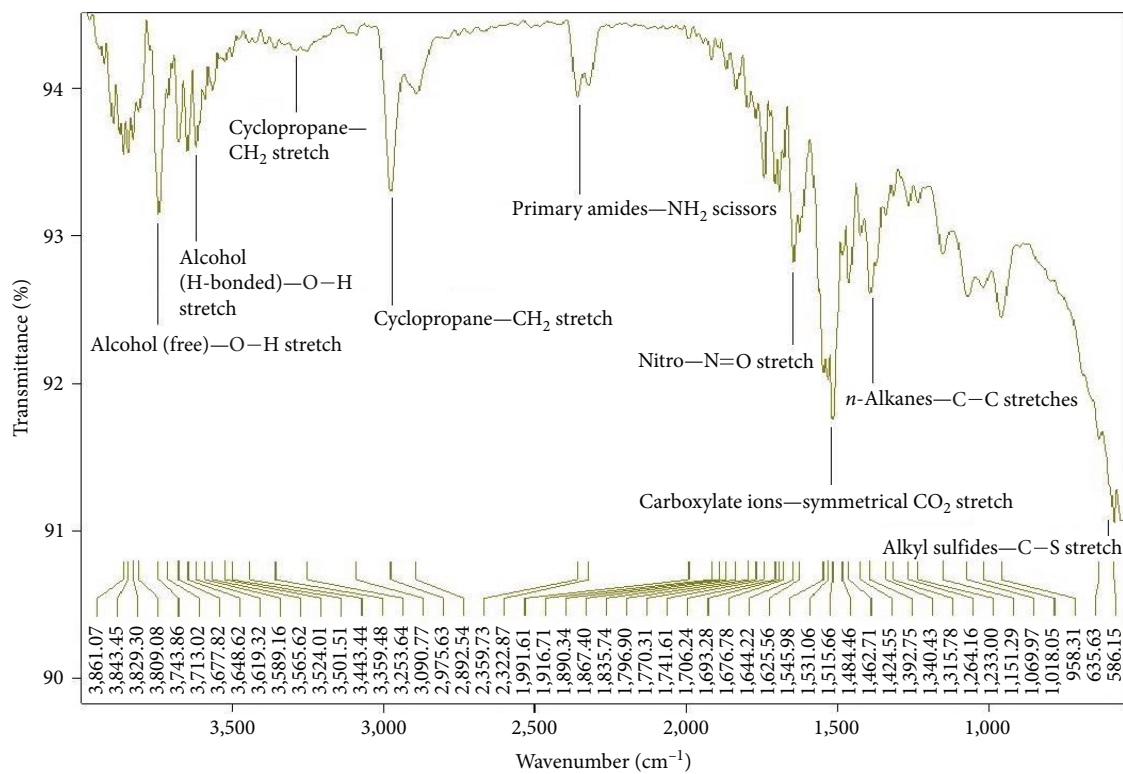
3.5. Energy Dispersive Diffraction Analysis. The elemental composition of mycosynthesized ZnO NPs coated with Ag from *G. lucidum* was investigated using EDX to confirm the presence of Zn in the nanoparticle solution that was purified using the ultracentrifugation process. The EDX findings (Figure 5) revealed a significant peak of zinc and silver in the suspension, confirming its existence [24]. The presence of silver alongside zinc shows that biomolecules were involved in the creation of ZnO nanoparticles coated with Ag and that they may have also functioned as stabilizing molecules to ensure the nanoparticles' stability. The obtained result from EDX was similar to the study of Santhoshkumar et al. [23]. In his study, the synthesis of zinc oxide nanoparticles was using the plant leaf extract of *Passiflora caerulea* L. (*Passifloraceae*), in which Zn was elevated in the nanoparticles suspension which was visible in the result of EDX analysis.

3.6. Transmission Electron Microscopy (TEM) Analysis. TEM analysis was carried out for further confirmation of the synthesized ZnO NPs coated with Ag from *G. lucidum*. The findings of the TEM are shown in Figure 6, which showed that the produced particles were mostly polydistributed and were spherical, hexagonal, and triangular. The selected area electron diffraction (SAED) pattern also reveals the crystalline structure of the ZnO nanoparticles coated with Ag. The particle sizes varied from 10 to 20 nm [25, 26]. In previous kinds of literature, it was observed that nanoparticles ranging from 2 to 20 nm are assumed to be good characteristics of a nanoparticle. So, the resultant product also has the same mentioned range in size, which was enough to conclude the good formation of synthesized ZnO NPs coated with Ag. A similar observation has been reported in the green synthesis of zinc oxide nanoparticles using flower extract of *Nyctanthes arbor-tristis* by Jamdagni et al. [27].

3.7. Alpha-Amylase Inhibition Assay and Alpha-Glycosidase Assay. Antidiabetic activity of synthesized ZnO NPs coated with Ag was evaluated by the inhibition assays of alpha-glucosidase and alpha-amylase enzymes. The results obtained from both enzyme inhibition assays shown in Tables 2 and 3 exhibited the concentration of both Ag-ZnO NPs and standard drug (acarbose) on their respective enzymes. It reveals the carbohydrate digestive enzyme inhibition effect of synthesized Ag-ZnO NPs from *G. lucidum*. So, the results exhibited the significant antidiabetic potential of Ag-ZnO NPs. With an increasing concentration of Ag-ZnO NPs, the enzyme inhibition level was automatically elevated remarkably, so it might be used to prepare effective antidiabetic drugs without any harmful actions. Thus, the Ag-ZnO NPs seem to be a promising and effective antidiabetic agent that can induce a significant reduction of enzymes. A similar



(a)



(b)

FIGURE 3: FTIR spectrum of Ag-coated ZnO NPs synthesized from *G. lucidum*: (a) control water-soluble extract (*G. lucidum*); (b) Ag-coated ZnO NPs with water-soluble extract of *G. lucidum*.

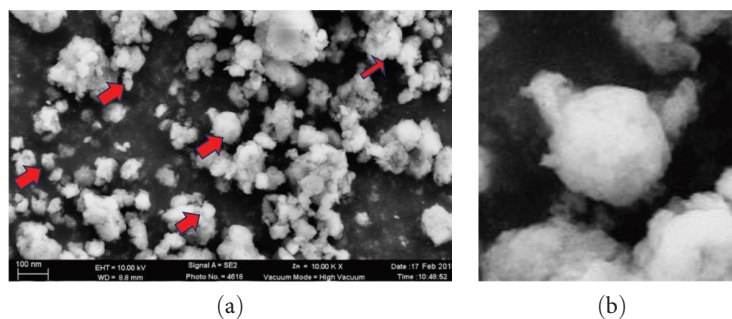


FIGURE 4: SEM analysis of Ag-coated ZnO NPs synthesized from *G. lucidum*: (a) synthesized nanoparticles; (b) enlarged portion of Ag-coated ZnO NPs.

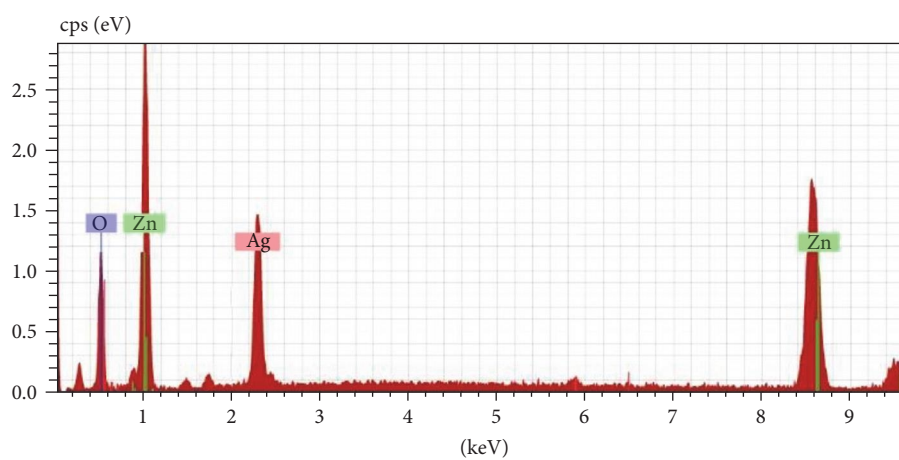


FIGURE 5: EDAX spectrum of Ag-coated ZnO NPs synthesized from *G. lucidum*.

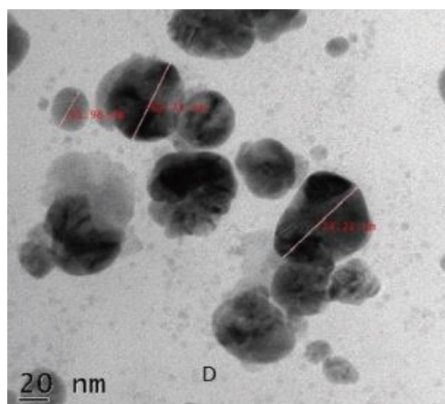


FIGURE 6: TEM analysis of Ag-coated ZnO NPs synthesized from *G. lucidum*.

carbohydrate digestive enzyme inhibition effect was reported earlier in the antidiabetic activity of Ag NPs from green synthesis using *Lonica japonica* leaf extract by Balan et al. [28].

3.8. Cytotoxicity–MTT Assay. MTT assay was performed on chemoresistance breast cancer MDA-MB 231 cell lines to investigate the anticancer activity of Ag–ZnO NPs synthesized from *G. lucidum*. The attained results shown in Figure 7 exhibits that the cell viability was significantly

decreased when increasing the concentration of both ZnO NPs coated with Ag synthesized from *G. lucidum* and crude extract of *G. lucidum* on cell lines. Trypan blue assay resulted in maximum quantity of more than 90% of dead cells stained by trypan blue assay counted using a hemocytometer on a basic upright microscope. Nanoparticles are a good therapeutic agent in anticancer therapy. *G. lucidum* is a good anticancer medicine since ancient days [29]; so, nanoparticle and *G. lucidum* will be a good combination in treating breast

TABLE 2: Alpha amylase inhibition assay effect of Ag-coated ZnO NPs synthesized from *G. lucidum*.

Sr. No.	Concentration ($\mu\text{g/ml}$)	Percent (%) inhibition of alpha-glucosidase activity	Standard (acarbose)
1.	10	32.33 ± 0.01	13.06 ± 0.01
2.	20	46.52 ± 0.10	20.09 ± 0.01
3.	40	58.90 ± 0.01	39.30 ± 0.01
4.	60	75.32 ± 0.01	53.59 ± 0.03
5.	80	82.21 ± 0.06	70.78 ± 0.01
6.	100	94.37 ± 0.06	85.34 ± 0.02
7.	IC 50 ($\mu\text{g/ml}$)	24	39

Values are mean \pm SD ($n=6$), values not sharing a common letter differ significantly at <0.05 by DMRT.

TABLE 3: Alpha-glucosidase inhibition effect of Ag-coated ZnO NPs synthesized from *G. lucidum*.

Sr. No.	Concentration ($\mu\text{g/ml}$)	Percent (%) inhibition of alpha-amylase activity	Standard (acarbose)
1.	10	14.01 ± 0.01	18.17 ± 0.01
2.	20	28.67 ± 0.01	21.34 ± 0.01
3.	40	37.25 ± 0.01	31.21 ± 0.02
4.	60	45.34 ± 0.02	42.78 ± 0.01
5.	80	68.12 ± 0.01	60.34 ± 0.03
6.	100	79.24 ± 0.01	74.71 ± 0.01
7.	IC 50 ($\mu\text{g/ml}$)	47	50

Values are mean \pm SD ($n=6$), values not sharing a common letter differ significantly at <0.05 by DMRT.

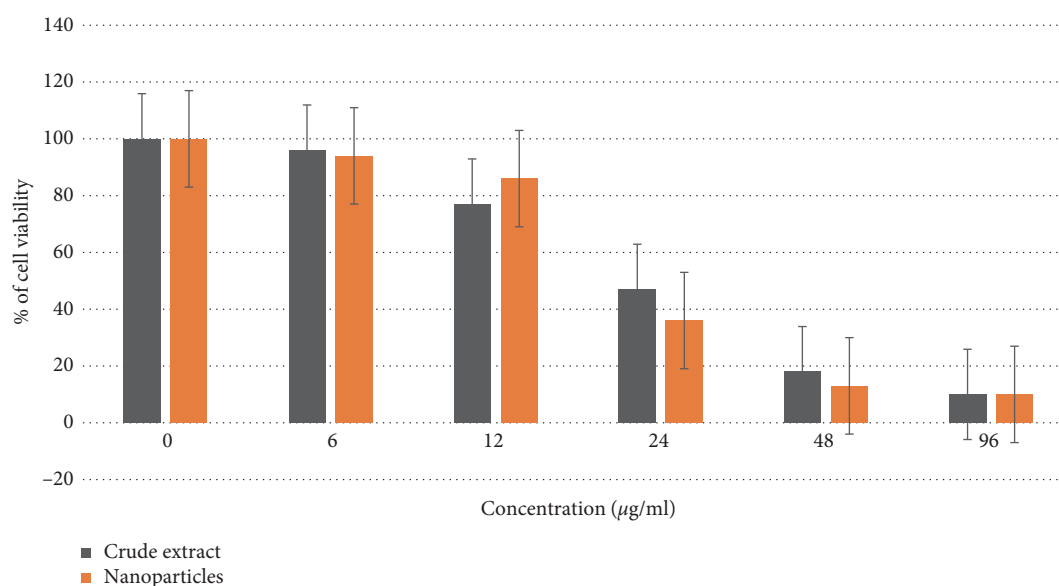


FIGURE 7: Percentage of cell viability for crude extract and synthesized ZnO NPs coated with Ag based on the MTT assay.

cancer. Our synthesized Ag-ZnO NPs might be an alternative treatment and therapeutic approach against cancer because other treatments include chemotherapy, radiotherapy, and drugs are potentially cause severe side effects like pain, strain, etc. In the future, the production of drugs by using natural sources instead of toxic chemicals will play a major role in pharmaceutical industries [30]. Currently, several studies are going on with the combination of nanoparticles and other

therapeutic techniques like infrared laser light for treating the various types of cancers. In those researches, the positive results are appearing in the animal models which were proved by many researchers. Hence, more clinical trials are needed to successfully approve nanoparticle-related treatments for testing on humans [31]. In this study, Ag-ZnO NPs and crude extract of mushroom were treated on human chemoresistance breast cancer MDA-MB 231 cell lines.

4. Conclusion

The biosynthesis method used in this study exhibited a simple, eco-friendly meanwhile budget-friendly process when compared to other methods. Thus, the results of the present study successfully proved the antidiabetic and anticancer potential of our mycosynthesized Ag–ZnO NPs. The effect of Ag–ZnO NPs on chemoresistance breast cancer MDA-MB 231 cell lines revealed promising cytotoxicity. Due to nontoxic and less usage of chemicals, these kinds of biosynthesized Ag–ZnO NPs will predominantly take their place in the pharmaceutical field.

Data Availability

The data used to support the findings of this study are included within the article.

Conflicts of Interest

The authors declare that they have no conflicts of interest.

Acknowledgments

The authors would like to acknowledge Department of Nano Science and Technology, Vellore Institute of Technology, Vellore, Tamil Nadu, India. The authors extend their thanks to Dr. P. Senthilkumar, Nehru College of Arts and Science, Coimbatore, Tamil Nadu, India for his immense support throughout the research. The authors are grateful to Dr. G. R. Damodaran College of Science, Coimbatore, Tamil Nadu, India for providing facilities and encouragement towards the research. The authors extend their appreciation to the researchers supporting project number (RRSP-2021-224) King Saud University, Riyadh, Saudi Arabia.

References

- [1] A. Arya, K. Gupta, T. S. Chundawat, and D. Vaya, “Biogenic synthesis of copper and silver nanoparticles using green alga *Botryococcus braunii* and its antimicrobial activity,” *Bioinorganic Chemistry and Applications*, vol. 2018, Article ID 7879403, 9 pages, 2018.
- [2] N. A. Martynova, V. N. Svishchev, L. S. Lepnev et al., “Electrochemical coprecipitation of zinc and aluminum in aqueous electrolytes for ZnO and AZO coverage deposition,” *International Journal of Photoenergy*, vol. 2019, Article ID 6808347, 10 pages, 2019.
- [3] A. Hussain, M. Oves, M. F. Alajmi et al., “Biogenesis of ZnO nanoparticles using *Pandanus odorifer* leaf extract: anticancer and antimicrobial activities,” *RSC Advances*, vol. 9, no. 27, pp. 15357–15369, 2019.
- [4] H. M. Fahmy, A. M. Mosleh, A. A. Elghany et al., “Coated silver nanoparticles: synthesis, cytotoxicity, and optical properties,” *RSC Advances*, vol. 9, no. 35, pp. 20118–20136, 2019.
- [5] J. Singh, T. Dutta, K. H. Kim, M. Rawat, P. Samddar, and P. Kumar, “Green synthesis of metals and their oxide nanoparticles: applications for environmental remediation,” *Journal of Nanobiotechnology*, vol. 16, Article ID 84, 2018.
- [6] P. D. Babu and R. S. Subhasree, “The sacred mushroom “Reishi”-a review,” *American-Eurasian Journal of Botany*, vol. 1, no. 3, pp. 107–110, 2008.
- [7] C. Kao, A. C. Jesuthasan, K. S. Bishop, M. P. Glucina, and L. R. Ferguson, “Anti-cancer activities of *Ganoderma lucidum*: active ingredients and pathways,” *Functional Foods in Health and Disease*, vol. 3, no. 2, pp. 48–65, 2013.
- [8] P. Batra, A. K. Sharma, and R. Khajuria, “Probing lingzhi or reishi medicinal mushroom *Ganoderma lucidum* (higher Basidiomycetes): a bitter mushroom with amazing health benefits,” *International Journal of Medicinal Mushrooms*, vol. 15, no. 2, pp. 127–143, 2013.
- [9] H. M. Abdelmigid, M. M. Morsi, N. A. Hussien, A. A. Alyamani, and N. M. Al Sufyani, “Comparative analysis of nanosilver particles synthesized by different approaches and their antimicrobial efficacy,” *Journal of Nanomaterials*, vol. 2021, Article ID 2204776, 12 pages, 2021.
- [10] P. Senthilkumar, R. S. Kumar, L. Surendran et al., “Potent antidiabetic activity of aqueous extract of brown seaweed *Padina boergesenii* in streptozotocin-induced diabetic rats,” *World Journal of Pharmaceutical Research*, vol. 6, no. 8, pp. 2022–2035, 2017.
- [11] D. S. Ranjith Santhosh Kumar, P. Senthilkumar, L. Surendran, and B. Sudhagar, “*Ganoderma lucidum*-oriental mushroom mediated synthesis of gold nanoparticles conjugated with doxorubicin and evaluation of its anticancer potential on human breast cancer mcf-7/dox cells,” *International Journal of Pharmacy and Pharmaceutical Sciences*, vol. 9, no. 9, pp. 267–274, 2017.
- [12] S. Abel, J. L. Tesfaye, N. Nagaprasad, R. Shanmugam, L. P. Dwarampudi, and R. Krishnaraj, “Synthesis and characterization of zinc oxide nanoparticles using moringa leaf extract,” *Journal of Nanomaterials*, vol. 2021, Article ID 4525770, 6 pages, 2021.
- [13] S. Vinodhini, B. S. M. Vithiya, and T. A. A. Prasad, “Green synthesis of palladium nanoparticles using aqueous plant extracts and its biomedical applications,” *Journal of King Saud University-Science*, vol. 34, no. 4, Article ID 102017, 2022.
- [14] T. Matsui, S. Ebuchi, K. Fukui, K. Matsugano, N. Terahara, and K. Matsumoto, “Caffeoylsophorose, a new natural α -glucosidase inhibitor, from red vinegar by fermented purple-fleshed sweet potato,” *Bioscience, Biotechnology, and Biochemistry*, vol. 68, no. 11, pp. 2239–2246, 2004.
- [15] C. Hansawasdi, J. Kawabata, and T. Kasai, “ α -Amylase inhibitors from roselle (*Hibiscus sabdariffa* Linn.) tea,” *Bioscience, Biotechnology, and Biochemistry*, vol. 64, no. 5, pp. 1041–1043, 2000.
- [16] L. Thangavelu, A. H. Adil, S. Arshad et al., “Antimicrobial properties of silver nitrate nanoparticle and its application in endodontics and dentistry: a review of literature,” *Journal of Nanomaterials*, vol. 2021, Article ID 9132714, 12 pages, 2021.
- [17] M. Ehsan, A. Waheed, A. Ullah et al., “Plant-based bimetallic silver-zinc oxide nanoparticles: a comprehensive perspective of synthesis biomedical applications, and future trends,” *BioMed Research International*, vol. 2022, Article ID 1215183, 20 pages, 2022.
- [18] P. Mulvaney, “Surface plasmon spectroscopy of nanosized metal particles,” *Langmuir*, vol. 12, no. 3, pp. 788–800, 1996.
- [19] M. M. Chikkanna, S. E. Neelagund, and K. K. Rajashekarappa, “Green synthesis of zinc oxide nanoparticles (ZnO NPs) and their biological activity,” *SN Applied Sciences*, vol. 1, Article ID 117, 2019.

- [20] J. Estrada-Urbina, A. Cruz-Alonso, M. Santander-González, A. Méndez-Albores, and A. Vázquez-Durán, "Nanoscale zinc oxide particles for improving the physiological and sanitary quality of a Mexican landrace of red maize," *Nanomaterials*, vol. 8, no. 4, Article ID 247, 2018.
- [21] M. D. Jayappa, C. K. Ramaiah, M. A. P. Kumar et al., "Green synthesis of zinc oxide nanoparticles from the leaf, stem and in vitro grown callus of *Mussaenda frondosa* L.: characterization and their applications," *Applied Nanoscience*, vol. 10, pp. 3057–3074, 2020.
- [22] T. Siva Vijayakumar, S. Karthikeyeni, S. Vasanth et al., "Synthesis of silver-doped zinc oxide nanocomposite by pulse mode ultrasonication and its characterization studies," *Journal of Nanoscience*, vol. 2013, Article ID 785064, 7 pages, 2013.
- [23] J. Santhoshkumar, S. V. Kumar, and S. R. Kumar, "Synthesis of zinc oxide nanoparticles using plant leaf extract against urinary tract infection pathogen," *Resource-Efficient Technologies*, vol. 3, no. 4, pp. 459–465, 2017.
- [24] R. Dobrucka and J. Długaszewska, "Biosynthesis and antibacterial activity of ZnO nanoparticles using *Trifolium pratense* flower extract," *Saudi Journal of Biological Sciences*, vol. 23, no. 4, pp. 517–523, 2016.
- [25] K. B. Narayanan and N. Sakthivel, "Green synthesis of biogenic metal nanoparticles by terrestrial and aquatic phototrophic and heterotrophic eukaryotes and biocompatible agents," *Advances in Colloid and Interface Science*, vol. 169, no. 2, pp. 59–79, 2011.
- [26] M. Ramesh, M. Anbuvarnan, and G. Viruthagiri, "Green synthesis of ZnO nanoparticles using *Solanum nigrum* leaf extract and their antibacterial activity," *Spectrochimica Acta Part A: Molecular and Biomolecular Spectroscopy*, vol. 136, Part B, pp. 864–870, 2015.
- [27] P. Jamdagni, P. Khatri, and J. S. Rana, "Green synthesis of zinc oxide nanoparticles using flower extract of *Nyctanthes arbor-tristis* and their antifungal activity," *Journal of King Saud University-Science*, vol. 30, no. 2, pp. 168–175, 2018.
- [28] K. Balan, W. Qing, Y. Wang et al., "Antidiabetic activity of silver nanoparticles from green synthesis using *Lonicera japonica* leaf extract," *RSC Advances*, vol. 6, no. 46, pp. 40162–40168, 2016.
- [29] S. D. Mankar, S. Thombare, T. Todmal, R. Waghe, and A. Borde, "Medicinal mushroom: an ancient culture towards new lifestyle," *Research Journal of Pharmacognosy and Phytochemistry*, vol. 14, no. 1, pp. 50–54, 2022.
- [30] S. Rajeshkumar, S. Menon, S. V. Kumar, M. Ponnaniakamideen, D. Ali, and K. Arunachalam, "Anti-inflammatory and antimicrobial potential of *Cissus quadrangularis*-assisted copper oxide nanoparticles," *Journal of Nanomaterials*, vol. 2021, Article ID 5742981, 11 pages, 2021.
- [31] P. Senthilkumar, G. Yaswant, S. Kavitha et al., "Preparation and characterization of hybrid chitosan-silver nanoparticles (Chi-Ag NPs): a potential antibacterial agent," *International Journal of Biological Macromolecules*, vol. 141, pp. 290–298, 2019.

Research Article

Mycosynthesis of Noble Metal Nanoparticle Using *Laetiporus versisporus* Mushroom and Analysis of Antioxidant Activity

M. R. Farzana Fathima ¹, A. Usha Raja Nanthini ^{1,2}, Fatimah S. Al-Khattaf,³
Ashraf Atef Hatamleh,³ and Sadib Bin Kabir ⁴

¹Department of Biotechnology, Mother Teresa Women's University, Kodaikanal, Tamil Nadu, India

²Department of Environmental Energy and Engineering, Kyonggi University, Youngtong-Gu, Suwon, Gyeonggi-Do 16227, Republic of Korea

³Department of Botany and Microbiology, College of Science, King Saud University, P.O. Box 2455, Riyadh 11451, Saudi Arabia

⁴Department of Civil Engineering, Military Institute of Science and Technology, Dhaka 1216, Bangladesh

Correspondence should be addressed to A. Usha Raja Nanthini; biotechurn@gmail.com and Sadib Bin Kabir; sadibb@pu.edu.bd

Received 21 July 2022; Accepted 15 September 2022; Published 7 October 2022

Academic Editor: Pounsamy Maharaja

Copyright © 2022 M. R. Farzana Fathima et al. This is an open access article distributed under the Creative Commons Attribution License, which permits unrestricted use, distribution, and reproduction in any medium, provided the original work is properly cited.

Nanoparticles being the backbone of nanotechnology gain more attention nowadays as they are entirely different from the colloids and also exhibit unique electrochemical, physical, and optical properties corresponding to their dimensions and shape. The core concept of getting nanoparticles from metal colloids lies on the traditional approach that is applied in both conventional and mechanical methods these days. Among those, the techniques that rely on the biological systems for the generation of nanoparticles have more merits and precedence over other environmental mechanisms as this mitigates the expense as well as toxicity. Considering both nutritional and medicinal values of mushrooms, they were properly managed, adopted, and accustomed in distinct skills to get desired products of nanosizes. Gold is commonly known as a noble metal, and it owns enormous medicinal values since long time in history. Here, a mycosynthesis approach was applied; by the way, the mushroom *Laetiporus versisporus* and gold ions collaborate to bring out gold nanoparticles (AuNPs) were synthesized by the involvement of *Laetiporus versisporus*. Mycosynthesis deals with an environmentally friendly process that leads to the extracellular synthesis of AuNPs. The *Laetiporus versisporus* were collected from hills of Kodaikanal, Tamil Nadu. The gold source turned into ultrafiner particles which were then computed and monitored through UV-Vis spectrophotometer and Fourier-transform infrared (FTIR) spectroscopy, and the texture of particles was affirmed with the help of peaks originated in X-ray diffraction (XRD). Transmission electron microscopy (TEM) techniques and scanning electron microscope (SEM) unveiled spherical AuNPs, and the overall scale of which was figured as 10 nm. Various concentrations of AuNPs by the concentration of extracted *Laetiporus versisporus* were evaluated for antioxidant activity using the standard in vitro methods like ferrous ion chelating effect, nitric oxide (NO) scavenging assay, and DPPH assay activity.

1. Introduction

Mushrooms, an omnipresent creature, are macrofungi, which can be found in the woodland and be cultivated on farmland. Some types of mushrooms like *Lentinus edodes*, *Lentinus polychrous*, *Pleurotus ostreatus*, *Pleurotus florida*, and *Cordyceps militaris* have medicinal benefits like targeting and defeating the cancer cells and proteins, antioxidant, antimicrobial, anti-diabetic, antihypercholesterolic, and antiarthritic activities [1].

Antioxidants have an extraordinary contribution in promoting the well-being of human by depleting the free radicals when they are supplemented every day. In recent days, there is an attentiveness towards the realization of antioxidant capacity of food stuffs. Edible mushrooms contain immense primary and secondary metabolites, which are responsible for their nutritional and medicinal properties. Antioxidants say an alkaloid, flavonoid, steroid, protein, or an amino acid prevent oxidative stress caused by the unstable compounds,

i.e., free radicals [2]. However, in recent years, interest in the biological and pharmacological activities of mushrooms is grown. Nanotechnology deals with the nanomaterials derived from natural resources and their impact with the same. It is a field that connects various networks of science and technology. Nanoparticles are the sole representatives in nanoworld, and their application in diverse fields makes them more influential. Many nanoparticles are presented, and among those nanoparticles, the gold nanoparticles (AuNPs) have many benefits. A present-day research finds the fact that the nanoparticles synthesized biologically are preferred as it is integrated with the phytoconstituents [3]. The nanoparticles have been widely used in high tech implementation [4]. Noble metal nanoparticles like silver, platinum, gold, and lead are explored and reviewed by various researches earlier [5, 6]. Among the abovesaid metal nanoparticles, the gold nanoparticle is considered to be vital due to the medicinal use ranging from cancer to arthritis dated back in history [7]. Also, their telescoping synthesis, with great biocompatibility and apoptosis with promising applications especially in the development of novel antibacterial agents, makes AuNPs more powerful [6, 8]. Not only in tumor targeting and imaging, gold nanoparticles (GNPs) made an impact in electronic applications, photothermal therapy, and photonics due to their unique surface plasmon resonance effect [9]. This individuality makes them more enhancing in the fields of medical science, bioengineering, and industrial applications [10]. AuNPs extend their implementation in endocytosis, chemical catalysts, gene expression, pharmacokinetics, sensors, and fuel cells [11]. Above all, gold is time honored as it has uses as remedial, restorative, and ornamental roles since primitive days. "Soluble gold" is a phrase which was pioneered in two different countries in different continents: Province of China during the 4th century and Egypt in the 5th century BC [12].

Gold nanoparticle (AuNP) obtained from the plants is a customary method that produces ultrafine particles, which have discrete benefits in the desired fields [13]. Physical and chemical methods of synthesizing metal nanoparticles often lead to some hazardous results such as the toxicity and excess time taken to get the end product, though the nanoparticles are almost pure and stable. To overcome the disadvantages of unconventional methods, living organisms, their components, and byproducts are being used for the production of nanoparticles that has steady and firm activity in an energy efficient way [14]. Exploiting natural resources to produce nanomaterials is quite common in today's world which is concise with the use of chemicals and that too are not dangerous [15]. The green mushroom nanoparticles were investigated as antimicrobial, antioxidant, and antitumor agents [16]. Using mushrooms in the formation of metallic nanoparticles, lean on the fruiting bodies, mycelia, and enzymes that are produced and nurtured in massive quantity and also in prescribed laboratory conditions [17]. As the nanoparticles were reared by some chemical and physical means, their usage in health science is limited due to the ill effects given out by them [18]. Several studies examined the antioxidant activity raised by the gold nanoparticles proved to be evident in different concentrations and at varied environmental factors [19]. This research

study presented the mycosynthesis of gold nanoparticles and a comparative analysis of different antioxidants.

Balakumaran et al. [20] described the antimicrobial properties of gold and silver nanoparticles from *Aspergillus terreus* (soil and food mold) harvested from hills located in the southern region of India. The reaction conditions were optimized, for the mushroom *Aspergillus terreus* strain Bios PTK 6 to develop nanoparticles that are highly firm and sturdy in a day or less. FTIR analyses gave a detailed idea about the proteins that were bound and capped during the reaction. The nanoparticles were responsible for the deterioration of bacterial cells which was portrayed in SEM image showing the damage of bacterial membrane of human pathogens *Staphylococcus* and *Bacillus* species [21] and concluded that the obtained nanoparticles have antimicrobial activity as that of the antibiotic which was already used against the growth of those pathogens.

Madakka et al. [22] reported *Fusarium* and *Aspergillus* species were indulged in the generation of silver nanoparticles extracellularly. Maximum absorption spectra were obtained between 420 and 450 nm in UV-visible spectroscopy, whereas the nonclustered spherical conformation was illustrated in SEM image. Nanoparticles obtained from fungi inhibit the growth of bacteria like *E.coli* and *Staphylococcus* species and *Pseudomonas* species with a great pharmacokinetic activity thereby promoting the silver nanoparticles to the next level in pharmacology.

A perennial plant, *Coleus forskohlii*, was utilized by [23] to show its yield of gold and silver nanoparticles in one pot synthesis method so as to avoid the drawback of synthetic resources. The crystal structure, size, and shape of the newly formed gold (AuNPs) and silver nanoparticles (AgNPs) were studied characteristically. UV-visible spectrophotometer followed the principle of SPR which then leads to the display of maximum band. High-resolution transmission electron microscopy (HR-TEM) and particle size analysis (PSA) led out the size of particles. Fourier-transform infrared spectroscopy (FTIR) exposed the active molecules behind the reduction of colloids and ions to nanoparticles. GC-MS analysis performed in the sample gave a clear picture to understand the phytoconstituents present in the plant. Moreover, DPPH assay deduced the antioxidant ability. Nanoparticles showed apoptotic effect by resisting the growth of liver cancer cells that was determined by formation of formazan crystals via MTT assay.

Certain polymers were also used by some researchers to undergo the synthesis of metal nanoparticles. Shuai et al. [24] carried out a procedure which supports the production of gold nanoparticles from chitosan being the reducer. Deacetylation and molecular weight were the major factors during the course of the reaction. At 0.1% of concentration of reaction mixture, they tend to give polygonal nanoparticles. Assays like ABTS, DPPH, and FRAP were done in order to find the capability of antioxidants in the sample and the novel nanoparticles generated from chitosan. It was understood that the antioxidant activity and the shape of the nanoparticles were correlated with each other. Spherical gold nanoparticles and gold colloids with 0.3% of concentration exhibited maximum antioxidant activity rather than the others.

Cornus mas, an ornamental and adaptable shrub, has the potential of serving as a reducer and stabilizer in the process of getting metallic nanoparticles at room temperature. Filip et al. [25] investigated the relative analysis of polyphenols from the shrub. Size and shape of the nanomaterials were examined by individual medium for characterization. Anti-inflammatory level of the coinage metal nanoparticles is inspected in paw tissues of Wistar rats at different intervals: 2 hours, 24 hours, and 48 hours. A partial response was observed by the nanoparticles, and the anti-inflammatory activity was similar to that of the carrageenan injected into the tissues.

Saraschandra and Li [26] found that *Actinidia deliciosa* (kiwi fruit) has profound bioactive compounds that reduce 4-nitrophenol and methylene blue during the formation of Au and Ag nanoparticles that are globular with the range of 7–20 nm particle size and 25–40 nm diameter, respectively. Reduction of chemicals was encouraged by the biomolecules present in the fruit that was confirmed by FTIR analysis. Face-centered cubic and crystalline structure was elucidated by the analytical techniques such as XRD, EDAX, and XPS for AgNPs as well as AuNPs.

2. Materials and Methods

The research study presented the mycosynthesis of AuNPs and a comparative analysis of different antioxidants. The pictorial representation for the present research is given in Figure 1.

2.1. Preparation of Mushroom Extract. Here, the mushrooms (*Laetiporus versisporus*) were freshly collected from the hills of Kodaikanal, Tamil Nadu. They are often wiped in times by double-purified water to get rid of the impurities present on the surface. The mushrooms were chopped into small chunks, shade dried, and powdered. It was then allowed to boil for a while, and the extract was filtered, separated, and allowed to cool at room temperature.

2.2. Biosynthesis of Gold Nanoparticles. The freshly prepared mushroom extract was added to the desired concentration of gold chloride solution and set aside in a dark place together with the control as it was the optimal condition for the reaction to occur. The color change was observed visually. The sample was then centrifuged at 8000 rpm for about 10 minutes. The water content in the resultant precipitate was evaporated when it was placed in a hot air oven for 24 hours, which leads to the formation of gold nanoparticles in powder form.

2.3. Evaluation of Antioxidant Potential. Here, the antioxidant activity is evaluated by the ferrous ion chelating effect, nitric oxide scavenging activity, and scavenging activity by 2,2'-diphenyl-1-picrylhydrazyl.

2.3.1. Ferrous Ion Chelating Effect. The chelating of ferrous ions was estimated by the method used by Puntel et al. [27]. 1 ml of the methanolic extract in a proportion of 50 to 250 $\mu\text{g/ml}$ with an increasing degree of 50 $\mu\text{g/ml}$ was formulated. To that, 0.2 ml of 2 mM FeCl_2 and 0.25 ml of 5 mM ferrozine were put on and kept undisturbed at normal temperature for 10 min to the incubated mixtures, 1.5 ml of

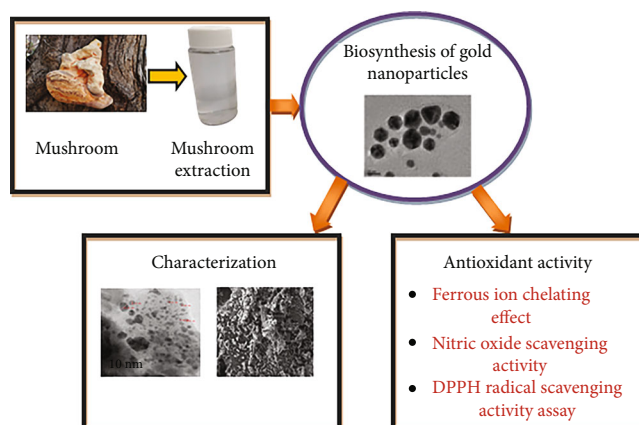


FIGURE 1: Pictorial representation for the present research study.

double distilled water was added, and the absorbance was measured at 562 nm. A triplicate of this assay was done parallel. EDTA was used as a standard to denote the changes in absorbance and chelation. The lowest OD values at 562 nm represent a greater chelation. Percent of chelation by the ferrous ion chelating assay is expressed by the following:

$$\left[1 - \left(\frac{\text{Absorbance of test sample}}{\text{Absorbance of blank}} \right) \right] \times 100. \quad (1)$$

2.3.2. Nitric Oxide Scavenging Activity. This method was proposed and inspected by Alderton et al. [28]. Sodium nitroprusside undergoes reaction in aqueous solution at pH of 7.4 to form nitric oxides. 1 ml of sodium nitroprusside at a concentration of 10 mM in phosphate-buffered saline was prepared, and it was mixed with increasing concentrations of mushroom extract (50, 100, 150, 200, and 250 $\mu\text{g/ml}$). For the next three hours, incubation occurred at 25°C. Meantime, an equal volume of 1% sulphanilamide, 0.1% naphthyl ethylenediamine dichloride, and 3% phosphoric acid were mixed to get Griess reagent (1 ml). Later, the incubated solution and Griess reagent were put together, and the optical density was studied at 546 nm. Similar procedure was followed for gold nanoparticles and standard ascorbic acid in which the mushroom sample was replaced by the nanoparticles and standard. The percentage of inhibition was determined using the formula:

$$\begin{aligned} &\text{Percentage of scavenging effect} \\ &= \left[\frac{(\text{Absorbance of control} - \text{Absorbance of sample})}{(\text{Absorbance of control})} \right] \times 100. \end{aligned} \quad (2)$$

2.3.3. DPPH Radical Scavenging Activity Assay. Brand-Williams and Berset [29] defined the standard procedure of DPPH analysis for determining the scavenging potential of mushroom samples in addition to the nanoparticles in a culture dish [29]. A stock solution of 24 mg DPPH in 100 ml of ethanol was prepared and preserved at 20°C for the consequent use. 3 ml aliquot of this solution was mixed with 1 ml of freshly prepared mushroom extract and gold nanoparticles in the order of 20 $\mu\text{g/ml}$ from 10 to 100 $\mu\text{g/ml}$. The test

samples along with the working solution were agitated thoroughly and placed at 37°C in an unilluminated area for about 15 minutes, and the OD was recorded at 517 nm. Likewise, a control tube was prepared with all ingredients except the test sample. Scavenging activity was evaluated depending on the rate of DPPH traced out which is calculated by the formula:

$$\begin{aligned} &\text{Percentage of inhibition} \\ &= \left[\frac{(\text{Optical density of control} - \text{Optical density of sample})}{(\text{Optical density of control})} \right] \times 100. \end{aligned} \quad (3)$$

3. Results and Discussion

In this section, the experimental analysis is carried out for this study. Here, the characterization of gold nanoparticles followed by the antioxidant activity is analyzed.

3.1. Characterization of Gold Nanoparticles. Current research connects the world of mushrooms with nanotechnology by the way of adapting mushroom *Laetiporus versisporus* in the formation of gold nanoparticles. Though the mushrooms are excellent source of nutrients and other metabolites, they support the biosynthesis perfectly. Appearance, physical model, and structural elucidation of the mushroom mediated gold nanoparticles are assessed by ultraviolet-visible (UV-Vis) spectroscopy, X-ray diffraction (XRD) patterns, Fourier-transform infrared (FTIR) spectroscopy, scanning electron microscope (SEM), and transmission electron microscope (TEM). Characterization of gold nanoparticles clearly says that they are crystalline with 10 nm in size. The size and composition of nanoparticles were characterized by different techniques and were reviewed by [30].

Figure 2 displays UV-visible spectroscopy of gold nanoparticles. The concrete evidence for the presence of gold nanoparticles was clearly understood by the colour change from yellow to purple and then deep purple that is further certified by UV-Vis spectroscopy studies. Colour variation is not concise, and some reactions result in an array of same colours [31]. Visual conformation was the first spotting in the current study followed by several other techniques that prop up the existing data. Transformation of colour from pale yellow to dark brown was observed in the mushroom *Inonotus obliquus* which showed the maximum spectra at 532 nm via UV-visible spectroscopy [32]. Some AuNps obtained from plants exhibit the surface plasmon which is greater than 570 nm [33]. Different proportions of ethanol used for the purpose of production of gold nanoparticles relate with the peak formed at different wavelengths, i.e., below 520 nm for shorter spectra and above 560 nm for a greater peak [34]. A change in the number of electrons possibly leads to a fluctuation in the plasmon resonance through which the fact of presence of nanoparticles comes true [35]. This spectroscopy helps to understand the maximum absorption spectra of gold nanoparticles. It was noted that it has high spectra at 566 nm.

Structural specification and characterization were executed by XRD analysis, and the outcome of the XRD pattern

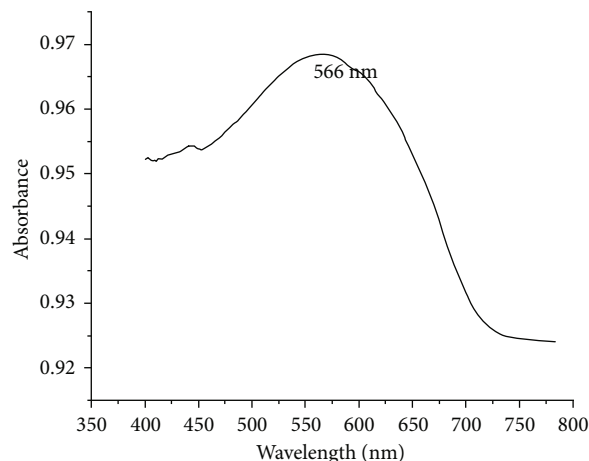


FIGURE 2: UV-Vis spectroscopy of mushroom-synthesized gold nanoparticles.

for gold nanoparticles synthesized from *L. versisporus* is displayed in Figure 3. Dehydrated and dried gold nanoparticles were examined by X-ray diffraction (XRD) patterns to ascertain and also confirm those peak intensity, corresponding position, and width of the peak. XRD analysis exhibits the diffraction peaks at 38.2° and 44.3° that correspond to the crystalline structure of gold (JCPDS no. 04 0784). X-ray diffraction studies provide information about the texture of the particles. The crystalline or amorphous nature can be easily detected with the help of XRD data. The XRD peaks obtained for *L. versisporus*-mediated AuNps are 38.2° and 44.3° that are quite similar to the crystalline nature of *Agaricus bisporus*-engaged gold nanoparticles studied by [36] where they found the 2 theta values at 38.18°, 44.38°, 64.56°, and 77.55°. The exact similar 2 theta values were observed in the study of gold nanoparticles obtained from aqueous extract of *Dolichos biflorus* [37]. Another four high peaks were observed in the XRD pattern of gold nanoparticles synthesized from marine organism [38]. Not only the mushrooms, AuNps extracted from actinomycetes [39], plants [40], and yeast [41] too which had the similar XRD patterns.

Figure 4 shows the FTIR analysis of gold nanoparticles. Fourier-transform infrared (FTIR) spectroscopy measurements are usually carried out to identify the functional groups of bioactive molecules that are accountable for capping and reducing gold ions to gold nanoparticles and ultimately maintaining the stability of them. FTIR bands were intense at 3444 cm⁻¹, which shows the O-H stretch of alcohols and phenols. Fusarium-mediated AuNps showed a band at the similar point which was noted as O-H stretch [12]. Band at 1634 cm⁻¹ conveys the C=O stretch of amide linkage of protein. This can be correlated with the work done in gold nanoparticles originated from *Pseudomonas species* [42] and citrate capped AuNps [43]. Also, the bands at 1557 cm⁻¹ and 1417 cm⁻¹ corresponds to the N-H bend of proteins which was discussed earlier for the nanoparticles got from penicillin [44]; thus, the entire spectra showing that the gold ions were capped majorly by the alcohols and phenols present in the mushroom that were reduced to gold nanoparticles. FTIR spectra delineate the bioactive compounds which were actively participated in

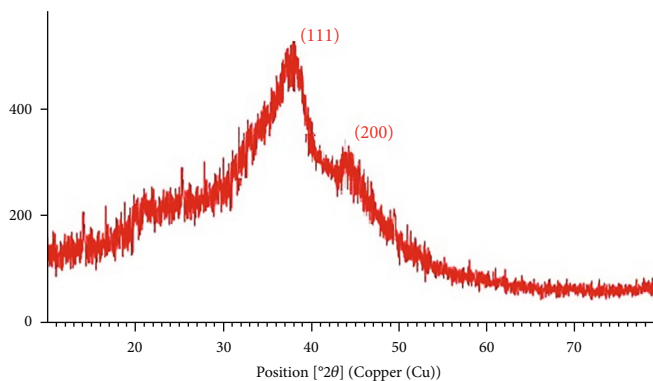


FIGURE 3: XRD of gold nanoparticles.

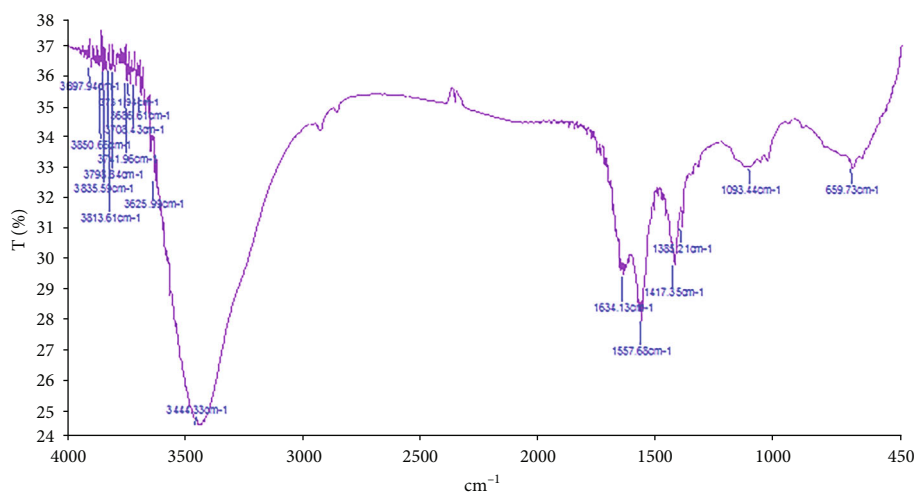


FIGURE 4: FTIR of gold nanoparticles.

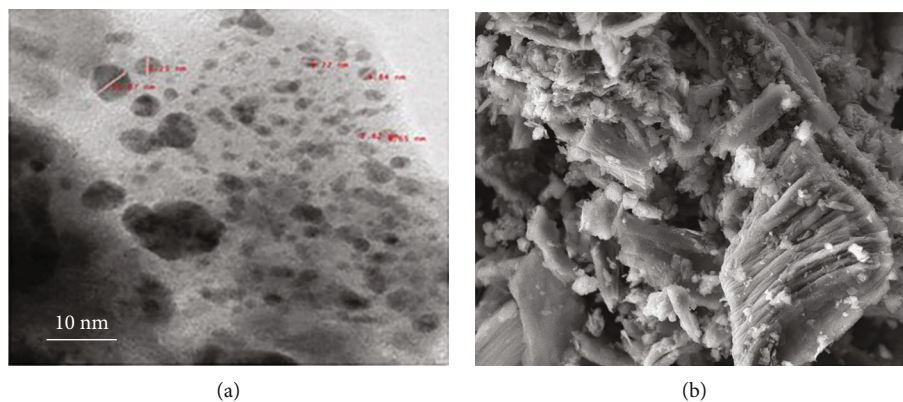


FIGURE 5: Analysis of gold nanoparticles by (a) TEM image and (b) SEM image.

the transmission process that resulted in the gold nanoparticles. Peaks appeared from 400 to 4000 cm^{-1} in which the peak at 3444 cm^{-1} shows OH stretching of alcohols and phenols that has an evidence of both N-H as well as the OH stretches of alcohol and phenol groups in aqueous extract of *Alpinia nigra*. The same showed peak at 1623 cm^{-1} which is in connection with 1634 cm^{-1} [35]. The nutraceutical study of *Laetiporus sulphureus* was reported by [45] indicating the presence of carbo-

hydrates, proteins, and fat in the decreasing order. A relevant study done by [46] explains the bioactive metabolites present in *Laetiporus versisporus*. The species of *Laetiporus* composing these metabolites are responsible for the biochemical conversion which took place in the current study.

Figure 5 displays the analysis of gold nanoparticles by (a) TEM image and (b) SEM image. SEM and TEM analyses of gold nanoparticles showed the size and shape as 10 nm on an

TABLE 1: Ferrous ion chelating assay.

Sample conc. ($\mu\text{g/ml}$)	Absorbance measurement data						
	Hexane	Chloroform	Ethyl acetate	Methanol	Aqueous	AuNps	Standard (EDTA)
50	7.3	8.2	9.8	21.3	21.6	21.2	22
100	12	13.5	11.5	26.8	27.5	26.4	26.3
200	15.8	17.4	20.2	35.5	32	34.7	35.6

average of spherical particles. AuNps of size lesser than 10 nm were isolated via self-assembly [13]. Transmission and scanning electron microscopy generally conveys the size and shape of the particles. Gold nanoparticles obtained here are 10 nm in size, and most of them show a spherical shape. Not only in the ecofriendly mechanism but also the chemical and physical modes of obtaining AuNps were previously studied by nanotechnologists. Spherical gold nanoparticles of diameters range 7-35 nm were obtained by the use of sodium citrate and sodium citrate/borohydride in citrate pathway [47]. On the other hand, saprophytic fungi acted as good reducers in the formation of polydispersed gold nanoparticles in a size range of 20–40 nm [48].

3.2. Analysis of Antioxidant Potential. Here, the antioxidant potentials were analyzed by the ferrous ion chelating effect, nitric oxide scavenging activity, and DPPH radical scavenging assay. These are the routine methods which were used earlier and still in use for observing the antioxidant activity of different live systems such as plants [31] and mushrooms [49]. Antioxidant nature of mushroom was found out quantitatively along with the mushroom-mediated gold nanoparticles. Assays to estimate the quantity and percentage of activity done by the antioxidants to chase the free radicals were different, and some common assays [50] like ferrous ion chelating assay, nitric oxide scavenging assay, and DPPH assays in association with earlier works that carried out these assays in food stuffs [51] are done here.

3.2.1. Ferrous Ion Chelating Effect. Here, the ferrous ion chelating effect is analyzed. It measures the capability of test samples to chelate-free ferrous ions existing in the sample solution.

Table 1 shows the ferrous ion chelating assay. The metal chelating assay involves colour reduction, which determines the chelating ability of the synthesized nanoparticles for ferrous ions. Here, three sample concentrations considered are 50, 100, and 200 $\mu\text{g/ml}$. For each sample concentration, the percentage of chelation is varied. This is quite similar to the studied conducted in methanolic extracts of mushrooms: *Lactarius semisanguifluus*, *Lactarius deliciosus*, *Lactarius sanguifluus*, *Russula delica*, and *Suillus bellinii*. *Lactarius* and *Russula* species exhibited major chelation, i.e., above 40 μmol ferrous ions/100 gm of the source, whereas the *Suillus* species had a chelating range of less than 30 μmol ferrous ions [52]. The graphical plot for the ferrous ion chelating assay is shown in Figure 6.

Table 2 shows the average IC₅₀ obtained from ferrous ion chelating assay. Here, the average value is higher for the ethyl acetate and hexane sample, i.e., 10.08 and

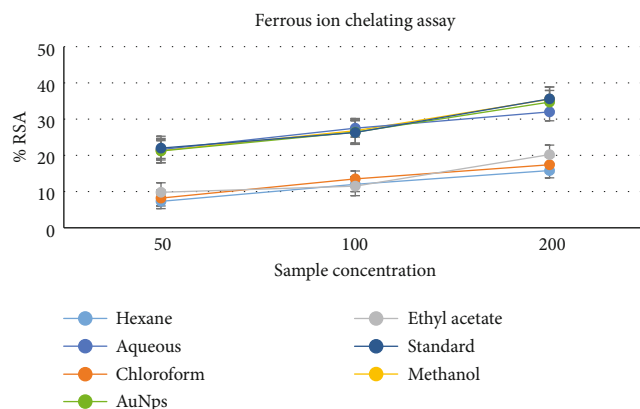
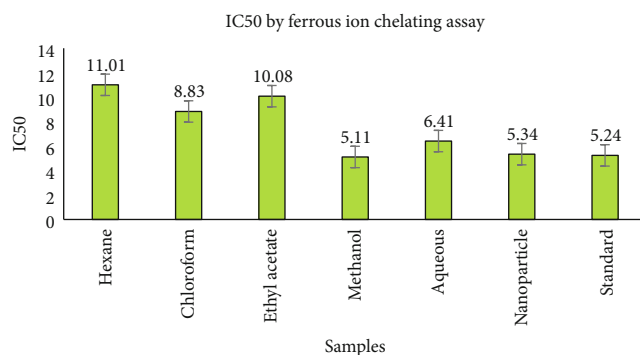


FIGURE 6: Analysis of ferrous ion chelating assay.

TABLE 2: Average IC₅₀ ferrous ion chelating assay.

Sl. no.	Sample	Average IC ₅₀ ($\mu\text{g/ml}$)
1	Hexane	11.01
2	Chloroform	8.83
3	Ethyl acetate	10.08
4	Methanol	5.11
5	Aqueous	6.41
6	Nanoparticle	5.34
7	Standard (EDTA)	5.24

FIGURE 7: Pictorial plot for the average IC₅₀ of ferrous ion chelating assay.

11.01 $\mu\text{g/ml}$, respectively. Thirdly, the chloroform sample has the IC₅₀ average of 8.83 $\mu\text{g/ml}$. The remaining samples such as methanol, aqueous, nanoparticle, and standard (EDTA) are lower than the above said samples which

TABLE 3: Nitric oxide scavenging assay.

Sample conc ($\mu\text{g/ml}$)	Absorbance measurement data						
	Hexane	Chloroform	Ethyl acetate	Methanol	Aqueous	AuNps	Standard (ascorbic acid)
50	15.7	14.4	10	20.3	21.1	21.2	27.1
100	22.4	23.8	17.6	34.6	31.6	33.5	39.2
200	25.6	28.8	27.8	53.6	54.7	54.8	63.4

describes that they have higher antioxidant activity. The pictorial plot for the average IC₅₀ ferrous ion chelating assay is shown in Figure 7.

Ferrous ion chelating assay was considerably used for the estimation of varied antioxidants that are seen in both body fluids and edibles [53]. The activity of methanol extract is more or less similar to the standard of same concentration followed by AuNps and aqueous extract of *L. versisporus*. IC₅₀ values of those were low compared to the other extracts, and this was correlated with the IC₅₀ values of edible mushroom, and *Cantharellus cibarius* was evaluated as 4.324 $\mu\text{g/ml}$ [54].

3.2.2. Nitric Oxide Scavenging Activity. In this subsection, the nitric oxide scavenging activity is analyzed. Nitric oxide scavenging assay being one of the antioxidant tests is done in bioproducts by silver nanoparticles [55]. The nitric oxide emerged from sodium nitroprusside was computed by the Greiss reaction, and the absorbance was tabulated.

Table 3 shows the nitric acid scavenging assay. Here, the nitric acid scavenging activity of nanoparticles was directly proportional to the sample concentration. For the sample concentration of 50 $\mu\text{g/ml}$, the RSA value varies between 15 and 27 RSA. The percentage of scavenging NO at 200 $\mu\text{g/ml}$ of hexane, ethyl acetate, chloroform, methanol, aqueous, nanoparticles, and standard (ascorbic acid) was found to be 25.6%, 28.8%, 27.8%, 53.6%, 54.7%, 54.8%, and 63.4% which is conveyed in either way as standard (ascorbic acid) > nanoparticles > aqueous > methanol > hexane > ethyl acetate > chloroform for all the sample concentrations. 100 to 1000 $\mu\text{g/ml}$ of different mushrooms were tested for nitric oxide scavenging and found that *Pleurotus floridanus* made a greater percentage of scavenging (44-64%) comparatively. The graphical plot for the nitric acid scavenging assay is shown in Figure 8,

Table 4 displays the average IC₅₀ of nitric acid scavenging assay. Here, the order of the samples are chloroform > ethyl acetate > hexane > methanol > aqueous > nanoparticle > standard (ascorbic acid), and hence, it is understood that methanol, aqueous extract, and nanoparticles have an antioxidant activity equivalent to the ideal and default ascorbic acid that is uniformly used as a standard component. The pictorial representation of Table 3 is shown in Figure 9,

The prime active participants of all the samples via nitric oxide assay are same, whereas the AuNps showed much more scavenging as that of the standard rather than the others. IC₅₀ values are lesser than 10 $\mu\text{g/ml}$. Scavenging activity of *Boletus edulis* was done by three different assays, and the IC₅₀ value was noted as 10.74 $\mu\text{g/ml}$ in nitric oxide scavenging assay [56].

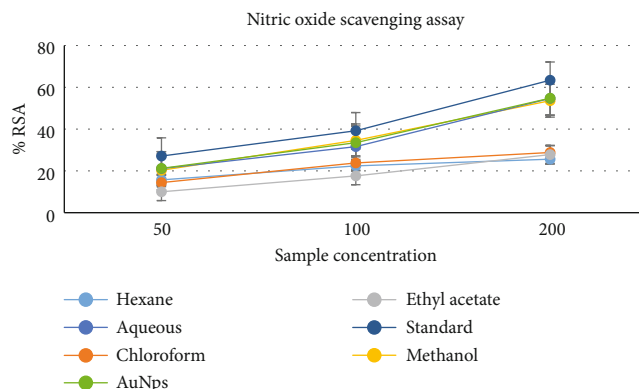
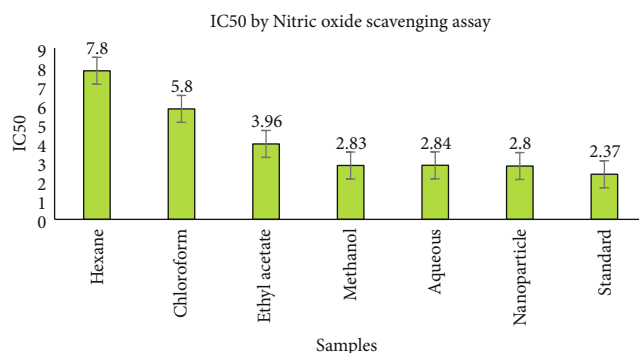


FIGURE 8: Graphical plot for the nitric acid scavenging assay.

TABLE 4: Average IC₅₀ nitric acid scavenging assay.

Sl. no.	Sample	Average IC ₅₀ ($\mu\text{g/ml}$)
1	Hexane	3.92
2	Chloroform	5.54
3	Ethyl acetate	3.96
4	Methanol	2.83
5	Aqueous	2.84
6	Nanoparticle	2.8
7	Standard (ascorbic acid)	2.37

FIGURE 9: Pictorial plot for the average IC₅₀ of nitric acid scavenging assay.

3.2.3. DPPH Radical Scavenging Activity Assay. Here, the DPPH radical scavenging activity of antioxidants is evaluated. Radical scavenging activities happen naturally in the human body to shut out the free radicals intervene in extensive amount of ailments and dreadful diseases. DPPH free

TABLE 5: DPPH radical scavenging activity assay.

Sample conc. ($\mu\text{g/ml}$)	Absorbance measurement data						
	Hexane	Chloroform	Ethyl acetate	Methanol	Aqueous	AuNps	Standard (ascorbic acid)
50	13.8	6	9.1	21.2	20.5	21.4	23.5
100	23.8	13	16.4	31.8	31.9	31.4	33
200	44.1	27.3	31.5	52.2	51.4	52.3	54.6

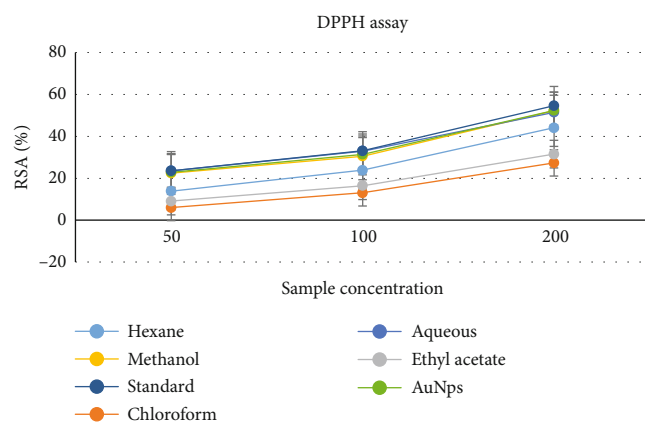


FIGURE 10: Analysis of DPPH assay.

radical scavenging is a customary technique for scanning the radicals that cause cell death.

Table 5 displays the RSA of different sample concentrations using DPPH radical scavenging activity assay. Here, the standard (ascorbic acid) is higher than the other samples that are 23.5% for 50 $\mu\text{g/ml}$, 33% for 100 $\mu\text{g/ml}$, and 54.6% for 200 $\mu\text{g/ml}$ which was similar to that of methanol, aqueous, and gold nanoparticles at lower concentrations. A similar activity was found in the mushrooms *Agaricus* species, *Lentinula* species, and *Flammulina* species, i.e., range from 13 to 50 $\mu\text{mol TE/g}$ [57]. The remaining samples have lesser DPPH activity than the standard sample. The graphical plot is represented in Figure 10.

The average IC₅₀ value by using the DPPH assay activity is displayed in Table 6. The order of the performance by average value is given as ethyl acetate > chloroform > hexane > methanol > aqueous > standard (ascorbic acid) > nanoparticle. Table 6 is presented as a figure format which is shown in Figure 11.

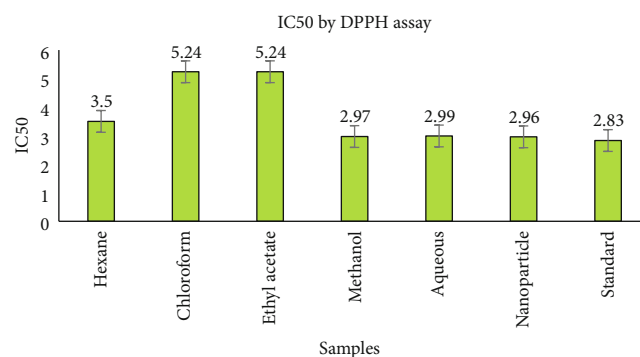
DPPH assay is used to explore the antioxidant ability of AuNps and methanol extract. IC₅₀ values extend from 2.8 to 5.4. *Trametes versicolor* exposed an IC₅₀ value of 5.6 $\mu\text{g/ml}$ by DPPH assay [30] (that is considerably similar to that of *L. versisporus* extracts, which means they possess better antioxidant activity).

Gold nanoparticles obtained from *Nerium oleander* leaf extract [58] showed remarkable increase in the antioxidant activity with the increase in concentration of the AuNps which is comparable to the current project that portrays the competent antioxidant activity of mushroom along with the gold nanoparticles.

Tables 1, 3, and 5 show a linear and steady correlation eventuated with the concentration of samples and radical

TABLE 6: Average IC₅₀ DPPH assay.

Sl. no.	Sample	Average IC ₅₀ ($\mu\text{g/ml}$)
1	Hexane	3.5
2	Chloroform	5.24
3	Ethyl acetate	5.24
4	Methanol	2.97
5	Aqueous	2.99
6	Nanoparticle	2.96
7	Standard (ascorbic acid)	2.83

FIGURE 11: Pictorial plot for the average IC₅₀ of DPPH assay.

scavenging in all the groups of ferrous ion chelating assay, nitric oxide scavenging assay, and DPPH assay. Furthermore, a remarkable and gradual rise ($p < 0.05$) of antioxidant activity of *L. versisporus* and nanoparticles is obtained from the mushroom along with the standard.

4. Conclusion

Although mycosynthesis of nanoparticles was implemented in the field of research involving living systems, an attempt with *Laetiporus versisporus* mushroom to get gold nanoparticles is unfamiliar. Comparatively, mushrooms make a suitable option for the generation of metallic nanoparticles as they are maneuverable and are loaded with various metabolites especially proteins thereby improving the productivity. The present study throws lights on the biological procedure for the production of AuNPs by using *Laetiporus versisporus* and the antioxidant activity. The gold nanoparticle of the current study undergone series of analytical studies including UV-Vis and FTIR spectroscopy. The size of particles was confirmed by XRD, TEM, techniques, and SEM. In UV-Vis spectrometer analysis, the maximum absorption

was found at 566 nm which lies on the standard range of gold nanoparticles, and FTIR gives a list of functional groups belonging to the biomolecules present in the mushroom. In the TEM and SEM analysis, the spherical structure was found and XRD analysis exhibits the diffraction peaks at 38.2° and 44.3°. In antioxidant analysis, six samples along with the standard were carried out that are hexane, chloroform, ethyl acetate, methanol, aqueous, nanoparticle, and standard (EDTA and ascorbic acid) to decipher the expected results. In all the antioxidant activity analyses, the standard attains higher RSA that was quite near with the methanol, aqueous, and gold nanoparticles. The lower IC50 values show a higher antioxidant activity. Thus, results conclude that the *Laetiporus versisporus* extraction and its synthesized AuNPs showed high antioxidant activity. Hence, it can be used in many biological and pharmacological applications.

Data Availability

All the experimental data are included in the manuscript. Hence, there are no other relevant data to be made available.

Conflicts of Interest

The authors declare no conflict of interest.

Acknowledgments

The authors thank collaborators from different universities for providing funds and facilities to complete this work successfully. The authors extend their appreciation to the researchers supporting project number (RSP-2021/224), King Saud University, Riyadh, Saudi Arabia.

References


- [1] O. Mustafa Nadhim and I. Jaleel Ibraheem, "Mycosynthesis of nanoparticles using edible and medicinal mushrooms," *European Journal of Nanomedicine*, vol. 21, pp. 5–23, 2017.
- [2] E. A. Adebayo, D. Martínez-Carrera, P. Morales et al., "Comparative study of antioxidant and antibacterial properties of the edible mushrooms *Pleurotus Levis*, *P. ostreatus*, *P. pulmonarius* and *P. tuber-regium*," *Journal of Applied Pharmaceutical Science*, vol. 53, pp. 1316–1330, 2018.
- [3] J. Parameshwar, L. Nageshwar, B. Hameeda et al., "Correction: Silver nanoparticles from insect wing extract: biosynthesis and evaluation for antioxidant and antimicrobial potential," *PLoS One*, vol. 16, no. 5, article e0241729, 2021.
- [4] S. Arthanari, P. Mei, G. Mani, J. Jayabalan, M. Murugan, and J. Hyun Tae, "Low-cost and eco-friendly green synthesis of silver nanoparticles using *Prunus japonica* (Rosaceae) leaf extract and their antibacterial, antioxidant properties," *Artificial Cells, Nanomedicine, and Biotechnology*, vol. 45, pp. 1165–1171, 2016.
- [5] D. Gopal, D. Panna, and S. Ajay Krishna, "Characterization, antimicrobial and α -amylase inhibitory activity of silver nanoparticles synthesized by using mushroom extract of *Lentinus tuber-regium*," *Proceedings of the National Academy of Sciences, India Section B: Biological Sciences*, vol. 90, pp. 30–37, 2019.
- [6] K. Haliza, S. Lim Chei, A. A. Y. H. Nor, B. Fhataheya, and M. B. M. Fauzi, "Antibacterial activity of biosynthesized gold nanoparticles using biomolecules from *Lignosus rhinocerotis* and chitosan," *Saudi Pharmaceutical Journal*, vol. 27, pp. 283–292, 2019.
- [7] C. E. A. Botteon, L. B. Silva, G. V. Ccana-Ccapatinta et al., "Biosynthesis and characterization of gold nanoparticles using Brazilian red propolis and evaluation of its antimicrobial and anticancer activities," *Scientific Reports*, vol. 11, article 1974, 2021.
- [8] S. Ahmed, S. I. Annu, and S. Y. Salprima, "Biosynthesis of gold nanoparticles: a green approach," *Journal of Photochemistry and Photobiology B: Biology*, vol. 161, pp. 141–153, 2016.
- [9] M. Y. Marcelino, F. A. Borges, L. Scorzoni et al., "Synthesis and characterization of gold nanoparticles and their toxicity in alternative methods to the use of mammals," *Journal of Environmental Chemical Engineering*, vol. 9, no. 6, article 106779, 2021.
- [10] D. Dhamecha, S. Jalalpure, and K. Jadhav, "Nepenthes khasiana mediated synthesis of stabilized gold nanoparticles characterization and biocompatibility studies," *Journal of Photochemistry and Photobiology B: Biology*, vol. 154, pp. 108–117, 2016.
- [11] M. Eskandari-Nojehdehi, H. Jafarizadeh-Malmiri, and J. Rahbar-Shahrouzi, "Optimization of processing parameters in green synthesis of gold nanoparticles using microwave and edible mushroom (*Agaricus bisporus*) extract and evaluation of their antibacterial activity," *Nanotechnology Reviews*, vol. 5, pp. 1–12, 2016.
- [12] A. Reiyhaneh and H. Jafarizadeh-Malmiri, "Green approach in gold, silver and selenium nanoparticles using coffee bean extract," *Open Agriculture*, vol. 5, no. 1, pp. 761–767, 2020.
- [13] O. Ekaterina, "Gold nanoparticles: biosynthesis and potential of biomedical application," *Journal of Functional Biomaterials*, vol. 12, no. 4, p. 70, 2021.
- [14] R. Muwafaq Ayesah, O. Mustafa Nadhim, A. Azlan Abdul, S. Mahmood Jameel, and D. Mohammed Ali, "Mycosynthesis of gold nanoparticles using the extract of *Flammulina velutipes*, Physalacriaceae and their efficacy for decolorization of methylene blue," *Journal of Environmental Chemical Engineering*, vol. 8, article 103841, pp. 1–30, 2020.
- [15] K. Gayathri, R. Sundaraganapathy, C. Icey, V. Vijayalakshmi, F. Shaikh, and A. Rahim, "Comparative studies on synthesized silver nanoparticles using *Artemisia vulgaris* Linn and *Cinnamomum zeylanicum* Nees for their antifungal activity," *Journal of Pharmaceutical Sciences*, vol. 11, pp. 2558–2565, 2019.
- [16] N. Ghassan Adnan, J. Ahmed Saadoun, O. Mustafa Nadhim, and M. Rasim Farraj, "Green synthesis of gold nanoparticles from *Coprinus comatus*, Agaricaceae, and the effect of ultraviolet irradiation on their characteristics," *Journal of Science and Technology*, vol. 18, no. 8, pp. 1–12, 2021.
- [17] O. Mustafa Nadhim, R. Mowafaq Ayesah, A. Azlan Abdul, S. Mahmood Jameel, and D. Mohammed Ali, "Mushroom-assisted synthesis of triangle gold nanoparticles using the aqueous extract of fresh *Lentinula edodes* (shiitake) Omphalotaceae," *Environmental Nanotechnology, Monitoring & Management*, vol. 12, article 100270, 2019.
- [18] M. A. Dheyab, M. N. Owaid, M. A. Rabeea, A. A. Aziz, and M. S. Jameel, "Mycosynthesis of gold nanoparticles by the *Portobello* mushroom extract, Agaricaceae, and their efficacy for decolorization of Azo dye," *Environmental Nanotechnology, Monitoring & Management*, vol. 14, article 100312, 2020.

- [19] P. Megha Desai, M. Geetanjali Sangaokar, and D. Kiran Pawar, "Kokum fruit mediated biogenic gold nanoparticles with photoluminescent, photocatalytic and antioxidant activities," *Process Biochemistry*, vol. 70, pp. 188–197, 2018.
- [20] M. D. Balakumaran, R. Ramachandran, P. Balashanmugam, D. J. Mukeshkumar, and P. T. Kalaichelvan, "Mycosynthesis of silver and gold nanoparticles optimization, characterization and antimicrobial activity against human pathogens," *Microbiological Research*, vol. 182, pp. 8–20, 2016.
- [21] B. Hamed, H. Soheila, E. Pouneh, M. Milad Ali, and A. A. N. Farzaneh, "Microbial mediated preparation, characterization and optimization of gold nanoparticles," *Brazilian Journal of Microbiology*, vol. 45, no. 4, pp. 1493–1501, 2014.
- [22] M. Madakka, N. Jayaraju, and N. Rajesh, "Mycosynthesis of silver nanoparticles and their characterization," *MethodsX*, vol. 5, pp. 20–29, 2017.
- [23] D. Manikandan, D. M. I. Jesse, M. Ayyar, N. N. Gandhi, K. Kathiravan, and B. Abdulhadi, "Biogenic synthesis, characterization of gold and silver nanoparticles from *Coleus forskohlii* and their clinical importance," *Journal of Photochemistry and Photobiology B: Biology*, vol. 183, pp. 251–257, 2018.
- [24] S. Pu, J. Li, L. Sun, L. Zhong, and Q. Ma, "An in vitro comparison of the antioxidant activities of chitosan and green synthesized gold nanoparticles," *Carbohydrate Polymers*, vol. 211, pp. 161–172, 2019.
- [25] F. Gabriela Adriana, M. Bianca, B. Ioana et al., "UV-light mediated green synthesis of silver and gold nanoparticles using Cornelian cherry fruit extract and their comparative effects in experimental inflammation," *Journal of Photochemistry and Photobiology B: Biology*, vol. 191, pp. 26–37, 2019.
- [26] N. Saraschandra and Y. Li, "Preliminary investigation of catalytic, antioxidant, anticancer and bactericidal activity of green synthesized silver and gold nanoparticles using *Actinidia deliciosa*," *Journal of Photochemistry and Photobiology B: Biology*, vol. 170, pp. 225–234, 2017.
- [27] R. L. Puntel, C. W. Nogueira, and C. J. B. T. Rocha, "Krebs cycle intermediates modulate thiobarbituric acid reactive species (TBARS) production in rat brain in vitro," *Neurochemical Research*, vol. 30, pp. 225–235, 2005.
- [28] K. Wendy Alderton, E. Chris Cooper, and G. Richard Knowles, "Nitric oxide synthases: structure, function and inhibition," *The Biochemist*, vol. 357, no. 3, pp. 593–615, 2001.
- [29] W. Brand-Williams and C. Berset, "Use of a free radical method to evaluate antioxidant activity," *LWT*, vol. 28, no. 1, pp. 25–30, 1995.
- [30] S. A. M. Ealia and M. P. Saravanakumar, "A review on the classification, characterisation, synthesis of nanoparticles and their application," *IOP Conference Series: Materials Science and Engineering*, no. article 032019, p. 263, 2017.
- [31] H. Mohamed Hasaan, N. F. A. Bakar, M. A. Najwa, L. Kim-Fatt, and O. N. H. A. Fatmawati, "Synthesis of various size gold nanoparticles by chemical reduction method with different solvent polarity," *Nanoscale Research Letters*, vol. 15, p. 140, 2015.
- [32] K. D. Lee, P. C. Nagajyothi, T. V. M. Sreekanth, and P. Soonhenum, "Eco-friendly synthesis of gold nanoparticles (AuNPs) using *Inonotus obliquus* and their antibacterial, antioxidant and cytotoxic activities," *Journal of Industrial and Engineering Chemistry*, vol. 26, pp. 67–72, 2015.
- [33] M. A. S. N. Khairunisa, M. N. M. Firdhaus, K. Shamel, and A. H. Mariani, "c," *Journal of Nanoscience and Nanotechnology*, vol. 2, pp. 12–29, 2021.
- [34] N. Kalogeropoulos, A. E. Yanni, G. Koutrotsios, and M. Aloupi, "Bioactive microconstituents and antioxidant properties of wild edible mushrooms from the island of Lesbos, Greece," *Food and Chemical Toxicology*, vol. 55, pp. 378–385, 2013.
- [35] K. Hyun-seok, S. Yu Seon, K. Kyeounghak, H. Jeong Woo, P. Youmie, and C. Seonho, "Concentration effect of reducing agents on green synthesis of gold nanoparticles: size, morphology, and growth mechanism," *Nanoscale Research Letters*, vol. 11, article 230, 2016.
- [36] B. G. Ershov, E. V. Abkhalimov, R. D. Solovova, and V. I. Roldughin, "Gold nanoparticles in aqueous solutions: influence of size and pH on hydrogen dissociative adsorption and Au(III) ion reduction," *Physical Chemistry Chemical Physics*, vol. 18, no. 19, pp. 13459–13466, 2016.
- [37] P. Daizy and C. Unni, "Extracellular biosynthesis of gold and silver nanoparticles using *Krishna tulsi* (*Ocimum sanctum*) leaf," *Physica E: Low-dimensional Systems and Nanostructures*, vol. 43, pp. 1318–1322, 2011.
- [38] B. Shibani, M. Priyankar, and G. Jhuma, "Biosynthesis, characterisation and antimicrobial activity of silver and gold nanoparticles by *Dolichos biflorus* Linn seed extract," *Journal of Experimental Nanoscience*, vol. 11, pp. 660–668, 2016.
- [39] O. Mohamed Habib, T. Lotfi Ben, and H. Abdel Halim, "Synthesis of ultra-small gold nanoparticles by polyphenol extracted from *Salvia officinalis* and efficiency for catalytic reduction of p-nitrophenol and methylene blue," *Green Chemistry Letters and Reviews*, vol. 13, no. 1, pp. 18–26, 2020.
- [40] B. Tahsin, K. Zainab Khan, J. Rujuta, and Z. S. Vaishali, "Biogenic gold nanoparticles from the actinomycete *Gordonia amarae*: application in rapid sensing of copper ions," *Sensors and Actuators B: Chemical*, vol. 233, pp. 684–690, 2016.
- [41] P. Daizy, "Green synthesis of gold and silver nanoparticles using *Hibiscus rosa sinensis*," *Physica E: Low-Dimensional Systems and Nanostructures*, vol. 42, pp. 1417–1424, 2010.
- [42] K. Somanjana and K. Acharya, "Water soluble antioxidative crude polysaccharide from *Russula senecis* elicits TLR modulated NF- κ B signaling pathway and pro-inflammatory response in murine macrophages," *Frontiers in Pharmacology*, vol. 9, p. 985, 2018.
- [43] S. R. Radhika Rajasree and T. Y. Suman, "Extracellular biosynthesis of gold nanoparticles using a gram negative bacterium *Pseudomonas fluorescens*," *Asian Pacific Journal of Tropical Disease*, vol. 2, pp. S796–S799, 2012.
- [44] K. Ramsingh, D. Manas Kanti, S. Kamlesh et al., "Citrate-capped gold nanoparticles as a sensing probe for determination of cetyltrimethylammonium surfactant using FTIR spectroscopy and colorimetry," *Analytical and Bioanalytical Chemistry*, vol. 411, pp. 6943–6957, 2019.
- [45] P. Jovana, S. Dejan, S. Filipa Reis et al., "Study on chemical, bioactive and food preserving properties of *Laetiporus sulphureus* (Bull.: Fr.) Murr," *Food & Function*, vol. 5, pp. 1441–1451, 2014.
- [46] G. Shoba, M. Vijayakumar, S. Al-Ghamdi et al., "Investigation of phytochemical profile and *in vivo* anti-proliferative effect of *Laetiporus versisporus* (Lloyd) Imazeki mushroom against diethylnitrosamine-induced hepatocellular carcinoma," *Journal of King Saud University - Science*, vol. 33, article 101551, 2021.
- [47] R. Vikram Singh, O. Miguel, H. Armin, P. Frank, and R. Klaus, "Deep eutectic solvents for the self-assembly of gold nanoparticles: a SAXS, UV-Vis, and TEM investigation," *Langmuir*, vol. 30, no. 21, pp. 6038–6046, 2014.

- [48] I. Samaneh, G. H. Shahidi Bonjar, and A. Baghizadeh, "Study of the biosynthesis of gold nanoparticles by using several saprophytic fungi," *SN Applied Sciences*, vol. 2, article 1851, 2020.
- [49] M. Irina Georgiana and A. Constantin, "Analytical methods used in determining antioxidant activity: a review," *International Journal of Molecular Sciences*, vol. 22, no. 7, p. 3380, 2021.
- [50] B. Aarti and T. Astha, "Evaluation of antioxidant and anti-inflammatory properties of aqueous extract of wild mushrooms collected from Himachal Pradesh," *Asian Journal of Pharmaceutical and Clinical Research*, vol. 10, pp. 467–472, 2017.
- [51] T. Akihiro, S. Takeshi, Y. Futoshi, and I. Hideyuki, "Evaluation of antioxidant activity of vanillin by using multiple antioxidant assays," *Biochimica et Biophysica Acta - General Subjects*, vol. 1810, no. 2, pp. 170–177, 2011.
- [52] J. Eulogio Llorent-Martinez, Z. Gokhan, L. M. F.-d. Cordova et al., "Traditionally used *Lathyrus* species: phytochemical composition, antioxidant activity, enzyme inhibitory properties, cytotoxic effects, and *in silico* studies of *L. czeczottianus* and *L. nissolia*," *Frontiers in Pharmacology*, vol. 8, p. 83, 2017.
- [53] T. Ferenc Pastor, M. Segan Dejan, Z. Gorjanovic Stanislava, M. Kalusevic Ana, and Z. Suznjevic Desanka, "Development of voltammetric methods for antioxidant activity determination based on Fe(III) reduction," *Microchemical Journal*, vol. 155, article 104721, 2020.
- [54] F. Bach, A. A. Zielinski, C. V. Helm et al., "Bio compounds of edible mushrooms: *in vitro* antioxidant and antimicrobial activities," *LWT*, vol. 107, pp. 214–220, 2019.
- [55] K. Masoumeh, E. Mohammad Ali, K. Mehrnoush, A. Abbasi, and M. Azadbakht, "Iron chelation and liver disease healing activity of edible mushroom (*Cantharellus cibarius*), *in vitro* and *in vivo* assays," *RSC Advances*, vol. 5, pp. 4804–4810, 2015.
- [56] P. Sivasankar, P. Seedeve, S. Poongodi et al., "Characterization, antimicrobial and antioxidant property of exopolysaccharide mediated silver nanoparticles synthesized by *Streptomyces violaceus* MM72," *Carbohydrate Polymers*, vol. 181, pp. 752–759, 2018.
- [57] B. Debjani and G. Monmi, "Biogenic synthesis of gold nanoparticles and their application in photocatalytic degradation of toxic dyes," *Journal of Photochemistry and Photobiology B: Biology*, vol. 186, pp. 51–58, 2018.
- [58] T. Kamran, N. Sadia, L. Baoshan et al., "Nerium oleander leaves extract mediated synthesis of gold nanoparticles and its antioxidant activity," *Materials Letters*, vol. 156, pp. 198–201, 2015.

Review Article

Recent Developments on Magnetically Separable Ferrite-Based Nanomaterials for Removal of Environmental Pollutants

Shreyas Pansambal ¹, **Arpita Roy** ², **Hamza Elsayed Ahmed Mohamed**,^{3,4}
Rajeshwari Oza ⁵, **Canh Minh Vu** ⁶, **Abdolrazagh Marzban** ⁷, **Ankush Chauhan** ⁸,
Suresh Ghotekar ⁹ and **H. C. Ananda Murthy** ^{10,11}

¹Department of Chemistry, Shri Saibaba College, Savitribai Phule Pune University, Shirdi, 423109 Maharashtra, India

²Department of Biotechnology, School of Engineering & Technology, Sharda University, Greater Noida, India

³UNESCO UNISA Africa Chair in Nanosciences and Nanotechnology, College of Graduate Studies,
University of South Africa, South Africa

⁴Nanosciences African Network (NANOAFNET), Material Research Department, IThemba LABS, Cape, South Africa

⁵Department of Chemistry, S.N. Arts, D.J.M. Commerce and B.N.S. Science College, Savitribai Phule Pune University, Sangamner,
422605 Maharashtra, India

⁶Advanced Institute of Science and Technology, The University of Da Nang, Da Nang 550000, Vietnam

⁷Razi Herbal Medicines Research Center, Lorestan University of Medical Sciences, Khorramabad, Iran

⁸Chettinad Hospital and Research Institute, Chettinad Academy of Research and Education, Chengalpattu District, Kelambakkam,
603103 Tamil Nadu, India

⁹Department of Chemistry, Smt. Devkiba Mohansinhji Chauhan College of Commerce and Science, University of Mumbai, Silvassa,
396 230 Dadra and Nagar Haveli (UT), India

¹⁰Department of Applied Chemistry, School of Applied Natural Sciences, Adama Science and Technology University, P.O. Box 1888,
Adama, Ethiopia

¹¹Department of Prosthodontics, Saveetha Dental College & Hospital, Saveetha Institute of Medical and Technical
Science (SIMATS), Saveetha University, Chennai, 600 077 Tamil Nadu, India

Correspondence should be addressed to Suresh Ghotekar; ghotekarsuresh7@gmail.com
and H. C. Ananda Murthy; anandkps350@gmail.com

Received 15 July 2022; Revised 4 September 2022; Accepted 8 September 2022; Published 26 September 2022

Academic Editor: Pounsamy Maharaja

Copyright © 2022 Shreyas Pansambal et al. This is an open access article distributed under the Creative Commons Attribution License, which permits unrestricted use, distribution, and reproduction in any medium, provided the original work is properly cited.

The current water supply situation demonstrates the predominance of contamination caused by industrial effluent runoff. Polluted waters have contributed to significant health and environmental risks, calling for an acceptable alternative to address the effects. However, diverse chemical and treatment physical stages commonly used for dye effluent processing are more cost-intensive, less effective, and time-consuming. Instead, nanomaterials have developed as a good alternative for dye removal and degradation because of their special chemical reactivity and superior surface features/properties. In this regard, the ability of modified or hybrid ferrite-based magnetically recoverable nanomaterials in dye effluent treatment has been extensively explored. The present study especially emphasizes magnetic ferrite ($\text{Fe}_3\text{O}_4 + \text{X}$) or metal-doped ferrite ($\text{MFe}_2\text{O}_4 + \text{X}$) nanocomposite for dye degradation (where M consists of Co, Cu, Zn, Mg, Mn, Ni, etc., and X consists of reduced graphene oxide, graphene oxide, metal, or metal oxide). Several dye degradation efficiencies of various ferrite and metal ferrite nanomaterial were discussed. Degradation is carried out using direct sunlight, and various lamps (e.g., visible light/UV-C lamp/halogen lamp/Mercury-Xenon lamp/UV lamp with UV filter for visible light) are used as a source. This review article covers the degradation of various dyes from wastewater using ferrite-based nanomaterial as an efficient catalyst and making water pollution free.

1. Introduction

The first commercially effective synthetic dye was explored in 1856, and till now, numerous dyes have been synthesized [1]. The releases of synthetic dyes in natural water sources increase pollution, causing severe harm to humans [2]. According to Jin et al., textiles discharged 280,000 tons of industrial effluents worldwide [3]. The effluent encompasses a wide range of pollutants, including organic and inorganic salts, surfactants, heavy metals, enzymes, oxidizing, and reducing agents [2, 4]. The human being swallows such contaminated water persuades respiratory tract, gastrointestinal tract irritation, and skin and eye irritation. Furthermore, the reports also prove the developmental, chronic, and neurotoxicity effects of dyes on human beings [5]. A huge volume of freshwater is essential to carry out the daily process in the textile industry. Scrutiny of the literature reveals that for the treatment of 1 kg of textile materials, about 100 L of water is essential [2]. Therefore, to avoid such environmental degradation due to synthetic dyes, the degradation of dyes is essential.

Diverse techniques are used for the effluent treatment [6–8], which are listed in Figure 1. Traditional techniques for the dye degradation used are adsorption utilizing activated carbon, reverse osmosis, ion exchange employing resins, etc. However, the technique mentioned earlier can only transform the phase creating secondary pollution, which needs additional treatment to regenerate the adsorbent [9]. Traditional technologies for the treatment of wastewater were unsuccessful by Forgacs et al. [10]. Furthermore, the report also states that these techniques are insufficient to degrade/treat certain azo dyes selected for the study. Recently, the advanced oxidation process (AOPs) has been used mostly to treat polluted water. Reactive oxygen species (ROS) produced using AOPs quickly oxidize dyes in the industrial effluent and make the water pollution free [11].

Magnetic nanomaterials are of massive enthusiasm for scientists from a vast variety of domains, including catalysis [12–14], magnetic fluids [15], biomedicine [16], data storage [17], magnetic resonance imaging [18, 19], biosensors [20], and environmental remediation [21–25]. While several effective approaches for the fabrication of selective magnetic nanomaterials of diverse compositions have been developed, the efficient uses of certain magnetic nanomaterials in the fields mentioned above are strongly reliant on the stability of the nanomaterials under a variety of situations. The nanomaterial works perfectly in most planned applications when the size of the nanomaterials is around a particular value, which relies on the nanomaterial. Then, when the temperature is beyond the so-called blocking temperature, each nanomaterial becomes a unified magnetic field and exhibits superparamagnetic conduct. These nanomaterials have a broad stable magnetic moment and operate as a large paramagnetic atom with a quick reaction with negligible coercivity and remanence to applied magnetic fields. These features render superparamagnetic nanomaterials very appealing for such a large scope of bioengineering uses since the possibility of agglomerations at room temperature is negligible [26].

Various strategies have been created, including adsorption, biological, electrochemical, ion exchange, membrane

processes, and solvent extraction techniques. These methods have a variety of disadvantages, including as high operating costs, pollution transfer from one phase to another, and the challenge of eliminating biologically or chemically persistent contaminants. Advanced oxidation processes (AOPs) are the most effective way to remove pollutants from water because they can produce powerful oxidizing agents at ambient temperature and normal atmospheric pressure [27–30]. Heterogeneous photocatalysis has proven to be a more successful method for addressing energy and environmental concerns as an oxidation mechanism. Heterogeneous photocatalysts can remove persistent nonbiodegradable organic pollutants by supplying strong oxidizing agents and converting them into mineral salts, H_2O , and CO_2 . Intriguing materials for CO_2 photoreduction, microbial disinfection, N_2 photofixation, and organic compound synthesis are also heterogeneous photocatalysts. An ideal heterogeneous photocatalyst will have a high quantum efficiency, be physiologically and chemically inert, have a considerable capacity to absorb solar energy, be nontoxic, be resistant to photocorrosion, and be inexpensive. Despite heterogeneous photocatalysts' potential for addressing energy and environmental problems, removing and recycling these parts from the reaction solution is difficult. Centrifugation and filtration techniques are used to separate used photocatalysts from systems that have been treated. Meanwhile, these methods are time- and money-consuming, restricting the widespread application of heterogeneous photocatalysts [31–33]. The fixation of heterogeneous photocatalysts has addressed this issue with an inert substrate. Despite the fact that this method lessens particle aggregation and makes it simpler to separate heterogeneous photocatalysts, photocatalytic performance is anticipated to suffer as a result of the decreased photocatalyst active sites. In order to separate and recover heterogeneous photocatalysts on a large scale, this problem is solved by combining photocatalysts with magnetic materials. Magnetic materials are more desirable in photocatalytic applications because they may show considerable photocatalytic activity and separability [34, 35].

Thus, this perspective review article intends to present reports on photocatalytic degradation of various dyes using ferrite-based nanocomposites.

2. Hazards of Dyes to Environment and Human Health

In addition to having adverse effects, the dye materials are often aesthetically undesirable in water. Several structure varieties are used in the textile industry, such as basic, acidic, disperse, reactive, azo, anthraquinone-based, diazo, and metal complex dyes [36]. Having more or less destructive consequences, it puts up. Increased heart rate, shock, vomiting, cyanosis, Heinz body formation, quadriplegia, human tissue necrosis, and jaundice are associated with extreme exposure to dyes [37]. Dyes such as metanil yellow seem to have a tumor-producing effect [38] and can generate human body enzyme disorders [39]. However, it is nonmutagenic, but it can change gene expression sequences [40]. It produces harmful methaemoglobinaemia [41] and cyanosis

Chemical process	Physical process
(i) Coagulation and flocculation (ii) Cucurbituril (iii) Oxidative processes (iv) Electrochemical destruction (v) Fenton's reagent (vi) Sodium hypochloride (NaOCl) (vii) Photochemical degradation (viii) Ozonation	(i) Adsorption (ii) Membrane filtration processes (iii) Biological methods (iv) Photocatalytic degradation techniques

FIGURE 1: Classification of methods of effluent treatments.

[42] in humans when taken orally, while skin interaction leads to allergic dermatitis [43]. Testicular lesions are caused by intratesticular and intraperitoneal administration or oral feeding of dyes in animals due to damage to seminiferous tubules and reduced spermatogenesis level [44, 45].

3. Magnetic Behavior of Ferrite-Based Magnetized Nanomaterials

The properties of magnetic nanomaterials are determined by the extrinsic magnetic field induced to materials. Descriptions of magnetic polarity in a nanomaterial help classify various types of magnetism found in nature. It is possible to define 5 main types of magnetism: antiferromagnetism, diamagnetism, ferrimagnetism, ferromagnetism, and paramagnetism [46]. Diamagnetism is a primary property of all atoms, and magnetization is quite low and opposite to the direction of the induced magnetic field. Lots of nanomaterials show paramagnetism property, whereas the orbit is raised from zero, a magnetization grows parallel to the induced magnetic field, but the magnetization efficiency is weak. Also, ferromagnetism is the property of such objects that are naturally magnetically arranged and which, even without using a field, develop spontaneous magnetization. Ferrimagnetism, where distinct atoms have various moment abilities, is different from ferromagnetism, but there is always an organized state under a specific critical temperature at that state. The magnetic substance, i.e., diamagnet, paramagnet, and ferromagnet, can be sorted according to its susceptibility. Many of the unique magnetic characteristics of nanomaterials are due to their strong surface-to-volume ratio [47, 48]. Saturation magnetism (M_s) changes through size before it reaches a threshold size above which magnetization is stable and near the bulk's value. In diverse disciplines, the linear dependency of M_s on size underneath this threshold was seen. Research on the shape effect affects magnetic nanocomposites' volume or associated size parameter properties. For spherical nanoparticles, the anisotropy value (magnetic anisotropy is the directional dependence of a material's magnetic properties) is greater than for cubic nanoparticles of a similar volume [49–52]. Composition is perhaps the most widely cited factor accountable for assessing a material's particular magnetic properties. These magnetic properties occur in the absence or presence of unpaired valence electrons deposited on metal ions or metal atoms present in magnetic nanomaterials [53, 54]. Magnetic behav-

our is characterized by the direction of the magnetic moment (μ) connected with the electrons. We can measure the magnetic moment in magnetic nanomaterial [45, 55, 56] using the magnetic moment of only one electron, 1.73 Bohr magnetons (BM).

4. Diverse Approaches for the Fabrication of Magnetically Ferrite-Based Nanomaterials

There are multifarious approaches employed for the practical synthesis of using ferrite-based nanocomposite [57, 58], for instance, hydrothermal, sol-gel, sonochemical, solvothermal, precipitation, coprecipitation, solution combustion, probe sonication method, green synthesis, ultrasonication, and microwave-assisted methods [59–63]. Particle size distribution, crystal structure, particle size and shape control, and alignment are the crucial factors in the manufacturing of ferrite-based nanocomposite. Such approaches help produce magnetic ferrite-based composites, which are selectively stable at normal room temperature, regular shape, uniform size, nonaggregate, high monodispersity, etc. These methods are further categorised into three different approaches, physical, chemical, and biological, as shown in Figure 2.

The aforementioned synthetic approaches require comparatively higher experimental duration and high pressure and energy and involve noxious compounds or solvents, and stability depends on capping agents. However, nanomaterial synthesized via these methods shows higher photocatalytic degradation efficiency.

5. General Procedure for the Dye Degradation

Magnetic metal Fe_2O_4 /doped metal Fe_2O_4 composite is taken as a catalyst for the dye degradation of different dye (Figure 3) solution (any one among the following: MB, MO, MG, CV, CR, EY, RR 198, RR120, IC, DY, RB. etc.); dye under magnetic stirring/ultrasound irradiation/microwave irradiation with or without the addition of H_2O_2 in the presence of visible light/UV-C lamp/halogen lamp/Mercury-Xenon lamp/UV lamp with UV filter for visible light is used as the source (Table 1). At the start of the reaction, the catalyst is added to the dye solution and stirred the solution in the absence of light for 30 mins to attain the absorption equilibrium. Then, after 30 mins, the dye solution is exposed to the source. Then, the absorbances are measured, and from the reading, calculate the efficiency of the catalyst and the

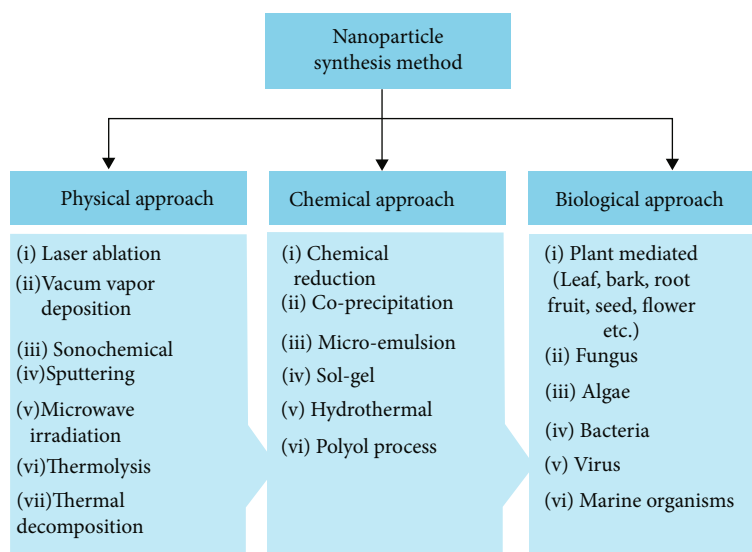


FIGURE 2: Diverse approaches for the efficient fabrication of ferrite-based nanomaterial.

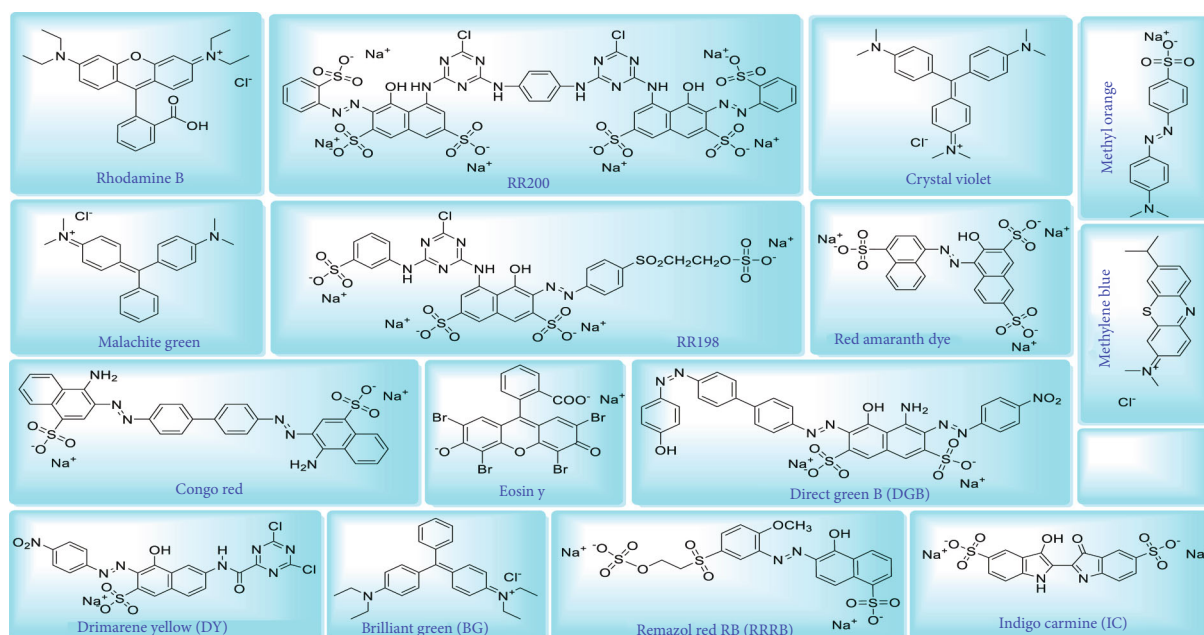


FIGURE 3: Various dye and their chemical structure.

time required for the dye degradation. Figure 4 represents the graphical representation of the dye degradation using magnetic ferrite NPs.

6. Dye Degradation Using Ferrite-Based Nanomaterials

Diverse dyes exist, which can be synthesized chemically in industry and occur in nature. The dyes we studied in this article are shown in Figure 3 with their name and structure for better understanding.

Farhadi et al. reported the ultrasound-assisted photocatalytic degradation of methylene blue (MB) dye (25 mg/L)

within 70 min using CoFe₂O₄@ZnS composite and H₂O₂ (4 mM). The composite shows excellent reusability up to five cycles with significant property changes [59]. Siadatnasab et al. stated that the dye degradation efficiency of CuS/CoFe₂O₄ nanohybrid towards methylene blue (MB) dye (25 mg/L) and rhodamine B (RhB) dye (25 mg/L) along with H₂O₂ was accomplished within 30 minutes with 100% and 72% efficiency, respectively, via sonocatalytic process. However, the reusability study shows 5% drop in the catalytical activity after the 4th cycle [60]. Kalam et al. specified that photocatalytic degradation of methylene blue (MB) dye (1 mg/L) with H₂O₂ in visible light CoFe₂O₄ sample MST-2 shows 80% degradation of MB dye within 140 min than

TABLE 1: Various dye degradation using ferrite and metal-doped ferrite nanoparticles with some additives.

Name of the catalyst	Synthetic method	Size (nm)	Shape	Light source	Degradation %	Time (min)	Additive	Dye degraded	Ref.
CoFe ₂ O ₄ @ZnS	Hydrothermal	18	Spheres	Ultrasonic bath power of 100 W and frequency of 37 kHz	100	70	H ₂ O ₂	Methylene blue dye	[59]
CuS/CoFe ₂ O ₄	Hydrothermal	17	Spherelike	Ultrasonic bath power of 100 W and frequency of 37 kHz	100	30	H ₂ O ₂	Methylene blue dye	[60]
CuS/CoFe ₂ O ₄	Hydrothermal	17	Spherelike	Ultrasonic bath power of 100 W and frequency of 37 kHz	72	30	H ₂ O ₂	Rhodamine B (RhB)	[60]
CoFe ₂ O ₄ (MST-2)	Solvothermal	15	Spherical	Visible light	80	140	H ₂ O ₂	Methylene blue dye	[61]
Ag ₃ PO ₄ -CoFe ₂ O ₄	Precipitation	<30	Spherical	Tungsten halogen lamp with 500 W	100	60	—	Methyl orange (MO)	[62]
Ag ₃ PO ₄ -CoFe ₂ O ₄	Precipitation	<30	Spherical	Tungsten halogen lamp with 500 W	100	60	—	Rhodamine B (RhB)	[62]
Co _{0.25} Zn _{0.75} Fe ₂ O ₄ @SiO ₂ /ZnO	Coprecipitation	10.6	Spherical	UV irradiation	100	120	—	Red amaranth dye	[63]
Cu Fe ₂ O ₄ /RGO	Solution combustion synthesis	—	Plate like	Two 100 W Xenon lamps with an UV cut-off filter ($\lambda = 420$ nm)	92	180	—	Methylene blue (MB)	[64]
Cu Fe ₂ O ₄ @GO	—	—	—	—	93.3	30	PMS	Methylene blue (MB)	[65]
Cu Fe ₂ O ₄ /GO	Hydrothermal	30-40	—	Visible light by 450 W Xe arc lamp	—	—	H ₂ O ₂	Rhodamine B (RhB) Acid orange II (AO7)	[66]
Cu Fe ₂ O ₄	Coprecipitation	25.4	—	—	91.3	60	H ₂ O ₂	Reactive red 2 (RR)	[67]
Cu Fe ₂ O ₄ -Fe ₂ O ₃	Pechini method	—	—	Solar radiation	100	180	H ₂ O ₂	Methylene blue (MB)	[68]
Fe ₃ O ₄ -C-cu	Green synthesis	25	Spherical	—	100	<1	NaBH ₄	Methyl orange (MO)	[69]
Fe ₃ O ₄ -C-cu	Green synthesis	25	Spherical	—	100	3.20	NaBH ₄	4-Nitrophenol	[69]
Fe ₃ O ₄ -C-cu	Green synthesis	25	Spherical	—	100	2.40	NaBH ₄	2,4-Dinitrophenylhydrazine	[69]
Ag-Fe ₃ O ₄ /graphene	—	—	Spherical	Two 40 W UV-C lamps	94.78	120	H ₂ O ₂	Methyl orange (MO)	[70]
Ag-Fe ₃ O ₄ /graphene	—	—	Spherical	Two 40 W UV-C lamps	99	120	H ₂ O ₂	Methylene blue (MB)	[70]
Ag-Fe ₃ O ₄ /graphene	—	—	Spherical	Two 40 W UV-C lamps	81	120	H ₂ O ₂	Crystal violet (CV)	[70]
Ag-Fe ₃ O ₄ /graphene	—	—	Spherical	Two 40 W UV-C lamps	89	120	H ₂ O ₂	Malachite green (MG)	[70]
Ag-Fe ₃ O ₄ /graphene	—	—	Spherical	Two 40 W UV-C lamps	75	120	H ₂ O ₂	Congo red (CR)	[70]
Ag-Fe ₃ O ₄ /graphene	—	—	Spherical	Two 40 W UV-C lamps	70	120	H ₂ O ₂	Eosin Y (EY)	[70]
S- Fe ₃ O ₄	Hydrothermal	10-20	Spherical	—	100	30	H ₂ O ₂	Rhodamine B (RhB)	[71]
(RGO)/Fe ₃ O ₄	Green synthesis	18	Spherical	—	95.18	12	NaBH ₄	Methylene blue dye	[72]
Ag ₃ PO ₄ @MgFe ₂ O ₄	Sol-gel	15-20	Irregular	300 W Xenon short arc lamps	98	30	H ₂ O ₂	Rhodamine B (RhB)	[73]
MgFe ₂ O ₄	Solid-state reaction	12.31	Spherical	Sunlight	100	<1	H ₂ O ₂	Malachite green (MG)	[74]
MgFe ₂ O ₄	Autocombustion	7-16	Irregular	—	—	—	—	Methylene blue (MB)	[75]
MgFe ₂ O ₄ /TiO ₂	Sol-gel	20-30	—	500 W Xenon lamp	—	—	—	Rhodamine B (RhB)	[76]
Ni _{0.2} Cu _x Mn _{0.2} Fe ₂ O ₄	Probe sonication	19	Irregular	UV light	98.1	120	—	Methylene blue (MB)	[77]

TABLE 1: Continued.

Name of the catalyst	Synthetic method	Size (nm)	Shape	Light source	Degradation %	Time (min)	Additive	Dye degraded	Ref.
$\text{Ni}_{0.2}\text{Cu}_x\text{Mn}_{0.2}\text{Fe}_2\text{O}_4$	Probe sonication	23	Irregular	UV light	43.3	120	—	Drimarene yellow (DY)	[77]
MnFe_2O_4	—	—	—	UV-C lamp (200–280 nm, 9 W, Philips)	>90	90	H_2O_2	Reactive red 120 (RR120)	[78]
MnFe_2O_4	—	—	—	UV-C lamp (200–280 nm, 9 W, Philips)	>90	90	H_2O_2	Reactive red 198 (RR198)	[78]
$\text{MnFe}_2\text{O}_4/\text{TA}/\text{ZnO}$	Hydrothermal	—	Spherical	Visible light	84.2	90	—	Congo red (CR)	[79]
$\text{MnFe}_2\text{O}_4/\text{rGO}$	Coprecipitation	—	Spherical	UV irradiation	97	60	—	Methylene blue (MIB)	[80]
MnFe_2O_4	Solvothermal	90–100	Spherical	Sunlight	98	180	H_2O_2	Methyl orange (MO)	[81]
NiFe_2O_4	Chemical precipitation	—	—	Microwave irradiation	97	2	—	Brilliant green (BG)	[82]
$\text{NiFe}_2\text{O}_4/\text{T}/\text{GOx}$	Solvothermal	—	Cluster	UV	98.6	90	—	Indigo carmine (IC)	[83]
$\text{NiFe}_2\text{O}_4/\text{TiO}_2$	Sol-gel	18.85	Spherical	UV lamp 300 W Xenon lamp	90.06	90	—	Methyl orange (MO)	[84]
$\text{BCN}/\text{NiFe}_2\text{O}_4$	Sol-gel	100	Sheet-like	Mercury-Xenon lamp (350 W)	98	80	—	Methylene blue (MB)	[85]
NiFe_2O_4	Sonochemical	9–17	Cube-like	UV light 400 W hg lamp	89.4	<80	—	Methylene blue (MB)	[86]
NiFe_2O_4	Sonochemical	9–17	Cube-like	UV light 400 W hg lamp	43	120	—	Drimarene yellow (DY)	[86]
$\text{ZnO}/\text{CF}/\text{NG}$	Hydrothermal	—	—	10 W LED lamp	98	140	—	Malachite green (MG)	[87]
$\text{ZnO}/\text{ZF}/\text{NG}$	Hydrothermal	—	—	10 W LED lamp	92	140	—	Malachite green (MG)	[87]
$\text{ZnO}/\text{CF}/\text{NG}$	Hydrothermal	—	—	10 W LED lamp	99	140	—	Methyl orange (MO)	[87]
$\text{ZnO}/\text{ZF}/\text{NG}$	Hydrothermal	—	—	10 W LED lamp	94	140	—	Methyl orange (MO)	[87]
ZnFe_2O_4	—	—	—	UV-C lamp 200–280 nm 9 W	—	—	H_2O_2	Reactive red 198 (RR198)	[88]
$\text{ZnFe}_2\text{O}_4/\text{ZnO}$	Microwave	17	—	Visible light 125 W hg lamp	100	540	—	Methyl orange (MO)	[89]
$\text{MIL-101}(\text{Cr})/\text{RGO}/\text{ZnFe}_2\text{O}_4$	Hydrothermal	24	Spherelike	Ultrasonic frequency of 37 kHz	95	50	H_2O_2	Methylene blue (MIB)	[90]
$\text{MIL-101}(\text{Cr})/\text{RGO}/\text{ZnFe}_2\text{O}_4$	Hydrothermal	24	Spherelike	Ultrasonic frequency of 37 kHz	100	2	H_2O_2	Congo red (CR)	[90]
$\text{MIL-101}(\text{Cr})/\text{RGO}/\text{ZnFe}_2\text{O}_4$	Hydrothermal	24	Spherelike	Ultrasonic frequency of 37 kHz	94	50	H_2O_2	Rhodamine B (RhB)	[90]
ZnFe_2O_4	Combustion reaction	—	Spherical	—	—	—	—	Rhodamine B (RhB)	[91]
$\text{Ni}_{0.4}\text{Zn}_{0.6}\text{Fe}_{1.8}\text{Al}_{0.1}\text{Gd}_{0.1}\text{O}_4$	Sol-gel	—	—	—	96	180	—	Reactive blue (RB-21)	[92]
$\text{MnCe}_{0.3}\text{Fe}_{1.7}\text{O}_4$	Microwave combustion	22–26	Sphere-shaped	Visible light (Xenon lamp 300 W; $\lambda > 400$ nm)	91.53	120	—	Methylene blue (MIB)	[93]
$\text{CuO}/\text{HAP}/\text{ferrite}$	Precipitation	<25	—	Visible irradiation	>90	60	—	Rhodamine B (RhB)	[94]

TABLE 1: Continued.

Name of the catalyst	Synthetic method	Size (nm)	Shape	Light source	Degradation %	Time (min)	Additive	Dye degraded	Ref.
CoFe ₂ O ₄ /SnO ₂	Sol-gel	13	Spherelike	Hg lamp at 365 nm a UV-A lamp (15 W)	<55	120	—	Indigo carmine (IC)	[95]
MnFe ₂ O ₄ /B. cla	Solid-state	8-38	Spherical	50 W tungsten halogenated lamp	71.6	8	H ₂ O ₂	Methylene blue (MB)	[96]
Co _{0.4} Mg _{0.4} Cu _{0.2} Fe _{1.9} Cr _{0.1} O ₄	Sol-gel	20-60	Spherical	—	84	150	—	Congo red (CR)	[97]
CoFe ₂ O ₄ -SiO ₂ -TiO ₂	Coprecipitation	—	Spherical	—	93.46	160	—	Methyl orange (MO)	[98]
Ca _{0.2} Cu _{0.8} Fe ₂ O ₄	Coprecipitation	19-32	Cubical and irregular	—	96	180	Fenton's agent	Methylene blue (MB)	[99]
Mn _{0.6} Zn _{0.4} Fe ₂ O ₄	Coprecipitation	3-47	Spherical	—	98	15	H ₂ O ₂	Synozol blue CA	[100]
NiFe ₂ O ₄	Solid state	40-50	—	Visible light	95	35	H ₂ O ₂	Malachite green (MG)	[101]

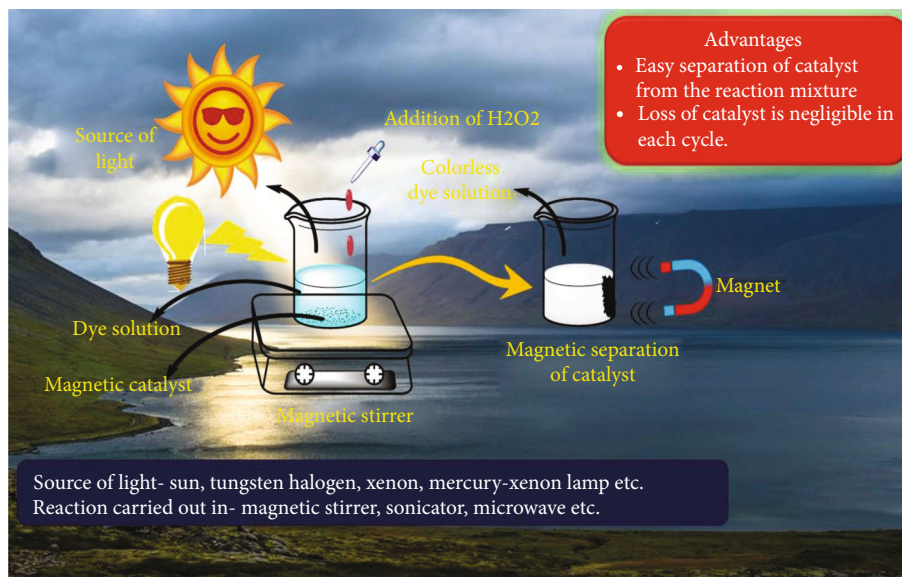


FIGURE 4: Dye degradation using magnetic ferrite and metal-doped ferrite nanocatalyst.

the MST-3 and MST-1 [61]. Gan et al. quantified the photocatalytic performance of $\text{Ag}_3\text{PO}_4\text{-CoFe}_2\text{O}_4$ nanocomposite in a tungsten halogen lamp with light 500 W output power towards methylene blue (MB) dye (10 mg/L) and rhodamine B (RhB) dye (10 mg/L) which completely degraded within 30 min. Increasing the dye concentration to 40 mg/L was degraded completely within 60 min. $\text{Ag}_3\text{PO}_4\text{-CoFe}_2\text{O}_4$ (7.5%) shows high degradation capacity that $\text{Ag}_3\text{PO}_4\text{-CoFe}_2\text{O}_4$ (10%) sample [62]. López et al. reported that the multifunctional $\text{Co}_{0.25}\text{Zn}_{0.75}\text{Fe}_2\text{O}_4\text{@SiO}_2$ with and without ZnO coated nanomaterial was used for the dye degradation of red amaranth dye (25 mg/L). The $\text{Co}_{0.25}\text{Zn}_{0.75}\text{Fe}_2\text{O}_4\text{@SiO}_2/\text{ZnO}$ degrades red amaranth dye by about 90% after 90 min under UV irradiation [63].

Moreover, Astaraki et al. specified the synthesis of $\text{CuFe}_2\text{O}_4/\text{RGO}$ nanocomposite for dye degradation of methylene blue (MB) (15 mg/L) with a light source as two 100 W Xenon lamps with a UV cut-off filter. The catalyst shows a 3% decrease in catalytic activity after the 4th cycle [64]. Lei et al. show the synthesis and catalytic activity of $\text{CuFe}_2\text{O}_4\text{@GO}$ hybrid for methylene blue (MB) dye degradation. The 200 mg/L catalysts and PMS dosage of 0.8 mmol/L are sufficient for 93.3% photocatalytic degradation of methylene blue (MB) dye (20 mg/L) in 30 min. Furthermore, an increase in the catalyst amount to 400 mg/L does not show a boost in the catalytic degradation rate of MB dye. In contrast, the rise in the PMS dosage to 1 mmol/L shows a small decline in MB degradation rate [65]. Chen et al. demonstrated the hydrothermal synthesis of magnetic $\text{CuFe}_2\text{O}_4/\text{GO}$ and their dye degradation potential towards acid orange II (AO7) and rhodamine B (RhB) without H_2O_2 in the presence visible light. The photocatalytic application of $\text{CuFe}_2\text{O}_4/\text{GO}$ (800 mg/L) for acid orange II (AO7) dye (0.05 mM) degradation at pH = 7 shows 77% efficiency [66]. Yu et al. testified dye degradation C.I. Reactive red 2 (RR) (100 mg/L), with 10 mg of the nanoscale-confined precursor of CuFe_2O_4

and 4 mL of H_2O_2 , displays 91.3% degradation in 60 min. Furthermore, the efficiency of the CuFe_2O_4 enhances to 94.3% by calcination at higher temperatures [67]. da Nóbrega Silva et al. revealed that the visible-light-driven photocatalytic performance of $\text{CuFe}_2\text{O}_4\text{-Fe}_2\text{O}_3$ (1 g/L) nanocatalyst for the methylene blue (MB) dye (50 mg/L) degradation in the presence of H_2O_2 (300 Mg/L) at neutral pH shows 64% efficiency with 0.6-FC-2. Furthermore, the recyclability study of the catalyst shows a 2.33% decrease in April and a 10.15% increase in May in the second cycle [68]. Kalantari et al. disclosed catalytic activity of $\text{Fe}_3\text{O}_4\text{-C-Cu}$ nanocatalyst (30 mg) and aqua solution of methyl orange (MO) (3.0×10^{-5} M, 25 mL) with aqueous NaBH_4 (5.3×10^{-3} M, 25 mL), and MO degradation takes place within 50 seconds. Moreover, there is no significant loss in the catalytic activity after 4th cycle [69].

In addition, Saleh and Taufik explained the ultraviolet-light-assisted degradation of the MO and MB (20 mg/L). $\text{Ag-Fe}_3\text{O}_4/\text{graphene}$ (0.4 gm) composites act as a catalyst with 4 mL 30% H_2O_2 . Furthermore, $\text{Ag-Fe}_3\text{O}_4/\text{graphene}$ composite (25 wt% $\text{Ag-Fe}_3\text{O}_4/\text{graphene}$ and 10 wt% of graphene) shows efficient catalyst reusability [70]. Tang et al. exhibited that sulfidation-modified Fe_3O_4 nanoparticle ($\text{S-Fe}_3\text{O}_4\text{NP}$) (50 mg/L) catalyst for the photocatalytic degradation of rhodamine B (10 mg/L) in the presence of H_2O_2 (13 mg/L) shows 99% degradation within 10 min. Recyclability study shows the catalyst 84.3% efficiency for rhodamine B dye after 3rd cycle [71]. Vinothkannan et al. showed that the synthesis of $\text{RGO/Fe}_3\text{O}_4$ nanocomposites (10 mg) for methylene blue (MB) (9.37×10^{-5} M) dye degradation with the addition of using 5.8×10^{-2} M of NaBH_4 under ultrasonicated shows 95.18% efficiency within 12 min. Moreover, the catalyst displays 89.4% efficiency after the 7th cycle [72]. Zhou et al. synthesised $\text{Ag}_3\text{PO}_4\text{@MgF}_2\text{O}_4$ composites for the dye degradation of rhodamine B using visible irradiation. The dye degradation experiment of aqueous RhB

(10 mg/L) was performed in the presence of 300 W Xenon short-arc lamps with a UV filter (≥ 400 nm), and the amount of $\text{Ag}_3\text{PO}_4/\text{MgFe}_2\text{O}_4$ (10%) catalyst (20 mg/100 mL) degrades 98% of dye in 20 min [73]. Das and Dhar publicized the photocatalytic degradation of malachite green (MG) by using MgFe_2O_4 nanocatalyst in the presence of H_2O_2 . The 40 mg of catalyst in 70 mL of MG (10 mg/L) and 0.1 mL 10% H_2O_2 in absence of light gives 100% degradation in 50 seconds [74].

Cabrera et al. manufacture nanostructured MgFe_2O_4 ferrites and check their methylene blue dye degradation efficiency. In 35 min, 60 and 75% of methylene blue (MB) dye degraded under light and dark conditions, respectively [75]. Zhang et al. testified the fabrication of $\text{MgFe}_2\text{O}_4/\text{TiO}_2$ and checked the degradation efficiency of rhodamine B (RB) dye in the presence of UV and visible light 500 W Xenon lamps as a source. The 2 wt% $\text{MgFe}_2\text{O}_4/\text{TiO}_2$ catalyst shows 100% efficiency in 40 min using UV light whereas 3 wt% $\text{MgFe}_2\text{O}_4/\text{TiO}_2$ catalysts evince excellent efficiency in visible light [76]. Amulya et al. manufacture Cu-doped $\text{NiMnFe}_2\text{O}_4$ (60 mg) nanoparticles using the probe sonication method and study their photocatalytic dye degradation activity under UV light towards Drimarene yellow (DY) and methylene blue (MB) dyes. The degradation efficiency of DY is 43.3% when dopant 0.1, whereas MB is 98.1% when 0.4 is dopant [77]. Mahmoodi reported the synthesis of MnFe_2O_4 and dye degradation ability for reactive red 120 (RR120) and reactive red 198 (RR198), concentration (100 mg/L), in the presence of H_2O_2 (1.2 mM) [78]. Boutra et al. described the synthesis of $\text{MnFe}_2\text{O}_4/\text{TA}/\text{ZnO}$ nanocomposites and studied their dye degradation performance for the Congo red (CR) using visible light radiations. Congo red (CR) (16 mg/L) dye degraded using 50 mg of the catalyst shows 84.2% efficiency in 90 min. Reusability study confirmations and degradation efficiency at the end of 5th cycle were 77.5% [79]. Mandal et al. investigated the methylene blue dye (MB) (10 mg/L) degradation utilizing $\text{MnFe}_2\text{O}_4/\text{rGO}$. The catalyst (0.03 g) shows 97% efficiency in 60 min in the presence of a UV lamp of 40 W [80]. Sahoo et al. described the synthesis of mesoporous silica encapsulated with magnetic MnFe_2O_4 nanoparticles for the dye degradation study. The methyl orange (MO) dye (0.6 mg/mL) is degraded utilizing mesoporous silica encapsulated MnFe_2O_4 (20 mg) along with 2 mL H_2O_2 , resulting in 98% degradation in the presence of sunlight in 180 min. Furthermore, the catalyst shows a negligible change in the efficiency after 5th cycle [81]. Zhang et al. showed NiFe_2O_4 powders as a nanocatalyst for the photocatalytic degradation of brilliant green (BG) dye (20 mg/mL) under microwave irradiation (output power 500 W) for 2 min to degrade 97% dye [82]. Atacan et al. explained the decolorization of indigo carmine (IC) dye (10 mg/L) using $\text{NiFe}_2\text{O}_4/\text{T}/\text{GOx}$ in 90 min. Decolorize 98.6% and 37.6% under a UV lamp and Fenton process, respectively [83]. Baig et al. explained that the synthesis of $\text{NiFe}_2\text{O}_4/\text{TiO}_2$ for dye degradation of methyl orange (MO) dye using a UV lamp (300 W Xenon) with a cut-off filter shows 90.06% activity. Furthermore, increasing the percentage of TiO_2 from 10% to 40% in the catalyst NiFe_2O_4 increases the photocatalytic activity from 72% to 90.06%, respectively [84].

Furthermore, Kamal et al. stated that boron-doped $\text{C}_3\text{N}_4/\text{NiFe}_2\text{O}_4$ nanocomposite was fabricated and investigated their use for methylene blue (MB) dye degradation. The catalyst $\text{BCN}/\text{NiFe}_2\text{O}_4$ (100 mg) is mixed with methylene blue (MB) dye (5 ppm) in a Mercury-Xenon lamp (350 W) as a source of visible light and shows 98% degradation efficiency in 80 min. However, the reusability study shows a 1.69% decrease in the catalyst after 3rd cycle [85]. Amulya et al. reported the sonochemical fabrication of NiFe_2O_4 nanocatalyst and studied their dye degradation activity for the Drimarene yellow (DY) and methylene blue (MB) dyes. The 60 mg NiFe_2O_4 is added to MB and DY dyes separately; each with 20 ppm concentration and irradiated with a 400 W Hg lamp shows 89.4% for MB and 43.3% for DY degradation. In addition, the catalyst shows a 10% decrease in efficiency after 5th consecutive cycle [86]. Chandel et al. elucidate the fabrication of $\text{ZnO}/\text{ZnFe}_2\text{O}_4/\text{NG}$ and $\text{ZnO}/\text{CoFe}_2\text{O}_4/\text{NG}$ nanocatalyst for the efficient degradation of malachite green (MG) and methyl orange (MO) dyes in the presence of halogen lamp. The $\text{ZnO}/\text{ZnFe}_2\text{O}_4/\text{NG}$ shows 92% and 98%, and with $\text{ZnO}/\text{CoFe}_2\text{O}_4/\text{NG}$ shows 98% and 99% for MG and MO dyes, respectively. A recyclability study shows an insignificant change in the catalytic activity after the 10th cycle [87]. Mahmoodi explained the synthesis of ZnFe_2O_4 and dye degradation capacity for reactive red 120 (RR120) and reactive red 198 (RR198) concentrations (100 mg/L) and the amount of nanocatalyst (0.20 g) and H_2O_2 (1.2 mM) at 25°C in the presence of UV-C lamp (200–280 nm, 9 W, Philips) [88]. Kulkarni et al. enlighten that the synthesis of core-shell $\text{ZnFe}_2\text{O}_4/\text{ZnO}$ nanocatalyst for degradation of methyl orange (MO) dye in visible light using 125 W Hg lamp 100% degradation takes place in 9 h. Reusability study shows a 5% decrease in the efficiency after 2nd reuse [89]. Nirumand et al. convey that the synthesis of $\text{MIL-101}(\text{Cr})/\text{RGO}/\text{ZnFe}_2\text{O}_4$ nanocatalyst (0.5 g/L) for the degradation of rhodamine B (RB) (25 mg/L) dye using ultrasound irradiation in the appearance of H_2O_2 is 95% in 50 min. The methylene blue (MB) and Congo red (CR) dyes degraded 100% and 95%, and the time required were 2 min and 50 min, respectively, under similar conditions. The catalyst study shows excellent recyclability after the 4th cycle [90]. Oliveira et al. explain the fabrication of ZnFe_2O_4 and examine the dye degradation performance using visible light degradation of rhodamine B (RB) and malachite green (MG) dye degradation using visible irradiation of 3 lamps from Taschibra® full spiral of 25 W as source [91].

7. Mechanistic Study of Dye Degradation Using Ferrite-Based Nanomaterials

The mechanistic study, which shows how the magnetic ferrite is responsible for the dye degradation and the graphical representation, was discussed in this section.

Nirumand et al. [90] reported the sonocatalytic dye degradation, which involves a sonoluminescence phenomenon capable of generating a relatively wide wavelength range that is used to excite the electron in both ZnFe_2O_4 and $\text{MIL-101}(\text{Cr})$, leading to the formation of holes. The transfer of an electron from CB of ZnFe_2O_4 to CB of $\text{MIL-101}(\text{Cr})$

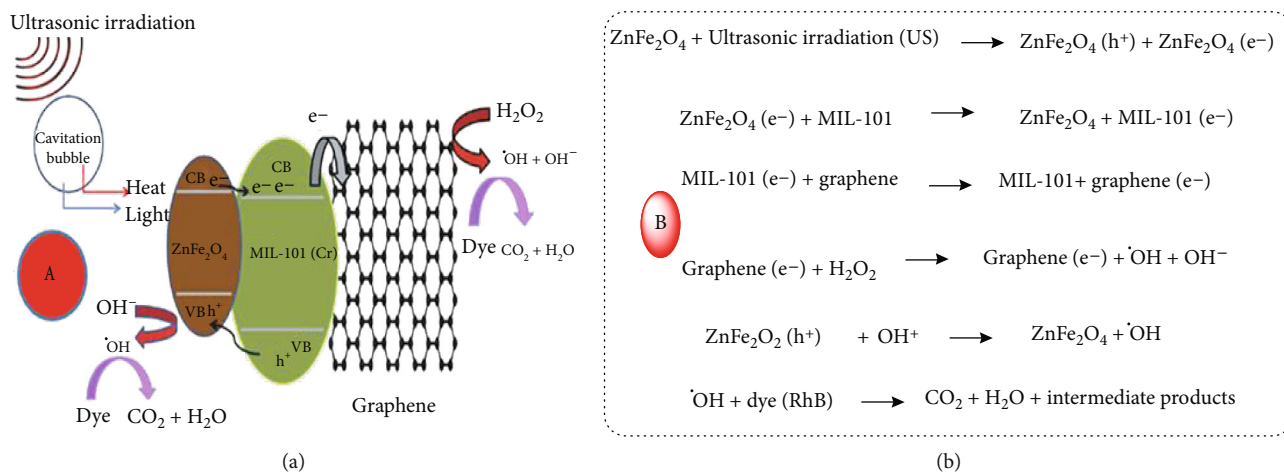


FIGURE 5: (a) A plausible mechanism for sonocatalytic degradation of dyes over MIL-101(Cr)/RGO/ZnFe₂O₄ nanocomposite using ultrasound irradiation. (b) Schematic representation of mechanism takes place during dye degradation (reproduce from [81]).

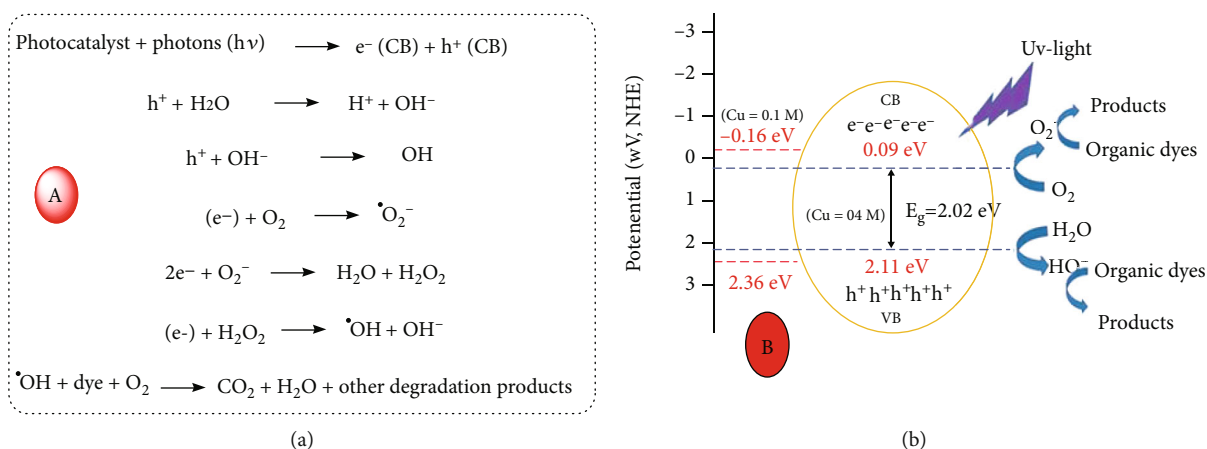


FIGURE 6: (a) A proposed mechanism for degradation of dyes using Cu-doped NiMnFe₂O₄ nano-photocatalyst under UV light. (b) Schematic representation of mechanism takes place during dye degradation (reproduce from [68]).

and the holes from VB of MIL-101(Cr) to VB of ZnFe₂O₄ and how it is utilized for the degradation is shown in Figure 5(a) graphically, and Figure 5(b) shows how the step-wise reaction takes place in the dye degradation.

Amulya et al. [77] specified the catalytic role of Cu-doped NiMnFe₂O₄ in dye degradation. The catalyst is subjected to light irradiation that excites the electron in CB, which leads to holes in the VB. Furthermore, the created holes react with water to generate OH[•] radicals which disintegrate dye molecules, and super oxide is generated using oxygen and excited electron in CB. The detailed reaction progress and schematic representation of dye degradation are shown in Figures 6(a) and 6(b), respectively.

Furthermore, Chandel et al. [87] elucidated how the ZnO/CoFe₂O₄/NG and ZnO/ZnFe₂O₄/NG magnetic nanocomposites degrade dye solution. When exposed to a visible-light source, the catalyst creates electrons and holes in CB and VB, respectively. The redox scale shows strong interfacial contact, and the positioning of CB facilitates the movement of an electron from CB of ZF to ZnO and avoids

the hole-electron recombination by forming heterojunction-type II. The detailed schematic representations of dye degradation using ZnO/ZnFe₂O₄/NG and ZnO/CoFe₂O₄/NG catalyst are shown in Figures 7(a) and 7(b), respectively.

Similarly, various reports on catalytic dye degradation using ferrites and metal ferrites are tabulated in Table 1.

8. Future Scope

This article compiled and reviewed the degradation of different dyes using ferrite-based nanomaterials. According to the literature, dye degradation using ferrite-based nanomaterials is supposed to have improved efficiency. However, the distinction between both the magnetic and ferrite-based composites is just a guideline. From this reconsideration, we also like to point out that it is necessary to choose a minimum manufacturing cost with strong dye degradation performance and also a multipurpose catalyst viable for various types of contaminants because the selection of the catalyst is an important event in the decision to introduce

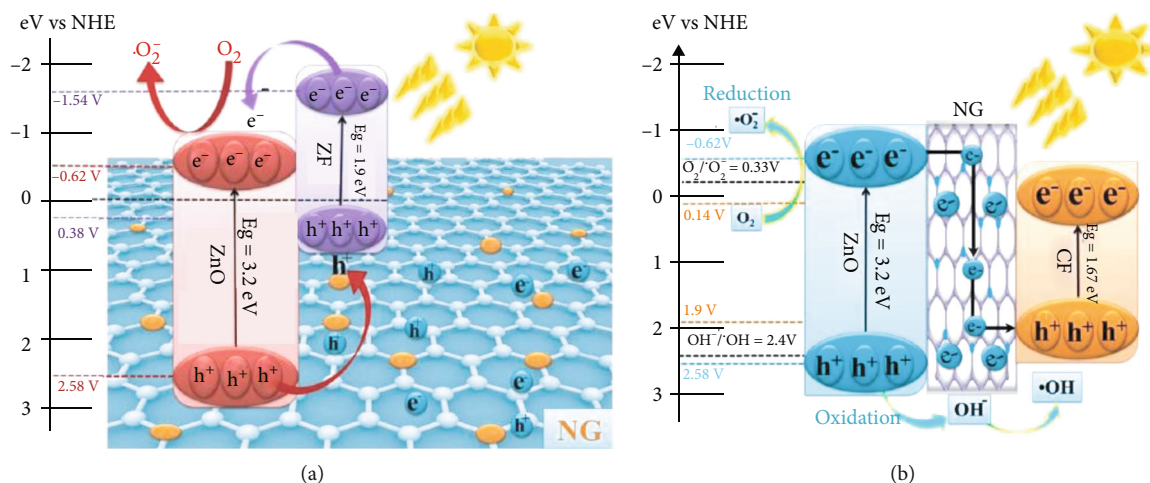


FIGURE 7: (a, b) Schematic representation of dye degradation using $\text{ZnO}/\text{ZnFe}_2\text{O}_4/\text{NG}$ and $\text{ZnO}/\text{CoFe}_2\text{O}_4/\text{NG}$ catalysts, respectively (reproduce from [78]).

a suitable large-scale magnetic catalyst. This article shows that the ferrite-based nanomaterial used for dye degradation contains a simple preparation method and cheap chemical reagents. However, by analyzing the efficacy of magnetic nanocomposite regeneration, economic viability should be improved, as regeneration studies can assess the reusability of magnetic nanocomposites. On the other hand, a lot of new, powerful software is built to resolve mathematical models and complex data that are supposed to be represented more adequately and help understand the mechanism's insight. In addition, the use of energy-dispersive X-ray spectroscopy (EDX), scanning electron microscope (SEM), Fourier transform infrared spectroscopy (FTIR), differential scanning calorimetry (DSC), electron spin resonance (ESR), scanning tunneling microscopy (STM), dynamic light scattering (DLS), X-ray diffraction (XRD) analysis, X-ray photoelectron spectroscopy (XPS), Brunauer-Emmett-Teller (BET), superconducting quantum interference device (SQUID), vibrating sample magnetometer (VSM), magnetic force microscopy (MFM), atomic force microscopy (AFM), X-ray absorption spectroscopy (XAS), zeta potential, and thermogravimetric analysis (TGA) is strongly recommended for characterization assessments.

Moreover, from an environmental point of view, developing a safer and more effective approach to dye degradation is necessary. Keeping this in mind, the study was carried out to find magnetic nanoparticles for dye degradation.

9. Conclusion

The article highlights the implications of the successful production of nanomaterials based on magnetic ferrite and its applications for the treatment of dye effluents. Special note should be made of the important mechanisms of action of magnetic nanomaterials in the treatment of dye effluents, like photocatalytic degradation and adsorption, concerning just the mitigation of dyes typically used throughout the textile sector. The use of renewable or environmentally friendly reductants to fabricate ferrite-based nanomaterials has been

shown to demonstrate the effective elimination of different dyes from wastewater. However, with recent research data, the possibility of ferrite-based nanomaterials discharged into the ecosystem and their exposure to terrestrial and marine biological systems at trace concentrations is known. In addition, the application of ferrite-based nanomaterials to dye effluent treatment procedures involves extensive obstacle evaluations, as well as there are also restricted environmental protection assessment studies. Furthermore, no legislation relating to the maximum allowable concentrations of ferrite-based nanomaterials in wastewater is in place to ensure the environment's safety and human health. Therefore, it is essential to evaluate ferrite-based nanomaterial harmful effects and hazards associated with the implementation of ferrite-based nanomaterials in the treatment of dye effluent. The sulphidation process has recently become one of the natural solutions for mitigating the toxicity of ferrite-based nanomaterials and their effects on sewage processing plants. The study on in vivo immunotoxicity, the effect of ferrite-based nanomaterials form on toxic effect, and the thorough advancement of ferrite-based nanomaterial adsorption kinetics on various biological macromolecules occur during infancy. The overall understanding of ferrite-based nanomaterial adsorption, distribution, and effective dye degradation is demonstrated in this study.

Conflicts of Interest

The authors declare no conflict of interest.

References

- [1] H. S. Rai, M. S. Bhattacharyya, J. Singh, T. K. Bansal, P. Vats, and U. C. Banerjee, "Removal of dyes from the effluent of textile and dyestuff manufacturing industry: a review of emerging techniques with reference to biological treatment," *Critical Reviews in Environmental Science and Technology*, vol. 35, no. 3, pp. 219–238, 2005.

- [2] S. Madhav, A. Ahamad, P. Singh, and P. K. Mishra, "A review of textile industry: wet processing, environmental impacts, and effluent treatment methods," *Environmental Quality Management*, vol. 27, no. 3, pp. 31–41, 2018.
- [3] X.-C. Jin, G. Q. Liu, Z. H. Xu, and W. Y. Tao, "Decolorization of a dye industry effluent by *Aspergillus fumigatus* XC6," *Applied Microbiology and Biotechnology*, vol. 74, no. 1, pp. 239–243, 2007.
- [4] Z. Badani, H. Ait-Amar, A. Si-Salah, M. Brik, and W. Fuchs, "Treatment of textile waste water by membrane bioreactor and reuse," *Desalination*, vol. 185, no. 1-3, pp. 411–417, 2005.
- [5] R. Jain, M. Mathur, S. Sikarwar, and A. Mittal, "Removal of the hazardous dye rhodamine B through photocatalytic and adsorption treatments," *Journal of Environmental Management*, vol. 85, no. 4, pp. 956–964, 2007.
- [6] D. Van Thuan, T. L. Nguyen, H. H. Thi et al., "Development of indium vanadate and silver deposited on graphitic carbon nitride ternary heterojunction for advanced photocatalytic degradation of residual antibiotics in aqueous environment," *Optical Materials*, vol. 123, article 111885, 2022.
- [7] S. Ghotekar, S. Pansambal, K. Y. A. Lin, D. Pore, and R. Oza, "Recent advances in synthesis of CeVO₄ nanoparticles and their potential scaffold for photocatalytic applications," *Topics in Catalysis*, pp. 1–15, 2022.
- [8] H. N. Cuong, S. Pansambal, S. Ghotekar et al., "New frontiers in the plant extract mediated biosynthesis of copper oxide (CuO) nanoparticles and their potential applications: a review," *Environmental Research*, vol. 203, article 111858, 2022.
- [9] U. G. Akpan and B. H. Hameed, "Parameters affecting the photocatalytic degradation of dyes using TiO₂-based photocatalysts: a review," *Journal of Hazardous Materials*, vol. 170, no. 2-3, pp. 520–529, 2009.
- [10] E. Forgacs, T. Cserhádi, and G. Oros, "Removal of synthetic dyes from wastewaters: a review," *Environment International*, vol. 30, no. 7, pp. 953–971, 2004.
- [11] C. Lops, A. Ancona, K. di Cesare et al., "Sonophotocatalytic degradation mechanisms of rhodamine B dye via radicals generation by micro- and nano-particles of ZnO," *Applied Catalysis B: Environmental*, vol. 243, pp. 629–640, 2019.
- [12] S. Pansambal, S. Ghotekar, S. Shewale, K. Deshmukh, N. Barde, and P. Bardapurkar, "Efficient synthesis of magnetically separable CoFe₂O₄@ SiO₂ nanoparticles and its potent catalytic applications for the synthesis of 5-aryl-1, 2, 4-triazolidine-3-thione derivatives," *Journal of Water and Environmental Nanotechnology*, vol. 4, no. 3, pp. 174–186, 2019.
- [13] R. Hudson, Y. Feng, R. S. Varma, and A. Moores, "Bare magnetic nanoparticles: sustainable synthesis and applications in catalytic organic transformations," *Green Chemistry*, vol. 16, no. 10, pp. 4493–4505, 2014.
- [14] R. Kalia, A. Chauhan, R. Verma et al., "Photocatalytic degradation properties of Li-Cr ions substituted CoFe₂O₄ nanoparticles for wastewater treatment application," *Physica Status Solidi*, vol. 219, no. 8, article 2100539, 2022.
- [15] S. Chikazumi, S. Taketomi, M. Ukita et al., "Physics of magnetic fluids," *Journal of Magnetism and Magnetic Materials*, vol. 65, no. 2-3, pp. 245–251, 1987.
- [16] A. K. Gupta and M. Gupta, "Cytotoxicity suppression and cellular uptake enhancement of surface modified magnetic nanoparticles," *Biomaterials*, vol. 26, no. 13, pp. 1565–1573, 2005.
- [17] T. Hyeon, "Chemical synthesis of magnetic nanoparticles," *Chemical Communications*, vol. 8, no. 8, pp. 927–934, 2003.
- [18] Q. Li, V. Kumar, Y. Li, H. Zhang, T. J. Marks, and R. P. H. Chang, "Fabrication of ZnO nanorods and nanotubes in aqueous solutions," *Chemistry of Materials*, vol. 17, no. 5, pp. 1001–1006, 2005.
- [19] S. Mornet, S. Vasseur, F. Grasset et al., "Magnetic nanoparticle design for medical applications," *Progress in Solid State Chemistry*, vol. 34, no. 2-4, pp. 237–247, 2006.
- [20] J. B. Haun, T. J. Yoon, H. Lee, and R. Weissleder, "Magnetic nanoparticle biosensors," *Wiley Interdisciplinary Reviews: Nanomedicine and Nanobiotechnology*, vol. 2, no. 3, pp. 291–304, 2010.
- [21] M. Takafuji, S. Ide, H. Ihara, and Z. Xu, "Preparation of poly (1-vinylimidazole)-grafted magnetic nanoparticles and their application for removal of metal ions," *Chemistry of Materials*, vol. 16, no. 10, pp. 1977–1983, 2004.
- [22] D. W. Elliott and W.-X. Zhang, "Field assessment of nano-scale bimetallic particles for groundwater treatment," *Environmental Science & Technology*, vol. 35, no. 24, pp. 4922–4926, 2001.
- [23] S. Ghotekar, H. C. A. Murthy, A. Roy, M. Bilal, and R. Oza, "Magnetic nanomaterials-based biosorbents," in *Nano-Biosorbents for Decontamination of Water, Air, and Soil Pollution*, pp. 605–614, Elsevier, 2022.
- [24] H. Dabhane, S. Chatur, S. Ghotekar et al., "Methods for the synthesis of nano-biosorbents for the contaminant removal," in *Nano-Biosorbents for Decontamination of Water, Air, and Soil Pollution*, pp. 61–73, Elsevier, 2022.
- [25] V. Dutta, J. Devasia, A. Chauhan et al., "Photocatalytic nanomaterials: applications for remediation of toxic polycyclic aromatic hydrocarbons and green management," *Advances*, vol. 11, article 100353, 2022.
- [26] A. H. Lu, E. E. Salabas, and F. Schüth, "Magnetic nanoparticles: synthesis, protection, functionalization, and application," *Angewandte Chemie International Edition*, vol. 46, no. 8, pp. 1222–1244, 2007.
- [27] V. Dutta, S. Sharma, P. Raizada et al., "Recent progress on bismuth-based Z-scheme semiconductor photocatalysts for energy and environmental applications," *Journal of Environmental Chemical Engineering*, vol. 8, no. 6, article 104505, 2020.
- [28] K. G. Kelele, A. Tadesse, T. Desalegn, S. Ghotekar, R. Balachandran, and H. C. A. Murthy, "Synthesis and characterizations of metal ions doped barium strontium titanate (BST) nanomaterials for photocatalytic and electrical applications: a mini review," *International Journal of Materials Research*, vol. 112, no. 8, pp. 665–677, 2021.
- [29] A. Khan, S. Malik, S. Shah et al., "Nanoadsorbents for environmental remediation," *Nanotechnology for Environmental Remediation*, pp. 103–120, 2022.
- [30] S. Pansambal, R. Oza, S. Borgave et al., "Bioengineered cerium oxide (CeO₂) nanoparticles and their diverse applications: a review," *Applied Nanoscience*, pp. 1–26, 2022.
- [31] H. Dabhane, S. Ghotekar, P. Tambade et al., "A review on environmentally benevolent synthesis of CdS nanoparticle and their applications," *Environmental Chemistry and Ecotoxicology*, vol. 3, pp. 209–219, 2021.
- [32] P.-H. Mao, N. N. Huy, S. Ghotekar et al., "Single-step synthesized functionalized copper carboxylate framework meshes as hierarchical catalysts for enhanced reduction of nitrogen

- containing phenolic contaminants,” *Catalysts*, vol. 12, no. 7, p. 765, 2022.
- [33] R. Kumar, P. Raizada, A. A. P. Khan et al., “Recent progress in emerging BiPO₄-based photocatalysts: synthesis, properties, modification strategies, and photocatalytic applications,” *Journal of Materials Science & Technology*, vol. 108, pp. 208–225, 2022.
- [34] A. Kumar, V. Hasija, A. Sudhaik et al., “Artificial leaf for light-driven CO₂ reduction: basic concepts, advanced structures and selective solar-to-chemical products,” *Chemical Engineering Journal*, vol. 430, article 133031, 2022.
- [35] S. Sharma, V. Dutta, P. Raizada et al., “An overview of heterojunctioned ZnFe₂O₄ photocatalyst for enhanced oxidative water purification,” *Journal of Environmental Chemical Engineering*, vol. 9, no. 5, article 105812, 2021.
- [36] I. M. Banat, P. Nigam, D. Singh, and R. Marchant, “Microbial decolorization of textile-dyecontaining effluents: a review,” *Bioresour. Technol.*, vol. 58, no. 3, pp. 217–227, 1996.
- [37] V. Vadivelan and K. V. Kumar, “Equilibrium, kinetics, mechanism, and process design for the sorption of methylene blue onto rice husk,” *Journal of Colloid and Interface Science*, vol. 286, no. 1, pp. 90–100, 2005.
- [38] S. Ramchandani, M. das, A. Joshi, and S. K. Khanna, “Effect of oral and parenteral administration of metanil yellow on some hepatic and intestinal biochemical parameters,” *Journal of Applied Toxicology*, vol. 17, no. 1, pp. 85–91, 1997.
- [39] M. Das, S. Ramchandani, R. K. Upreti, and S. K. Khanna, “Metanil yellow: a bifunctional inducer of hepatic phase I and phase II xenobiotic-metabolizing enzymes,” *Food and Chemical Toxicology*, vol. 35, no. 8, pp. 835–838, 1997.
- [40] S. Gupta, M. Sundararajan, and K. Rao, “Tumor promotion by metanil yellow and malachite green during rat hepatocarcinogenesis is associated with dysregulated expression of cell cycle regulatory proteins,” *Teratogenesis, Carcinogenesis, and Mutagenesis*, vol. 23, no. S1, pp. 301–312, 2003.
- [41] S. Sachdeva, K. V. Mani, S. K. Adaval, Y. P. Jalpota, K. C. Rasela, and D. S. Chadha, “Acquired toxic methaemoglobinemia,” *The Journal of the Association of Physicians of India*, vol. 40, no. 4, pp. 239–240, 1992.
- [42] S. Chandro and T. Nagaraja, “A food poisoning outbreak with chemical dye—an investigation report,” *Medical Journal of Armed Forces India*, vol. 43, no. 4, pp. 291–293, 1987.
- [43] B. Hausen, “A case of allergic contact dermatitis due to metanil yellow,” *Contact Dermatitis*, vol. 31, no. 2, pp. 117–118, 1994.
- [44] H. Tiwari, “Assessment of teratogenicity and embryo toxicity of dye waste-water untreated sludge from Sanganer on Swiss albino mice when administered during growth period of gestation,” *Water Resources Development*, vol. 2, pp. 48–53, 2012.
- [45] R. Sivashankar, A. B. Sathya, K. Vasantharaj, and V. Sivasubramanian, “Magnetic composite an environmental super adsorbent for dye sequestration - a review,” *Environmental Nanotechnology, Monitoring & Management*, vol. 1-2, pp. 36–49, 2014.
- [46] A. Akbarzadeh, M. Samiei, and S. Davaran, “Magnetic nanoparticles: preparation, physical properties, and applications in biomedicine,” *Nanoscale Research Letters*, vol. 7, no. 1, pp. 1–13, 2012.
- [47] N. A. Frey, S. Peng, K. Cheng, and S. Sun, “Magnetic nanoparticles: synthesis, functionalization, and applications in bioimaging and magnetic energy storage,” *Chemical Society Reviews*, vol. 38, no. 9, pp. 2532–2542, 2009.
- [48] S. Singamaneni, V. N. Bliznyuk, C. Binek, and E. Y. Tsybmal, “Magnetic nanoparticles: recent advances in synthesis, self-assembly and applications,” *Journal of Materials Chemistry*, vol. 21, no. 42, pp. 16819–16845, 2011.
- [49] S. H. Noh, W. Na, J. T. Jang et al., “Nanoscale magnetism control via surface and exchange anisotropy for optimized ferrimagnetic hysteresis,” *Nano Letters*, vol. 12, no. 7, pp. 3716–3721, 2012.
- [50] Q. Song and Z. J. Zhang, “Shape control and associated magnetic properties of spinel cobalt ferrite nanocrystals,” *Journal of the American Chemical Society*, vol. 126, no. 19, pp. 6164–6168, 2004.
- [51] A. M. Salgueiro, A. L. Daniel-da-Silva, A. V. Girão, P. C. Pinheiro, and T. Trindade, “Unusual dye adsorption behavior of κ -carrageenan coated superparamagnetic nanoparticles,” *Chemical Engineering Journal*, vol. 229, pp. 276–284, 2013.
- [52] G. Salazar-Alvarez, J. Qin, V. Šepelák et al., “Cubic versus spherical magnetic nanoparticles: the role of surface anisotropy,” *Journal of the American Chemical Society*, vol. 130, no. 40, pp. 13234–13239, 2008.
- [53] G. Zhen, B. W. Muir, B. A. Moffat et al., “Comparative study of the magnetic behavior of spherical and cubic superparamagnetic iron oxide nanoparticles,” *The Journal of Physical Chemistry C*, vol. 115, no. 2, pp. 327–334, 2011.
- [54] A. Williams, V. L. Moruzzi, C. D. Gelatt Jr., J. Kübler, and K. Schwarz, “Aspects of transition-metal magnetism,” *Journal of Applied Physics*, vol. 53, no. 3, pp. 2019–2023, 1982.
- [55] A. R. West, *Basic solid state chemistry*, John Wiley & Sons Incorporated, 1999.
- [56] A. G. Kolhatkar, A. Jamison, D. Litvinov, R. Willson, and T. Lee, “Tuning the magnetic properties of nanoparticles,” *International Journal of Molecular Sciences*, vol. 14, no. 8, pp. 15977–16009, 2013.
- [57] R. Suresh, S. Rajendran, P. S. Kumar, D. V. N. Vo, and L. Cornejo-Ponce, “Recent advancements of spinel ferrite based binary nanocomposite photocatalysts in wastewater treatment,” *Chemosphere*, vol. 274, article 129734, 2021.
- [58] K. K. Kefeni, B. B. Mamba, and T. A. Msagati, “Application of spinel ferrite nanoparticles in water and wastewater treatment: a review,” *Separation and Purification Technology*, vol. 188, pp. 399–422, 2017.
- [59] S. Farhadi, F. Siadatnasab, and A. Khataee, “Ultrasound-assisted degradation of organic dyes over magnetic CoFe₂O₄@ZnS core-shell nanocomposite,” *Ultrasonics Sonochemistry*, vol. 37, pp. 298–309, 2017.
- [60] F. Siadatnasab, S. Farhadi, and A. Khataee, “Sonocatalytic performance of magnetically separable CuS/CoFe₂O₄ nano-hybrid for efficient degradation of organic dyes,” *Ultrasonics Sonochemistry*, vol. 44, pp. 359–367, 2018.
- [61] A. Kalam, A. G. al-Sehemi, M. Assiri et al., “Modified solvothermal synthesis of cobalt ferrite (CoFe₂O₄) magnetic nanoparticles photocatalysts for degradation of methylene blue with H₂O₂/visible light,” *Results in Physics*, vol. 8, pp. 1046–1053, 2018.
- [62] L. Gan, L. Xu, and K. Qian, “Preparation of core-shell structured CoFe₂O₄ incorporated Ag₃PO₄ nanocomposites for photocatalytic degradation of organic dyes,” *Materials & Design*, vol. 109, pp. 354–360, 2016.

- [63] J. López, A. A. Ortiz, F. Muñoz-Muñoz et al., "Magnetic nanostructured based on cobalt-zinc ferrites designed for photocatalytic dye degradation," *Journal of Physics and Chemistry of Solids*, vol. 150, article 109869, 2021.
- [64] H. Astaraki, S. Masoudpanah, and S. Alamolhoda, "Effects of fuel contents on physicochemical properties and photocatalytic activity of CuFe_2O_4 /reduced graphene oxide (RGO) nanocomposites synthesized by solution combustion method," *Journal of Materials Research and Technology*, vol. 9, no. 6, pp. 13402–13410, 2020.
- [65] X. Lei, M. You, F. Pan et al., " CuFe_2O_4 @GO nanocomposite as an effective and recoverable catalyst of peroxymonosulfate activation for degradation of aqueous dye pollutants," *Chinese Chemical Letters*, vol. 30, no. 12, pp. 2216–2220, 2019.
- [66] P. Chen, X. Xing, H. Xie, Q. Sheng, and H. Qu, "High catalytic activity of magnetic CuFe_2O_4 /graphene oxide composite for the degradation of organic dyes under visible light irradiation," *Chemical Physics Letters*, vol. 660, pp. 176–181, 2016.
- [67] D. Yu, H. Ni, L. Wang, M. Wu, and X. Yang, "Nanoscale-confined precursor of CuFe_2O_4 mediated by hyperbranched polyamide as an unusual heterogeneous Fenton catalyst for efficient dye degradation," *Journal of Cleaner Production*, vol. 186, pp. 146–154, 2018.
- [68] E. da Nóbrega Silva, I. L. Brasileiro, V. S. Madeira et al., "Reusable CuFe_2O_4 - Fe_2O_3 catalyst synthesis and application for the heterogeneous photo-Fenton degradation of methylene blue in visible light," *Journal of Environmental Chemical Engineering*, vol. 8, no. 5, article 104132, 2020.
- [69] E. Kalantari, M. A. Khalilzadeh, D. Zareyee, and M. Shokouhimehr, "Catalytic degradation of organic dyes using green synthesized Fe_3O_4 -cellulose-copper nanocomposites," *Journal of Molecular Structure*, vol. 1218, article 128488, 2020.
- [70] R. Saleh and A. Taufik, "Ultraviolet-light-assisted heterogeneous Fenton reaction of Ag- Fe_3O_4 /graphene composites for the degradation of organic dyes," *Journal of Environmental Chemical Engineering*, vol. 7, no. 1, article 102895, 2019.
- [71] X. Tang, Z. Li, K. Liu et al., "Sulfidation modified Fe_3O_4 nanoparticles as an efficient Fenton-like catalyst for azo dyes degradation at wide pH range," *Powder Technology*, vol. 376, pp. 42–51, 2020.
- [72] M. Vinothkannan, C. Karthikeyan, G. Gnana kumar, A. R. Kim, and D. J. Yoo, "One-pot green synthesis of reduced graphene oxide (RGO)/ Fe_3O_4 nanocomposites and its catalytic activity toward methylene blue dye degradation," *Spectrochimica Acta Part A: Molecular and Biomolecular Spectroscopy*, vol. 136, pp. 256–264, 2015.
- [73] T. Zhou, G. Zhang, P. Ma et al., "Efficient degradation of rhodamine B with magnetically separable Ag_3PO_4 @ MgFe_2O_4 composites under visible irradiation," *Journal of Alloys and Compounds*, vol. 735, pp. 1277–1290, 2018.
- [74] K. C. Das and S. S. Dhar, "Rapid catalytic degradation of malachite green by MgFe_2O_4 nanoparticles in presence of H_2O_2 ," *Journal of Alloys and Compounds*, vol. 828, article 154462, 2020.
- [75] A. Cabrera, C. E. Rodríguez Torres, S. G. Marchetti, and S. J. Stewart, "Degradation of methylene blue dye under dark and visible light conditions in presence of hybrid composites of nanostructured MgFe_2O_4 ferrites and oxygenated organic compounds," *Journal of Environmental Chemical Engineering*, vol. 8, no. 5, article 104274, 2020.
- [76] L. Zhang, Y. He, Y. Wu, and T. Wu, "Photocatalytic degradation of RhB over MgFe_2O_4 /TiO₂ composite materials," *Materials Science and Engineering: B*, vol. 176, no. 18, pp. 1497–1504, 2011.
- [77] M. S. Amulya, H. P. Nagaswarupa, M. R. A. Kumar, C. R. Ravikumar, and K. B. Kusuma, "Enhanced photocatalytic and electrochemical properties of Cu doped $\text{NiMnFe}_2\text{O}_4$ nanoparticles synthesized via probe sonication method," *Applied Surface Science Advances*, vol. 2, article 100038, 2020.
- [78] N. M. Mahmoodi, "Manganese ferrite nanoparticle: synthesis, characterization, and photocatalytic dye degradation ability," *Desalination and Water Treatment*, vol. 53, no. 1, pp. 84–90, 2015.
- [79] B. Boutra, N. Güy, M. Özacar, and M. Trari, "Magnetically separable MnFe_2O_4 /TA/ZnO nanocomposites for photocatalytic degradation of Congo red under visible light," *Journal of Magnetism and Magnetic Materials*, vol. 497, article 165994, 2020.
- [80] B. Mandal, J. Panda, P. K. Paul, R. Sarkar, and B. Tudu, " MnFe_2O_4 decorated reduced graphene oxide heterostructures: nanophotocatalyst for methylene blue dye degradation," *Vacuum*, vol. 173, article 109150, 2020.
- [81] B. Sahoo, S. K. Sahu, S. Nayak, D. Dhara, and P. Pramanik, "Fabrication of magnetic mesoporous manganese ferrite nanocomposites as efficient catalyst for degradation of dye pollutants," *Catalysis Science & Technology*, vol. 2, no. 7, pp. 1367–1374, 2012.
- [82] L. Zhang, X. Liu, X. Guo, M. Su, T. Xu, and X. Song, "Investigation on the degradation of brilliant green induced oxidation by NiFe_2O_4 under microwave irradiation," *Chemical Engineering Journal*, vol. 173, no. 3, pp. 737–742, 2011.
- [83] K. Atacan, N. Güy, S. Çakar, and M. Özacar, "Efficiency of glucose oxidase immobilized on tannin modified NiFe_2O_4 nanoparticles on decolorization of dye in the Fenton and photo-biocatalytic processes," *Journal of Photochemistry and Photobiology A: Chemistry*, vol. 382, article 111935, 2019.
- [84] M. M. Baig, E. Pervaiz, and M. J. Afzal, "Catalytic activity and kinetic studies of core@ shell nanostructure NiFe_2O_4 @ TiO₂ for photocatalytic degradation of methyl orange dye," *Journal of the Chemical Society of Pakistan*, vol. 42, no. 4, p. 531, 2020.
- [85] S. Kamal, S. Balu, S. Palanisamy, K. Uma, V. Velusamy, and T. C. K. Yang, "Synthesis of boron doped C_3N_4 / NiFe_2O_4 nanocomposite: an enhanced visible light photocatalyst for the degradation of methylene blue," *Results in Physics*, vol. 12, pp. 1238–1244, 2019.
- [86] M. S. Amulya, H. P. Nagaswarupa, M. R. A. Kumar, C. R. Ravikumar, S. C. Prashantha, and K. B. Kusuma, "Sonochemical synthesis of NiFe_2O_4 nanoparticles: characterization and their photocatalytic and electrochemical applications," *Applied Surface Science Advances*, vol. 1, article 100023, 2020.
- [87] N. Chandel, K. Sharma, A. Sudhaik et al., "Magnetically separable $\text{ZnO}/\text{ZnFe}_2\text{O}_4$ and $\text{ZnO}/\text{CoFe}_2\text{O}_4$ photocatalysts supported onto nitrogen doped graphene for photocatalytic degradation of toxic dyes," *Arabian Journal of Chemistry*, vol. 13, no. 2, pp. 4324–4340, 2020.
- [88] N. M. Mahmoodi, "Zinc ferrite nanoparticle as a magnetic catalyst: synthesis and dye degradation," *Materials Research Bulletin*, vol. 48, no. 10, pp. 4255–4260, 2013.
- [89] S. D. Kulkarni, S. Kumbar, S. G. Menon, K. S. Choudhari, and C. Santhosh, "Magnetically separable core-shell ZnFe_2O_4 @ZnO nanoparticles for visible light photodegradation of methyl orange," *Materials Research Bulletin*, vol. 77, pp. 70–77, 2016.

- [90] L. Nirumand, S. Farhadi, A. Zabardasti, and A. Khataee, "Synthesis and sonocatalytic performance of a ternary magnetic MIL-101(Cr)/RGO/ZnFe₂O₄ nanocomposite for degradation of dye pollutants," *Ultrasonics Sonochemistry*, vol. 42, pp. 647–658, 2018.
- [91] T. P. Oliveira, G. N. Marques, M. A. Macedo Castro et al., "Synthesis and photocatalytic investigation of ZnFe₂O₄ in the degradation of organic dyes under visible light," *Journal of Materials Research and Technology*, vol. 9, no. 6, pp. 15001–15015, 2020.
- [92] S. Ahmed, M. Oumezzine, and E.-K. Hlil, "Sol-gel synthesis of ferrites nanoparticles and investigation of their magnetic and photocatalytic activity for degradation of reactive blue 21 dye," *Journal of Molecular Structure*, vol. 1235, article 130262, 2021.
- [93] S. A. Al-Zahrani, A. Manikandan, K. Thanrasu et al., "Influence of Ce³⁺ on the structural, morphological, magnetic, photocatalytic and antibacterial properties of spinel MnFe₂O₄ nanocrystallites prepared by the combustion route," *Crystals*, vol. 12, no. 2, p. 268, 2022.
- [94] E. C. Paris, J. O. D. Malafatti, A. J. Moreira et al., "CuO nanoparticles decorated on hydroxyapatite/ferrite magnetic support: photocatalysis, cytotoxicity, and antimicrobial response," *Environmental Science and Pollution Research*, vol. 29, no. 27, pp. 41505–41519, 2022.
- [95] N. AbouSeada, M. Ahmed, and M. G. Elmahgary, "Synthesis and characterization of novel magnetic nanoparticles for photocatalytic degradation of indigo carmine dye," *Materials Science for Energy Technologies*, vol. 5, pp. 116–124, 2022.
- [96] A. Almahri, "The solid-state synthetic performance of bentonite stacked manganese ferrite nanoparticles: adsorption and photo-Fenton degradation of MB dye and antibacterial applications," *Journal of Materials Research and Technology*, vol. 17, pp. 2935–2949, 2022.
- [97] A. Selmi, H. Teymourinia, A. Zarei, M. Timoumi, and A. Ramazani, "CMCFO-Cr_{0.1} Nanoferrites: sol-gel synthesis, structural, and magnetic studies: applications for photo-degradation of Congo red dye," *Iranian Journal of Catalysis*, vol. 12, no. 1, pp. 97–106, 2022.
- [98] P. L. Hariani, M. Said, S. Salni, N. Aprianti, and Y. Naibaho, "High efficient photocatalytic degradation of methyl orange dye in an aqueous solution by CoFe₂O₄-SiO₂-TiO₂ magnetic catalyst," *Journal of Ecological Engineering*, vol. 23, no. 1, pp. 118–128, 2022.
- [99] T. Ajeesha, A. Manikandan, A. Anantharaman et al., "Structural investigation of Cu doped calcium ferrite (Ca_{1-x}Cu_xFe₂O₄; x=0, 0.2, 0.4, 0.6, 0.8, 1) nanomaterials prepared by co-precipitation method," *Journal of Materials Research and Technology*, vol. 18, pp. 705–719, 2022.
- [100] M. A. Tony and M. Eltabey, "End-of-life waste criteria: synthesis and utilization of Mn-Zn ferrite nanoparticles as a superparamagnetic photocatalyst for synergistic wastewater remediation," *Applied Water Science*, vol. 12, no. 2, pp. 1–17, 2022.
- [101] A. Hakimiyfard and S. Khademinia, "Hirshfeld surface analysis of solid-state synthesized NiFe₂O₄ nanocomposite and application of it for photocatalytic degradation of water pollutant dye," *International Journal of Nano Dimension*, vol. 13, no. 2, pp. 155–167, 2022.

Research Article

Green Catalytic Pyrolysis: An Eco-Friendly Route for the Production of Fuels and Chemicals by Blending Oil Industry Wastes and Waste Furniture Wood

M. D. Mohan Gift,¹ Savita Verma,² Kalapala Prasad,³ K. Kathiresan,⁴ Rohi Prasad,⁵ T. Logeswaran,⁶ Suresh Ghotekar,⁷ D. V. Thao,⁸ and J. Isaac JoshuaRamesh Lalvani ⁹

¹Department of Mechanical Engineering, Panimalar Engineering College, Chennai, 600123 Tamil Nadu, India

²Department of Applied Sciences, Galgotias College of Engineering and Technology, Greater Noida, 201306 Uttar Pradesh, India

³Department of Mechanical Engineering, University College of Engineering, Kakinada, Jawaharlal Nehru Technological University, Kakinada, Kakinada, 533003 Andhra Pradesh, India

⁴Department of Physics, PSNA College of Engineering and Technology, Dindigul, 624622 Tamil Nadu, India

⁵Department of Mechanical Engineering, Guru Gobind Singh Educational Society's Technical Campus, Chas, 827013 Jharkhand, India

⁶Department of Electrical and Electronics Engineering, Kongu Engineering College, Perundurai, Erode, 638060 Tamil Nadu, India

⁷Department of Chemistry, Smt. Devkiba Mohansinhji Chauhan College of Commerce and Science, University of Mumbai, Dadra and Nagar Haveli (UT), Silvassa 396230, India

⁸Technology and International Cooperation Department, Thai Nguyen University of Agriculture and Forestry, Thai Nguyen, Vietnam

⁹Faculty of Mechanical Engineering, Arba Minch Institute of Technology, Arba Minch University, P.O. Box 21, Arba Minch, Ethiopia

Correspondence should be addressed to J. Isaac JoshuaRamesh Lalvani; isaac.jrl@amu.edu.et

Received 13 July 2022; Revised 4 August 2022; Accepted 13 August 2022; Published 6 September 2022

Academic Editor: Pounsamy Maharaja

Copyright © 2022 M. D. Mohan Gift et al. This is an open access article distributed under the Creative Commons Attribution License, which permits unrestricted use, distribution, and reproduction in any medium, provided the original work is properly cited.

Lignocellulosic biomass is converted into liquid products through pyrolysis, which can be used as an alternative fuel for heating applications and industrial chemicals. Pyrolysis liquid is a mixture of many oxygenated fractions which deteriorates its burning properties. Through specific bond cleavage reactions like deoxygenation, cracking, and decarbonylation, catalysts in the pyrolysis process can be used to improve the quality of pyrolysis liquid. In this study, biochar produced by carbonization of printed circuit boards was used for catalytic reforming processes to produce energy-rich liquids and chemicals from a mixture of karanja seed oil cake and waste furniture wood. The catalytic process was performed by changing the reactor temperature from 300°C to 700°C at 50°C intervals. The results showed a maximum liquid oil recovery of 53.9 wt% at 500°C. Compared to the noncatalytic reaction, pyrolysis of biomass with biochar recovered 11.59% more liquid. This study demonstrated a viable technique to recover more liquid products and industrial chemicals by employing sustainable catalysts from e-waste. The physical analysis of the liquid showed that the liquid can be used as a fuel for boilers and furnaces. The chemical characterization through gas chromatography-mass spectroscopy (GC-MS) showed the presence of various chemical elements used for medicinal and industrial applications.

1. Introduction

Due to the reduction of fossil fuels, researchers have turned their attention to find possible alternate energy sources such

as wind, solar, and biomass, which have the ability to regenerate themselves. Every year, a huge amount of biomass is generated, which is not used properly. The improper handling of biomass is also causing environmental problems

[1]. A variety of methods can be used to transform waste biomass into more useful energy sources and chemicals. Biomass contributes 10% of the global total energy needs. The total energy potential of the biomass is estimated as 1.08×10^{11} tonnes of oil equivalent [2].

Enormous availability, renewability, CO₂ neutrality, and technical availability are the driving forces for the use of waste biomass materials for producing fuels and chemicals [3]. Heat applied to waste biomass materials under an inert atmosphere can trigger a variety of thermochemical processes. Char, condensable pyrolysis liquid, and noncondensable gases are the three types of products produced in these processes. The condensed pyrolysis liquid may be separated from an aqueous phase which contains the majority of lignin-derived compounds [4]. The feed, process, and its parameters influence the composition and yields of these products. Numerous conversion routes for biomass waste and feedstock have been investigated, and some are currently under growth. The two main categories of conversion processes are thermochemical and biological [5]. Among various conversion methods, pyrolysis is the ultimate one due to carbon neutrality and economic viability. Pyrolysis is inexpensive technology for the conversion of variety of feedstocks. It reduces the emission of greenhouse gases as well as wastes. This process also reduces the risk of waster pollutions. Compared to slow and intermediate pyrolysis, fast pyrolysis is the advanced one which gives more bio-oil yield (70 wt%) with reduced char formation [6]. The production of pyrolysis liquid is varied with respect to the method of pyrolysis and reaction parameters. The production of focused yield can be optimized experimentally by changing process variables. The liquid produced during pyrolysis may be utilized as a fuel or a chemical feedstock. [7]. Many literatures have produced pyrolysis liquid through the fast pyrolysis method and utilized it for various applications. Bridgwater et al. [8] produced bio-oil through a pyrolysis method and utilized it for heating boilers and furnaces. In addition to that, it can be used to operate engines to produce power. The use of pyrolysis liquid for engine operation has received favourable comments since it emits fewer greenhouse gases than fossil fuels [9].

India has around 250 species of plants and trees, which produce oil-bearing seeds. Every seed almost has 30 to 40% oil which is extracted by various processes. Oilseed cakes are the derivatives produced next to the extraction of oils from the seeds. Oil cakes are the potential biomass generally used as a feed for the poultry industry. Every year, a massive amount of deoiled cakes are produced. According to Mohanty et al. [10], 158.7 million tonnes of oil cakes were produced globally between 2020 and 2021, which was more than the production achieved between 2018 and 2019 [11]. The oil cakes are rich in protein and a perfect source for biochemical and thermochemical processes. A variety of oil cakes, especially edible oil cakes, have many advantages to being used as a feedstock for pyrolysis since they cannot be used as a feed material for animals [12]. Gerçel [13] conducted pyrolysis experiments using sunflower oil cake. The authors investigated the impact of sweep gas flow rate and temperature on pyrolysis yields. In this study, 48.69 wt% of

pyrolysis liquid was produced at 550°C with 53% of aliphatic and aromatic subfractions. The chemical elements appeared in the liquid are used as chemical feedstocks for fertilizers and food industries. Pütün et al. [14] carried out slow pyrolysis experiments on soybean cake. At 550°C, the study produced a maximum of 33.78 wt% pyrolysis liquid. In this study, column chromatography was used to characterize the produced pyrolysis liquid. The analysis showed that the pyrolysis liquid has similar properties to transportation fuel. The experiments were conducted at different pyrolysis temperatures and at different heating rates. The pyrolysis liquid in this study had a higher heating value of 36.79 MJ/kg. Karanja seed oil cake is the residue left after karanja seed is crushed for karanja oil. Karanja seed oil cake is widely used as an organic soil input. As part of the bioenergy mission initiative, India is working on the extensive planting of Karanja and Jatropha trees. In 2020, around 0.145 MT of karanja seed cake was produced. These seeds cannot be utilized as live feedstock directly because of their toxicity. Many authors have previously pyrolyzed karanja seeds to produce pyrolysis liquid char and gaseous products [15–17]. Nayan et al. [18] conducted pyrolysis experiment to produce higher energy pyrolysis liquid. The authors produced diesel closed pyrolysis liquid. The chemical analysis of the liquid showed the existence of alkanes, alkenes, ketones, and carboxylic acids which can be used a feed chemical for various industries. Singh et al. [19] conducted thermal cracking experiment on karanja seed oil cake to produce fuel for transportation. The study yielded 65.56 wt% of pyrolysis liquid under optimized process conditions. Due to lower heating value, the pyrolysis liquid was upgraded using a transesterification process and utilized for engine analysis.

Plywood and furniture industries have been growing fast for the last few years. The Indian market is increasing with an annual growth rate of 30%. Recycling waste furniture woods like plywood, particleboard, and medium-density fiberboard benefits the environment. It promotes environmental cleanliness and the preservation of trees. Waste furniture wood contains a variety of adhesives which are used during fabrication [20]. These additives are hazardous to human health when they are burning in the open air [21]. Moreover, furniture woods are covered with wax and paint to resist water and fire, which contains a variety of additives and binders. These woods cannot be used for direct energy recovery since the burning of these woods in an open atmosphere causes severe health issues for all living organisms [22, 23]. Thus, land filling and burning are unfavourable to the environment, a thermochemical pathway such as pyrolysis is considered as a possible way to dispose waste furniture wood [24]. Waste furniture woods are useful as feedstock in pyrolysis due to their higher lignocellulosic content [25]. Thirugnanam et al. [26] carried out a pyrolysis experiments on waste medium-density fiberboard (MDF) with the aim of finding an appropriate recycling method. The findings indicate that pyrolyzing MDF may provide fuels while avoiding the environmental difficulties. Foong et al. [27] utilized pyrolysis as a disposable and recovery method to convert waste furniture boards into valuable chemicals. According to FT-IR analysis, the pyrolysis liquid

produced at a temperature between 250–550°C has more volatile materials. The products obtained through pyrolysis had a higher concentration of phenols, which can be used as additives for various applications.

Catalytic pyrolysis is a potential option which produces more hydrocarbons with greater quality than the conventional route [28]. Dhanalakshmi et al. [29] utilized nanoHZSM-5 zeolite for maximum pyrolysis liquid yield from blended cotton shells and municipal plastic wastes. Compared to conventional pyrolysis, catalytic pyrolysis produced 4.21% more pyrolysis liquid. Use of an ecofriendly catalyst for pyrolysis has been under consideration for recent years. Valizadeh et al. [30] utilized eggshell-type Ni/Al₂O₃ for pyrolysis of food waste. This investigation indicated that the food waste can be disposed of safely using Ni/Al₂O₃ catalyst, which also serves as a clean, reliable source of energy. Kaliappan et al. [31] processed forestry wood through a waste eggshell-catalytic pyrolysis process. The authors produced 16.95% more pyrolysis liquid than a noncatalytic pyrolysis. In another study, Areeprasert and Khaobang [32] used ecofriendly biochar produced from printed circuit boards as a catalyst for liquid production from e-wastes. In the present investigation, mixed biomass wastes of karanja seed oil cake and waste furniture wood were pyrolyzed on a fluidized bed reactor at various temperatures ranging from 300°C to 700°C at 50°C intervals. From the collected literature survey, it can be known that there has been no work published on pyrolysis with the combination of karanja seed oil cake and waste furniture wood. For all the experiments, the particle size, heating rate, and sweep gas flow rate were maintained constant. The pyrolysis product yields were analyzed and characterized using various chromatographic techniques. The analysis was done with the aim of investigating its potential use for fuels and chemicals.

2. Materials and Methods

2.1. Materials. The karanja seed oil cake used for this study was supplied by M/s Srinivasa Oil Industries, Coimbatore, India. The seed oil cake has a particle size of 1 mm to 2 mm. The waste furniture wood was obtained from a local furniture manufacturing unit. The collected wood was initially in solid form with irregular shapes, which was cut into small pieces using a manual cutter. The cut wood materials were also converted into wood particles of a size between 1 mm and 2 mm. The samples were initially dried for 15 days and dried further in an oven for 2 hours before conducting pyrolysis experiments. The biochar catalyst used for this study was derived from printed circuit board. A traditional carbonization process was employed to prepare the biochar. The slow pyrolysis was conducted at 300°C with a longer residence time of 5 hours. For the production of char, a fixed bed reactor was employed. The temperature for the reactor was raised at the rate of 10°C/min.

2.2. Analysis Procedure. The analysis procedure consists of two stages, such as feedstock analysis and product analysis. Proximate and ultimate analyses (N2410650CHNS 2400 Elemental Analyzer) of the sample materials and liquid

samples were conducted by following ASTM standards. The liquid oil obtained through pyrolysis has a mixture of aqueous and organic phases. The aqueous phase from the organic phase was separated by centrifuging the pyrolysis liquid at 2000 rpm. The obtained organic phase was tested to find its physical and chemical nature. The basic physical properties of the liquid were found using a standard viscometer (Neminath Instruments, India), pH meter (Lutronmake, Sunshine Instruments, India), and Pensky-Martens closed-cup (EIE Instruments, India) apparatus. A gas chromatograph with a mass selective detector was used for the identification of different chemical compounds in the liquid sample. The NIST library of mass spectra was used for the identification of the substances in the liquid sample.

2.3. Reactor Facility. The fluidized bed reactor employed for this work has an internal diameter of 50 mm with 1 m height. The cylindrical reactor is fully surrounded by an insulating material. The reactor consists of a biomass feeding system, water cooled condenser, a char collection system, and a liquid collection system. The reactor can be connected with compressed air and nitrogen. Nitrogen is supplied during the pyrolysis experiment since it is inert. The cutoff valve is used to change air and nitrogen. Sand particles of an average size of 0.5 mm are used as a fluidization agent. Initially, air is admitted to get the material to fluidize. Then, the compressed air was cut to supply nitrogen. The nitrogen was admitted through the bottom of the reactor and fluidize along with the sand particles. The reactor is heated with the aid of an electrical heater and controlled with the help of an autotransformer. Once the temperature of the reactor reaches the desired temperature, the cut-out unit stops the current supply. Hence, the temperature of the reactor throughout the experiment was maintained constant. The temperature at five different points can be measured with the aid of thermocouples. An ammeter and voltmeter are used to give proper heat input. The whole setup is provided with an auto cut off unit which helps to keep the temperature constant for the particular run.

2.4. Experimental Procedure. The fast pyrolysis experiments were conducted by varying the temperature from 300°C to 700°C. The feedstocks for the experiments were prepared by blending oil cakes and waste furniture wood dust at 1:1 ratio. The biochar catalyst was also mixed with the raw material for the catalytic pyrolysis process. 20 grams of biochar was mixed with 100 grams of blended material. The nitrogen flow rate was set at 1.25 m³/hr for all experimental runs. The flow rate of the nitrogen is maintained more than the minimum fluidization velocity of 0.11 m³/hr. Once the reactor reaches the desired temperature, the screw feeder starts to feed the blended material along with the catalyst. The gaseous products released from the reactor were condensed to recover the liquid oil products. The condenser is provided with surplus ice water at the temperature of 5°C. Upon heating, the feed materials started to volatilize, and it is admitted through the condenser. The condensed liquid was collected and stored separately. The char products were collected from the reactor and cyclone separator. For every

TABLE 1: Feedstock characteristics.

Material	Proximate analysis (wt%)		Ultimate analysis (ash free basis in wt%)		Calorific value (MJ/kg)	
	Volatiles matter	Fixed carbon	Hydrogen	Nitrogen		Sulphur
Standard	ASTM D3175	ASTM D3173	ASTM D3174	ASTM D5373	ASTM D5373	ASTM D240
Karanja seed oil cake	75.3	13.1	5.30	48.52	—	18.34
Waste furniture wood	68.4	26.3	1.4	52.4	0.08	20.84

%of O = 100% - (C% + H% + N% + S%).

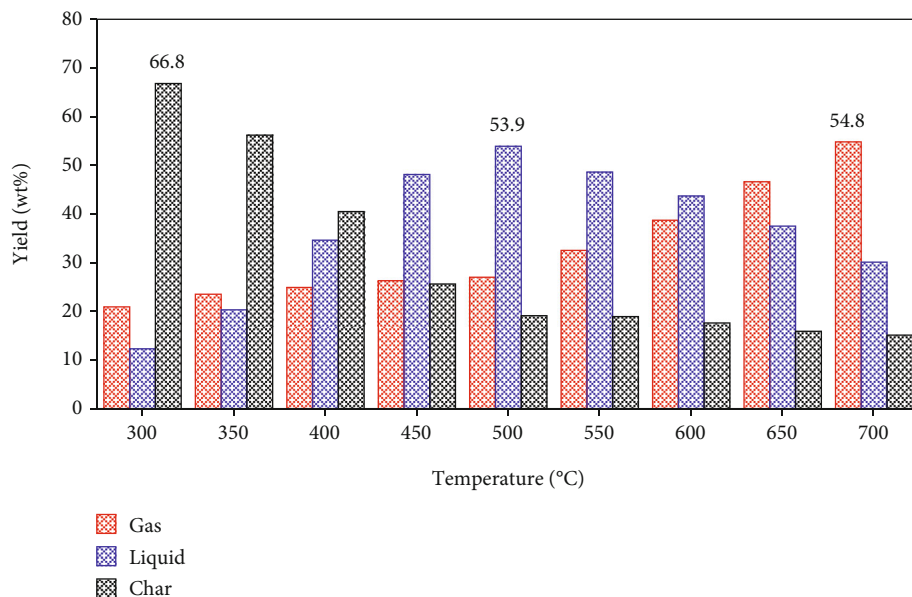


FIGURE 1: Product distribution at different pyrolysis temperature.

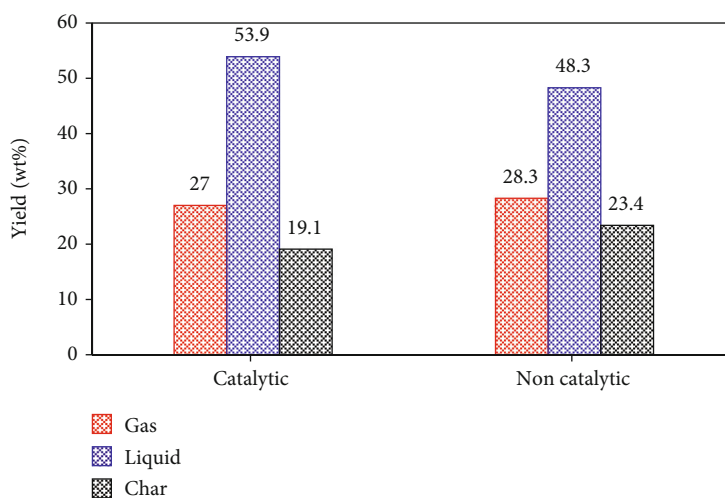


FIGURE 2: Catalytic and noncatalytic process yield.

run, the yield products were measured, and the effect of temperature on product yields was assessed. The mass of char and liquid products was found using a digital weighing machine and the weight of gaseous products was found by material balance. The liquid products obtained at the maximum yield point were collected and analyzed to determine their physical and chemical nature.

3. Results and Discussion

3.1. Feedstock Characterization. Table 1 shows the properties of the feedstock materials. From the table, it can be understood that both materials have a higher percentage of volatile materials, which gives a higher confidence to produce maximum liquid products during pyrolysis. Compared to waste furniture wood, karanja seed oil cake has a higher volatile

TABLE 2: Properties of the fuel.

Items	Pyrolysis liquid	Diesel [39]
Density (kg/m ³)	975	850
Viscosity (cSt)	4.0	3.9
Flash point (°C)	67	57
pH	1.4	0.1
Calorific value in MJ/kg	22.41	43.60

content (75.3 wt%). Higher volatile materials in the materials can be devolatilized easily [33]. The table also gives information about the heating value of the substance. The lower moisture content of both the substances is lower than 10 wt%, which is most suitable for the pyrolysis process [34]. Ash content is the other property that indicates the

TABLE 3: GC-MS analysis of the liquid.

RT/min	Compound	Molecular formula	% Area
2.34	2,3-Dihydro-benzofuran	C ₈ H ₈ O	0.41
2.95	2-Pyridone	C ₅ H ₅	1.92
4.02	3-Pyridinol, 2-Nitro-	C ₅ H ₄ N ₂ O ₃	2.11
5.22	3-Methoxy-1,2-benzenediol	C ₇ H ₈ O ₃	1.09
6.57	n-Methyloctadecanamide	C ₁₉ H ₃₉ NO	2.70
7.55	2-Isopropyl-2,5-dihydrofuran	C ₇ H ₁₂ O	2.04
7.94	Indole	C ₈ H ₇ N	2.11
8.30	Phenol, 2,6-dimethoxy	C ₈ H ₁₀ O ₃	6.94
8.58	Furfural	C ₅ H ₄ O ₂	0.79
9.01	Cyclohexanone	C ₆ H ₁₀ O	1.87
10.22	Ethanone, 1-(2-furanyl)-	C ₈ H ₁₀ O	0.74
11.05	Hydroquinone	C ₆ H ₆ O ₂	1.36
11.67	6,7-Benzo-phenothiazine-5,5-dioxide	C ₁₆ H ₁₁ NO ₂ S	9.03
11.93	Palmitamide	C ₁₆ H ₃₃ NO	4.10
14.37	Acetic acid, mercapto-, methyl ester	C ₃ H ₆ O ₂ S	3.60
14.55	Hexadecanenitrile	C ₁₆ H ₃₁ N	3.83
14.70	Acetone	C ₃ H ₆ O	2.18
14.98	2-Methyl-1-buten-3-yne	C ₅ H ₆	6.44
16.02	3-Furanmethanol	C ₅ H ₆ O ₂	3.13
17.55	Benzene, (1-methylethyl)-	C ₉ H ₁₂	0.91
18.32	Vanillin	C ₈ H ₈ O ₃	3.71
19.78	β -Alanine, N-(2-bromobenzoyl)-, pentyl ester	C ₁₅ H ₂₀ BrNO ₃	2.76
20.03	Phenol, 2-methyl-	CH ₃ C ₆ H ₄	1.45
20.37	2,4-Hexadiyne	C ₆ H ₆	3.70
20.97	Vinylsyringol	C ₁₀ H ₁₂ O	2.52
21.60	Pyridine	C ₅ H ₅ N	1.77
22.83	Oleic acid amide	C ₁₈ H ₃₅ NO	6.43
24.01	Erucylamide	C ₂₂ H ₄₃ NO	1.20
25.39	2,2'-Dioxospirilloxanthin	C ₄₂ H ₅₆ O ₄	0.84
26.08	Phenol, 2-methoxy	C ₇ H ₈ O ₂	1.48
27.91	2,6-Dimethylphenol	C ₈ H ₁₀ O	2.15
28.33	2,3,5-Trimethoxytoluene	C ₁₀ H ₁₄ O ₃	0.85
29.94	Methyl palmitate	C ₁₇ H ₃₄ O ₂	2.70
30.12	Dodecamethylcyclohexasiloxane	C ₁₂ H ₃₆ O ₆ Si ₆	4.55
30.57	<i>trans</i> -Propenylsyringol	C ₁₁ H ₁₄ O ₃	4.14

amount of inorganic waste that remains after combustion. According to the results of the previous studies, the value of ash in the feedstocks should be a minimum [35]. The ash content in waste furniture wood is very low (1.4 wt%) compared to karanja seed oil cake (5.3 wt%). The ash in the feedstock always restricts the production of pyrolysis biofuel and its quality. So, the ash in the feedstock is advised to be minimum. Both the materials have higher carbon content with reduced nitrogen and sulphur content. The lower nitrogen and sulphur are always recommended since they produce lower SO_x and NO_x during pyrolysis. The lower oxygen content compared to other biomass materials produces liquid products with a higher heating value.

3.2. Pyrolysis Product Yield. Figure 1 illustrates the yield of products at different reaction temperatures. For this analysis, the reactor was set at nine different temperatures. Until the reactor reaches 200°C, no liquid oil can be received. Around 250°C, a small amount of liquid oil was obtained. By increasing the temperature of the reactor, the yield of liquid collection is increased. At 200°C, the yield of liquid is very low compared to char and gas products. At this point, a maximum amount of char of 66.8 wt% was obtained. Generally, lower pyrolysis temperatures are favoured for the production of char products [36]. It was discovered that the largest amount of liquid yield (53.9 wt%) came from pyrolysis at 500°C and that increasing the pyrolysis temperature had an

unfavorable effect on the liquid yield. Beyond 500°C, the yield of liquid is decreased gradually with increasing gas fractions. At 500°C, the yield of gas was 27.0 wt% which was increased to 54.8 wt% at 700°C. At 700°C, the production of liquid was only 30.1 wt%. The char yield is continuously decreasing. At 300°C, the maximum of 66.8 wt% char was produced, and it reached 15.1 wt% at 700°C. Despite the fact that a single karanja seed oil cake and waste furniture wood component had a different spectrum of thermal breakdown, the oil cake and furniture wood mixture disintegrated in a significant overlapping step [36]. At lower temperatures, the heat transfer to the center core of the feedstock is very low, leading to incomplete decomposition. The low heat transfer to material increases the formation of char [37]. At higher temperatures, the resistance to heat transfer is very low, which helps to decompose the feedstocks. At higher temperatures, the gas yield was increased due to secondary cracking reactions [38]. Figure 2 displays the comparison between the products obtained through catalytic and noncatalytic process at optimized condition (500°C). Pyrolysis of karanja seed oil cake and waste furniture wood combination without biochar catalyst produced lower liquid yield. At optimized temperature, catalytic pyrolysis yielded 11.59% more liquid. The difference in liquid yield can be explained by the presence of high volatile biochar as a catalyst within the reactor which enhances the production of condensable volatiles [32]. The higher pyrolysis liquid during catalytic process represents the effects of synergistic effect. It is considered a beneficial effect during the reaction process.

3.3. Physical Characterization of the Liquid. Table 2 shows various physical properties of the liquid products collected from the catalytic process. The produced liquid oil is more dense and viscous compared to diesel fuel, which may impair the injection within in the engine. By blending the liquid products with commercial diesel, the density and viscosity can be reduced. The flash point is within a reasonable range. The liquid produced from pyrolysis has a heating value that is roughly 50% lower than that of diesel, which means it would not operate engines well. The reduced calorific value of the bio-oil represents the presence of higher oxygen molecules. The presence of oxygen in the pyrolysis liquid not only affects the calorific value but also corrodes the engine or furnace parts while it is used as a fuel.

3.4. Chemical Characterization of the Liquid. A GC-MS analysis was conducted to analyze the existence of various elements in the pyrolysis liquid. Table 3 shows the result of GC analysis. There are several different compounds, but they all have relatively low peak areas. The liquid products contain more than 40 elements, which gives the liquid oil a complex nature. The majority of the elements are used as a feedstock for various chemical and pharmaceutical industries. In the pyrolysis liquid, 6,7-benzo-phenothiazine-5,5-dioxide ($C_{16}H_{11}NO_2S$), oleic acid amide ($C_{18}H_{35}NO$), 2-methyl-1-buten-3-yne (C_5H_6), phenol and 2,6-dimethoxy ($C_8H_{10}O_3$), palmitamide ($C_{16}H_{33}NO$), dodecamethylcyclohexasiloxane ($C_{12}H_{36}O_6Si_6$), and *trans*-propenylsyringol ($C_{11}H_{14}O_3$) were identified as major elements with more

area percentage. From the identified chemical compounds, 2-pyridone is identified with an area percentage of 1.92. It is used as a solvent. Pyridone's tautomerization and use as a ditopic receptor are responsible for its significant impact on the reaction between activated esters and amines in non-polar solvents. *n*-Methyloctadecanamide is another element available with the liquid sample having a molecular weight of 297.5. Indole is an aromatic heterocyclic organic compound available in pyrolysis liquid which is used for many medicinal applications. Against tuberculosis, malaria, and diabetes, indoles and their derivatives can function effectively [40]. Phenol and 2,6-dimethoxy are major elements occupying a significant portion of the pyrolysis liquid. It is a member of phenol with a molecular weight of 134.1. It is a light brown solidified substance with a boiling point of 261°C. It is used as a flavouring agent for food. Another element, palmitamide, present in the pyrolysis liquid, is used as a lubricant and lubricant additive. Hexadecanenitrile showed an area percentage of 3.83, having a molecular weight of 237.4, which is used as an industrial intermediate. Oleic acid amide, which appeared in the liquid sample, is a colourless waxy solid. It is medicinally used for treating sleep disorders. It is used for a variety of industrial applications as a slip agent for lubricants and as a corrosion inhibitor.

4. Conclusion

This study conducted preliminary research on biomass catalytic pyrolysis in order to evaluate the effectiveness of green catalysts for hydrocarbons and chemicals production. A fast pyrolysis experiment on a fluidized bed reactor was carried out on the mixture of karanja seed oil cake and waste furniture wood at a reaction temperature ranging from 300°C to 700°C to determine the effect of temperature on pyrolysis product yield. In this study, the liquid collection was increased and char yield decreased with increased temperature. At higher pyrolysis temperatures, the production of gas was increased due to secondary cracking reactions. A maximum of 53.9 wt% of liquid was collected at 500°C. The catalytic process produced more liquid than the noncatalytic process due to the presence of high volatile biochar as a catalyst inside the reactor. The higher heating value of the pyrolysis liquid showed that the liquid can be used as a medium grade fuel for heating applications. The chemical characterization of the liquid showed the presence of various chemicals used for treating various ailments, additives for lubricants, and flavouring agents for food.

Data Availability

The data used to support the findings of this study are included within the article.

Conflicts of Interest

The authors declare that there is no conflict of interest regarding the publication of this article.






References

- [1] B. Koul, M. Yakoob, and M. P. Shah, "Agricultural waste management strategies for environmental sustainability," *Environmental Research*, vol. 206, article 112285, 2022.
- [2] T. Kan, V. Strezov, and T. J. Evans, "Lignocellulosic biomass pyrolysis: a review of product properties and effects of pyrolysis parameters," *Renewable and Sustainable Energy Reviews*, vol. 57, pp. 1126–1140, 2016.
- [3] C. S. Dhanalakshmi and P. Madhu, "Recycling of wood bark of *Azadirachta indica* for bio-oil and chemicals by flash pyrolysis," *Indian Journal of Ecology*, vol. 46, no. 2, pp. 347–353, 2019.
- [4] P. Madhu, L. Vidhya, S. Vinodha et al., "Co-pyrolysis of hardwood combined with industrial pressed oil cake and agricultural residues for enhanced bio-oil production," *Journal of Chemistry*, vol. 2022, Article ID 9884766, 12 pages, 2022.
- [5] P. Madhu, M. Sasireka, R. Samikannu et al., "Production and characterization of maximum liquid oil products through individual and copyrolysis of pressed neem oil cake and waste thermocol mixture," *Advances in Polymer Technology*, vol. 2022, Article ID 5258130, 11 pages, 2022.
- [6] F. Campuzano, R. C. Brown, and J. D. Martínez, "Auger reactors for pyrolysis of biomass and wastes," *Renewable and Sustainable Energy Reviews*, vol. 102, pp. 372–409, 2019.
- [7] B. M. Lakshmi, M. Mathew, A. M. J. Kinol et al., "An integrated CRITIC-TOPSIS-and entropy-TOPSIS-based informative weighting and ranking approach for evaluating green energy sources and its experimental analysis on pyrolysis," *Environmental Science and Pollution Research*, vol. 29, pp. 61370–61382, 2022.
- [8] A. V. Bridgwater, D. Meier, and D. Radlein, "An overview of fast pyrolysis of biomass," *Organic Geochemistry*, vol. 30, no. 12, pp. 1479–1493, 1999.
- [9] S. Vitolo, M. Seggiani, P. Frediani, G. Ambrosini, and L. Politi, "Catalytic upgrading of pyrolytic oils to fuel over different zeolites," *Fuel*, vol. 78, no. 10, pp. 1147–1159, 1999.
- [10] A. Mohanty, P. R. Rout, B. Dubey, S. S. Meena, P. Pal, and M. Goel, "A critical review on biogas production from edible and non-edible oil cakes," *Biomass Conversion and Biorefinery*, vol. 12, pp. 949–966, 2021.
- [11] Food and Agricultural Organization (FAO), "Food and Agricultural Organization (FAO)," 2020, <http://www.fao.org/economic/est/est-commodities/oilcrops/en/>.
- [12] S. Ramachandran, S. K. Singh, C. Larroche, C. R. Soccol, and A. Pandey, "Oil cakes and their biotechnological applications - a review," *Bioresource Technology*, vol. 98, no. 10, pp. 2000–2009, 2007.
- [13] H. F. Gerçel, "The production and evaluation of bio-oils from the pyrolysis of sunflower-oil cake," *Biomass and Bioenergy*, vol. 23, no. 4, pp. 307–314, 2002.
- [14] A. E. Pütün, E. Apaydin, and E. Pütün, "Bio-oil production from pyrolysis and steam pyrolysis of soybean-cake: product yields and composition," *Energy*, vol. 27, no. 7, pp. 703–713, 2002.
- [15] L. Zhu, H. Lei, Y. Zhang, X. Zhang, Q. Bu, and Y. Wei, "A review of biochar derived from pyrolysis and its application in biofuel production," *SF Journal of Material and Chemical Engineering*, vol. 1, no. 1, article 1007, 2018.
- [16] R. S. Chutia, R. Katakai, and T. Bhaskar, "Characterization of liquid and solid product from pyrolysis of *Pongamia glabra* deoiled cake," *Bioresource Technology*, vol. 165, pp. 336–342, 2014.
- [17] D. Kumar and K. K. Pant, "Production and characterization of biocrude and biochar obtained from non-edible de-oiled seed cakes hydrothermal conversion," *Journal of Analytical and Applied Pyrolysis*, vol. 115, pp. 77–86, 2015.
- [18] N. K. Nayan, S. Kumar, and R. K. Singh, "Characterization of the liquid product obtained by pyrolysis of karanja seed," *Bioresource Technology*, vol. 124, pp. 186–189, 2012.
- [19] C. S. Singh, N. Kumar, and R. Gautam, "Thermal cracking of Karanja de-oiled seed cake on pyrolysis reactor for producing bio-oil with focus on its application in diesel engine," *IOP Conference Series: Materials Science and Engineering*, vol. 804, no. 1, article 012014, 2020.
- [20] T. A. Khan, A. Gupta, S. S. Jamari et al., "Synthesis of micro carbonaceous material by pyrolysis of rubber wood and its effect on properties of urea-formaldehyde (UF) resin," *International Journal of Adhesion and Adhesives*, vol. 99, article 102589, 2020.
- [21] Z. Zhao, S. Sakai, D. Wu et al., "Further exploration of sucrose-citric acid adhesive: investigation of optimal hot-pressing conditions for plywood and curing behavior," *Polymers*, vol. 11, no. 12, p. 1996, 2019.
- [22] K. M. Rodgers, D. Bennett, R. Moran et al., "Do flame retardant concentrations change in dust after older upholstered furniture is replaced?," *Environment International*, vol. 153, article 106513, 2021.
- [23] S. Wi, J. H. Park, Y. U. Kim, and S. Kim, "Evaluation of environmental impact on the formaldehyde emission and flame-retardant performance of thermal insulation materials," *Journal of Hazardous Materials*, vol. 402, article 123463, 2021.
- [24] Y. D. Chen, F. Liu, N. Q. Ren, and S. H. Ho, "Revolutions in algal biochar for different applications: state-of-the-art techniques and future scenarios," *Chinese Chemical Letters*, vol. 31, no. 10, pp. 2591–2602, 2020.
- [25] A. Undri, M. Abou-Zaid, C. Briens et al., "Bio-oil from pyrolysis of wood pellets using a microwave multimode oven and different microwave absorbers," *Fuel*, vol. 153, pp. 464–482, 2015.
- [26] S. Thirugnanam, R. Srinivasan, K. Anand et al., "Utilization possibilities of waste medium-density fiberboard: a material recycling process," *Materials Today: Proceedings*, vol. 59, Part 2, pp. 1362–1366, 2021.
- [27] S. Y. Foong, R. K. Liew, C. L. Lee et al., "Strategic hazard mitigation of waste furniture boards via pyrolysis: pyrolysis behavior, mechanisms, and value-added products," *Journal of Hazardous Materials*, vol. 421, article 126774, 2022.
- [28] L. Zhang, Z. Bao, S. Xia, Q. Lu, and K. B. Walters, "Catalytic pyrolysis of biomass and polymer wastes," *Catalysts*, vol. 8, no. 12, article catal8120659, p. 659, 2018.
- [29] C. S. Dhanalakshmi, N. Ahalya, P. Vidhyalakshmi et al., "Individual and catalytic co-pyrolysis of agricultural outcomes and polymeric materials over nano-HZSM-5 zeolite: synergistic effects and yield analysis for heating applications," *Journal of Nanomaterials*, vol. 2022, Article ID 3743299, 11 pages, 2022.
- [30] S. Valizadeh, C. H. Ko, J. Lee et al., "Effect of eggshell- and homo-type Ni/Al₂O₃ catalysts on the pyrolysis of food waste under CO₂ atmosphere," *Journal of Environmental Management*, vol. 294, article 112959, 2021.
- [31] S. Kaliappan, M. Karthick, P. P. Patil et al., "Utilization of eco-friendly waste eggshell catalysts for enhancing liquid product

- yields through pyrolysis of forestry residues,” *Journal of Nanomaterials*, vol. 2022, Article ID 3445485, 10 pages, 2022.
- [32] C. Areeprasert and C. Khaobang, “Pyrolysis and catalytic reforming of ABS/PC and PCB using biochar and e-waste char as alternative green catalysts for oil and metal recovery,” *Fuel Processing Technology*, vol. 182, pp. 26–36, 2018.
- [33] A. K. Varma, L. S. Thakur, R. Shankar, and P. Mondal, “Pyrolysis of wood sawdust: effects of process parameters on products yield and characterization of products,” *Waste Management*, vol. 89, pp. 224–235, 2019.
- [34] M. Asadullah, M. A. Rahman, M. M. Ali et al., “Production of bio-oil from fixed bed pyrolysis of bagasse,” *Fuel*, vol. 86, no. 16, pp. 2514–2520, 2007.
- [35] P. McKendry, “Energy production from biomass (part 1): overview of biomass,” *Bioresource Technology*, vol. 83, no. 1, pp. 37–46, 2002.
- [36] B. Perret, K. Pawlowski, and B. Schartel, “Fire retardancy mechanisms of arylphosphates in polycarbonate (PC) and PC/acrylonitrile-butadiene-styrene,” *Journal of Thermal Analysis and Calorimetry*, vol. 97, no. 3, pp. 949–958, 2009.
- [37] I. Kathir, K. Haribabu, A. Kumar et al., “Utilization of tea industrial waste for low-grade energy recovery: optimization of liquid oil production and its characterization,” *Advances in Materials Science and Engineering*, vol. 2022, Article ID 7852046, 9 pages, 2022.
- [38] Y. K. Rao, C. S. Dhanalakshmi, D. K. Vairavel et al., “Investigation on forestry wood wastes: pyrolysis and thermal characteristics of *Ficus religiosa* for energy recovery system,” *Advances in Materials Science and Engineering*, vol. 2022, Article ID 3314606, 9 pages, 2022.
- [39] D. Raguraman, A. Kumar, S. Prasanna Raj Yadav et al., “Performance and emission characteristics of pyrolysis oil obtained from neem de oiled cake and waste polystyrene in a compression ignition engine,” *Advances in Materials Science and Engineering*, vol. 2021, Article ID 3728852, 10 pages, 2021.
- [40] D. Ramesh, A. Joji, B. G. Vijayakumar, A. Sethumadhavan, M. Mani, and T. Kannan, “Indole chalcones: Design, synthesis, *in vitro* and *in silico* evaluation against *Mycobacterium tuberculosis*,” *European Journal of Medicinal Chemistry*, vol. 198, article 112358, 2020.

Research Article

Enhancing the Production Yield of Jatropha and Pongamia Oil-Based Biodiesel by Introducing Nanocatalyst

Sathiesh Kumar Nagaraj ¹, Paranthaman Ponnusamy ¹, P. M. Gopal ¹,
Huu Tap Van ², Lan Huong Nguyen,³ and Sadib Bin Kabir ⁴

¹Department of Mechanical Engineering, Karpagam Academy of Higher Education, Coimbatore, India

²Faculty of Natural Resources and Environment, TNU-University of Sciences, Thai Nguyen City, Vietnam

³Faculty of Biology and Environment, Ho Chi Minh City University of Food Industry (HUFI), 140 Le Trong Tan Street Tay Thanh Ward, Tan Phu District, Ho Chi Minh City, Vietnam

⁴School of Engineering, Presidency University, Dhaka 1212, Bangladesh

Correspondence should be addressed to Sadib Bin Kabir; sadibb@pu.edu.bd

Received 20 June 2022; Revised 20 July 2022; Accepted 29 July 2022; Published 16 August 2022

Academic Editor: Balasubramani Ravindran

Copyright © 2022 Sathiesh Kumar Nagaraj et al. This is an open access article distributed under the Creative Commons Attribution License, which permits unrestricted use, distribution, and reproduction in any medium, provided the original work is properly cited.

Fossil fuel depletion, increasing demands of energy, and harmful emission production led to do research on biofuels. In this research, biodiesel is developed by blending of Jatropha and Pongamia oil with the help of magnetic stirrer-assisted transesterification process. Heterogeneous copper-doped titanium oxide catalyst was synthesized by wet impregnation method. The developed catalyst is characterized through XRD and HRTEM analyses and used to enrich the biodiesel yield and fuel properties, viz., viscosity, flashpoint, and fire point. The maximum yield of 90.2% is obtained with catalyst concentration of 3 wt%, reaction time of 3 hrs, temperature of 60°C, and methanol to oil molar ratio of 20:1.

1. Introduction

Worldwide depletion of fossil fuels, higher consumption of diesel, increasing environmental pollution, and higher usage of nonrenewable energy resources move the researchers towards sustainable development that promotes the significance of alternative fuel [1–3]. Among the alternative fuels, nonedible oils are preferred most owing to its economically low cost and its simplified processing. In India, nonedible oils such as Jatropha and Pongamia harvests are increased owing to its favorable climatic conditions and its potential to grow at water-scarce areas. Further, these oils are free from fatty acid content that makes them to be suitable for producing biofuel. Previous research augmented that biofuel extract from fat and vegetable oils has better cetane rating while compared with conventional fuel. Likewise, these biofuel consist of higher oxygen content that leads to better combustion [4–6]. The main drawback in biofuel extraction is poor yield from their raw substance. In general, transester-

ification process is normally adopted by the research for bio-fuel synthesis with the help of catalyst which might be base or acidic. Generation of more waste water and difficulties in catalyst separation from biodiesel are two major limitations in base catalyst [7, 8]. In order to overcome these limitations, heterogeneous catalyst is preferred by researchers since these are environmental friendly, easy for separation [9, 10], reusable, and noncorrosive [11, 12]. Metal oxide and carbon-based nanomaterials, viz., SiO₂, TiO₂, graphene, and MWCNT, have excellent properties such as stability, insolubility, and recyclability that can be used for development of biofuel. Likewise, higher surface area and lower particle size of nanocatalyst help to improvise the yield of biodiesel extraction [13–16]. Among the available catalyst, titanium dioxide- (TiO₂-) based catalyst has better capability to catalyze the esterification and transesterification process for biodiesel production, and it can be easily separated from the reaction mixture for further use. Titanium-based catalyst synthesis is economically feasible that increases the

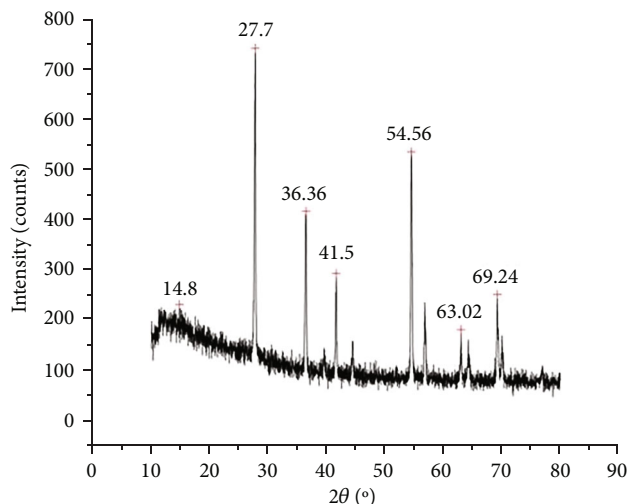


FIGURE 1: XRD of prepared catalyst.

possibility of low-cost biodiesel extraction [17–19]. Herein, research based on TiO_2 performance on biofuel depicts that doping or composting of metal oxide or metal nanoparticles improve the yielding performance of biofuel. Maximum yield of 90.5% was obtained when Pongamia oil is used as a feedstock biodiesel with nanocatalyst transesterification process under optimal condition of 3% catalyst loading (w/w), 12:1 methanol to oil molar ratio, and 60°C temperature [20]. For Jatropha oil with nanocatalyst, the maximum yield of biodiesel 93% was obtained with optimal parameters like time of 3 hrs, temperature of 57.5°C , catalyst concentration of 7 wt%, and methanol molar ratio of 1:10 [21], and for mixed vegetable oil, maximum yield of 76% biodiesel is obtained with help of prepared catalyst under the following condition of 240 min reaction time, 20:1 methanol to oil molar ratio, 80°C temperature, and catalyst concentration of 7 wt% [22–26].

Based on clear-cut literature survey, it can be noted that the yield of biodiesel production can be increased by maintaining optimum level of various parameters like time of reaction, temperature of reaction, methanol to oil molar ratio, and catalyst. Likewise, addition of nanocatalyst improve the yield of biodiesel. However, efficiency of doped nanocatalyst was rarely reported. Likewise, efficiency of nanocatalyst for dual-blended oil was not yet reported. Hence, in this research, an attempt has been to understand the effect of copper-doped TiO_2 as nanocatalysts on yielding efficiency on dual-blended Jatropha and Pongamia oils. Copper-doped TiO_2 nanoparticles were synthesized by wet impregnation method, and transesterification process was adopted to extract biodiesel from dual-blended oil, viz., Jatropha and Pongamia oils.

2. Materials and Method

Titanium dioxide (TiO_2) and cupric sulphate ($\text{CuSO}_4 \cdot 5\text{H}_2\text{O}$) were purchased from Merck in India with purity of 98%. Jatropha and Pongamia oils are purchased from Coimbatore local market, and it is used without any further purification.

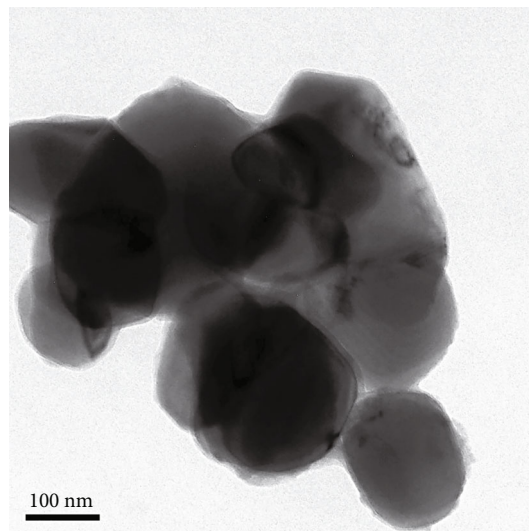


FIGURE 2: HRTEM of prepared catalyst.

Methanol (CH_3OH) with purity of 95% was supplied by Krishna Chemicals Limited, Tamil Nadu, India.

2.1. Synthesis of Cu-Doped TiO_2 . The Cu-doped TiO_2 nanomaterials were synthesized by using wet impregnation method [27]. Initially, the TiO_2 nanoparticles were mixed with calculated concentration of distilled water and added with 10 wt% of aqueous cupric sulphate solution, followed by stirring at 1250 rpm up to one hour with the help of hot plate coupled magnetic stirrer. The precursor was kept in hot air oven at 150°C to remove the water content. The dried concentrated powder was calcinated at 550°C for 5 hrs with furnace cooling.

2.2. Transesterification Process of Biodiesel. The reaction was carried in a 250 ml flat bottom flask, and the constant temperature of reaction was maintained keeping the flask under oil bath. The reaction setup is equipped with a magnetic stirrer (0 to 1500 rpm) with heater range of 0 to 100°C , coupled with condenser to reduce the vaporization of methanol during reaction, and a thermometer was utilized to measure the reaction temperature. Throughout, the experiment stirrer speed was maintained at 800 rpm. Jatropha and Pongamia oils were mixed at equal ratio for production of mixed oil biofuel. The reactor catalyst concentration (1, 3, 9, and 12% w/w), oil to methanol ratio (10:1, 15:1, 20:1, and 25:1), temperature (40, 50, 60, and 70°C), and reaction time (1, 2, 3, and 4 hrs) varied during the transesterification reaction. Finally, after the reaction, the biofuel was separated using separating funnel. The yield of biodiesel produced was calculated by the following equation.

$$\text{Yield of biodiesel (\%)} = \frac{\text{Weight of biodiesel produced}}{\text{Weight of oil}} \times 100. \quad (1)$$

TABLE 1: Properties of the biodiesel.

Catalyst	Density (kg/m ³)	Kinematic viscosity (m ² /s)	Flash point (°C)	Fire point (°C)	Diesel index	Cetane number
KOH	848	0.0212	61	68	34.22	34.28
CuTiO ₂	776	0.0114	65	71	47.16	44.91

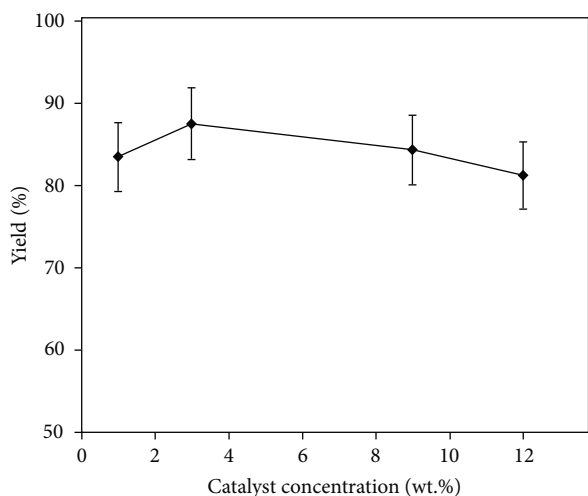


FIGURE 3: Variation of yield based on catalyst concentration.

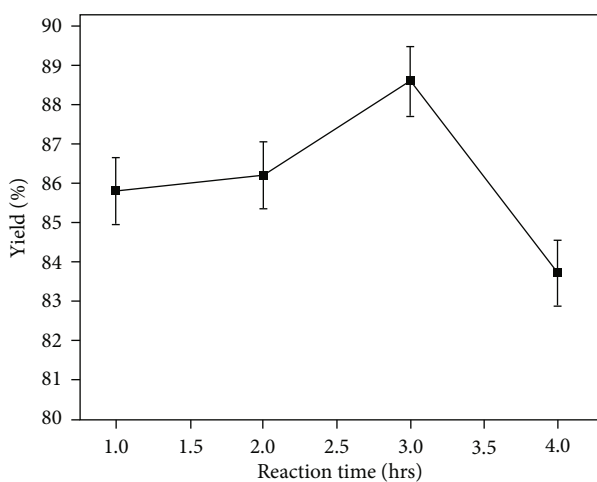


FIGURE 4: Variation of yield based on reaction time.

3. Results and Discussion

3.1. Characterization of Nanoparticles. Surface morphology and particle size of the CuTiO₂ nanoparticles were analyzed with the aid of HRTEM. Phase evaluation and particle confirmation of synthesized nanocatalyst were investigated by powder X-ray diffraction (XRD). The obtained XRD patterns of TiO₂-copper-added nanocatalyst confirm the hexagonal copper formation and tetragonal TiO₂. The attained patterns matched with JCPDS nos. 89-1397 and 89-6975. It represents that copper and TiO₂ were clearly mixed in the form of hexagonal and tetragonal crystallites of produced

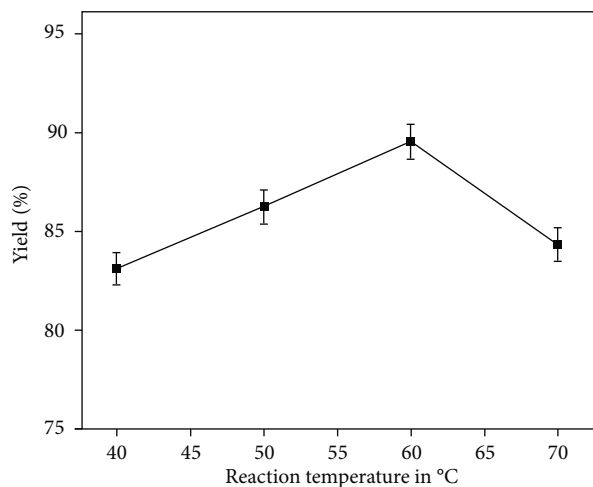


FIGURE 5: Variation of yield based on reaction temperature.

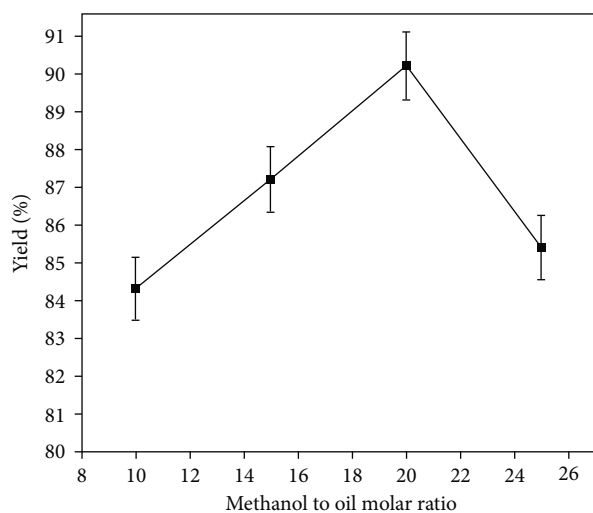


FIGURE 6: Variation of yield based on methanol to oil molar ratio.

nanoparticles. The attained XRD pattern and the obtained peaks are depicted in Figure 1.

High resolution transmission electron microscopy (HRTEM) is an imaging mode of the transmission electron microscope (TEM) that allows for direct imaging of the atomic structure of the sample. The prepared sample was analyzed using HRTEM, and the size of the nanomaterial was measured as ~100 nm as shown in Figure 2. The copper particles were adsorbed on the surface of titania, which is evident from the distinct coloration at the outer periphery.

The biodiesel properties such as viscosity and density are measured and compared with homogeneous (KOH) and heterogeneous (CuTiO₂) catalyst. When compared with both, the catalyst CuTiO₂ reduces the kinematic viscosity of biodiesel. Better surface area of catalyst leads to improvement in the quality of biodiesel yield and also influences band gap energy during transesterification; it enhances the catalytic activity. Other essential properties of biodiesel such as flash and fire point are evaluated and listed in Table 1.

TABLE 2: Comparative table for proposed research.

Sl no.	Oil	Catalyst	Yield (%)	Reference
1	Jatropha	ZnO–CaO	98.2	[41]
2	Neem oil	Cu doped ZnO	73.95	[42]
3	Waste cooking oil	Cu doped ZnO	97.71	[43]
4	Waste cooking oil	TiO ₂ /PrSO ₃ H	98.3	[44]
5	Jatropha and Pongamia oils	Cu@TiO ₂	90.2 (present work)	—

3.2. Effect of Nanocatalyst Concentration. The transesterification reactions of Jatropha and Pongamia mixed oil were performed with the help of CuTiO₂ nanocatalyst by varying its concentration from 1 to 12 (Figure 3). Herein, three parameters are maintained constant such as reaction time of 3 hrs, temperature of 60°C, and methanol to oil molar ratio of 15:1. From Figure 3, it can be identified that the higher yield percentage is attained at 3 wt% concentration of nanocatalyst. Further increase in the concentration of nanocatalyst results in the decrement in the yield of biodiesel. When the catalyst concentration is increased, interaction among the catalyst and methanol increases that promotes number of active sites up to 9 wt% [28, 29]. Further increase in mass ratio (10 wt%) decreases the biodiesel conversion yield percentage due to reactant high viscosity and high resistance of mass transfer [30, 31].

3.3. Effect of Reaction Time. The reaction period was an important parameter to study the behavior of transesterification biodiesel yield. The experiment time range was studied from 1 hr to 4 hrs where other three parameters catalyst concentration 3 wt%, temperature 60°C, and methanol to oil molar ratio 15:1 maintained as constant. Biodiesel production yield was increased up to 3 hrs at 88.6% after that yield reduces due to reduced activities of catalyst [32] as illustrated in Figure 4. During reaction after 3 hrs, high immiscibility occurs between Jatropha and Pongamia mixed oil with added methanol. So, the biodiesel yield was reduced after 3 hrs of reaction [33, 34]. In the liquid phases during reaction, immiscibility problem should be avoided by longer reaction time to enrich the biodiesel conversion rate [35, 36].

3.4. Effect of Reaction Temperature. Temperature of reaction was varied from 40°C to 70°C to find out the optimized value for higher biodiesel yield. Other parameters catalyst concentration 3 wt%, time 3 hrs, and methanol to oil molar ratio 15:1 maintained as constant. From Figure 5, it is noted that maximum yield was obtained up to 60°C, and it decreases due to various factors. Specifically, the transesterification reaction involved is endothermic, and however, increase in temperature lowers the viscosity of oil and it increases the rate of mass transfer thus improving the mixing properties [37]. One more important factor to be considered is vaporization of methanol that affects the yield during the transesterification process [38]. Optimal temperature of this condition was found to be 60°C.

3.5. Effect of Methanol to Oil Molar Ratio. The effect of methanol to oil molar ratio in CuTiO₂ involving reaction

was studied from 10:1 to 25:1, and the results are depicted in Figure 6. Other parameters maintained as catalyst concentration 3 wt%, time 3 hrs, and temperature 60°C. In this reaction, optimal methanol to oil molar ratio is 20:1, and at this condition, maximum yield obtained is 90.2%. Methanol addition to transesterification process is an important parameter because triglyceride is a reversible reaction which happens if sufficient methanol is not supplied. Appropriate ratio of methanol leads to forward direction of equilibrium to get the higher yield of biodiesel [39].

Higher volume content of methanol or molar ratio after 20:1 leads to decreases in the biodiesel yield due to methanol deactivation of the products, dilution of oil, and glycerol byproduct dissolving with excess content of methanol [40]. The comparison table for the proposed research is illustrated in Table 2.

Reusability of the synthesized nanocatalyst was measured after drying the catalyst that are collected from reaction mixture. At stage one, ~70% of biodiesel was produced, followed by ~61% on second stage; further, 52% of biodiesel yield was produced at the final stage. The residuals can be blended with diesel; this fact helps in decreasing usage of fossil full and promotes ecofriendly sustainable environment.

4. Conclusion

Biodiesel production with the help of transesterification reaction was investigated using heterogeneous nanocatalyst (CuTiO₂). The different parametric condition was carried out in this research from overall reaction; the maximum biodiesel yield obtained was 90.2%. The optimized time of reaction is 3 hrs, methanol to oil molar ratio is 20:1, temperature is 60°C, and 3 wt% of catalyst concentrations. Biodiesel physicochemical properties were also studied in order to identify particle confirmation of nanocatalyst. From the overall analysis, CuTiO₂ can be used as the heterogeneous nanocatalyst for biodiesel transesterification process when feedstock is vegetable oils. Usage of these biofuels helps in decreasing the usage of fossil fuels that promote ecofriendly environment.

Data Availability

Data are available upon request from the author.

Conflicts of Interest

The authors declare no conflict of interest.

References

- [1] S. K. Nagaraj, B. M. Nagarajan, and P. Ponnusamy, "Performance analysis of solar still with quartzite rock as a sensible storage medium," *Materials Today: Proceedings*, vol. 37, pp. 2214–2218, 2021.
- [2] S. K. Nagaraj, P. Ponnusamy, G. Pudhupalayam Muthukutti, and R. Ponnusamy, "Emission evaluation on 3-hole and 4-hole nozzle diesel engine with *Jatropha* and *Pongamia* (Karanja) mixed bio oil," *Sustainable Environment Research*, vol. 29, no. 1, pp. 1–7, 2019.
- [3] S. K. Nagaraj, P. Ponnusamy, and B. M. Nagarajan, "Evaluation of emission in a diesel engine with neem and *Pongamia* (Karanja) mixed bio oil using 3-hole and 4-hole nozzle," *Materials Today: Proceedings*, vol. 37, pp. 2010–2013, 2021.
- [4] W. Xie, Y. Han, and H. Wang, "Magnetic Fe₃O₄/MCM-41 composite-supported sodium silicate as heterogeneous catalysts for biodiesel production," *Renewable Energy*, vol. 125, pp. 675–681, 2018.
- [5] W. Xie and F. Wan, "Basic ionic liquid functionalized magnetically responsive Fe₃O₄@HKUST-1 composites used for biodiesel production," *Fuel*, vol. 220, pp. 248–256, 2018.
- [6] W. Xie and F. Wan, "Immobilization of polyoxometalate-based sulfonated ionic liquids on UiO-66-2COOH metal-organic frameworks for biodiesel production via one-pot transesterification-esterification of acidic vegetable oils," *Chemical Engineering Journal*, vol. 365, pp. 40–50, 2019.
- [7] W. Xie and H. Wang, "Grafting copolymerization of dual acidic ionic liquid on core-shell structured magnetic silica: a magnetically recyclable Bronsted acid catalyst for biodiesel production by one-pot transformation of low-quality oils," *Fuel*, vol. 283, p. 118893, 2021.
- [8] W. Xie and H. Wang, "Immobilized polymeric sulfonated ionic liquid on core-shell structured Fe₃O₄/SiO₂ composites: a magnetically recyclable catalyst for simultaneous transesterification and esterifications of low-cost oils to biodiesel," *Renewable Energy*, vol. 145, pp. 1709–1719, 2020.
- [9] A. De and S. S. Boxi, "Application of Cu impregnated TiO₂ as a heterogeneous nanocatalyst for the production of biodiesel from palm oil," *Fuel*, vol. 265, p. 117019, 2020.
- [10] A. Sharma, P. Kodgire, and S. S. Kachhwaha, "Investigation of ultrasound-assisted KOH and CaO catalyzed transesterification for biodiesel production from waste cotton-seed cooking oil: process optimization and conversion rate evaluation," *Journal of Cleaner Production*, vol. 259, p. 120982, 2020.
- [11] S. Mohebbi, M. Rostamizadeh, and D. Kahforoushan, "Effect of molybdenum promoter on performance of high silica MoO₃/B-ZSM-5 nanocatalyst in biodiesel production," *Fuel*, vol. 266, p. 117063, 2020.
- [12] E. F. de Medeiros, B. M. Vieira, C. M. P. de Pereira, W. C. Nadaleti, M. S. Quadro, and R. Andreazza, "Production of biodiesel using oil obtained from fish processing residue by conventional methods assisted by ultrasonic waves: heating and stirring," *Renewable Energy*, vol. 143, pp. 1357–1365, 2019.
- [13] B. Paramasivam, S. Kumanan, V. Kavimani, and M. Varatharajulu, "Fuzzy-based prediction of compression ignition engine distinctiveness powered by novel graphene oxide nanosheet additive diesel–Aegle marmelos pyrolysis oil ternary opus," *International Journal of Energy and Environmental Engineering*, vol. 13, no. 2, pp. 683–701, 2022.
- [14] S. Padmanabhan, K. Giridharan, B. Stalin et al., "Energy recovery of waste plastics into diesel fuel with ethanol and ethoxy ethyl acetate additives on circular economy strategy," *Scientific Reports*, vol. 12, no. 1, pp. 1–13, 2022.
- [15] V. Kavimani, K. Soorya Prakash, T. Thankachan, and R. Udayakumar, "Synergistic improvement of epoxy derived polymer composites reinforced with graphene oxide (GO) plus titanium di oxide (TiO₂)," *Composites. Part B, Engineering*, vol. 191, p. 107911, 2020.
- [16] A. G. Mohan Das Gandhi, K. Soorya Prakash, and V. Kavimani, "Effect of r-GO/TiO₂ hybrid composite as corrosion-protective coating on magnesium in Sulphur-based electrolyte," *Anti-Corrosion Methods Materials*, vol. 65, no. 4, pp. 375–382, 2018.
- [17] E. Davies, P. Deutz, and S. H. Zein, "Single-step extraction-esterification process to produce biodiesel from palm oil mill effluent (POME) using microwave heating: a circular economy approach to making use of a difficult waste product," *Biomass Conversion Biorefinery*, vol. 12, no. 7, pp. 2901–2911, 2022.
- [18] J. Emrani and A. Shahbazi, "A single biobased catalyst for bio-fuel and biodiesel," *Journal of Biotechnology & Biomaterials*, vol. 2, no. 1, pp. 1–7, 2012.
- [19] H. M. Khan, C. H. Ali, T. Iqbal et al., "Current scenario and potential of biodiesel production from waste cooking oil in Pakistan: an overview," *Chinese Journal of Chemical Engineering*, vol. 27, no. 10, pp. 2238–2250, 2019.
- [20] V. L. Gole and P. R. Gogate, "Intensification of synthesis of biodiesel from non-edible oil using sequential combination of microwave and ultrasound," *Fuel Processing Technology*, vol. 106, pp. 162–169, 2013.
- [21] J. Goli and O. Sahu, "Development of heterogeneous alkali catalyst from waste chicken eggshell for biodiesel production," *Renewable Energy*, vol. 128, pp. 142–154, 2018.
- [22] M. Li, Y. Zheng, Y. Chen, and X. Zhu, "Biodiesel production from waste cooking oil using a heterogeneous catalyst from pyrolyzed rice husk," *Bioresource Technology*, vol. 154, pp. 345–348, 2014.
- [23] S. S. Vieira, Z. M. Magriotis, I. Graça et al., "Production of biodiesel using HZSM-5 zeolites modified with citric acid and SO₄²⁻/La₂O₃," *Catalysis Today*, vol. 279, pp. 267–273, 2017.
- [24] L. di Bitonto and C. Pastore, "Metal hydrated-salts as efficient and reusable catalysts for pre-treating waste cooking oils and animal fats for an effective production of biodiesel," *Renewable Energy*, vol. 143, pp. 1193–1200, 2019.
- [25] F. Abnisa, W. M. A. W. Daud, and J. N. Sahu, "Optimization and characterization studies on bio-oil production from palm shell by pyrolysis using response surface methodology," *Biomass and Bioenergy*, vol. 35, no. 8, pp. 3604–3616, 2011.
- [26] K. Rajkumari and L. Rokhum, "A sustainable protocol for production of biodiesel by transesterification of soybean oil using banana trunk ash as a heterogeneous catalyst," *Biomass Conversion Biorefinery*, vol. 10, no. 4, pp. 839–848, 2020.
- [27] M. S. Gad and S. Jayaraj, "A comparative study on the effect of nano-additives on the performance and emissions of a diesel engine run on *Jatropha* biodiesel," *Fuel*, vol. 267, p. 117168, 2020.
- [28] Z. Zhang, M. D. Harrison, D. W. Rackemann, W. O. S. Doherty, and I. M. O'Hara, "Organosolv pretreatment of plant biomass for enhanced enzymatic saccharification," *Green Chemistry*, vol. 18, no. 2, pp. 360–381, 2016.

- [29] S. Gan, H. K. Ng, P. H. Chan, and F. L. Leong, "Heterogeneous free fatty acids esterification in waste cooking oil using ion-exchange resins," *Fuel Processing Technology*, vol. 102, pp. 67–72, 2012.
- [30] H. Wu, J. Zhang, Q. Wei, J. Zheng, and J. Zhang, "Transesterification of soybean oil to biodiesel using zeolite supported CaO as strong base catalysts," *Fuel Processing Technology*, vol. 109, pp. 13–18, 2013.
- [31] G. R. Moradi, S. Dehghani, and R. Ghanei, "Measurements of physical properties during transesterification of soybean oil to biodiesel for prediction of reaction progress," *Energy Conversion and Management*, vol. 61, pp. 67–70, 2012.
- [32] Y.-C. Chen, D.-Y. Lin, and B.-H. Chen, "Transesterification of acid soybean oil for biodiesel production using lithium metasilicate catalyst prepared from diatomite," *Journal of the Taiwan Institute of Chemical Engineers*, vol. 79, pp. 31–36, 2017.
- [33] M. R. Abukhadra and M. A. Sayed, " K^+ trapped kaolinite (Kaol/ K^+) as low cost and eco-friendly basic heterogeneous catalyst in the transesterification of commercial waste cooking oil into biodiesel," *Energy Conversion and Management*, vol. 177, pp. 468–476, 2018.
- [34] A. H. Chowdhury, S. Ghosh, and S. M. Islam, "Flower-like AgNPs@m-MgO as an excellent catalyst for CO_2 fixation and acylation reactions under ambient conditions," *New Journal of Chemistry*, vol. 42, no. 17, pp. 14194–14202, 2018.
- [35] A. M. Rabie, M. Shaban, M. R. Abukhadra, R. Hosny, S. A. Ahmed, and N. A. Negm, "Diatomite supported by CaO/MgO nanocomposite as heterogeneous catalyst for biodiesel production from waste cooking oil," *Journal of Molecular Liquids*, vol. 279, pp. 224–231, 2019.
- [36] P. B. Devaraja, D. N. Avadhani, S. C. Prashantha et al., "Synthesis, structural and luminescence studies of magnesium oxide nanopowder," *Spectrochimica Acta Part A: Molecular and Biomolecular Spectroscopy*, vol. 118, pp. 847–851, 2014.
- [37] R. Shan, C. Zhao, H. Yuan, S. Wang, and Y. Wang, "Transesterification of vegetable oil using stable natural diatomite-supported catalyst," *Energy Conversion and Management*, vol. 138, pp. 547–555, 2017.
- [38] D. Zeng, L. Yang, and T. Fang, "Process optimization, kinetic and thermodynamic studies on biodiesel production by supercritical methanol transesterification with CH_3ONa catalyst," *Fuel*, vol. 203, pp. 739–748, 2017.
- [39] D. M. Marinković, M. V. Stanković, A. V. Veličković et al., "Calcium oxide as a promising heterogeneous catalyst for biodiesel production: current state and perspectives," *Renewable and Sustainable Energy Reviews*, vol. 56, pp. 1387–1408, 2016.
- [40] H. A. Choudhury, S. Chakma, and V. S. Moholkar, "Mechanistic insight into sonochemical biodiesel synthesis using heterogeneous base catalyst," *Ultrasonics Sonochemistry*, vol. 21, no. 1, pp. 169–181, 2014.
- [41] G. Joshi, D. S. Rawat, B. Y. Lamba et al., "Transesterification of Jatropha and Karanja oils by using waste egg shell derived calcium based mixed metal oxides," *Energy Conversion and Management*, vol. 96, pp. 258–267, 2015.
- [42] B. Gurunathan and A. Ravi, "Biodiesel production from waste cooking oil using copper doped zinc oxide nanocomposite as heterogeneous catalyst," *Bioresource Technology*, vol. 188, pp. 124–127, 2015.
- [43] B. Gurunathan and A. Ravi, "Process optimization and kinetics of biodiesel production from neem oil using copper doped zinc oxide heterogeneous nanocatalyst," *Bioresource Technology*, vol. 190, pp. 424–428, 2015.
- [44] J. Gardy, A. Hassanpour, X. Lai, M. H. Ahmed, and M. Rehan, "Biodiesel production from used cooking oil using a novel surface functionalised TiO_2 nano-catalyst," *Applied Catalysis B: Environmental*, vol. 207, pp. 297–310, 2017.

Research Article

Properties Evaluation of Electroless Ni-Coated Low-Carbon Steels

**M. S. Senthil Saravanan,¹ V. Ananda,² S. P. Kumaresh Babu,² G. Ramalingam^{1,3},
A. Haiter Lenin^{1,4}, Jemal Mohammed Yimer^{1,4}, J. B. Sajin,¹ and Trijo Tharayil¹**

¹Department of Mechanical Engineering, Sree Buddha College of Engineering, Pattoor, Alappuzha, Kerala, India

²Department of Metallurgical and Materials Engineering, National Institute of Technology, Tiruchirappalli, India

³Department of Nanoscience and Technology, Science Campus, Alagappa University, Karaikudi, 630003 Tamil Nadu, India

⁴Department of Mechanical Engineering, WOLLO University, Kombolcha Institute of Technology, Kombolcha, Ethiopia Post Box No: 208

Correspondence should be addressed to Jemal Mohammed Yimer; jemalm@kiot.edu.et

Received 18 April 2022; Revised 19 May 2022; Accepted 19 July 2022; Published 8 August 2022

Academic Editor: Balasubramani Ravindran

Copyright © 2022 M. S. Senthil Saravanan et al. This is an open access article distributed under the Creative Commons Attribution License, which permits unrestricted use, distribution, and reproduction in any medium, provided the original work is properly cited.

Electroless deposition or chemical coating is a well-established industrial technique that is gaining popularity. The purpose of the current investigation was to determine how long a heat treatment process had on the mechanical and corrosion performances of a Ni-P coating on low-carbon steel. The coating is performed on the low-carbon steel using Ni-P salt bath. The coated samples were heat treated at 400°C under atmospheric condition using muffle furnace. The heat treatment offers greater corrosion resistance and mechanical qualities. The coated samples were analysed using scanning electron microscope for morphological studies and X-ray diffraction analysis for phase change during heat treatment. According to the experimental findings, a heat treatment prior to coating with Ni-P layer increases hardness and corrosion resistance while lowering friction.

1. Introduction

An autocatalytic chemical process called electroless nickel plating (EN) is used to deposit a coating of nickel-phosphorus or nickel-boron alloy on a solid work piece made of metal or plastic. The presence of a reducing agent, in which the metal ions react to deposit metal, is required for the process [1]. It is possible to create alloys with phosphorus percentages ranging from 2 to 5 (low phosphorus) to 11 to 14 (high phosphorus) [1]. The metallurgical properties of alloys are determined by the percentage of phosphorus present. This plating technique is used to protect against corrosion and wear. By suspending powder in the bath, composite coatings can also be created using EN methods [2]. There are several advantages to electroless nickel plating over electroplating. It offers a consistent deposit independent of the shape of the work piece and is free from flux density and power supply problems. With

the right preplate catalyst, it can even deposit on nonconductive surfaces. Electroless nickel is used as a barrier coating. Rather than galvanic or sacrificial action, it protects the underlying metal by sealing it off from the environment. Due to its passivity and amorphousness, electroless nickel has excellent corrosion resistance, which, in most situations, outperforms pure nickel or chromium alloys [3]. The coating is nearly impervious to alkalis, salt solutions and brines, chemical and petroleum conditions, and all kinds of hydrocarbons and solvents when it is correctly applied. Additionally resistant to reducing acids, organic acids, and ammonia solutions is the electroless deposit. They are only significantly affected by extremely oxidising environments, like strong nitric acid. The most important maintenance requirement for industry is the replacement and prevention of corrosion in industrial components. The cost of corrosion in the United States is estimated to be 70 billion dollars per year, or 4.2 percent of the gross national product. In India, the

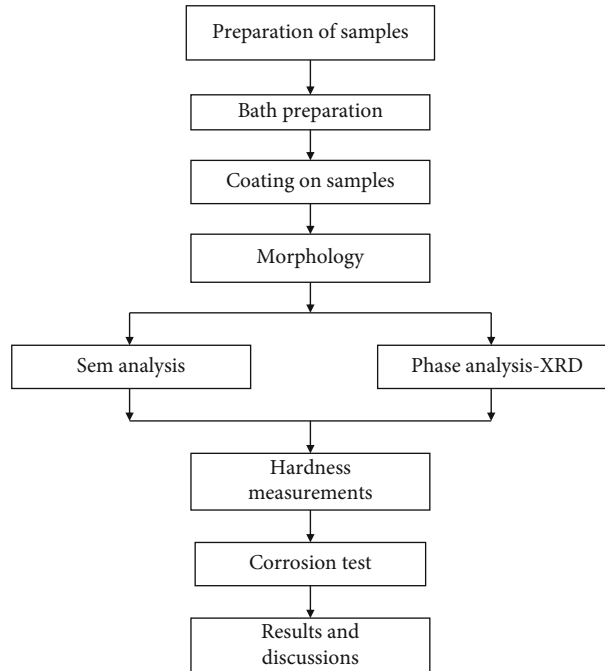


FIGURE 1: Flowchart for the experimental procedure.

annual GDP growth rate is only 4.5 percent. There are numerous methods and solutions available to prevent corrosion. To reduce corrosion, one method is to coat the metals with thin layers of less reactive metals or alloys. One of the processes that reduces corrosion is electroless nickel coating. Other, more expensive processes exist in addition to electroless nickel coating. This process is the least expensive when compared to others. Electroless deposition can be performed not only on pure metals but also on ferrous and nonferrous metals to improve surface properties. Electroless nickel coatings are well known for their unique set of properties [2]. In this paper, a cheap and economical coating technique called electroless nickel coating (EN) is used to coat low-carbon steel with Ni in this work. The coated samples are heat treated to change their state from amorphous to crystalline. The samples' corrosion resistance was compared to the impact of coating and heat treatment.

2. Experimental Procedure

The current experiment was carried out using a low-carbon steel sample. For the current work, a low-carbon steel cylindrical rod (diameter 1 cm) cut into small pieces 5 mm thick was used as the working substrate. The specimens were ground to remove corrosion and polished to achieve a smooth surface. Emery sheets were used to polish the surface to eliminate the scratches, which was then reduced in acetone, cleaned with distilled water, and dried in the absence of moisture. The specimens were then ultrasonically cleaned in deionized water. Prior to plating, all specimens were etched for three minutes in a sulfuric acid solution and then cleaned with deionized water and acetone before being weighed. Electroless nickel coating bath contains 20 g nickel

chloride, 24 g sodium hypophosphite, 40 g sodium citrate, and 25 g ammonium chloride per litre. The bath was maintained at a pH of 8 and a temperature of 363 degrees Celsius. The samples were washed in KOH at 333 K for 15 minutes prior to coating and then rinsed in distilled water. They were then rinsed one more in distilled water after spending a minute in an HCl bath. The deposition time was 2 hours, and a 70 percent KOH solution was intermittently supplied to keep the pH stable and make up for the water loss brought on by the baths [4]. The samples are classified as base metal, coated, and heat treated in a muffle furnace at 400 degrees Celsius for one hour. The heat treatment temperature is chosen based on the literature survey [5, 6]. At 400°C, the hardness of the sample gets peak value due to the transition of amorphous phase into crystalline phase of the Ni-P coating and the formation of Ni₃P precipitate which further improves the corrosion resistance. Following the coating and heat treatment, XRD is used to investigate the composition of coated samples and phase changes [7–9]. The hardness of the specimens was determined using a Vickers hardness tester with a load of 100 g and a time of 10 seconds. Finally, the electrochemical corrosion test was performed using an electrochemical corrosion tester equipped with a polarisation cell that includes an electrolyte solution (3.5 percent NaCl solution), to gauge the rate of corrosion of the samples, and a specimen holder was linked to a reference electrode, counter electrode(s), and the relevant metal sample [10, 11]. The flowchart in Figure 1 explains the details of the experiments.

3. Results and Discussion

3.1. Morphology. Figure 2 shows the SEM surface morphology of the low-carbon steel substrate, coated sample, and

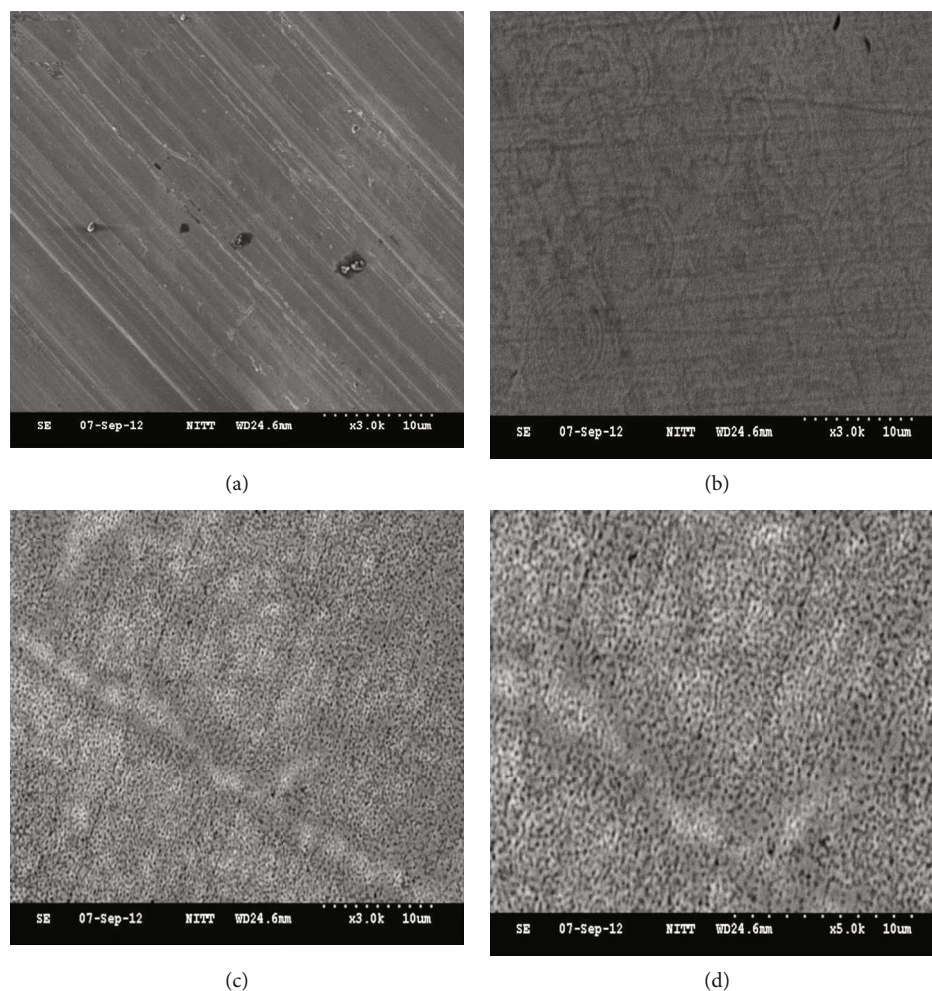


FIGURE 2: (a) Base metal, (b) coated sample, and (c and d) heat treated about 400°C/1 hour.

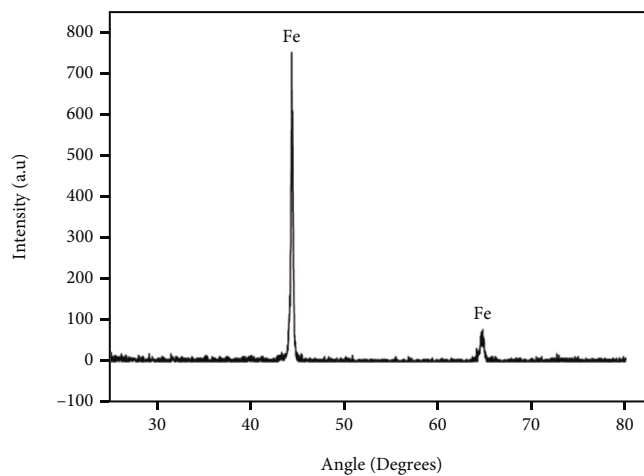
heat-treated sample. The base sample or low-carbon steel shows a clear surface, and minor particles were seen. The surface roughness of the coated sample and heat-treated samples is increased. The electroless Ni-P layers have a characteristic spherical nodular shape and are compact and homogeneous [12]. On the coated surface, there are no evident imperfections or holes, but the heat treatment changes their size and distribution. The formation of phosphides can be viewed in Figures 2(c) and 2(d) which is a heat-treated sample. Due to cracks developing in the coating as a result of heat treatment, it also affects how resistant the coating is to corrosion. The base substrate that does not undergo heat treatment is the smoothest, and remaining are rough ones. The surface roughness of the sample consistently increases which is evident in the SEM morphology.

3.2. XRD Analysis. Figure 3 shows the XRD analysis of base metal, as-deposited, and heat-treated samples. Figure 3(a) depicts the XRD patterns of a base metal containing Fe phases. Figure 3(b) shows the changes in phase after coating the sample. Because of the phosphorous content, the coated sample contains Ni and Ni₃P phases. Because of its amorphous structure, the coating is classified as high phosphorous. The crystal-

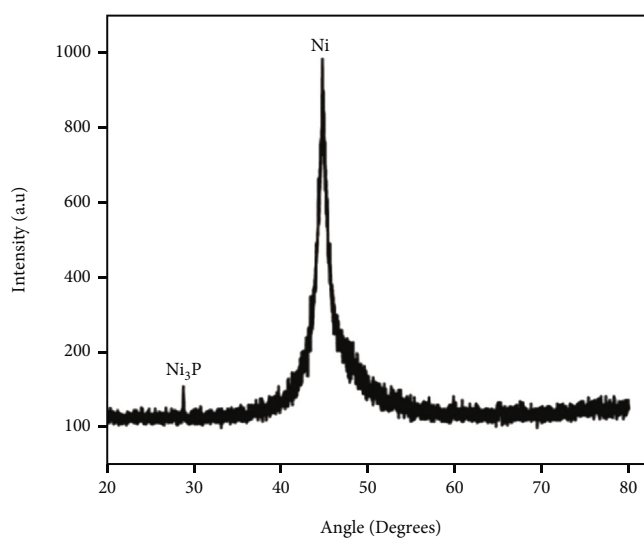
line structure of Ni-P alloy became amorphous as the phosphorus content in the metal matrix increased. The wide peak seen in the AD coating's XRD pattern at 44.5° is the same as the nickel FCC (111) diffraction peak. Due to the fine crystallite size and/or microstrain present in the coatings, XRD peak widening may be attributed [13, 14].

In Figures 3(c) and 3(d), the XRD patterns of heat-treated samples are displayed. The heat-treated samples have two peaks, one each for Ni and Ni₃P. Higher intensity and narrower peak widths suggest that the heat-treated coatings on low-carbon steel have higher levels of crystallinity and larger crystallite sizes. During the heat treatment process, all samples pass through an intermediate metastable phase [15].

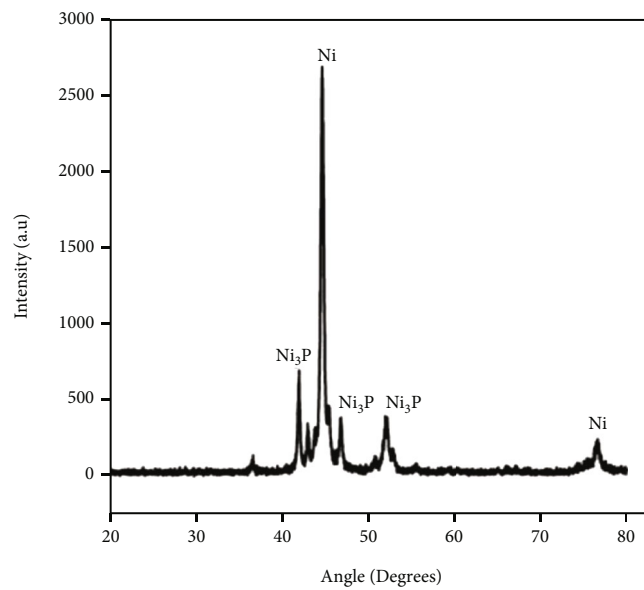
3.3. Hardness. With a 10 gf applied for 10 seconds, the hardness of the coatings and interface was assessed using a micro-Vickers hardness tester. The base metals shows a hardness of 214 HV, whereas the coated samples and heat-treated samples show high hardness values in Table 1. The increment in the hardness of the coated sample is attributed to the presence of phosphorous. The heat-treated samples shows more improved hardness value. During heat treatment, the coatings become crystalline due to the



(a)



(b)



(c)

FIGURE 3: Continued.

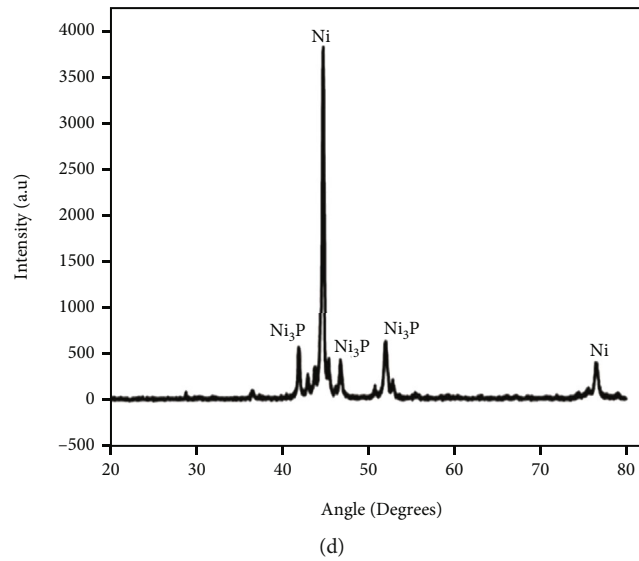


FIGURE 3: (a) XRD patterns of base metal (b), coated sample, and (c and d) heat-treated samples.

TABLE 1: Hardness values of the samples.

Sl no.	Samples	Hardness values (HV _{0.1})
1	Base metal	214 ± 10
2	Coated sample	482 ± 10
3	Heat-treated sample 1	936 ± 10
4	Heat-treated sample 2	948 ± 10

TABLE 2: Corrosion results.

Si no.	Samples	E_{corr} (mV)	I_{corr} (mA/cm ²)	Corrosion rate (mpy)
1	Base metal	630.84	0.080372	0.03
2	Coated sample	52	0.0003984	0.00019
3	Heat-treated sample 1	300.94	0.0040372	0.0019
4	Heat-treated sample 2	300.94	0.0040372	0.0019

arrangement of rearrangement of atoms [16, 17]. Heat treatment leads to the formation of hard body-centered tetragonal Ni₃P precipitate which attributed to the high hardness value. The formation of the Ni₃P precipitates was confirmed in XRD results [18].

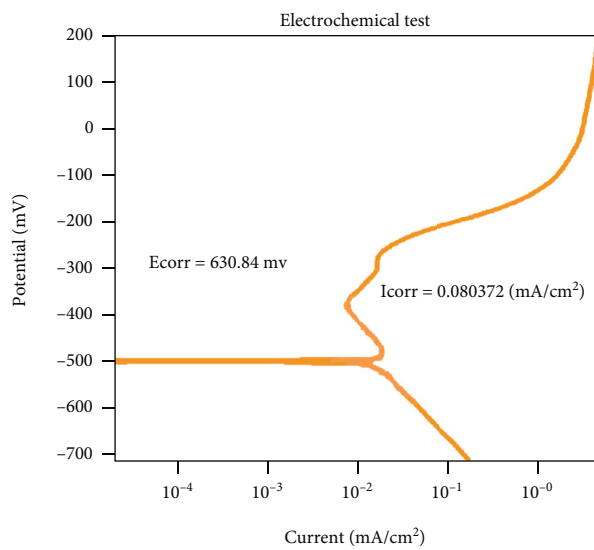
3.4. Corrosion Results. The corrosion results of all specimens are shown in Table 2. The corrosion rate for the all the specimens was calculated by the formula below.

$$\text{Corrosion rate} = \frac{0.13EWI_{corr}}{d} \text{ mpy}, \quad (1)$$

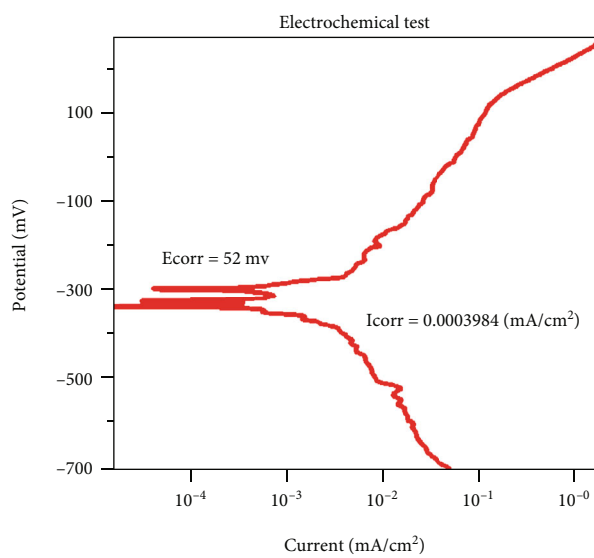
where I_{corr} is the corrosion current in amps, EW is the equivalent weight of corroded sample, and d is the density of the corroded sample in g/cm³.

The results in Figure 4 show that the coated sample has very good corrosion resistance due to its amorphous nature. Phosphorus stimulates anodic and cathodic reactions during the corrosion process, which increases the anodic dissolution of nickel. It also increases the corrosion potential and decreases the corrosion current. Accelerated nickel corrosion creates the conditions for concentrating phosphorous and, as a result, the surface-level synthesis of stable intermediate molecules with the formula Ni₃P, which serve as a passive barrier film. The literature publi-

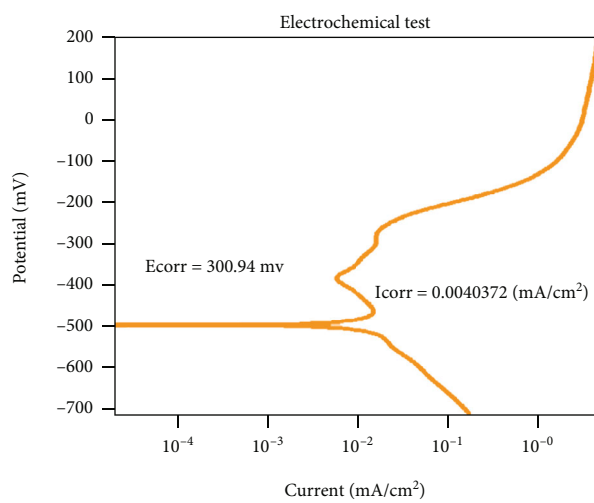
cations on Ni-P coatings claim that preferential nickel dissolution leads to phosphorus enrichment on the surface layer. When this enhanced phosphorous combines with water, a layer of adsorbed hypophosphite anions is created (H₂PO₂). The development of either soluble Ni²⁺ species or a passive nickel film is assumed to begin with the hydration of nickel, which is prevented by this layer by blocking the flow of water to the electrode surface. As a result, phosphorus enrichment on the electrode surface is what gives electroless Ni-P coatings their higher corrosion resistance. However, the corrosion resistance of heat-treated samples is reduced [3]. Because when the samples were heated, the electroless nickel began to crystallise and lose its amorphous nature. At higher temperatures, the particles congregate, forming a matrix of Ni₃P-forming active corrosion cells. As nickel phosphides particles form within the coating, the remaining material's phosphorous content drops. This decreases its passivity while increasing its corrosion. The particles also form small active/passive corrosion cells, which contribute to the deposit's demise [19, 20]. Heat treatment causes the deposit to shrink as it hardens, resulting in cracks through the coating that can expose the substrate to attack. The consequence is a reduction in the corrosion resistance of heat-treated samples. When nickel phosphide particles form in the coating,



(a)



(b)



(c)

FIGURE 4: Continued.

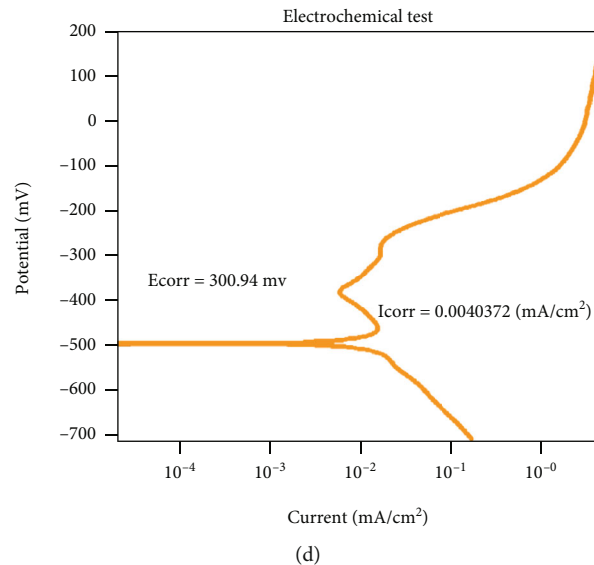


FIGURE 4: (a) Corrosion graph of base metal, (b) coated sample, and (c and d) heat-treated samples.

the phosphorous content of the remaining material decreases. The decrease in phosphorous passivity will increase the corrosion rate [21, 22].

3.5. Conclusion

- (i) Electroless deposition technique was used to successfully deposit nickel-phosphorus coatings on low-carbon steel substrates. The coated samples were then heated at 400°C for one hour
- (ii) According to the XRD examination, heat treatment of Ni-P composite coatings caused the amorphous Ni phase to crystallise and the Ni₃P phase to precipitate
- (iii) The microstructure of deposited phosphorous shows amorphous character, whereas the heat-treated samples shows high crystalline nature
- (iv) The heat-treated samples show high hardness values than the as-deposited coatings. This is due to the formation of Ni₃P precipitates

Data Availability

There are no relevant data to be made available.

Conflicts of Interest

The authors declare no conflict of interest.

References

- [1] W. Riedel, *Electroless Nickel Plating*, Finishing Publications Ltd., 1991.
- [2] G. O. Mallory and J. B. Hajdu, *Electroless Plating: Fundamentals and Applications*, William Andrew, 1990.
- [3] F. Delaunois and P. Lienard, "Heat treatments for electroless nickel-boron plating on aluminium alloys," *Surface and Coatings Technology*, vol. 160, no. 2-3, pp. 239–248, 2002.
- [4] F. Delaunois, J. P. Petitjean, P. Lienard, and M. Jacob-Duliere, "Autocatalytic electroless nickel-boron plating on light alloys," *Surface and Coatings Technology*, vol. 124, no. 2-3, pp. 201–209, 2000.
- [5] C. A. León-Patiño, J. García-Guerra, and E. A. Aguilar-Reyes, "Tribological characterization of heat-treated Ni-P and Ni-P-Al₂O₃ composite coatings by reciprocating sliding tests," *Wear*, vol. 426-427, pp. 330–340, 2019.
- [6] S. Chockalingam, U. Natarajan, M. Selvam, and A. G. Cyril, "Investigation on machinability and damping properties of nickel-phosphorus coated boring bar," *Arabian Journal for Science and Engineering*, vol. 41, no. 2, pp. 669–676, 2016.
- [7] A. Chiba, H. Haijima, and K. Kobayashi, "Effect of sonication and vibration on the electroless Ni-B deposited film from acid bath," *Surface and Coatings Technology*, vol. 169-170, pp. 104–107, 2003.
- [8] J. N. Balaraju, T. S. N. Sankara Narayanan, and S. K. Seshadri, "Electroless Ni-P composite coatings," *Journal of Applied Electrochemistry*, vol. 33, no. 9, pp. 807–816, 2003.
- [9] J. N. Balaraju, P. Radhakrishnan, V. Ezhilselvi, A. A. Kumar, Z. Chen, and K. P. Surendran, "Studies on electroless nickel polyalloy coatings over carbon fibers/CFRP composites," *Surface and Coatings Technology*, vol. 302, pp. 389–397, 2016.
- [10] N. S. Sangaj and V. C. Malshe, "Permeability of polymers in protective organic coatings," *Progress in Organic Coatings*, vol. 50, no. 1, pp. 28–39, 2004.
- [11] R. C. Agarwala and V. Agarwala, "Electroless alloy/composite coatings: a review," *Sadhana*, vol. 28, no. 3-4, pp. 475–493, 2003.
- [12] E. S. Puchi, M. H. Staia, H. Hintermann, A. Pertuz, and J. Chitty, "Influence of Ni-P electroless coating on the fatigue behavior of plain carbon steels," *Thin Solid Films*, vol. 290-291, pp. 370–375, 1996.
- [13] P. Sahoo and S. K. Das, "Tribology of electroless nickel coatings - a review," *Materials & Design*, vol. 32, no. 4, pp. 1760–1775, 2011.

- [14] M. H. Staia, E. J. Castillo, E. S. Puchi, B. Lewis, and H. E. Hintermann, "Wear performance and mechanism of electroless Ni-P coating," *Surface and Coatings Technology*, vol. 86-87, pp. 598–602, 1996.
- [15] S. M. Monir Vaghefi and K. Zangeneh-Madara, "The effect of thermochemical treatment on the structure and hardness of electroless Ni-P coated low alloy steel," *Surface and Coatings Technology*, vol. 182, no. 1, pp. 65–71, 2004.
- [16] C. J. Wang and C. C. Li, "Corrosion behaviors of AISI 1025 steels with electroless nickel/aluminized coatings in NaCl-induced hot corrosion," *Surface and Coatings Technology*, vol. 177-178, pp. 37–43, 2004.
- [17] S. Balaji, P. Maniarasan, S. V. Alagarsamy et al., "Optimization and Prediction of Tribological Behaviour of Al-Fe-Si Alloy-Based Nanograin-Refined Composites Using Taguchi with Response Surface Methodology," *Journal of Nanomaterials*, vol. 2022, 2022.
- [18] K. Parker, "Effects of heat treatment on the properties of electroless nickel deposits," *Plating and Surface Finishing*, vol. 68, no. 12, pp. 71–77, 1981.
- [19] B. R. Forman, H. L. Gilles, and M. Faul, "Thermally induced bond failure of electroless nickel/IVD aluminum coatings deposited on steel," *Surface and Coatings Technology*, vol. 123, no. 2-3, pp. 106–111, 2000.
- [20] A. R. Di Giampaolo, J. G. Ordonez, J. M. Gugliemacci, and J. Lira, "Electroless nickel-boron coatings on metal carbides," *Surface and Coatings Technology*, vol. 89, no. 1-2, pp. 127–131, 1997.
- [21] A. H. Graham, R. W. Lindsay, and H. J. Read, "The structure and mechanical properties of electroless nickel," *Journal of the Electrochemical Society*, vol. 112, no. 4, p. 401, 1965.
- [22] S. N. Jenq, H. W. Yang, Y. Y. Wang, and C. C. Wan, "Discharge performance of Ti_{0.35}Zr_{0.65}Ni_{1.2}V_{0.6}Mn_{0.2} alloy electrode modified by electroless nickel plating," *Materials Chemistry and Physics*, vol. 48, no. 1, pp. 10–16, 1997.

Retraction

Retracted: Copper Oxide Nanoparticles Incorporated in the Metal Mesh Used to Enhance the Heat Transfer Performance of the Catalytic Converter and to Reduce Emission

Journal of Nanomaterials

Received 20 June 2023; Accepted 20 June 2023; Published 21 June 2023

Copyright © 2023 Journal of Nanomaterials. This is an open access article distributed under the Creative Commons Attribution License, which permits unrestricted use, distribution, and reproduction in any medium, provided the original work is properly cited.

This article has been retracted by Hindawi following an investigation undertaken by the publisher [1]. This investigation has uncovered evidence of one or more of the following indicators of systematic manipulation of the publication process:

1. Discrepancies in scope
2. Discrepancies in the description of the research reported
3. Discrepancies between the availability of data and the research described
4. Inappropriate citations
5. Incoherent, meaningless and/or irrelevant content included in the article
6. Peer-review manipulation

The presence of these indicators undermines our confidence in the integrity of the article's content and we cannot, therefore, vouch for its reliability. Please note that this notice is intended solely to alert readers that the content of this article is unreliable. We have not investigated whether authors were aware of or involved in the systematic manipulation of the publication process.

Wiley and Hindawi regrets that the usual quality checks did not identify these issues before publication and have since put additional measures in place to safeguard research integrity.

We wish to credit our own Research Integrity and Research Publishing teams and anonymous and named external researchers and research integrity experts for contributing to this investigation.

The corresponding author, as the representative of all authors, has been given the opportunity to register their agreement or disagreement to this retraction. We have kept a record of any response received.

References

- [1] M. Prabhakar, S. Prakash, M. Saravana Kumar et al., "Copper Oxide Nanoparticles Incorporated in the Metal Mesh Used to Enhance the Heat Transfer Performance of the Catalytic Converter and to Reduce Emission," *Journal of Nanomaterials*, vol. 2022, Article ID 9169713, 9 pages, 2022.

Research Article

Copper Oxide Nanoparticles Incorporated in the Metal Mesh Used to Enhance the Heat Transfer Performance of the Catalytic Converter and to Reduce Emission

M. Prabhakar¹, **S. Prakash**¹, **M. Saravana Kumar**¹, **S. Sendilvelan**², **M. V. Sreerag**¹, **B. S. Akhil Vishnu**¹, **Asif Samad**¹, **B. Jansi Rani**³, **Haider Lenin Allasi**⁴, **Adisu Haile**⁴, and **Praveen Kumar Issac**⁵

¹Department of Mechanical Engineering, Aarupadai Veedu Institute of Technology, Vinayaka Mission Research Foundation, Tamil Nadu 603 104, India

²Department of Mechanical Engineering, Dr. M.G.R. Educational and Research Institute, Chennai 600095, Tamil Nadu, India

³Nano Energy & Catalysts Research Lab, Department of Materials Science and Engineering, Engineering Research Institute, Ajou University, Suwon, Republic of Korea

⁴Department of Mechanical Engineering, Wollo University, Kombolcha Institute of Technology, Kombolcha, Ethiopia Post Box No. 208

⁵Department of Medical Biotechnology and Integrative Physiology, Institute of Biotechnology, Saveetha School of Engineering, Saveetha Institute of Medical and Technical Sciences, Thandalam, Chennai, 602 105 Tamil Nadu, India

Correspondence should be addressed to M. Prabhakar; mprabhakar@gmail.com and Adisu Haile; adisu.haile@wu.edu.et

Received 24 May 2022; Accepted 2 July 2022; Published 25 July 2022

Academic Editor: Balasubramani Ravindran

Copyright © 2022 M. Prabhakar et al. This is an open access article distributed under the Creative Commons Attribution License, which permits unrestricted use, distribution, and reproduction in any medium, provided the original work is properly cited.

Heating the catalysts chemically at a cold start is indeed an approach to achieving catalytic performance. The purpose of this effort is to reduce cold flow emissions to background levels during regular engine operation. To address this issue, a thermal model was created, and a temperature study of various configurations was performed utilizing the computational dynamics method. This was followed by a regression model to confirm the results of the experiment. The article discusses how using a computational fluid dynamic to simulate the transient temperature profile of a chemically heated catalytic converter (CHCC) in exhaust may aid in the development of a much more powerful and energy-efficient catalytic converter. In this research, nanoparticles have been used as a heat transfer enhancement agent to improve the thermal conductivity of the exhaust gases. This work has been proposed to calculate the flow behaviour and heat transfer of nanoparticles in the proposed catalytic converter. The nanomaterial composite, created by incorporating copper oxide nanoparticles (CuO_2) on the surfaces of metal mesh, is used in the catalytic converter. The analytical technique has previously demonstrated its use in better predicting and comprehending the dynamic behaviour of a tightly linked catalyst and its thermally light-off period. The converter was evaluated in this study together with the SI (spark ignition) engine, and the data collected has been verified using analysis of regression. It is seen that in the converter with nanocopper oxide configuration, 50% carbon monoxide (CO) conversion efficiency is possible when the temperature of the main converter reaches 250°C and the CO is initially 2.7% Vol, and after reaching light off, it is 1.95% Vol. The time it takes to reach 250°C is 48 seconds after a cold start. In the case of hydrocarbons (HC), 50% HC conversion is reached during the test period of 168 seconds after the cold start. The HC is 605 ppm initially, and after light off, it is 130 ppm. The time taken to reach the HC light-off temperature is 300°C , with nanocopper oxide reaching this temperature in 168 seconds.

1. Introduction

The automotive sector is critical to emerging countries' economic stability and development. For a long period in our country, individual transport was seen as a privilege and a demand of the rich. However, as private transportation is now a fundamental and universal feature of contemporary life, India's automotive segment is all set to take off in a big way. The majority of the world's automobiles are establishing manufacturing facilities in India. Such rapid growth in the automotive sector brings numerous difficulties to light, one of which is vehicle emissions. It is not necessary to stress the significance of clean air in maintaining a decent and healthy lifestyle. As a result, emissions must be significantly reduced in order to preserve a relatively secure planet for future generations [1–7].

Global ecological degradation has prompted academics to concentrate on the construction of LEV (low emission vehicles) and ULEV (ultralow emission vehicles). Automobiles produce large amounts of HC (hydrocarbons), CO (carbon monoxide), and PM (particulate matter) [8–10]. Catalytic emission controls are universally acknowledged as one of the most economical methods of pollution reduction. A catalyst exhaust control system transforms the toxic components of the vehicle's emissions chemically into innocuous gases using a precious metal catalyst. This method is likely to lower carbon and hydrocarbon emissions by up to 80% and particulate matter by more than 50% [11].

The current generation of gasoline automobiles evaluated as shown in the FTP (Federal Test Procedure) generates between 70% and 80% of exhaust within the first 1 or 2 minutes after cold starting. It is mostly owing to the catalytic converter's lack of effectiveness until it hits light-off temperature. Thus, immediately raising the catalytic converter's temperature during the cold start of the vehicle is critical for lowering carbon and hydrocarbon emissions [12]. The problem of complying with ULEV and LEV standards has led to the development of a variety of novel converter ideas aimed at reducing cold-start emission levels. However, one novel notion is the pre-cold-start electrothermal catalyst method. The primary challenge in using the electrothermal catalyst technique is the significant electrical energy consumption and heat-up time [13]. Significant advancements have been achieved in the last several years to lower usage of power to the 2 and 3 kW range. To generate between two and three kW from 12-volt batteries, huge wire widths and a complex switching power system are required. Even a little power need of two kilowatts does have a noticeable effect on the life of the battery. Even more likely would be to heat the catalyst with energy from renewable sources, like electricity, heat, or the chemical energy in the exhaust [14].

Placing the hot catalyst nearer to the primary converter enhances the engine's backpressure. The primary converter and hot catalyst being located nearer the engine accelerated the thermal deterioration of the catalyst and backpressure. The reduced mass of the hot catalyst results in a lower electrical power requirement and a shorter heat-up time. The rate of temperature rise is proportional to the mass of the converter [15]. By maximizing the hot mass, it is possible

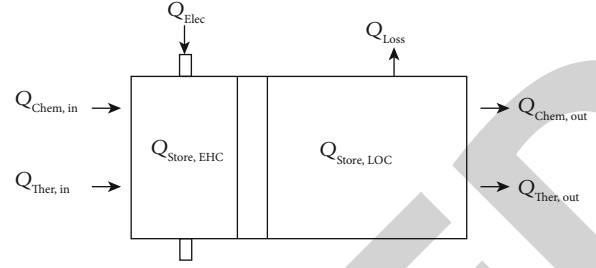


FIGURE 1: Energy balance diagram.

TABLE 1: Properties of nanoparticle copper oxide.

Item	Specifications
Name (chemical)	Copper oxide (CuO_2)
Molecular weight	79.545 g/mol
Color	Black
Density	6.4 g/cm^3
Thickness	30-50 nm
Purity	99.90%

to accelerate the rate of temperature rise, which results in an exothermic reaction [16]. When the exothermic reaction occurs, a large amount of chemical energy is generated, which functions as a heat source for the primary converter. As a result, the time necessary to activate the catalyst is slightly decreased. This energy depends on the temperature of the catalyst. You can utilize this energy by starting the catalytic activity as quickly as possible. One way to start the catalytic activity as quickly as possible is to produce a more rapid temperature rise in the converter. The exothermic reaction from the oxidation of HC and CO releases an abundance of chemical energy. This energy must be added rapidly and be sufficient to maintain an effective catalyst temperature for high conversion efficiency. The quantity of energy stored in the electrically heated catalyst (EHC) and light-off converter (LOC) is critical because it determines the operating temperature of these components. Recent EHC activities have focused efforts on electrical energy reductions. To achieve a high conversion rate at low electric power, the electric energy has to be used to heat small portions of the catalyst intensively and rapidly, thus inducing the catalytic reaction within a few seconds. The reactions not only reduce emissions but also add a significant amount of exothermic energy to the gas stream. The rate of temperature rise is proportional to the mass of the converter. By optimizing the heated mass, it is possible to greatly increase the rate of temperature rise. Thus, by heating only a small volume of catalyst, it is possible to reach the temperature where catalytic activity begins and releases the chemical energy of the exhaust very rapidly. Once the exothermic reaction begins, an abundance of chemical energy is released, which acts to heat the main converter (1.5% CO removal results in a 220 K Temperature rise). The chemically heated catalytic converter (CHCC) rapidly achieves high temperatures, and the heat created by exothermic oxidation

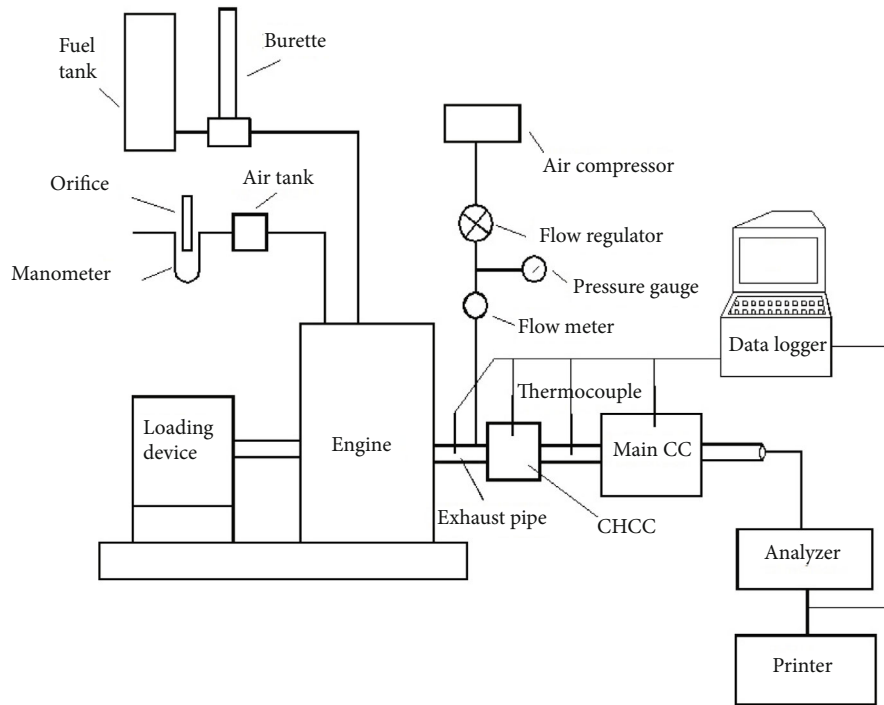


FIGURE 2: Experimental setup.

(1), we can say

$$Q_{\text{Chem,out}} + Q_{\text{Ther,out}} = Q_{\text{Chem,in}} + Q_{\text{Ther,in}} + Q_{\text{Elec}} - Q_{\text{Store,EHC}} - Q_{\text{Store,LOC}} - Q_{\text{Loss}}, \quad (1)$$

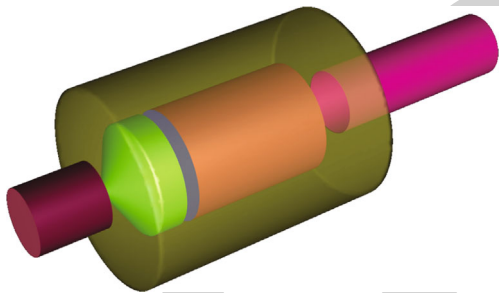


FIGURE 3: New proposed CHCC model.

is transferred by the exhaust gas to the primary converter, where it achieves a faster light off, resulting in reduced emissions at power levels in the range of 1.5 kW [17]. The walls of the metal mesh are incorporated with copper oxide nanocomposite to enhance the conduction rate. The goal of this work is to look at how well CHCC works using CFD analysis and regression analysis.

One technique to get the catalytic activity started as quickly as possible is to increase the converter's temperature. The rate of temperature rise is proportional to the mass of the converter. It is feasible to considerably accelerate the rate of temperature rise by optimizing the heated mass. Catalytic activity can be initiated, and exhaust chemical energy is released extremely quickly by heating a small volume catalyst to a high temperature. A large amount of chemical energy is released during the exothermic reaction, which in turn heats the primary converter. Figure 1 schematically depicts the system's energy balance. The catalytic converter produces chemical energy and thermal energy, as can be seen in the energy balance. In terms of energy equation

where $Q_{\text{Chem,out}}$ is the chemical energy that comes out of the converter, $Q_{\text{Ther,out}}$ is the thermal energy that comes out of the converter, $Q_{\text{Chem,in}}$ is the chemical energy that enters the converter, $Q_{\text{Ther,in}}$ is the thermal energy that enters the converter, Q_{Elec} is the electrical energy supplied, $Q_{\text{Store,EHC}}$ is the energy stored in the EHC converter, $Q_{\text{Store,LOC}}$ is the energy stored in the LOC converter, and Q_{Loss} is the loss of energy that goes out of the converter.

These are the energy sources available to heat the converter. The electrically heated catalytic (EHC) converter is extremely effective in lowering cold-start CO and HC emissions. EHC preheating or postheating reduced emissions significantly. These systems typically require 600-700 A current and a high electrical output of more than 4 kW. A heavy-duty alternator, either a big-size battery or a separate battery for EHC, large diameter wires, and a heavy-duty semiconductor switch are required to supply this high power of 4 kW to a conventional EHC [18]. As a result of the added weight, the cost rises, and the fuel economy suffers. Recent EHC operations have focused on reducing the amount of electrical energy required. 1.5 kW of heating is possible with the available battery. The EHC and LOC are coated with CuO_2 nanoparticles at a size of 30–50 nm. The properties of nanoparticles are given in Table 1. The experimental setup is also shown in Figure 2.

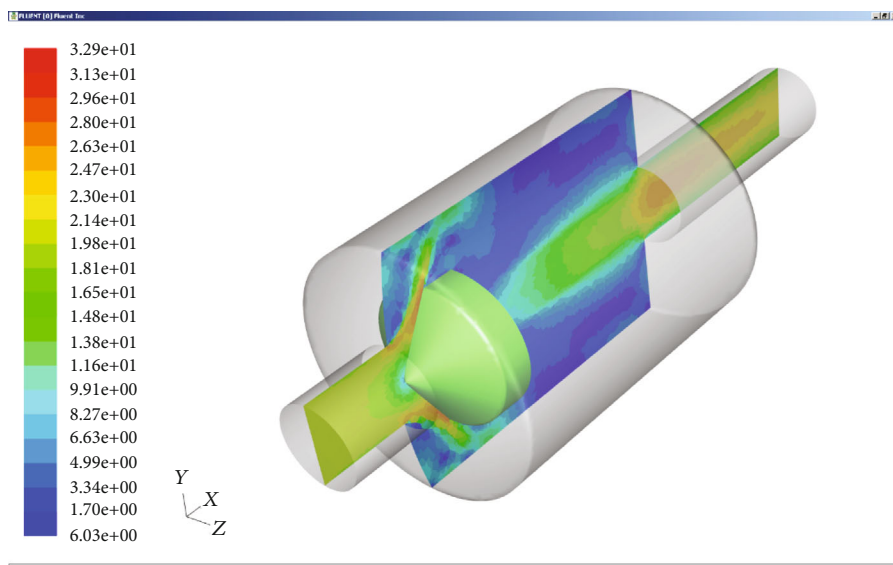


FIGURE 4: Velocity contours.

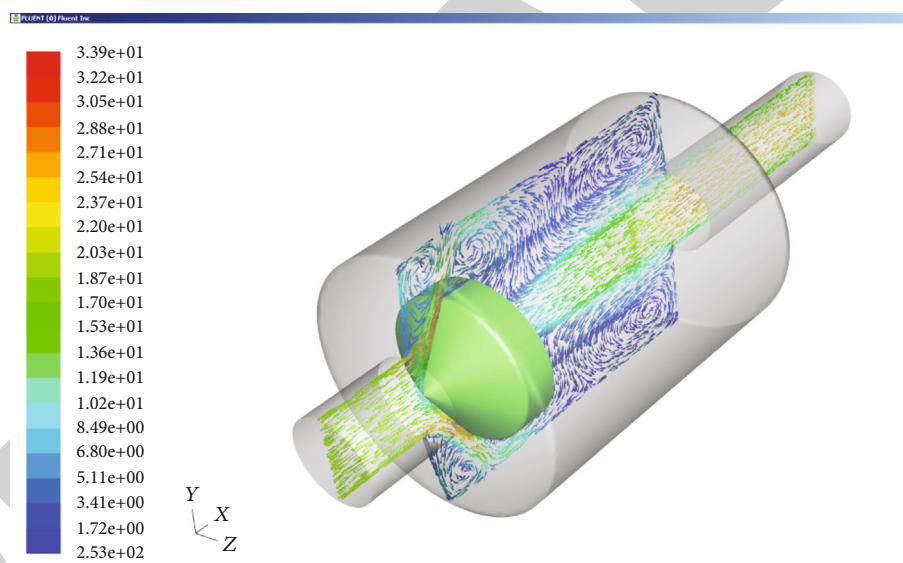


FIGURE 5: Velocity vector contours.

2. Analysis of the New Proposed Model

This CFD analysis is aimed at determining the temperature at the outlet of the manifold for the varying inlet temperature that varies unsteadily. There is a heater kept in the path of the fluid which heats the fluid, which leads to a further increase in the temperature of the fluid at the outlet as shown in Figure 3.

The models detailed are indeed part of an initial study to investigate the significance of accounting for multidimensional impacts in designing vehicle catalytic converters [19]. Although simulating a single system of a catalytic converter is useful in analyzing core difficulties, it is far from suitable for comprehensive catalytic converter modeling and evalua-

tion. For CFD (computational fluid dynamics) to create an influence on building designs within the automobile industry, it is of greatest significance to be capable of simulating the full catalytic converter, as compared to a traditional channel of the catalyst. CHCC is represented as a porous block.

The heater element (EHC) and LOC are assumed to be made of copper with a density of 8978 kg/m^3 , $C_p = 381 \text{ J/kg-k}$, and thermal conductivity of 387.6 W/m-k . The CFD domain is discretized into 1385443 triangles and 708987 tetrahedrons. The problem is assumed to be unsteady, compressible, and turbulent. Fluent is used to solve the problem. The K- ϵ (K-epsilon) standard model, which is a two-equation model in nature, is used to model turbulence. The energy equation is activated to see the conjugate heat

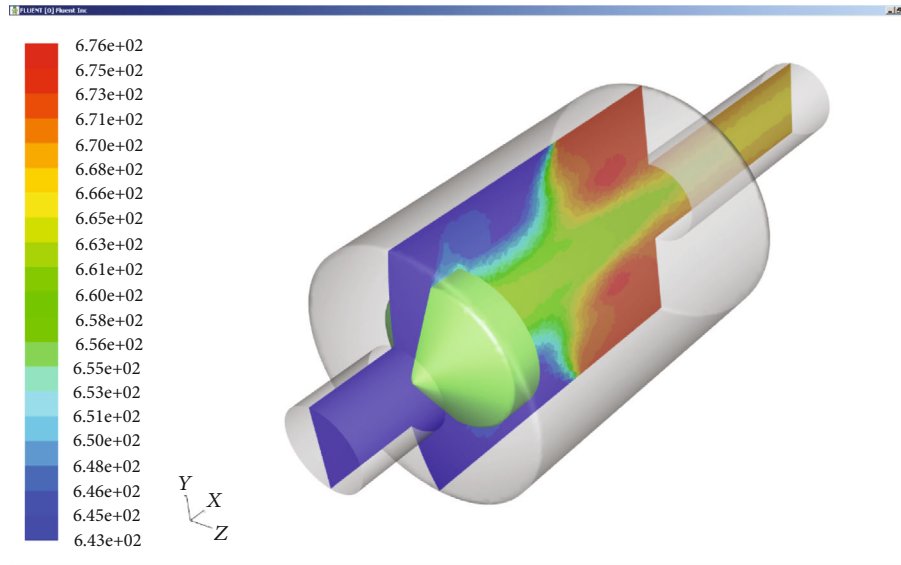


FIGURE 6: Temperature distribution 120 sec after engine start.

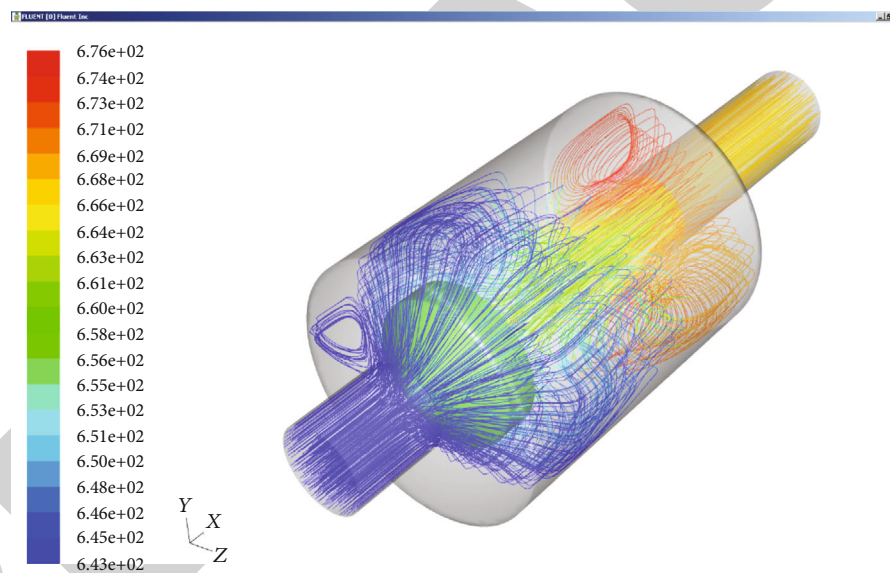


FIGURE 7: Temperature path lines 120 sec after engine start.

transfer, which solves heat transfer with convection. The unsteady profile is given at the inlet using a profile file option. The scheme of second-order discretization is used. The heater element (EHC) is set to 400°C [20]. It is discovered through pressure distribution. The backpressure developed due to this configuration is slightly higher between the outlet of the engine and the inlet of CHCC. Figures 4 and 5 show how the speed of CHCC changed at different times during the simulation.

It is found from the velocity contour that the velocity is higher at the inlet and outlet of CHCC. It is also found that the velocity is remarkably high near the conical surface and the centerline of the outlet exhaust pipe. It is found from velocity vector distribution that the conical portion helps

to divert the exhaust effectively and creates better turbulence for maximum heat transfer from the heater element. A vortex is formed at all four corners of the CHCC, and the swirl motion is desirable for better mixing of the exhaust with any incoming secondary air. The introduction of secondary air helps the unburnt hydrocarbons react with the incoming air to oxidize into CO_2 and H_2O [21]. It is also found that the vortex created in front of the conical section is not desirable, which must be removed by modifying the outer case of the CHCC design. The velocity vector also indicates that the flow finally passes through the center portion of the LOC, which is also desirable to activate the LOC as quickly as possible so that more will be generated and carried to the main catalytic converter. The velocity contour depicts that the

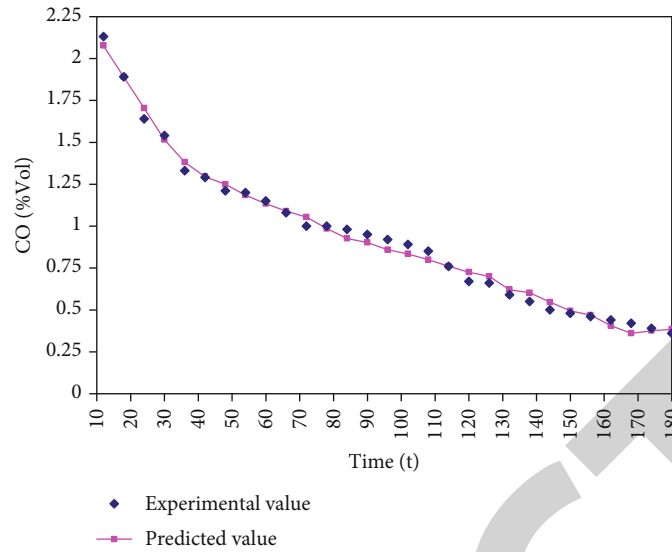


FIGURE 8: Variation in the rate of CO in % Vol. over time following a cold start.

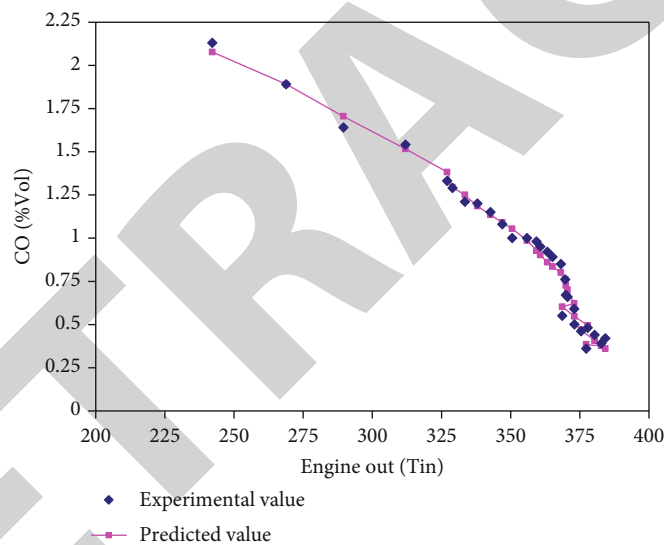


FIGURE 9: Variation in the rate of CO in % Vol. with engine exhaust temperature.

exhaust gas needs some residence time to convert CO to CO_2 . The model was proposed to give enough time and required temperature to attain.

Figure 6 indicates that the heat created due to the nanoparticles carried down to the main catalytic converter heats it more effectively than the previous configuration. Figure 7 depicts the temperature path lines, which show the way the heat is carried away to heat the main converter. Once the main converter is heated up to the light-off temperature, its efficiency is around 98% as per the previous work [22].

3. Theoretical Investigation: Multiple Regression Analysis

The benefit of this strategy would be that no prior predictions about the correlation's shape are required. The tech-

nique is validated based on preliminary results. Regression is a method for determining the shape of the finest correlation, including its constants, while genetic algorithms are one approach to accomplish this. Comparisons based on empirical results are frequently used to estimate the rate of heat generation in thermoelectric elements. Most of the time, this transition from empirical observations to correlations is done by first choosing a certain functional form of the relationship and then figuring out the constants [23].

The efficiency of CO conversion rate, CHCC is temperature-dependent on the emission well before CHCC, the temperature of both MC and the duration of the engine's cold start, all of which are managed as independent factors. The following data from a trial run of 1.5 kW heating and 90 lpm air supply is being used to correlate the condition required for CHCC.

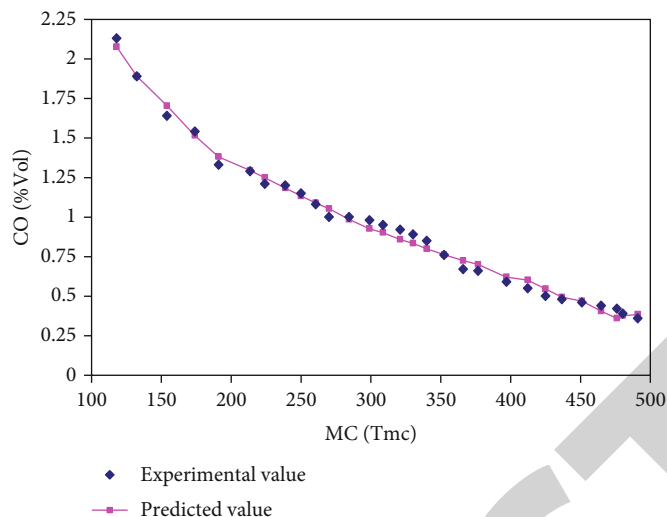


FIGURE 10: Variation in the rate of CO conversion as a function of MC temperature.

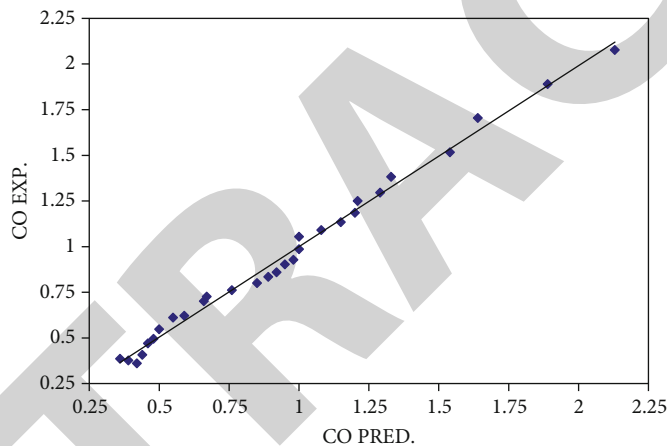


FIGURE 11: Differences in CO experimental and projected values.

TABLE 2: Time to reach light off for different configurations.

Catalytic converter configuration	Time taken to reach light-off temperature for CO reduction	Time taken to reach light-off temperature for HC reduction
145 cubic centimeter EHC catalytic converter without copper oxide nanoparticle coating	156 seconds after the engine started	180 seconds after the engine started
145 cubic centimeter EHC catalytic converter with copper oxide nanoparticle coating	48 seconds after the engine started	168 seconds after the engine started

With this method, the experimental data is used to test the procedure. Regression is a way to find the best-fitting correlation’s shape and constants, and genetic programming gives you a way to do it. The heat rate in thermal components is estimated by using correlations that were found through experiments. This process of turning experimental data into correlations is done by first choosing a specific functional form of the correlation and then figuring out the constants for that form.

The CO conversion rate, which is a measure of how well the converter works, depends on the temperature of the

exhaust before the converter, the temperature of the main converter (MC), and how long it has been since the engine was cold started. These factors are treated as independent variables, and data from a test run with 1.5 kW of heating is shown in

$$CO(\%conversion) = 51.87132 - 0.24151t - 0.0009T_{in} + 0.173323 T_{mc}, \tag{2}$$

where t is the number of seconds since the engine was

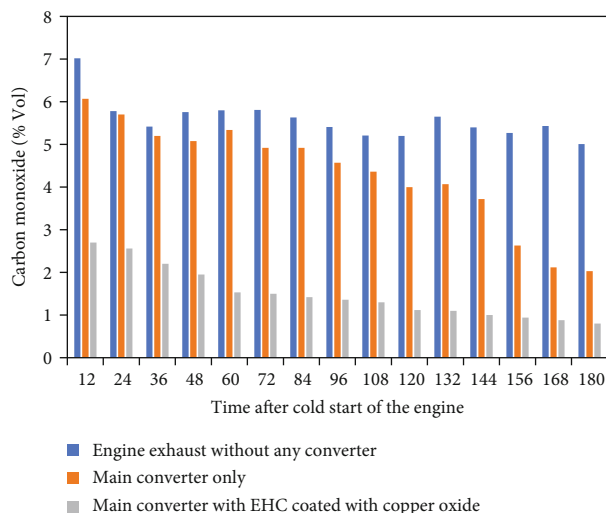


FIGURE 12: Variation between the CO with time after a cold start of the engine in seconds.

turned on cold, T_{in} is the exhaust temperature before the converter in $^{\circ}\text{C}$, and T_{mc} is the main converter's surface temperature in $^{\circ}\text{C}$.

This equation is a useful engineering tool for figuring out how well the converter will work with the nanocopper oxide.

The above method is a useful engineering method for quantifying the CHCC's performance under specified conditions. Figures 8–10 illustrate the projected and empirical rate of conversion in CO vs. period in seconds after a cold start, engine exhaust temperatures before CHCC, and main catalytic converter temperature, respectively. By setting the third independent variable and the matching rate of conversion of CO, all two independent variables may be predicted [24]. As can be seen from the graphs, the projected values and experimental data are very congruent.

The projected and observed results of the rate of CO conversion are shown in Figure 11. According to a study of the sample data, the projected results are quite similar to the experimental standards [25]. As a result, the established model may be utilized confidently to assess the condition required. The time to reach light off for the catalytic converter coated with copper oxide nanoparticles is given in Table 2.

According to Table 2, the main catalytic converter reaches the light-off temperature at different times after the cold start for different configurations. The MC quickly approaches the CO and HC light-off temperatures. This could be because the heat made by the oxidation reactions raises the temperature of the exhaust gas, making the catalyst light off faster. According to Figure 12, the CO percent by volume is larger at the start of the engine in all situations and subsequently drops as the duration after the cold start increases. It is also seen that, except for engine exhaust and MC alone, the CO decrease in percent by volume is more than 50% before the CO light-off temperature is reached. This could be because of CO oxidation in the presence of air and a copper oxide nanocatalyst. According to Figure 13, the hydrocarbon concentration in ppm is higher at the start of the engine and subsequently drops over time

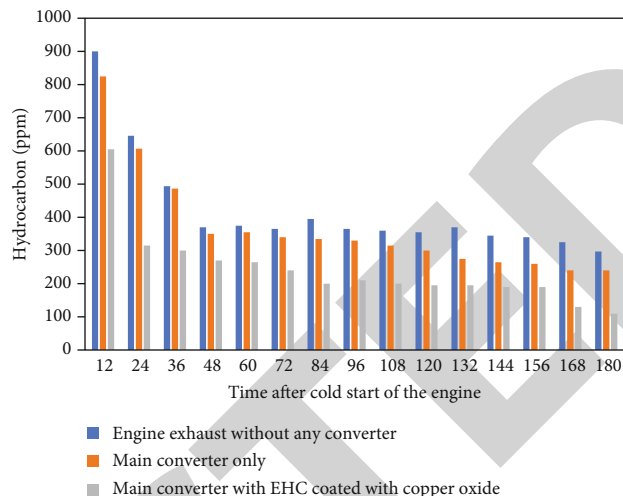


FIGURE 13: Variation between the HC with time after a cold start of the engine in seconds.

for all configurations examined. The hydrocarbon content in ppm is lower for EHC and even lower for EHC with nanocopper oxide. This could be because there is enough oxygen in the exhaust, which raises the temperature at which the light goes out and makes the conversion process more efficient.

4. Conclusion

The new proposed model has analyzed the thermal conductivity and flow characteristics of copper oxide nanoparticles incorporated in the metal mesh used to enhance the heat transfer performance of the catalytic converter. The newly created model is very effective at receiving heat from EHC while passing through it. The velocity vector and magnitude show that the flow pattern creates turbulent and vortex space in the CHCC. The heat from the EHC is shown to be carried by the flow, which then accumulates it as required towards the conclusion of the CHCC. It is seen that the analyses give a better picture of the internal flow of the exhaust gas and heat transfer path. This program may be utilized for converter modelling and evaluation, although exothermic heat generation is far more essential than catalytic converter temperature analysis, even though exothermic heat generation is much more important than the temperature analysis in the catalytic converter. The regression analysis shows that the experimental value and predicted values are conformed in the validation.

Data Availability

The data used to support the findings of this study are included within the article

Conflicts of Interest

The authors declare that they have no conflicts of interest.

Research Article

Synthesis of a Novel Nanoparticle $\text{BaCoO}_{2.6}$ through Sol-Gel Method and Elucidation of Its Structure and Electrical Properties

Fareenpoornima Rafiq,¹ Parthipan Govindsamy¹ and Selvakumar Periyasamy²

¹Department of Physics, Vel Tech Multi Tech Dr. Rangarajan Dr. Sakunthala Engineering College, Chennai 600062, India

²Department of Chemical Engineering, Adama Science and Technology University, Adama, Ethiopia

Correspondence should be addressed to Parthipan Govindsamy; phdparthipan@gmail.com and Selvakumar Periyasamy; selvakumar.periyasamy@astu.edu.et

Received 25 April 2022; Revised 7 June 2022; Accepted 9 June 2022; Published 19 July 2022

Academic Editor: Balasubramani Ravindran

Copyright © 2022 Fareenpoornima Rafiq et al. This is an open access article distributed under the Creative Commons Attribution License, which permits unrestricted use, distribution, and reproduction in any medium, provided the original work is properly cited.

The physical properties of cobalt oxide with varied oxidation states, and coordination numbers, in the transition series, have numerous applications. The present study explores the physical properties of $\text{BaCoO}_{2.6}$ nanoparticles synthesized through the sol-gel method. The X-ray diffraction figure exhibits a 25 nm crystallite size hexagonal phase. The observational data shows the reduction in the real part of impedance (Z'), dielectric constant (ϵ'), dielectric loss (ϵ''), and a raise in ac conductivity of mixed type of conduction with an elevation in frequency analyzed through impedance spectroscopy. The conductivity due to grain and grain boundaries is shown foremost in the complex impedance analysis. The plot of $\Delta V/\Delta T$ (Seebeck coefficient) in the low-temperature range indicates p-type behavior and the metal-insulator transition in the as-synthesized sample. The sample characteristics suggest applications in optical and switching devices. The Seebeck coefficient is the generation of potential difference when subjected to temperature difference. Thermoelectric materials are associated with the concept of high electrical conductivity like crystals and low thermal conductivity to that of glass. Nanothermoelectric materials can decrease further the thermal conductivity through phonon scattering. Electrical characterization suggests the presence of both NTCR and PTCR behavior in the sample, and hence, it explores the application in thermistor/resistance temperature detector's (RTD) and low dielectric constant and loss to electro-optical and higher conversion efficiency to storage devices. Additionally, impedance spectroscopy helps in the study of electrochemical systems and solid-state devices wherein the transition of metal-insulator is an add-on to the research.

1. Introduction

Strongly correlated electron systems consisting of insulators and electronic materials show uncommon, productive properties including colossal magnetoresistance, electromagnetic, spin-charge partition, transitions into metal-insulator, half-metallicity, and heavy fermion behavior and superconductivity. Cobalt in the transition metal oxides $A_{n+2}\text{Co}_{n+1}\text{O}_{2n+2}$ ($A = \text{Ca, Ba, Sr}$) adopt different oxidation states and probes its entry into electrochemistry and medical diagnostics. The overture studies of the $\text{BaCoO}_{3-\delta}$ system on powder samples revealed numerous hexagonal polytypes [1] that have not

been discretely distinguished, accredited to $\text{BaCoO}_{3-\delta}$ (15H $3-\delta < 2.23$, 12H $(2.43 < 3-\delta < 2.49)$, 7H $(2.52 < 3-\delta < 2.575)$, 2H $2.85 < 3-\delta < 3.0$), and orthorhombic $\text{BaCoO}_{2.07}$ and BaCoO_2 , while orthorhombic $\text{BaCoO}_{2.63}$ formed after annealing in O_2 had two other phases assigned to the cubic $\text{BaCoO}_{2.72}$ with a co-precipitate product non-indexed phase $\text{BaCoO}_{2.31}$ [2]. The specimen prepared by the sol-gel method is a low-temperature process involving the precursor solution inclusive of metal salts, a chelating agent (citric acid), and a diol (ethylene glycol). The advantages of the method are chemical composition with varied parameters of temperature, time, and atmosphere and are controllable to synchro-

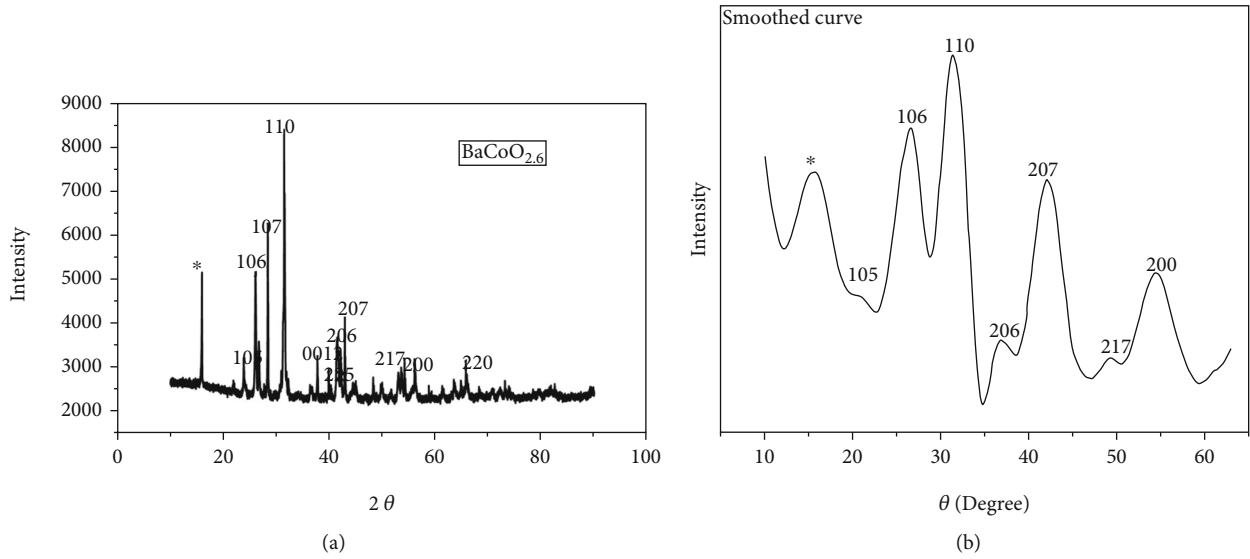


FIGURE 1: (a) Powder X-ray diffraction pattern (XRD) of the sample $\text{BaCoO}_{2.6}$ prepared by conventional sintering. (b) Main peaks of Figure 1(a) are highlighted.

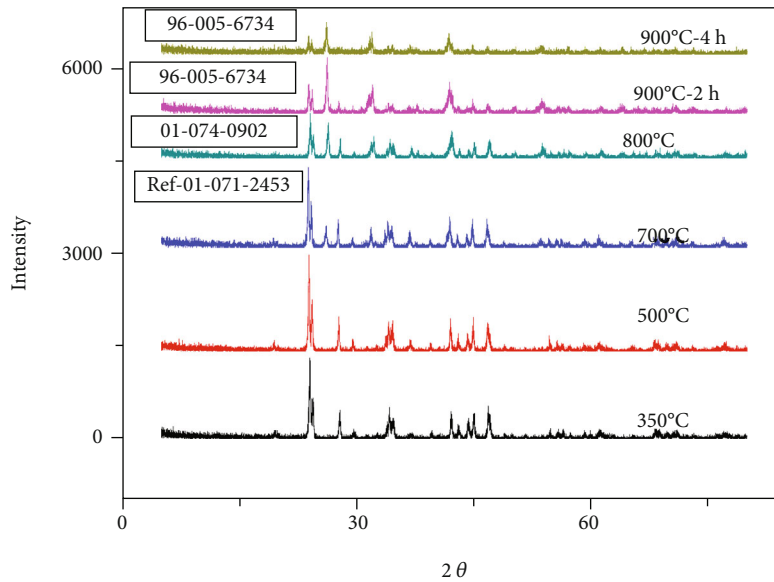


FIGURE 2: The multiphase transitions of the resultant product over an extrinsic temperature range.

nize with the structural and morphological characteristics of the specimen. Eventhough there are disadvantages like sensitive to moisture and time-consuming process with several steps, the advantages such as low-cost, flexible synthetic route, easy to implement overshadows.

Though several methods have been adopted for the synthesis of $\text{BaCoO}_{3-\delta}$ using BaNO_3 and CoNO_3 (600°C-12 h, 900°C-10 h) and BaCO_3 , Co_3O_4 precursors ($\approx 1200\text{ K}$ -2 days) [3–6], this is the first study to synthesize nano powder $\text{BaCoO}_{2.6}$ using the sol-gel method with lesser annealing time and analyze its physicochemical properties that include Seebeck coefficient, ac and dc conductivity studies, dielectric properties, PTCR/NTCR behavior, and the metal-insulator transition.

2. Materials and Methods

2.1. Experimental Details. The nanocrystalline sample has been prepared by a citrate-nitrate gel method using varying compositions of starting materials, such as $\text{Ba}(\text{NO}_3)_2$, $\text{Co}(\text{NO}_3)_2 \cdot 6\text{H}_2\text{O}$, citric acid, and ethylene glycol, which were taken in a stoichiometric ratio of $\text{Ba}_3\text{Co}_4\text{O}_9$, dissolved in deionized water with pH 2 at 309 K, and placed on a hot plate with a magnetic stirrer at 80°C for 2 hours to form the gel, which was then transferred to a platinum crucible and kept in an electric furnace and heated at 700°C for 5 hours. At 310°C, auto-combustion lasting for a few seconds occurred [7, 8], and the ash product was manually ground and then pressed into pellets at 1 Gpa, sintered for 120

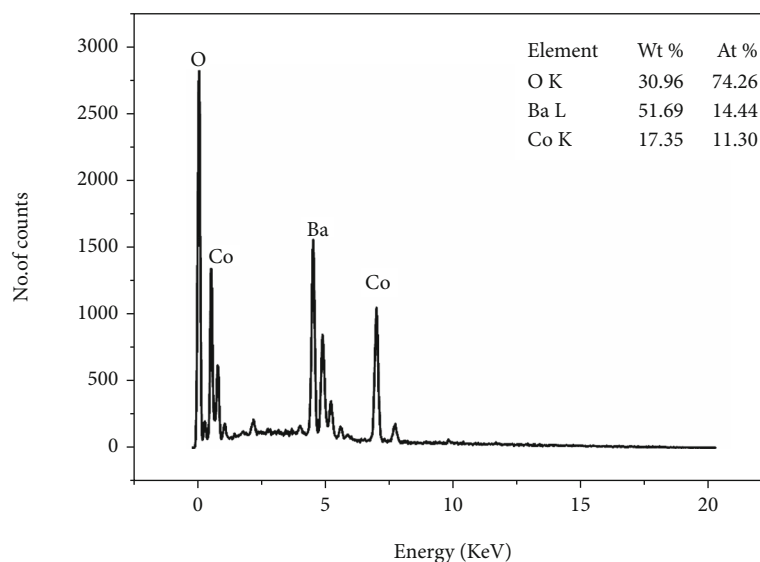


FIGURE 3: The elemental analysis (EDAX, 1 KeV to 20 KeV) of the synthesized sample.

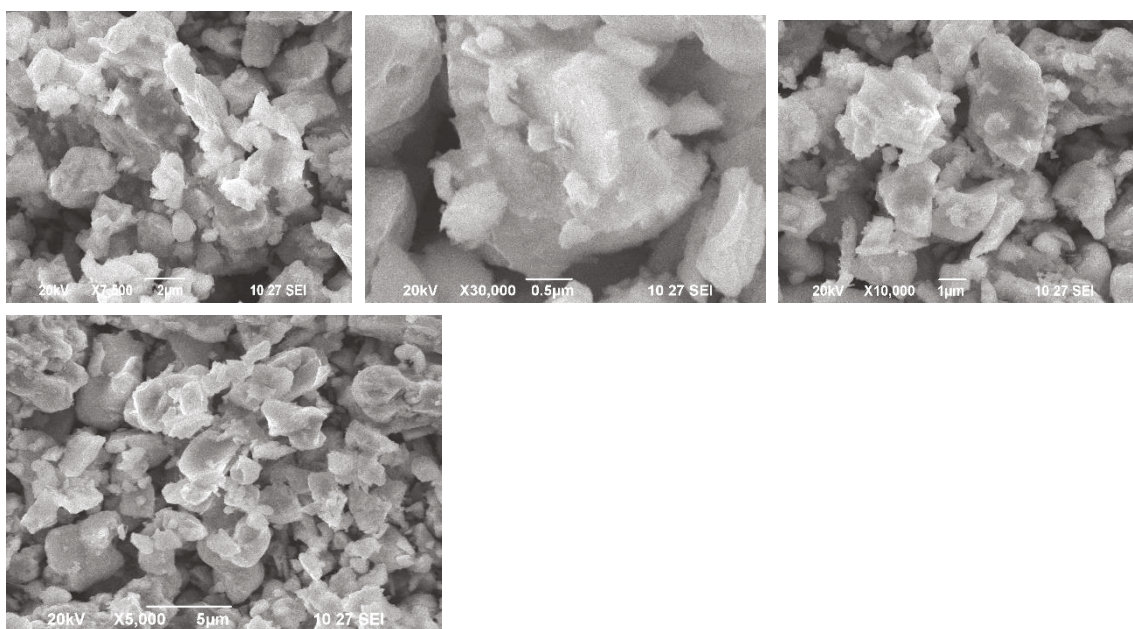


FIGURE 4: SEM image with different magnifications of $\text{BaCoO}_{2.6}$.

minutes at 900°C in the atmosphere, and left in the furnace for natural cooling [9] (precaution: due to the release of nitrogen oxides, heating has to be done in a closed chamber with adequate care).

2.2. Analysis of the Structure

2.2.1. X-Ray Diffraction (XRD) Method. The prepared sample was characterized by XRD with a Bruker-axs D8 diffractometer (40 KV, 30 mA) and DIFFRAC software, Bragg-Brentano reflection geometry, and treatment with $\text{CuK}\alpha$ ($=1.05418 \text{ \AA}$). The data was collected between 10°C and 90°C in steps of 0.005 and at a scanning rate of 1/minute.

The microstructural features and composition were studied using a scanning electron microscope (JOELJSM6390, Japan) having (EDAX) capability.

2.3. FTIR Analysis of the Synthesized Nanomaterial. Infrared spectra (FT-IR) from the sample were observed in the $400\text{--}4000 \text{ cm}^{-1}$ via Fourier transform-infrared spectrometer (Perkin-Elmer spectrum).

2.4. Electrical Transport Measurements. Shaped rectangular bars of $12 \text{ mm} \times 4 \text{ mm} \times 4 \text{ mm}$ of the sample was used for the recording of Seebeck coefficient (S) and electrical resistance simultaneously (Seebssys, NorECS AS Norwegian

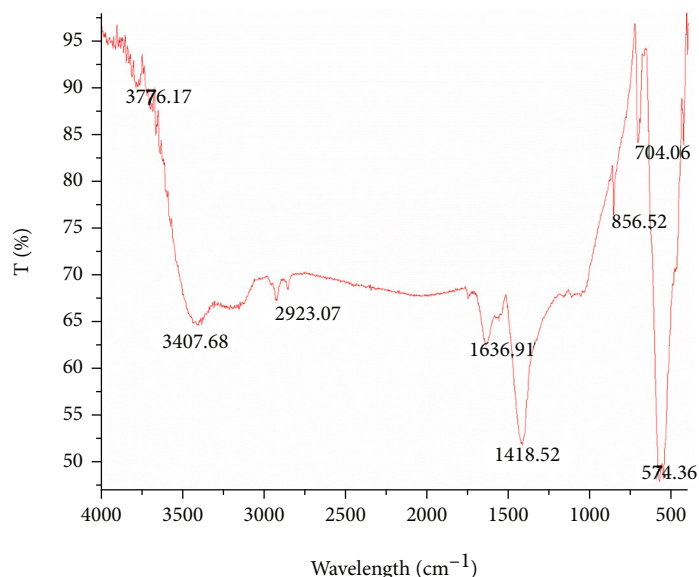


FIGURE 5: FTIR spectrum of synthesized nanomaterial $\text{BaCoO}_{2.6}$.

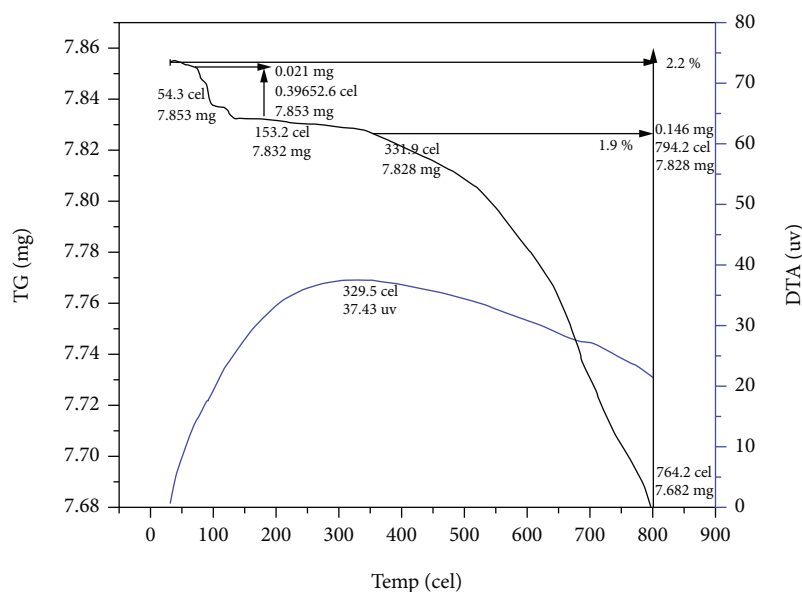


FIGURE 6: TG/DTA curve synthesized nanomaterial $\text{BaCoO}_{2.6}$.

Electro Ceramics) for the temperature of 30°C to 600°C in atmospheric air for a standard 4-probe technique with wide frequency range to evaluate dielectric constant as well as ac conductivity (Waynker multicomponent precision analyzer 6440B).

3. Result and Discussion

3.1. Structural Analysis

3.1.1. XRD of the $\text{BaCoO}_{2.6}$ Nanoparticle. Figure 1 displays the powder XRD of the $\text{Ba}_3\text{Co}_4\text{O}_9$ nanoparticle prepared by conventional sintering. The different crystalline phases

present in the sample were confirmed by comparing the XRD pattern to reference phases of the Xpert high score plus software. Major peaks had been associated with the $\text{BaCoO}_{2.6}$, specified by its reflection planes (Figure 1), in concurrence with the preceding reports JCPDS01-071-2453) [6]. The compound $\text{BaCoO}_{2.6}$ becomes crystalline in the space group P63/m m c symmetry in the lattice parameter, $a = b = 5.6710\text{\AA}$ and $c = 28.5450\text{\AA}$, and the unit cell volume (V) = 795.024\AA^3 . With the XRD data, the evaluation of the size of the crystallite was carried out by Scherrer equation, $D = k\lambda/\beta\text{Cos}\theta$, where D is the crystallite size (nm); β is the full width at half maximum of the diffraction peak; k is the shape factor (0.9); λ is the X-ray wavelength, and θ is

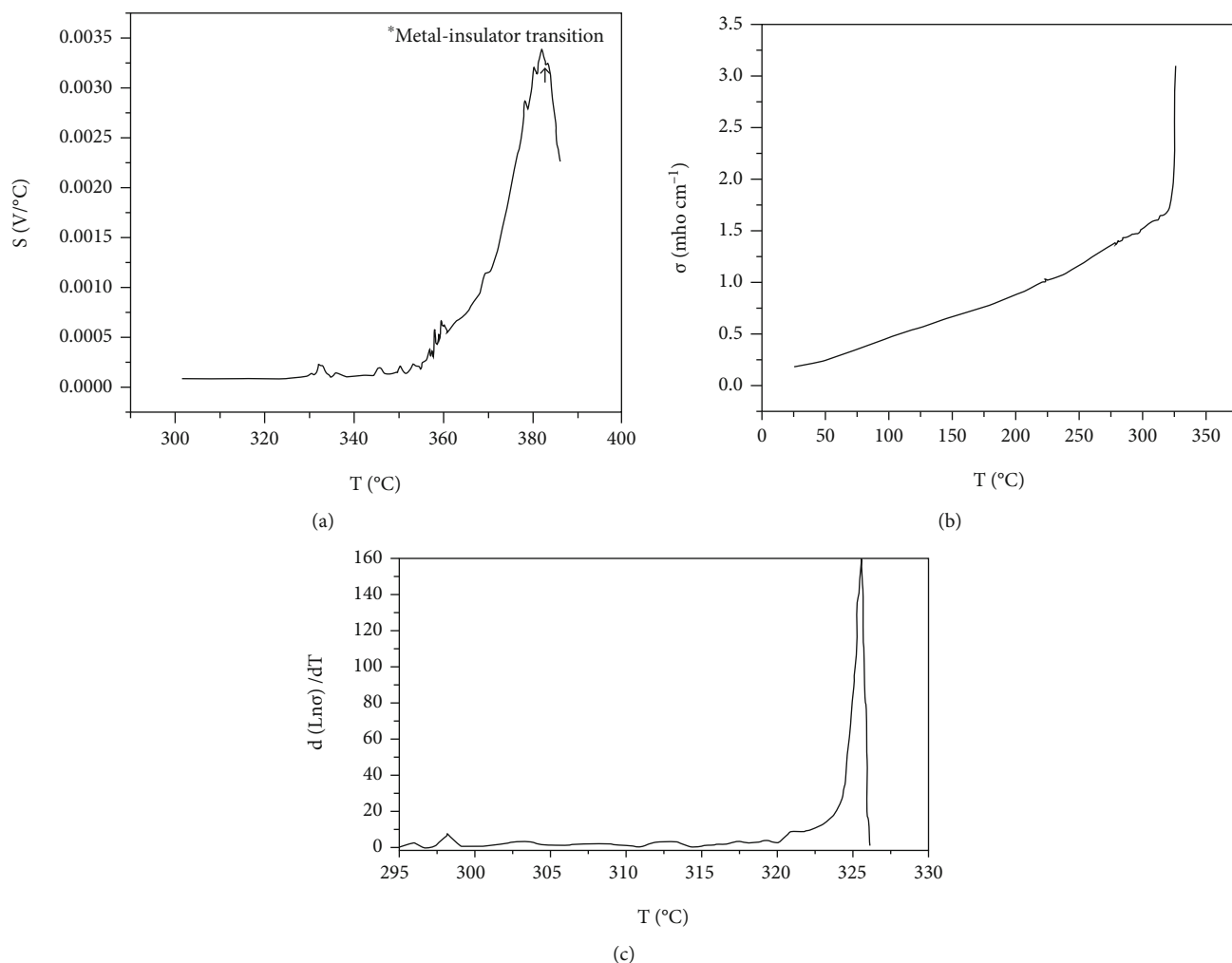


FIGURE 7: (a) The Seebeck coefficient (S). (b) Electrical conductivity. (c) $(\partial W) = \partial \ln \sigma / \ln T$. of synthesized nanomaterial $\text{BaCoO}_{2.6}$.

the diffracting angle. The average crystallite size of the most intense peak (110) plane of $\text{BaCoO}_{2.6}$ was assessed and found to be approximately 25.26 nm. The crystallite size corresponds to the coherently diffracting domain size and not to the particle size. The peak with an asterisk (*) may correspond to $\text{Ba}_3\text{Co}_4\text{O}_9$ or BaCo_2O_4 (JCPDS23-110) secondary phase [8–10].

The multiphase transitions of the $\text{BaCoO}_{2.6}$, over an extrinsic temperature range are shown in Figure 2. A selective list of efficient compounds certified as crystal structures is only specified completely in recent studies ($\text{BaCoO}_{2.6} \rightarrow \text{BaCoO}_3 \rightarrow \text{Ba}_3\text{Co}_2\text{O}_6$ (CO_3)_{0.6}) from 973 K to 1173 K and is the successive phase transition sequence. Not much detectable phase of barium cobaltite was found in annealing temperatures of 623 K and 773 K. Comparing the plot's e and f, we find that the diffraction peak of (e) is higher than the diffraction peak of (f), indicating that crystallization of (e) to be more than the crystallization of (f) [3, 11]. Hence, the start-up temperature for the synthesis of $\text{Ba}_3\text{Co}_2\text{O}_6$ (CO_3)_{0.6} may be assumed to be 900°C for 2 h. The different characteristic properties of BaCoO_3 and $\text{Ba}_3\text{Co}_2\text{O}_6$ (CO_3)_{0.6} will be analyzed in our future work.

3.2. Elemental Analysis of the Sample. The elemental analysis (EDAX, 1 KeV to 20 KeV) of the synthesized sample in Figure 3 shows the presence of expected elements. Figure 4 represents the SEM image with different magnification and the images reveal the grains in the range of 0.5 μm –5 μm .

3.3. FTIR Analysis of the Sample. FT-IR analysis was carried out for detecting the presence of the functional groups and for analyzing the reaction mechanisms during the sol-gel process (Figure 5). The band specific to the NO_3^- is found at 1419.62 cm^{-1} , and the peak around 842 cm^{-1} is associated with the distortion vibration of N-H bending mode. The absorption peak situated below 836 cm^{-1} is due to barium-cobalt-oxygen stretching vibrations [12, 13]. The slight shoulder around 1636.51 cm^{-1} denotes the asymmetrical stretched vibration of carboxylate anion and carbonyl groups [14]. The OH- group at 3407.68 cm^{-1} and 2923.07 cm^{-1} owes to the absorbed water during the sample preparation [15].

3.4. Thermal Properties. The TGA/DTA spectrum for $\text{BaCoO}_{2.6}$ is illustrated in the Figure 6. The reduction in

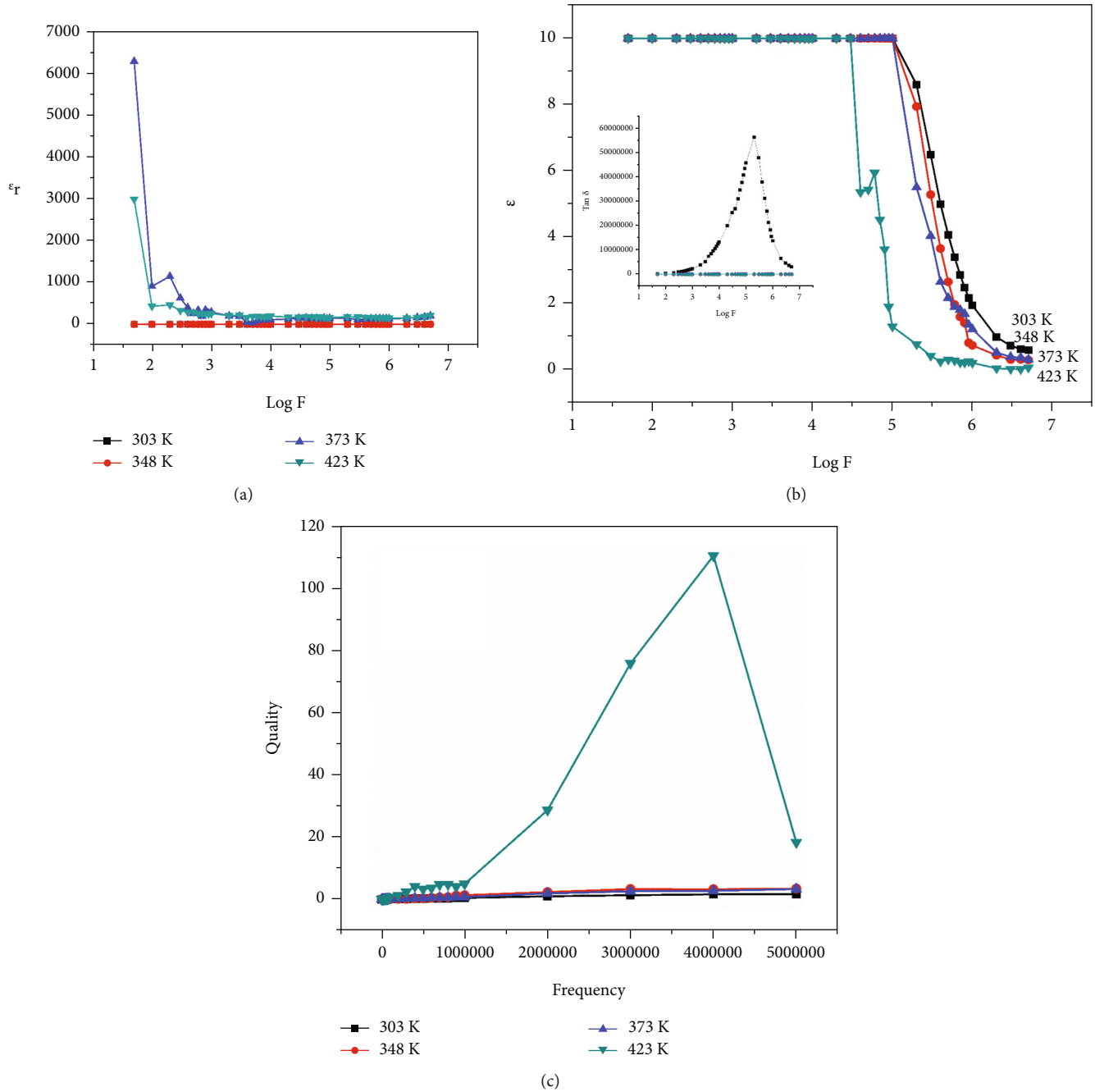


FIGURE 8: (a) Dielectric constant (ϵ'). (b) Dielectric loss and inset: loss factor ($(\tan \delta = \epsilon''/\epsilon')$). (c) Quality concerning variation in the frequency of synthesized nanomaterial BaCoO_{2.6}.

weight ($\approx 0.3\%$) at $T < 150^\circ\text{C}$ is mainly due to the loss of constituents such as water, solvents with low molecular weight, or gas desorption between 150°C and 250°C ($\approx 1.9\%$), additives, or crystallization and first decomposition products. The total weight loss accounts for $\approx 2.2\%$ at 300°C , and henceforth, no weight loss occurs indicating the completion of the combustion process and the formation of oxide phases.

3.5. Transport Properties. The Seebeck coefficient (S) is the ratio of the magnitude of the induced voltage to the temper-

ature gradient across a material. It is caused by charge carriers diffusion and phonon drag. The (S) is very low for metals and much larger for semiconductors. The value of S determined in the present study increases with temperature ($\approx 40 \mu\text{V}/\text{C}$) indicating a metallic phase from 35°C to 150°C , thereafter decreasing with increasing temperature in the insulating phase as shown in Figure 7(a). The rise and fall in the magnitude of (S) with temperature increase imply the predominance of both thermally accessible transport states and the carrier density [12–14]. To further characterize the temperature-dependent conductivity, the graph was

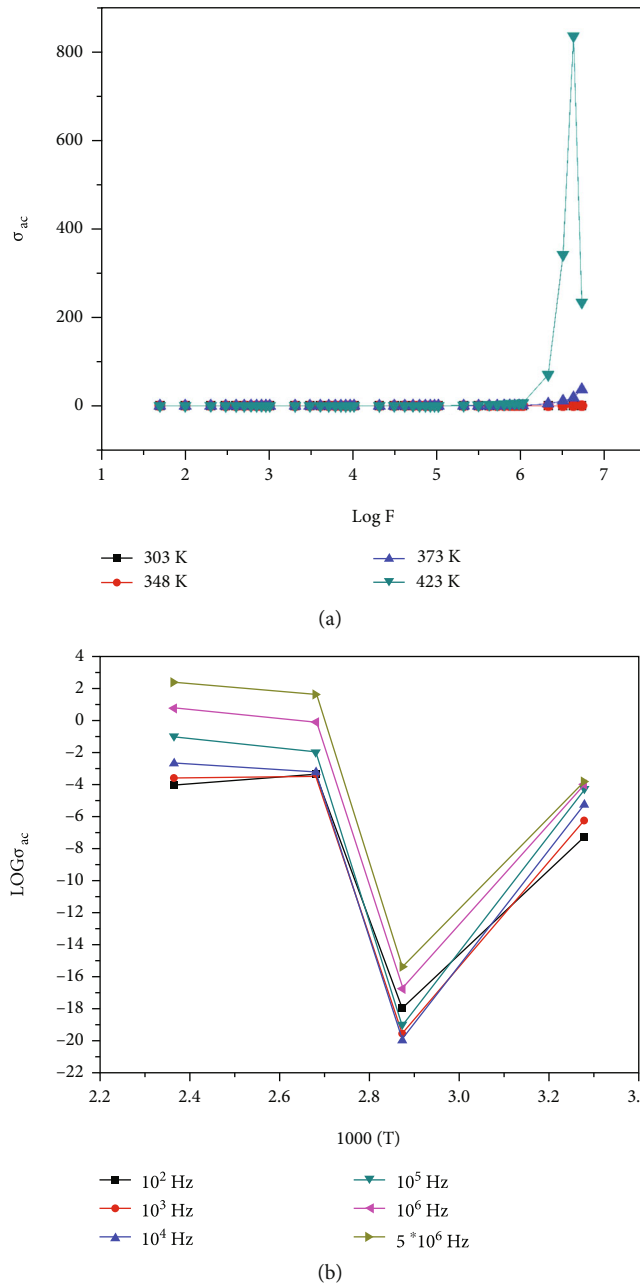


FIGURE 9: (a and b) Variation of ac conductivity concerning frequency and temperature.

plotted against the charge carrier transport properties, the reduction in activation energy, $W((\partial W) = \partial \ln \sigma / \ln T)$, and temperature. The slope of W exemplifies the conduction mechanism as per Mott's metal-to-insulator transition (MIT) model for disordered semiconductors (Figure 7(c)). The raise in electrical conductivity (positive slope) with an increase in temperature up to 325°C and thereafter decline (negative slope) with an increase in temperature may be attributed to PTCR/NTCR behavior, respectively, wherein the PTCR's usage in current overload protection devices [15–17]. Figure 7(b) shows a transition at 325°C in conductivity of the sample, and this may be due to the casting back of charge carriers in the material. Transport properties like

TABLE 1: Activation energy of the sample.

Frequency (Hz)	Activation energy E_a (eV)	
	Temperature range	
	Region I	Region II
10^2	1.35	1.16
10^3	1.38	1.09
10^4	0.91	1.24
10^5	1.27	1.14
10^6	1.10	0.97
$5 * 10^6$	1.09	0.83

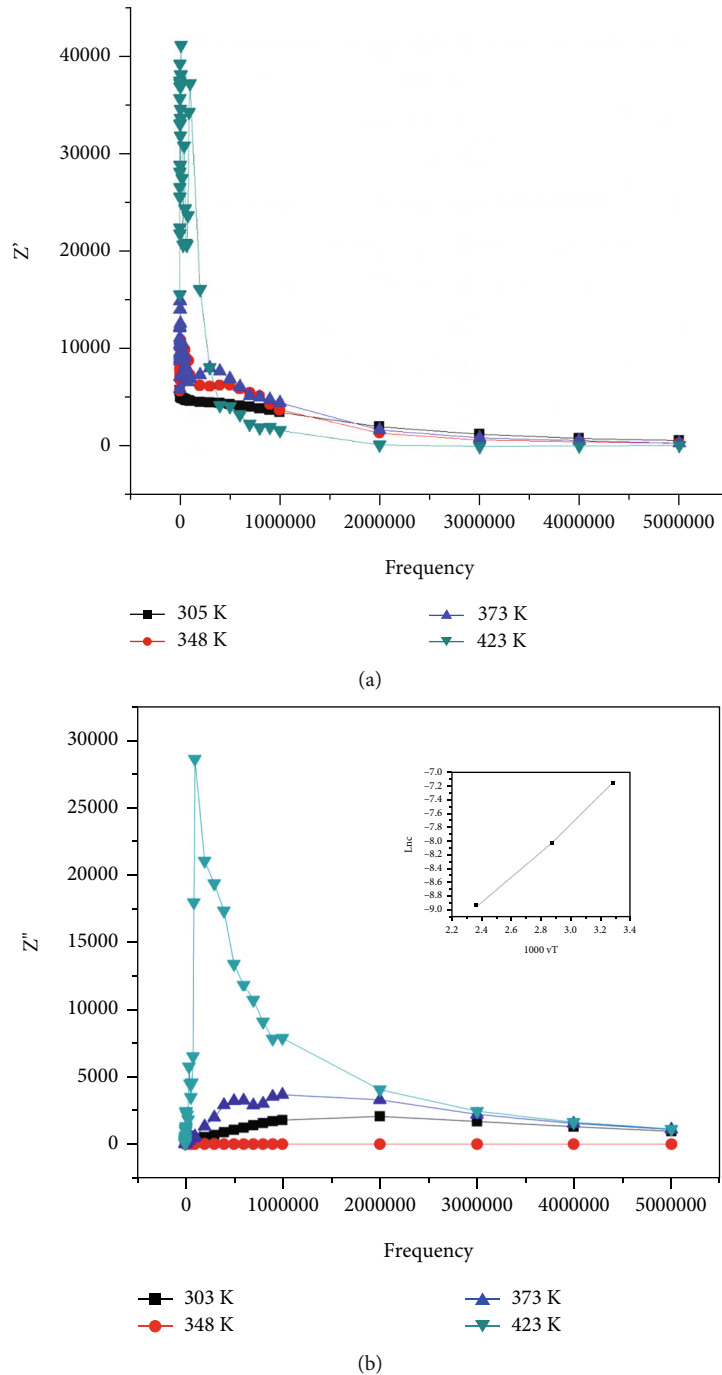


FIGURE 10: (a and b) Z' and Z'' variation with frequency and inset: relaxation time.

electrical conductivity and Seebeck coefficient may be enhanced through doping, and by increasing the density of the sample, the density of the sample remains 74% theoretical density [18].

3.6. Dielectric Properties. The enriched knowledge about dielectric analysis may shed light on the electrical properties of a material medium with varied temperatures and frequency. Dielectric constant (ϵ') shown in Figure 8(a) initially decreases abruptly with the rise in frequency and is stable at

higher frequency assuring that at the further side of a specific frequency of applied electric field, the exchange of electrons does not follow the alternating field. Therefore, polarization reduces resulting in a reduction in the dielectric constant (ϵ') [19]. From Figure 8(b), it is observed that the constant low-frequency dielectric loss may be due to the blocking of charge carriers at the cathode resulting in the formation of space charge polarization, and the abrupt decrease at 100 kHz may be the sign of thermal activation and hopping of charge carriers on a lattice surface.

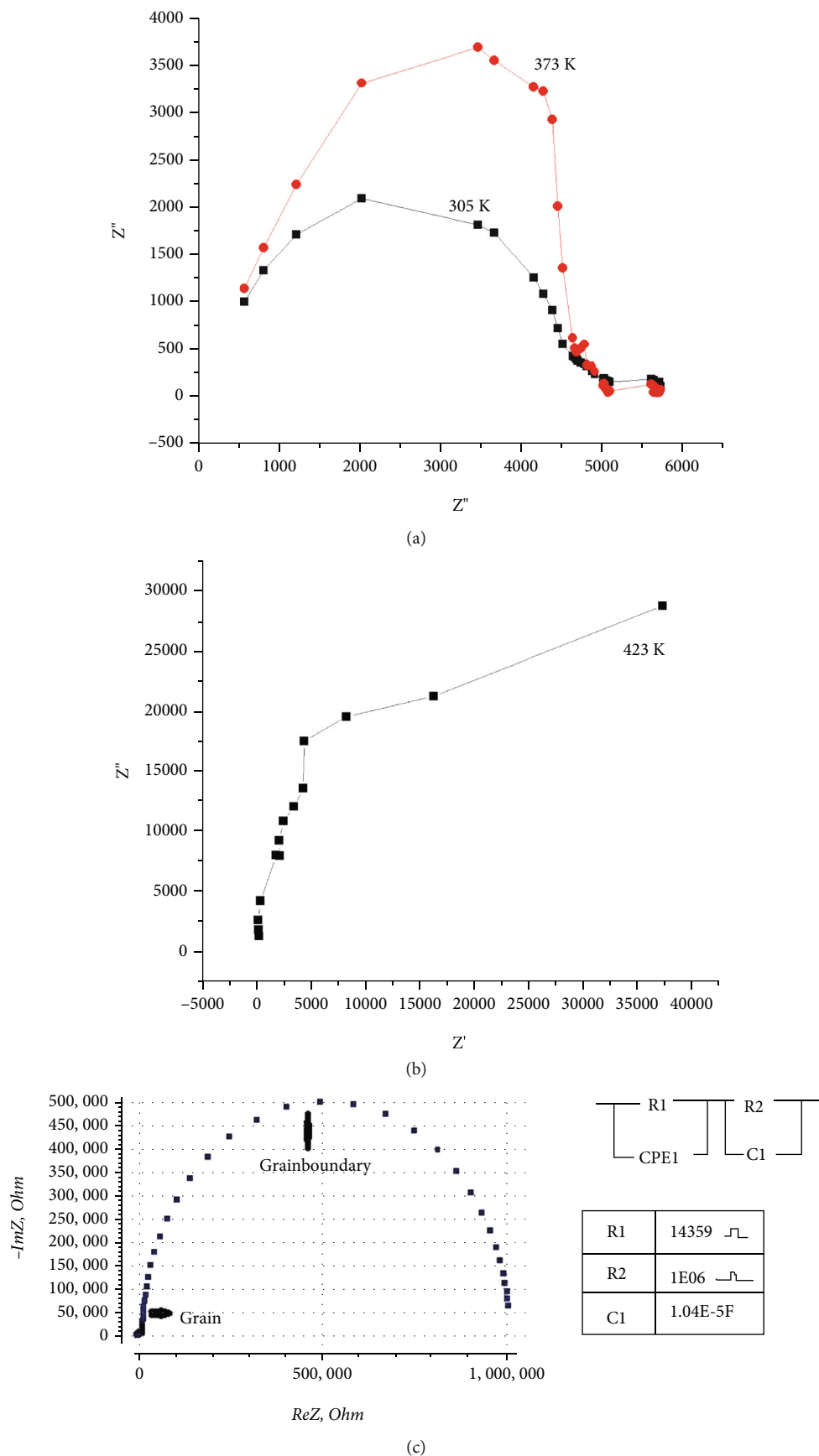


FIGURE 11: (a-c) Nyquist plot at room temperature, 373 K and 423 K, and equivalent circuit of synthesized nanomaterial BaCoO_{2.6}.

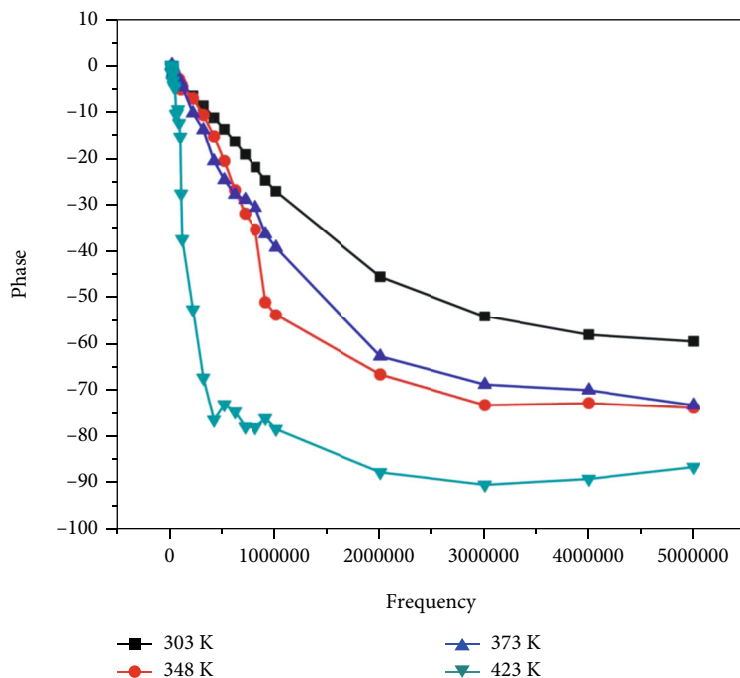


FIGURE 12: Variation of phase with frequency.

Figure 8(b)-inset shows the loss tangent ($\tan \delta = \epsilon''/\epsilon'$) curve wherein the resonating hopping frequency of electrons to the frequency of the applied electric field marks the peak indicating maximum electric energy being transmitted to the electrons and shooting up of loss at resonance [20]. Thus, the sample is more of energy storage with an extended lifetime and reduced charge-discharge time and less energy dissipater (Figure 8(c)) with applied frequency and temperature indicating high conversion efficiency [21, 22].

3.7. Ac Conductivity Studies. Figure 9(a) of ac conductivity figures the NTCR (negative coefficient of the temperature) behavior of the synthesized nanoproducr.

Figure 9(b) denotes calculations of (σ_{ac}) and (E_a) ac conductivity and activation energy, respectively, of the sample using the relation $\sigma = \omega \epsilon' \epsilon_0 \tan \delta$ and $\sigma = \sigma_0 \exp(-E_a/k_B T)$, where ϵ_0 is the vacuum permittivity, k_B is the Boltzmann constant, $\omega = 2\pi f$ is the angular frequency, and σ_0 is the preexponential factor [23]. For most dielectric ceramics, conduction has a high value and also remains constant for all frequencies at higher temperatures (region III). In the region I, the ac conductivity (σ_{ac}) does not follow the conductivity relation and is considered a metallic behavior, also observed in the Seebeck measurement (Figure 7(a)). In the region II (mid-temperature region), the conductivity differs exponentially with the temperature that is no longer linear wherein the change in slope (from positive to negative) may be attributed to the facts such as a mixed type of conduction inducted by thermally activated charge carriers and the oxygen vacancies in the nanoproducr [24–27]. The presence of oxygen vacancies and transfer of charge carriers concerning metal-insulator connects the sample probe into the analysis of critical temperature of high-temperature superconducting cuprates, usage as catalysts for hydrogen evolution reaction in support of green energy, as

the secondary power supply in integrated circuits, and current overload protection devices [28–30].

3.8. The Activation Energy of the Synthesized Nanomaterial.

The activation energy (E_a) of the product evaluated from the slope of $\log \sigma_{ac}$ vs $1/T$ curve is listed in Table 1. It is clear that the lower mobility (i.e., low conductivity) with higher activation energies corresponds to the ionic conduction in region I. On the other hand, electronic conduction in the region II is connected to relatively highest mobility (i.e., high conductivity) as well as the lowest activation energy [31, 32]. The E_a value in the region I and region II of the sample varies from 0.9 eV to 1.3 eV and 0.8 eV to 1.2 eV, respectively.

3.9. Impedance Analysis. This technique aids in separating the imaginary and real components of the complex impedance quantities to comprehend the structural property relationship of the sample. Figure 10(a) exhibits the difference in the real part of impedance (Z') as a function of frequency at various temperatures. The data indicate a decrease in (Z') in the low-frequency region followed by saturation in the high-frequency region (>100 kHz). The values of Z' merging at higher frequencies suggest the discharge of space charge carriers [24]. The differences in the imaginary part of impedance (Z'') with frequency (i.e., loss spectrum) at various temperatures in Figure 10(b) reveal that peaks are found at temperatures $>100^\circ\text{C}$. The distinct shift among peaks with a magnitude increase of Z'' for temperature suggests the contribution of immobile electrons. The position of the Z'' peaks shifting to the lower frequency on enhancing temperature and moderation in a peak width indicates the chances of the relaxation times distributed and the series capacitance presence [33, 34]. The occurrence of more polarization

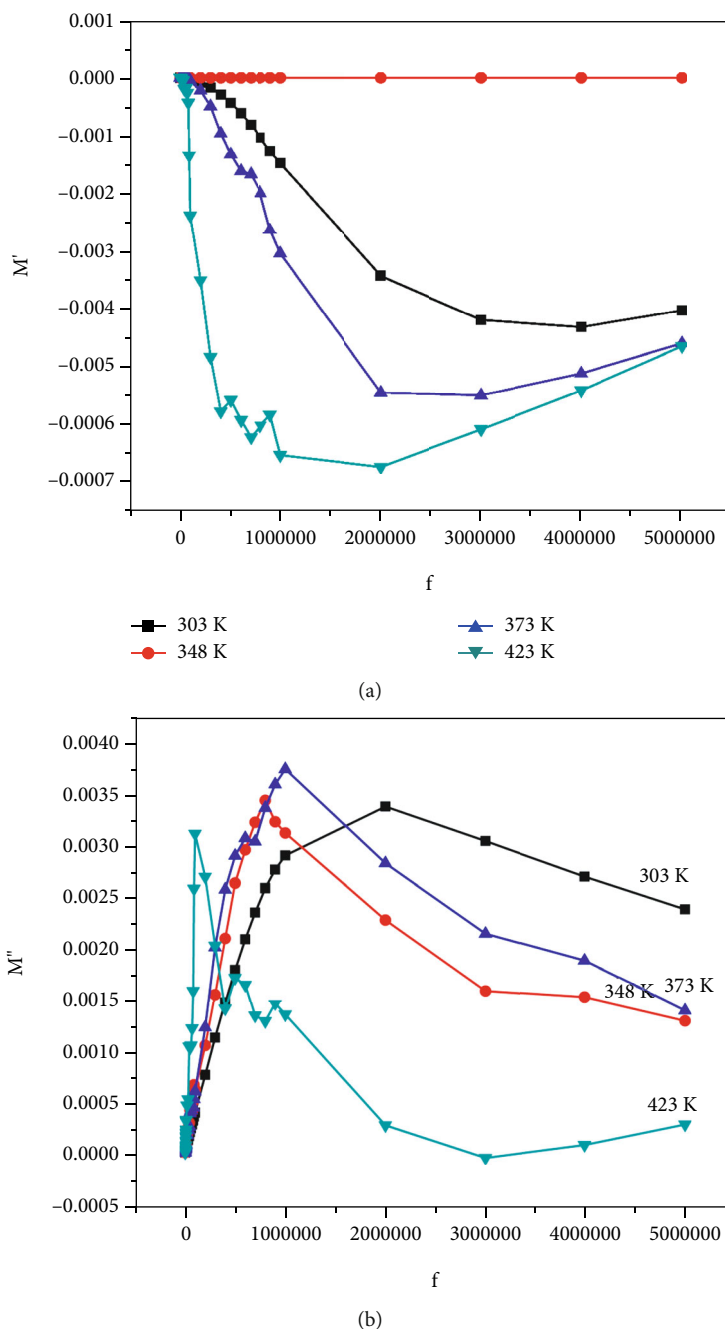


FIGURE 13: (a and b) Variation of M' and M'' with the frequency of the synthesized nanomaterial $\text{BaCoO}_{2.6}$.

charge transfer processes can be inferred in the impedance plot through the presence of greater than one arc [26]. The frequency consistent with the maximum of Z'' correlates with the relaxation time with the expression: $\zeta \omega_{\max} = 1$, where ω is the angular frequency [29]. Hence, the relaxation effect, as well as asymmetric peak broadening, is indicative of the non-Debye type of relaxation.

Figure 10(b)-inset indicates the difference of relaxation time (inferred from loss spectrum) with an inverse of absolute temperature ($10^3/T$) following the Arrhenius law given by $\zeta = \zeta_0 \exp(E_a/k_B T)$, where k_B is the Boltzmann constant, ζ_0 is the preexponential factor, and E_a is the activation

energy. The typical data confirms a temperature-dependent relaxation process with the distribution of relaxation time in 10^{-6} to 10^{-4} sec indicating an escalation in the process dynamics (i.e., charge/carrier transport) in the material due to elevation in temperature [35].

3.10. Nyquist Plot at Different Temperature. Nyquist plot points out the overall contribution percentage of bulk or grain boundary components which is accredited to the quality and electrical homogeneity of the material as for the bonding between the sintering/microstructure to the AC response. The plot also contributes to the magnitudes of the component

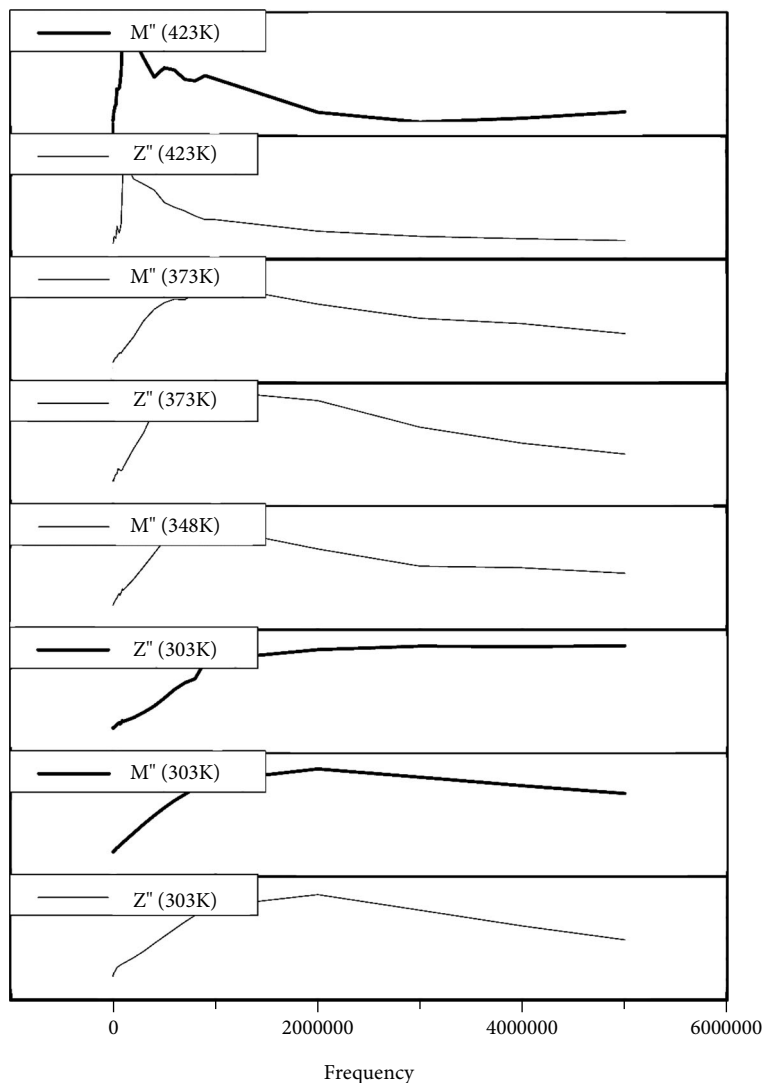


FIGURE 14: Combined plot of Z'' and M'' of synthesized nanomaterial $\text{BaCoO}_{2.6}$.

resistances and capacitances and picturization of redox reactions occurring at the electrode cells [36]. Nyquist plot (Z' vs. Z'') at room temperature, 373 K and 423 K, with corresponding equivalent circuit is best fit obtained using electrochemical impedance analyzer (EIS) software (for 100 C as shown in Figures 11(a)–11(c) with the possibility of two semicircles, highlighting the presence of grain boundaries and grains within the sample. The observed increase in the size of semicircular arcs with an increase in temperatures is related to the increase of capacitance, indicating dielectric (capacitive) behavior of the sample (resulting in phase -90° C, Figure 12) in the sample [37]. As the size (height) of the semicircles observed in the impedance plot depends on the resistive responses of the components in the sample, it is hard to acknowledge the responses emerging from the grain and grain boundary relating to their high capacitance values [24, 38, 39].

3.11. Modulus Studies. To identify the nature of relaxation behavior and to distinguish long-range conduction from short-range hopping motion, frequency dependence on the

imaginary part of electric modulus is observed (Figure 13(a)). The M value is low in the range of low frequency. Moreover, dispersion is seen with an increase in the frequency that can be corroborated by an insufficient restoring force regulating the movement of the charge carriers influenced by an induced electric field. The result affirms the exclusion of the electrode effect in the test sample [24]. In the plot of M'' (f) shown in Figure 13(b), the peaks shift to a lower frequency side with the elevation in temperature, and the bit sharper peak exists at a low frequency (~ 460 Hz) at the highest temperature (150°C) indicating that the ions can travel over long distances, i.e., charge carriers can carry out hopping well between the sites. The high-frequency peaks corresponding to lower temperatures suggest the confinement of ions within their wells with localized motion. This behavior shows that the dielectric relaxation is an unusual thermally activated type wherein the hopping mechanism of charge carriers dominated intrinsically [38].

The power of synergistic use of both impedance and modulus spectroscopy Z'' vs. Z' plot emphasizes the phenomenon of largest resistance. Contrastingly, M'' vs M'

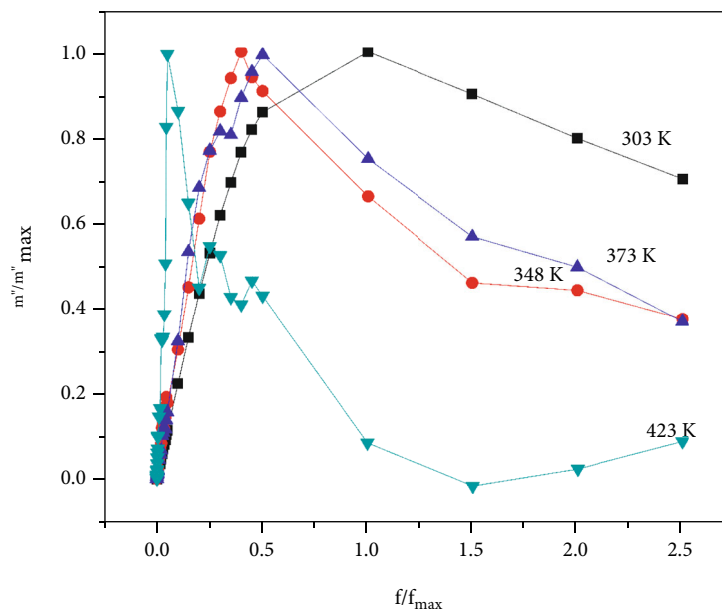


FIGURE 15: M''/M''_{\max} vs f/f_{\max} of synthesized nanomaterial $\text{BaCoO}_{2.6}$.

picks up those of the smallest capacitance highlighting that the relaxation process is a short- or long-range motion of charge carriers. The impedance peaks (Z'') correspond to $R/2$ and the modulus peak to that of $\epsilon_0/2C$ of that particular element [40]. Figure 14 shows the selective plot of impedance (Z''), modulus (M'') variation, and frequency due to different temperatures. The highest values coincide at a specific frequency in the synthesized $\text{BaCoO}_{2.6}$ indicating a similar time gap of impedance as well as modulus spectra, and also the matching of peaks at all temperatures suggests the long-range movement of charge carriers [41, 42]. Additionally, in the short-range peaks, Z' and M' are observed in diverse frequencies, and long-range transmission of charge carrier peaks is seen at the same cycles.

The validation of the distribution of relaxation times with temperature dependence was done by plotting the M'' in weighted coordinates, i.e., M''/M''_{\max} vs f/f_{\max} (f_{\max} - loss peak frequency) (Figure 15). A perfect overlapping of curve bands in a single master curve was not observed. The result conveys the conduction mechanism being altered with temperature exhibiting non-Debye type behavior and mixed conduction at high temperatures [39, 43].

4. Conclusion

The synthesized $\text{BaCoO}_{2.6}$ powder using the sol-gel method was characterized by different techniques. The Seebeck coefficient (S) is positive, indicating p-type behavior and the graph confirms the metal-insulator transition in the material. The FTIR study confirmed the presence of functional groups, and the positive value of the Seebeck coefficient (S) indicates p-type behavior. The electrical studies suggest both NTCR and PTCR behavior in the sample and its applications in thermistor/RTD. The characteristics of low dielectric constant, dielectric loss, and low dissipation factor with

high frequency indicate enhanced optical quality and higher conversion efficiency, hence the sample's research in electro-optical and storage devices with less charge-discharge time. The characteristic reduction in low dielectric constant and high-frequency dielectric loss concludes the enhanced optical quality and low dissipation factor to energy storage/capacitors, and the features of MI transition suggest the sample probe into electrical and optical switching devices and secondary power supply in integrated devices. The electrical studies suggest both NTCR and PTCR behavior in the sample and its applications in thermistor/RTDs. The impedance studies of the sample affirm the existence of grain in bulk as well as the grain boundary effects. The complex impedance spectroscopy study suggests the long-term mobility of charge carriers as well as non-Debye type with mixed conduction in the material. More studies are required to shower an insight into deducing further information and discern for a better interpretation of the results obtained.

Data Availability

All data generated or analyzed during this study are included in the published article.

Conflicts of Interest

There exists no conflict of interests.

Acknowledgments

The author (Fareenpoornima Rafiq) is grateful to ARCI lab, Chennai, for having extended the facilities for X-ray diffraction studies and electrical conductivity and Seebeck coefficient measurements, to Karunya University for SEM/EDX measurements, and to the Department of Physics, Loyola College, Chennai, for dielectric studies.







References

- [1] M. Zanne and C. Gleitzer, "Bafeo₃-X Polytype," *Bulletin de la Societe Chimique de France*, vol. 5, p. 1567, 1971.
- [2] O. Mentré, M. Iorgulescu, M. Huvé et al., "BaCoO_{2.22}: the most oxygen-deficient certified cubic perovskite," *Dalton Trans*, vol. 44, no. 23, pp. 10728–10737, 2015.
- [3] J.-J. Choi, W. Qin, M. Liu, and M. Liu, "Preparation and characterization of (La_{0.8}Sr_{0.2})_{0.95}MnO_{3-δ}(LSM) thin films and LSM/LSCF interface for solid oxide fuel cells," *Journal of the American Ceramic Society*, vol. 94, no. 10, pp. 3340–3345, 2011.
- [4] P. M. Botta, V. Pardo, D. Baldomir, C. de La Calle, J. A. Alonso, and J. Rivas, "Dynamic magnetic behavior of BaCoO₃ quasi-one-dimensional perovskite," *Physical Review B*, vol. 74, no. 21, article 214415, 2006.
- [5] K. Iwasaki, T. Yamamoto, H. Yamane et al., "Thermoelectric properties of Ba₃Co₂O₆ (CO₃)_{0.9} containing one-dimensional CoO₆ octahedral columns," *Journal of Applied Physics*, vol. 106, no. 3, article 034905, 2009.
- [6] A. J. Jacobson and J. I. Hutchison, "The structure of BaCoO_{2.6} by a combination of high-resolution electron microscopy and neutron powder diffraction," *Journal of the Chemical Society, Chemical Communications*, vol. 3, pp. 116–117, 1976.
- [7] C. Callea, J. A. Alonso, and M. T. Fernández-Díaz, "Polymorphism of Ba_{1-x}Sr_xCoO_{3-δ} (0 ≤ x ≤ 1) Perovskites: a thermal and structural study by neutron diffraction," *Verlag der Zeitschrift für Naturforschung*, vol. 63, no. 6, pp. 647–654, 2008.
- [8] P. Carvillo, Y. Chen, C. Boyle, P. N. Barnes, and X. Song, "Thermoelectric performance enhancement of calcium cobaltite through barium grain boundary segregation," *Inorganic Chemistry*, vol. 54, no. 18, pp. 9027–9032, 2015.
- [9] G. Constantinescu, S. Rasekh, M. A. Torres, M. A. Madre, A. Sotelo, and J. C. Diez, "Improvement of thermoelectric properties in Ca₃Co₄O₉ ceramics by Ba doping," *Journal of Materials Science: Materials in Electronics*, vol. 26, no. 6, pp. 3466–3473, 2015.
- [10] J. Liu, X. Huang, D. Yang, G. Xu, and L. Chen, "Synthesis and physical properties of layered Ba_xCoO₂," *Dalton Transactions*, vol. 43, no. 41, pp. 15414–15418, 2014.
- [11] M. Sopicka-Lizer, P. Smaczynski, and K. Kozłowska, "Preparation and characterization of calcium cobaltite for thermoelectric application," *Journal of the European Ceramic Society*, vol. 25, no. 12, pp. 1997–2001, 2005.
- [12] C. Lamsel, *Electronic, thermoelectric and optical properties of vanadium oxides: VO₂, V₂O₃, and V₂O₅*, [Ph.D. thesis], University of New Jersey, 2015.
- [13] A. Chamoire, F. Gascoin, C. Estournes, T. Caillat, and J. C. Tedenac, "High-temperature transport properties of complex antimonides with anti-Th₃P₄ structure," *Dalton Transactions*, vol. 39, no. 4, pp. 1118–1123, 2010.
- [14] X. Huang and W. Zhang, "How does the spin-state of Co ions affect the insulator-metal transition in Bi₂A₂Co₂O₈ (A = Ca, Sr, Ba)," *Scientific Reports*, vol. 6, no. 1, pp. 1–9, 2016.
- [15] X. Granados-García, X. Obradors, and J. B. Torrance, "Metallic state and the metal-insulator transition of NdNiO₃," *Physical Review B*, vol. 48, no. 16, pp. 11666–11672, 1993.
- [16] M. Wang, C. Bi, L. Li et al., "Thermoelectric Seebeck effect in oxide-based resistive switching memory," *Nature Communications*, vol. 5, no. 1, p. 4598, 2014.
- [17] D. Ruzmetov and S. Ramanathan, "Metal-insulator transition in thin film vanadium dioxide," in *Thin film metal-oxides: fundamentals and applications in electronics and energy*, Springer, Boston, MA, 2010.
- [18] Z. E. Doktorgrades, *Anionic substitution in perovskite-type oxides*, [Ph.D. thesis], Materials Science & Technology, Empa, CH-8600 Dübendorf, 2008.
- [19] V. S. Shanthala, S. N. Shobha Devi, and M. V. Murugendrappa, "AC conductivity and dielectric studies of polypyrrole copper zinc iron oxide nanocomposites," *IOSR Journal of Applied Physics*, vol. 8, no. 5, pp. 83–90, 2016.
- [20] N. Singh, A. Agarwal, S. Sanghi, and S. Khasa, "Dielectric loss, conductivity relaxation process and magnetic properties of Mg substituted Ni–Cu ferrites," *Journal of Magnetism and Magnetic Materials*, vol. 324, no. 16, pp. 2506–2511, 2012.
- [21] K. P. Priyanka, S. Joseph, S. Thankachan, E. M. Mohammed, and T. Varghese, "Effect of electron beam irradiation on optical properties of manganese tungstate nanoparticles," *Journal of Nanotechnology*, vol. 2013, Article ID 580308, 6 pages, 2013.
- [22] K. Shreekrishna, U. Kumar, and B. S. N. Sarma, "Design, development, and analysis of thin film coated coir fibre for electronic and industrial applications," *Cer*, vol. 7, pp. 81–91, 2011.
- [23] A. Prasad and A. Basu, "Dielectric and impedance properties of sintered magnesium aluminum silicate glass-ceramic," *Journal of Advanced Ceramics*, vol. 2, no. 1, pp. 71–78, 2013.
- [24] M. Buchi Suresh and R. Johnson, "Synthesis and high temperature dielectric and complex impedance spectroscopic studies of dense ZnAl₂O₄ ceramics," *Journal of Materials Engineering and Performance*, vol. 1, pp. 1–8, 2017.
- [25] D. Rao and S. Asthana, "The impedance and conductivity studies on BiFeO₃ and 0.90BiFeO₃-0.10Bi_{0.5}Na_{0.5}TiO₃ ceramics," *AIP Conference Proceedings*, vol. 1663, 2015.
- [26] B. Kaur, V. Lakbir Singh, A. Reddy, D.-Y. Jeong, N. Dabra, and J. S. Hundal, "AC impedance spectroscopy, conductivity, and optical studies of Sr doped bismuth ferrite nanocomposites," *International Journal of Electrochemical Science*, vol. 11, pp. 4120–4135, 2016.
- [27] R. M. Al-Haddad, I. M. Ali, I. M. Ibrahim, and I. M. Al-Essa, "DC and AC conductivity measurements of Se₆₀Te₃₀Ge₁₀ films," *Al-Nahrain Journal of Science*, vol. 12, no. 4, pp. 72–77, 2009.
- [28] C. Cheng, W. Cao, S. Huang et al., "Oxygen-vacancy-ordering-induced metal-insulator transition in MgO single crystals," *Results in Physics*, vol. 36, article 105452, 2022.
- [29] B. Véliz, A. Orpella, and S. Bermejo, "Capacitance study of a polystyrene nanoparticle capacitor using impedance spectroscopy," *Nanotech*, vol. 30, no. 40, article 405702, 2019.
- [30] P. Liu, C. Sun, G. Liu, Z. Jiang, and H. Zhao, "Ultra-small-sized multi-element metal oxide nanofibers: an efficient electrocatalyst for hydrogen evolution," *Nanoscale Adv*, vol. 4, no. 7, pp. 1758–1769, 2022.
- [31] A. B. J. Kharrata, S. Moussa, N. Moutiaab, K. Khirounib, and W. Boujelbena, "Structural, electrical and dielectric properties of Bi-doped Pr_{0.8-x}Bi_xSr_{0.2}MnO₃ manganite oxides prepared by sol-gel process," *Journal of Alloys and Compounds*, vol. 724, pp. 389–399, 2017.
- [32] M. H. Khan and S. Pal, "Frequency and Temperature Dependent impedance study in 50% BaTiO₃- 50% La_{0.7}Sr_{0.3}MnO₃ nanocomposite," *Advanced Materials Letters*, vol. 5, no. 7, pp. 384–388, 2014.

- [33] L. M. Housel, C. D. Quilty, A. Abraham et al., "Investigation of conductivity and ionic transport of $\text{VO}_2(\text{M})$ and $\text{VO}_2(\text{R})$ via electrochemical study," *Chemistry of Materials*, vol. 30, no. 21, pp. 7535–7544, 2018.
- [34] S. Halder, M. S. Sheikh, B. Ghosh, and T. P. Sinha, "Electronic structure and electrical conduction by polaron hopping mechanism in A_2LuTaO_6 (A= Ba, Sr, Ca) Double Perovskite Oxides," *Ceramics International*, vol. 43, no. 14, pp. 11097–11108, 2017.
- [35] P. Manimuthu, M. N. J. G. Mariam, R. Murugaraj, and C. Venkateswaran, "Metal-like to insulator transition in $\text{Lu}_3\text{Fe}_5\text{O}_{12}$," *Physics Letters A*, vol. 378, no. 20, pp. 1402–1406, 2014.
- [36] S. Pandey, D. Kumar, O. Prakash, and L. Pandey, "Impedance spectroscopy: a powerful technique for the study of electronic ceramics," in *Ceramic Materials - Synthesis, Characterization, Applications and Recycling*, Intechopen Book series, 2019.
- [37] R. Jacob, H. G. Nair, and J. Isac, "Impedance spectroscopy and dielectric studies of nanocrystalline iron doped barium strontium titanate ceramics," *Processing and Application of Ceramics*, vol. 9, no. 2, pp. 73–79, 2015.
- [38] S. K. Barik, R. N. P. Choudhary, and A. K. Singh, "Ac impedance spectroscopy and conductivity studies of $\text{Ba}_{0.8}\text{Sr}_{0.2}\text{TiO}_3$ ceramics," *Advanced Materials Letters*, vol. 2, no. 6, pp. 419–424, 2011.
- [39] K. L. L. Maldonado, P. de la Presa, M. A. de la Rubia et al., "Effects of grain boundary width and crystallite size on conductivity and magnetic properties of magnetite nanoparticles," *Journal of Nanoparticle Research*, vol. 16, no. 7, 2014.
- [40] H. S. Magar, R. Y. A. Hassan, and A. Mulchandani, "Electrochemical impedance spectroscopy (EIS): principles, construction, and biosensing applications," *Sensors*, vol. 21, no. 19, p. 6578, 2021.
- [41] A. K. Roy, K. Prasad, and A. Prasad, "Piezoelectric, impedance, electric modulus and AC conductivity studies on $(\text{Bi}_{0.5}\text{Na}_{0.5})_{0.95}\text{Ba}_{0.05}\text{TiO}_3$," *Processing and Application of Ceramics*, vol. 7, no. 2, pp. 781–791, 2013.
- [42] R. Tang, C. Jiang, W. Qian et al., "Dielectric relaxation, resonance and scaling behaviors in $\text{Sr}_3\text{Co}_2\text{Fe}_{24}\text{O}_{41}$ hexaferrite," *Scientific Reports*, vol. 5, no. 13645, pp. 1–11, 2015.
- [43] J. Hou and R. V. Kumar, "B-site multi-element doping effect on electrical properties of bismuth titanate ceramics," pp. 242–274, 2011, <http://Intechopen.com/books/ferroelectrics-physicaleffects>.

Research Article

Polymeric Droplets on SiO₂ Nanoparticles through Wastewater Treatment of Carbon-Based Contaminants in Photocatalytic Degradation

Abel Saka ¹, Jule Leta Tesfaye ^{1,2}, Lamessa Gudata ¹, S. Karthi,³ N. Nagaprasad ⁴,
Suraj Kumar Bhagat ⁵, Muhammad Yaqub,⁶ and Krishnaraj Ramaswamy ^{2,7}

¹College of Natural and Computational Science, Department of Physics, Dambi Dollo University, Ethiopia

²Centre for Excellence-Indigenous Knowledge, Innovative Technology Transfer and Entrepreneurship,
Dambi Dollo University, Ethiopia

³Department of Manufacturing Engineering and Technology, Central Institute of Petrochemicals Engineering and Technology,
Institute of Petrochemicals Technology, Bhubaneswar, Odisha, India

⁴Department of Mechanical Engineering, ULTRA College of Engineering and Technology, Madurai, 625 104 Tamil Nadu, India

⁵Department of Civil Engineering, Ton Duc Thang University, Ho Chi Minh City, Vietnam

⁶College of Civil and Environmental Engineering, Kumoh National Institute of Technology, Gumi, Republic of Korea

⁷Department of Mechanical Engineering, Dambi Dollo University, Ethiopia

Correspondence should be addressed to Jule Leta Tesfaye; laterajule@gmail.com, Lamessa Gudata; lamessagudata21@gmail.com, and Krishnaraj Ramaswamy; prof.dr.krishnaraj@dadu.edu.et

Received 3 May 2022; Revised 3 June 2022; Accepted 21 June 2022; Published 1 July 2022

Academic Editor: Balasubramani Ravindran

Copyright © 2022 Abel Saka et al. This is an open access article distributed under the Creative Commons Attribution License, which permits unrestricted use, distribution, and reproduction in any medium, provided the original work is properly cited.

The current work focus is on utilizing sunlight to catalyze the destruction of carbon-based (organic) pollutants. To increase the morphological area and improve the proficiency of the photocatalytic technique, sodium alginate was used as a polymeric tool and arranged as drop practice. SiO₂ nanoparticles were doped into sodium alginate droplets. The developed SiO₂ nanomaterials were able to spread the wavelength diversity throughout a significant wavelength constituency. In the photocatalytic technique employing the lot photoreactor, MB was used as a sample of carbon-based pollutants. The sunlight catalytic procedure was implemented from UV-Vis or photo light droplets. The analysis of the synthesized droplets was tested using devices X-ray diffraction (XRD), scanning electron microscopy (SEM), and photoluminescence (PL) analysis. Correspondingly, the influences of different concentrations of SiO₂ nanosolution (5 ml, 10 ml, 15 ml, and 20 ml) on the photocatalytic effectiveness of the deposited nanoparticles were studied. The output result revealed that sodium alginate beads doped with SiO₂ at 20 ml were able to reduce (degrade) 98.9% underneath UV-visible light. However, in the case of using other concentrations, SiO₂ at 5, 10, and 15 ml were able to degrade 50%, 56.7%, and 67.9% under sunlight, respectively, after 2 h.

1. Introduction

Nanotechnologies are making their way into all features of our survival; these technologies are being progressively used in pharmacological and medicinal applications, makeups and individual products, energy storing and effectiveness, water treatments and air purification, environmental remediation, chemical as well as biological antennas, military defense and explosives [1], and in numerous consumer products and

material. For instance, in the area of food, nanomaterials can be used to provide new tastes and flavors; functional food; hygienic food dispensation and packing; intelligent, frivolous, and strong packing; extended shelf life; and concentrated agrochemicals, colors, flavors, and preservers [2].

Nanotechnology is fundamentally operating a material at the molecular and atomic levels to create a novel structure, practical system with more significant electronic, optical, magnetic, conductive, and mechanical behavior [3, 4].

Nanotechnology is being travelled as hopeful machinery and has confirmed extraordinary undertakings in numerous fields together with wastewater desalination. Nanostructures suggest unmatched occasions to make more operative reagents as well as redox-active means for wastewater decontamination due to their minor size, great surface area, and ease of functionalization [5, 6]. Nanoparticles have been originated to be operative in the removal of numerous contaminants from wastewater such as weighty metals, carbon-based and inorganic diluters, dye as well as biological poisons, and pathogens that cause diseases like cholera and typhoid [7, 8].

Ecological contamination has extreme getting deleterious magnitudes in human life. Degradation of carbon-based contaminants, which have a poisonous influence on the health of manhood, has become an important title of the study [9]. Universally, about 1.2 billion populaces have no access to harmless drinking water, 2.6 billion people fight to fulfill basic hygiene, and millions of persons, predominantly children, have missed their survival from sicknesses interconnected via hazardous and contaminated water [10].

During the coloring and ultimate processes, fabric munches substantial volumes of water [11]. Usually, it used water dealing procedure of industrial wastes including chemical sleet, lime clotting, ion altercation, reverse osmosis, solvent withdrawal, and oxidation procedures [12–14]. Chemical corrosion management can be commonly effective toward the obliteration of chromophoric constructions of colorants. The kinds of oxidation procedures depend on ozone, hydrogen peroxide, and improved oxidation procedures with photocatalysis [15, 16]. Difficulties around using ozone (O_3) comprise its unpredictability and its dangerous nature because of solid and nonselective oxidizing energy. In the current study technique, water pigmentation was detached, but habitually complete mineralization is not accomplished; chlorination and ozonation cause decolonization through chemical retorts [17–19]. The spin-offs of chlorination are chlorinated carbon-based that may be more poisonous than the colorant itself. Varied photocatalysis is painstaking the most significant method in advanced oxidation procedures, which can be effectively used to corrode many carbon-based contaminants existing in aqueous arrangements [20–22].

The important benefit of the photocatalytic procedure is its inherent damaging nature; it does not include quantity transmission, it can take place under a normal state of affairs, and may transform the principal mineralization of carbon-based carbon into carbon dioxide (CO_2) [23–26]. Photocatalytic degradation includes the use of convinced semiconductors as reagents for the preparation of anions. The tenderness of silica dioxide (SiO_2) as a reagent for the photooxidation of carbon-based composites gains conventional attention because SiO_2 is abundant, cheap, influential, and environmentally friendly [27]. Sunlight power of a convinced wavelength is completed to reduction onto a semiconductor. The power of the incident light is comparable to the energy bandgap of the semiconductor; as electrons enthusiastically move from the valence band to the semiconductor's conduction band, holes move to the left [28, 29].

The electrons and holes can undergo successive oxidation and reduction responses to any classes that also impact the adsorbed on the surface of the semiconductor to make a contribution to the essential merchandise [30]. The electrons and holes can encounter successive oxidation and reduction reactions with any class. In brown algae, sodium alginate (SA) is a polysaccharide derived from β -D-mannuronic acid as well as an acid that polymerizes through a 1,4-glycosidic bond formed between the two acids. As a carrier for nanomaterials, it is a nontoxic, logically biodegradable green material that is environmentally friendly. Occurrences of sodium alginate (SA) as a biopolymer rise bond of nanoparticles. A rationale for using sodium alginate as an important carrier substantial for nanoparticles was based on the likelihood of having accurate adsorption of carbon-based molecules; the outcome depends on their electrical custody, as a result of collaboration with the undesirable carboxylate collections on alginate as a carrier substantial for nanoparticles [31].

Numerous researches have been conducted to attain the operation of observable light for TiO_2 material, like transitional metallic ions (ZnO , SiO_2) and nonmetal element doping such as carbon nanotube (C-N-T). Nonmetal element doping conventions bandgap of titanium dioxide by providing a novel mixture energy band whose excite level is slightly higher than that of the valence band of titanium dioxide (TiO_2) [32–35]. But these methods of preparation cannot improve wastewater treatment unless the alteration of property of SiO_2 nanoparticle. The objective of the current study is the deal with the carbon-based contaminant by deposition of sodium alginate droplets doped with SiO_2 and varying the concentration of SA-doped SiO_2 nanoparticles (5, 10, 15, and 20 ml). The enactment of the synthesized polymeric droplets in water treatment of carbon-based contaminant using photocatalysis procedure was assessed.

2. Experimental Detail

2.1. Constituents and Chemicals. Sodium alginate (SA) was used as a polymeric substrate because it was readily available from laboratory supplies, Ethiopia. Methyl blue that serves as a specimen of carbon-based substance was purchased from Addis Ababa, Ethiopia. The supplementary chemicals such as diluters and inorganic salts were of logical reagent rating and lacked supplementary sanitization.

2.2. The Process of Preparing Droplets. It was necessary to liquefy sodium alginate in order to use rousing double-distilled water. In this study, silica nanoparticles (SiO_2) were isolated in water over a 2-hour period and spread out using sonication; the spreading was varied depending on the polymer elucidation. In a conical flask containing cross-linking solution that controlled glutaraldehyde (99.8%) in an 80:20 mixture of acetones (99.9%) and water, the combination was decanted as a drop way to custom droplets after stringing and allowing a doped polymer bath with nanomaterials. The obtained droplets were allowed to harden in this solution for 48 hours before being washed so many times with tap water until the pH value reached 7, at which point

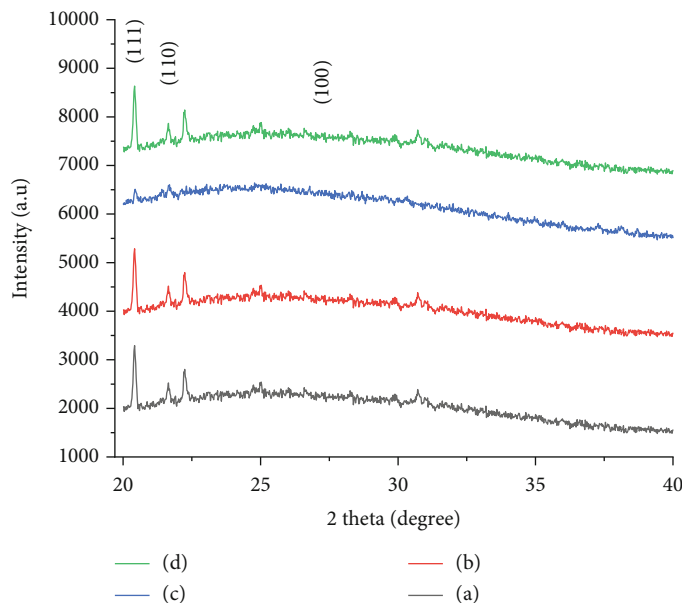


FIGURE 1: XRD pattern of SA-doped SiO_2 nanomaterials at a different concentration as (a) 5 ml, (b) 10 ml, (c) 15 ml, and (d) 20 ml, respectively.

TABLE 1: The crystalline parameters gained from XRD results.

Samples	The volume of SA concentration	2 theta (2θ)	The volume of SA concentration	Theta (2θ)	Crystal size D (nm)
1	5	19.94396	9.97198	3.55557	2.268595
2	10	21.67296	10.83648	0.0883	91.60278
3	15	23.83215	11.916075	16.85256	0.481781
4	20	43.98658	21.99329	5.27112	1.62542

it was pounded and stored in double-distilled water until the next characterization.

2.3. Photocatalytic Experimentations. Consignment photo reactor involves double covers which were through Pyrex. An innermost tube has a radius of 2.50 cm and 35 cm lengthy. An Ultra Violet-C spotlight with a 20 W tiny pressure mercury type lamp was assembled in the middle of the reactor. The outer tube was covered with protective black foils, which collected all of the UV lamp radiations that entered the object constituent of methyl blue liquid. Air was completely eradicated from the mixture by using an air drive, which created a good spreading and an incessant motion of the used droplet all over the laboratory space. The experimental procedure was started after 25 minutes of interaction time in complete darkness, in the midst of the ready methyl blue solution as well as the utilized droplets that have been motioned into the ultraviolet reactor and achieved a noble dispersal. Subsequently, the ultraviolet lamp was opened to start the photocatalytic procedure. The specimen of the verified solution was created by taking a 10 millilitre volume syringe every 1 h.

The concentration alteration of methyl blue (MB) was dogged by the UV-Vis spectrophotometer. The following formula was used to evaluate the degradation rate of MB solution:

$$d = \frac{C_0 - C}{C_0} \times 100\% = \frac{A_0 - A}{A_0} \times 100\%, \quad (1)$$

where d is the deprivation rate and C_0 , A_0 , C , and A are indicating meditation and absorbance of the MB solution at the absorption topmost and 464 nm in adsorption steadiness prior to and following ultraviolet treatment, respectively [36].

2.4. Analysis of Polymeric Droplets

2.4.1. Enlargement, Transfiguration, and Gelation (%) Calibration. The enlargement, transfiguration, and gelation (%) for droplets were restrained as a suggestion of impenetrable sodium alginate percentage in aquatic. Dry droplet well-known weights were engrossed in water at 27°C till equilibrium had been get hold. Droplets were detached and strategized by a permeable paper rapidly deliberated. The enlargement (%) was

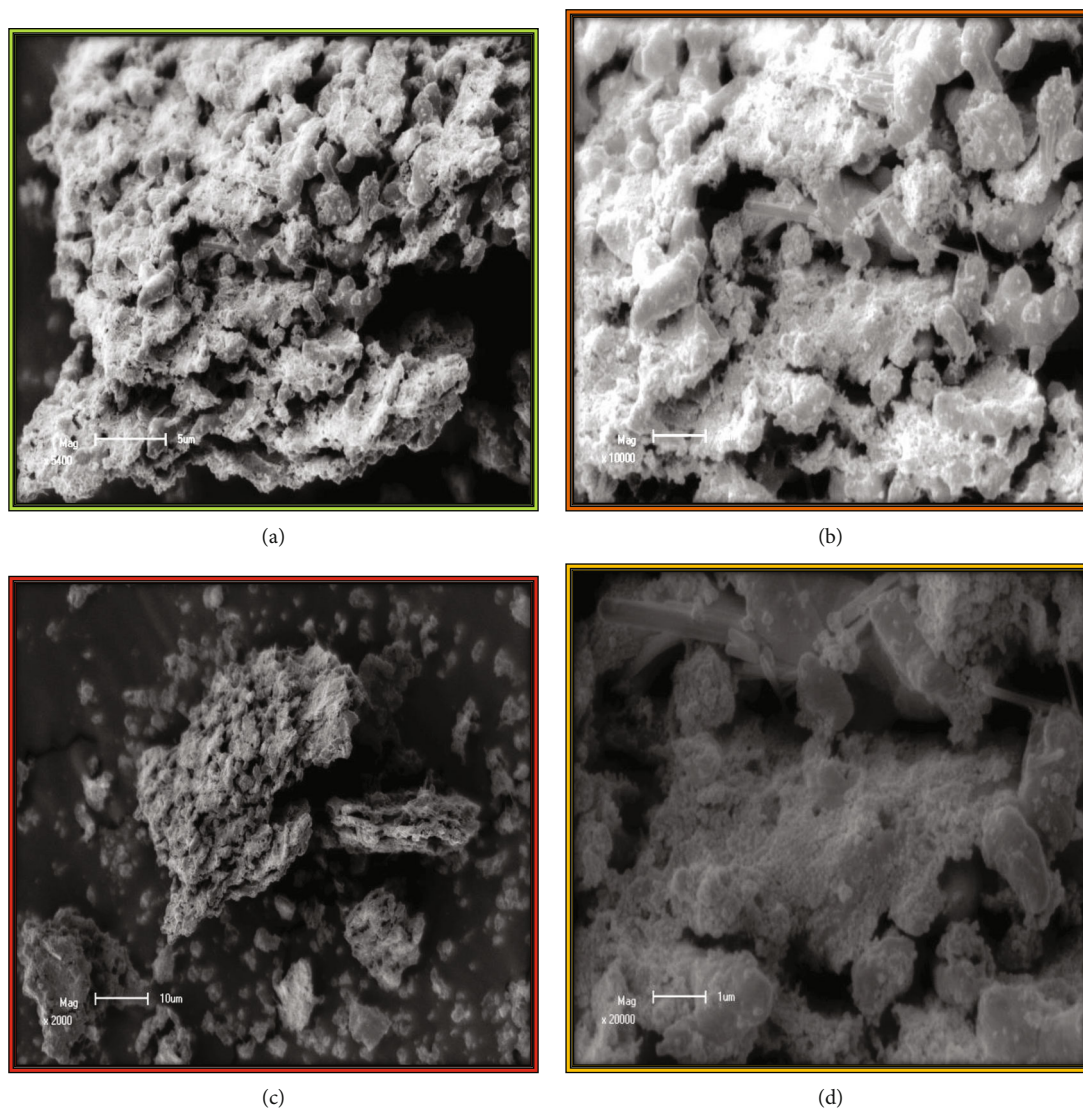


FIGURE 2: SEM micrograph of SA-doped SiO_2 nanomaterials at a different concentration as (a) 5 ml, (b) 10 ml, (c) 15 ml, and (d) 20 ml, respectively.

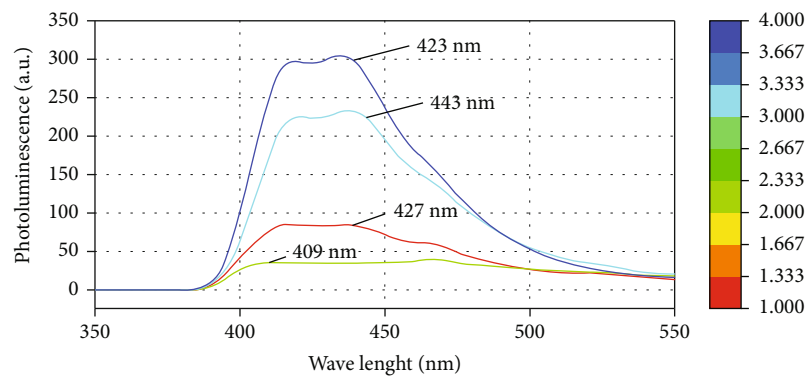


FIGURE 3: Photoluminescence spectral analysis of SA-doped SiO_2 nanomaterials at a different concentration as (a) 5 ml, (b) 10 ml, (c) 15 ml, and (d) 20 ml, respectively.

TABLE 2: The influence of SA concentration on parameters is discussed.

Sample	Sodium alginate concentration (ml)	Enlargement (%)	Transfiguration (%)	Gelation (%)
1	5 ml	58.8	93.3	88.7
2	10 ml	67.1	95.1	90.9
3	15 ml	75.6	92.9	91.5
4	20 ml	82.7	96.5	93.9

measured as follows:

$$\text{Enlargement}(\%) = \frac{(W_{\text{wet}} - W_{\text{dry}})}{W_{\text{dry}}} \times 100, \quad (2)$$

where W_{dry} and W_{wet} indicate the weights of the dry and wet droplets, correspondingly.

The percentages of transfiguration and gelation of the synthesized droplets were deliberated as follows:

$$\text{Transfiguration}(\%) = \frac{W_{\text{dry}}}{W_0} \times 100, \quad (3)$$

$$\text{Gelation}(\%) = \frac{W_{\text{dryhot}}}{W_0} \times 100. \quad (4)$$

3. Results and Discussion

3.1. Structural Characterization. The rock crystal configurations of the organized droplets were characterized by X-ray diffractometry (X'Pert PRO, PANalytical) using copper potassium alpha (α) particle emission in the angular district of $2\theta = 19^\circ$ to 43° . The apparatus was activated at 40 kilovolt, and the spectra were noted down at a skimming speed of $8^\circ/\text{minute}$.

As piloted in Figure 1, XRD pattern reveals that the deposited beads were crystalline with hkl indexes crystal plane of (111), (110), and (100), and the shape of the prepared materials was regular spherical. As the concentration of SA increased, the peaks were increased. This result is in agreement with the reported works [37].

By using the Scherer formula, the average crystal size $D = 23.99$ nm is calculated.

The crystalline parameters gained from XRD results are discussed in Table 1.

3.2. Morphological Characterization. The microscopic micrograph of the arranged and the doped sodium alginate droplets with silicate (SiO_2) nanoparticles was conducted using a scanning electron microscopy (SEM) FEI, Quanta 250 FEG type.

All sodium alginate droplet pictures with a scanning electron microscope (SEM) showed a comparatively regular spherical form. The external surface was rather uneven and grooved with many crinkles and wrinkles, which increased contact surface area between carbon-based dyes and the composite droplets and afford more vigorous places, thus refining their adsorption enactments, as shown in Figure 2, and this result was in agreement with previous work of [38–40]. Doping SA with SiO_2 (Figures 2(b) and 2(d)) reveal the dispersion of SiO_2 nanomaterial from low to high con-

centrations. By increasing SiO_2 concentration, there was an agglomeration of nanomaterial on the superficial. Images of droplets in Figures 2(a) to 2(d) divulge the SA doped with a mixture of SiO_2 ; there is uneven arrival caused by the existence of nanomaterial, which establishes themselves as combinations throughout the SA environment [41].

3.3. Photoluminescence (PL) Spectral Analysis. Photoluminescence spectroscopy (PL) is a noncontact, nondestructive technique to investigate the optical properties of the prepared materials. Strength and specter at the ease of producing photoluminescence is a straight calibration of significant material behaviors, including bandgap determination, impurity stages, and defect discovery; that is, the photoluminescence spectroscopy at low specimen temperature habitually tells ghostlike peaks related with contaminations involved within the multitude material [42–45]. An extraordinary sensitivity of these methods is possible to classify enormously little meditations of premeditated and unintentional doping which can powerfully upset material quality and instrumental enactment.

To explain the optical behaviors of the prepared SA-doped SiO_2 nanomaterials, photoluminescence is also applied. In the wavelength range from 350 nm to 550 nm at low concentration, shown in Figure 3, the photoluminescence (PL) spectra of the synthesized were testified. The maximum PL hardness is mostly due to self-trapped exciton recombination, prepared from particle size, which what we call defect centres. The PL intensity decreases instantaneously with the ageing time for all higher concentrations [46–48]. In comparison, the photoluminescence intensity for wavelengths of higher wavelength for 60 min and 50 min is smaller than 40 min for wavelength.

Figure 3 shows the optical properties of the prepared material with the application in organic wastewater treatment.

The influence of SA concentration in the preparation of beads is calculated and explained in Table 2. As the concentration of SA increases, the enlargement (%) increases, and gelation (%) increases while transfiguration increases for samples 1 and 2. The decreases at sample 3 then increase at sample 4 [49, 50].

4. Conclusion

A novel SA nanocomposite with high enlargement volume and relatively high adsorption efficiency for methyl blue (MB) dyes was prepared. Methyl blue solution was successfully decolorized by photocatalytic reaction under feeble illumination conditions. In the current work, the concerning issue is the sunlight catalytic degradation procedure to

eradicate the carbon-based (organic) contaminants. The prepared SiO₂ nanomaterials were accomplished to spread wavelength variety to the visible wavelength constituency. Methyl blue (MB) was taken as a specimen of carbon-based contaminants in the photocatalytic procedure using the lot photo reactor. The sunlight catalytic procedure was implemented from UV-Vis or photo light droplets. The analysis of synthesized droplets was tested using XRD, scanning electron microscopy (SEM), and photoluminescence (PL) characterization devices. Correspondingly, the influences of different concentrations of SiO₂ nanosolution (5 ml, 10 ml, 15 ml, and 20 ml) on the photocatalytic effectiveness of the deposited nanoparticles were studied. The output result revealed that sodium alginate beads doped with SiO₂ at 20 ml were able to reduce (degrade) 98.9% underneath UV-visible light, although in the case of using other concentrations, SiO₂ at 5, 10, and 15 ml were able to degrade 50%, 56.7%, and 67.9% under sunlight, respectively, after 2 h. Therefore, the nanocomposite is promising for the degradation of carbon-based contaminants.

Data Availability

The data used to support the findings of this study are included within the article.

Conflicts of Interest

The authors declare no conflict of interest.

Acknowledgments

This study was performed as a part of the employment of the authors (Dambi Dollo University).

References

- [1] K. Jain, A. S. Patel, V. P. Pardhi, and S. J. S. Flora, "Nanotechnology in wastewater management: a new paradigm towards wastewater treatment," *Molecules*, vol. 26, no. 6, p. 1797, 2021.
- [2] M. Batool, A. Shafeeq, B. Haider, and N. M. Ahmad, "TiO₂ nanoparticle filler-based mixed-matrix PES/CA nanofiltration membranes for enhanced desalination," *Membranes*, vol. 11, no. 6, p. 433, 2021.
- [3] Y. S. Khoo, W. J. Lau, Y. Y. Liang, M. Karaman, M. Gürsoy, and A. F. Ismail, "Eco-friendly surface modification approach to develop thin film nanocomposite membrane with improved desalination and antifouling properties," *Journal of Advanced Research*, vol. 36, pp. 39–49, 2022.
- [4] B. Shrestha, M. Ezazi, and G. Kwon, "Engineered nanoparticles with decoupled photocatalysis and wettability for membrane-based desalination and separation of oil-saline water mixtures," *Nanomaterials*, vol. 11, no. 6, p. 1397, 2021.
- [5] G. Ma, Z. Almansoori, B. Khorshidi, and M. Sadrzadeh, "Development of antifouling thin film nanocomposite polyamide membrane using ITO nanoparticles," *Journal of Material Sciences & Engineering*, vol. 10, no. 5, 2021.
- [6] A. Ghaffar, S. Kiran, M. A. Rafique et al., "Citrus paradisi fruit peel extract mediated green synthesis of copper nanoparticles for remediation of Disperse Yellow 125 dye," *Desalination and Water Treatment*, vol. 212, pp. 368–375, 2021.
- [7] O. N. Borisova, I. G. Doronkina, and V. M. Feoktistova, "Resource-saving nanotechnologies in waste water treatment," *Nanotechnologies in Construction*, vol. 13, no. 2, pp. 124–130, 2021.
- [8] D. A. Tatarinov, S. R. Sokolnikova, and N. A. Myslitskaya, "Applying of chitosan-TiO₂ nanocomposites for photocatalytic degradation of anthracene and pyrene," *Journal of Biomedical Photonics & Engineering*, vol. 7, no. 1, p. 010301, 2021.
- [9] A. M. El Shafey, M. K. Abdel-Latif, and H. M. Abd El-Salam, "The facile synthesis of poly (acrylate/acrylamide) titanium dioxide nanocomposite for groundwater ammonia removal," *Desalination and Water Treatment*, vol. 212, pp. 61–70, 2021.
- [10] A. Juliani, S. Rahmawati, and M. Yoneda, "Heavy metal characteristics of wastewater from batik industry in Yogyakarta Area, Indonesia," *International Journal*, vol. 20, no. 80, pp. 59–67, 2021.
- [11] E. Wibowo, M. Rokhmat, D. Y. Rahman, R. Murniati, and M. Abdullah, "Batik wastewater treatment using TiO₂ nanoparticles coated on the surface of plastic sheet," *Procedia Engineering*, vol. 170, pp. 78–83, 2017.
- [12] B. M. P. Pereira and B. P. Backx, "Nanotechnology in water treatment: an optimistic perspective for the near future," *Journal of Nanotechnology and Nanomaterials*, vol. 2, no. 1, pp. 51–56, 2021.
- [13] K. R. Reyes and D. B. Robinson, *WO₃/TiO₂ Nanotube Photocatalysts for Solar Water Splitting with Simultaneous Wastewater Treatment*, Sandia National Laboratories, Springfield, 2013.
- [14] A. O. Sojobi, T. F. Awolusi, G. B. Aina, O. L. Oke, M. Oladokun, and D. O. Oguntayo, "Ternary and quaternary blends as partial replacement of cement to produce hollow sandcrete blocks," *Heliyon*, vol. 7, no. 6, p. e07227, 2021.
- [15] M. Dabaieh, J. Heinonen, D. El-Mahdy, and D. M. Hassan, "A comparative study of life cycle carbon emissions and embodied energy between sun-dried bricks and fired clay bricks," *Journal of Cleaner Production*, vol. 275, p. 122998, 2020.
- [16] D. Prasad, A. Pandey, and B. Kumar, "Sustainable production of recycled concrete aggregates by lime treatment and mechanical abrasion for M40 grade concrete," *Construction and Building Materials*, vol. 268, p. 121119, 2021.
- [17] R. Roychand, J. Li, S. De Silva, M. Saberian, D. Law, and B. K. Pramanik, "Development of zero cement composite for the protection of concrete sewage pipes from corrosion and fatbergs," *Resources, Conservation and Recycling*, vol. 164, p. 105166, 2021.
- [18] A. M. Ghrair, A. J. Said, N. Aldaoud, R. Miqdadi, and A. A. Ahmad, "Characterisation and reverse engineering of eco-friendly historical mortar: qasr tuba, desert castles in Jordan," *Journal of Ecological Engineering*, vol. 22, no. 3, pp. 121–134, 2021.
- [19] O. Lawrence, "Preventing Water Ingress into Asphaltic Pavement through Application of the Hydrated Lime," vol. 1, 2021.
- [20] D. Vaičiukynienė, A. Mikelionienė, A. Kantautas, A. Radzevičius, and D. Bajare, "The influence of zeolitic by-product containing ammonium ions on properties of hardened cement paste," *Minerals*, vol. 11, no. 2, p. 123, 2021.
- [21] E. Kokkinos and A. I. Zouboulis, "The chromium recovery and reuse from tanneries: a case study according to the principles of circular economy," in *Leather and Footwear Sustainability: Manufacturing, Supply Chain, and Product Level Issues*, pp. 123–157, Springer, Singapore, 2020.

- [22] G. Kaladharan, T. Szeles, S. M. Stoffels, and F. Rajabipour, "Novel admixtures for mitigation of alkali-silica reaction in concrete," *Cement and Concrete Composites*, vol. 120, p. 104028, 2021.
- [23] B. A. Mir, "Laboratory study on the effect of plastic waste additive on shear strength of marginal soil," in *Sustainable Civil Engineering Practices*, pp. 89–99, Springer, Singapore, 2020.
- [24] F. Jroundi, K. Elert, E. Ruiz-Agudo, M. T. Gonzalez-Muñoz, and C. Rodriguez-Navarro, "Bacterial diversity evolution in Maya plaster and stone following a bio-conservation treatment," *Frontiers in Microbiology*, vol. 11, p. 2824, 2020.
- [25] K. R. Ahern, "Analysis of late preclassic period lime plaster floors at Holmul, Guatemala," *Journal of Archaeological Science: Reports*, vol. 36, p. 102883, 2021.
- [26] E. M. Abdel Hamid, "Investigation of using granite sludge waste and silica fume in clay bricks at different firing temperatures," *HBRC Journal*, vol. 17, no. 1, pp. 123–136, 2021.
- [27] K. C. Onyelowe, F. E. Jalal, M. E. Onyia, I. C. Onuoha, and G. U. Alaneme, "Application of gene expression programming to evaluate strength characteristics of hydrated-lime-activated rice husk ash-treated expansive soil," *Applied Computational Intelligence and Soft Computing*, vol. 2021, Article ID 6686347, 17 pages, 2021.
- [28] Q. D. Nguyen, A. Castel, T. Kim, and M. S. Khan, "Performance of fly ash concrete with ferronickel slag fine aggregate against alkali-silica reaction and chloride diffusion," *Cement and Concrete Research*, vol. 139, p. 106265, 2021.
- [29] A. Al-Hamrani, M. Kucukvar, W. Alnahhal, E. Mahdi, and N. C. Onat, "Green concrete for a circular economy: a review on sustainability, durability, and structural properties," *Materials*, vol. 14, no. 2, p. 351, 2021.
- [30] A. R. Kushnir, M. J. Heap, L. Griffiths et al., "The fire resistance of high-strength concrete containing natural zeolites," *Cement and Concrete Composites*, vol. 116, p. 103897, 2021.
- [31] M. F. Iqbal, Q. F. Liu, I. Azim et al., "Prediction of mechanical properties of green concrete incorporating waste foundry sand based on gene expression programming," *Journal of Hazardous Materials*, vol. 384, p. 121322, 2020.
- [32] A. M. Pitarch, L. Reig, A. Gallardo, L. Soriano, M. V. Borrachero, and S. Rochina, "Reutilisation of hazardous spent fluorescent lamps glass waste as supplementary cementitious material," *Construction and Building Materials*, vol. 292, p. 123424, 2021.
- [33] K. Amreen and S. Goel, "Review—Miniaturized and microfluidic devices for automated nanoparticle synthesis," *ECS Journal of Solid State Science and Technology*, vol. 10, no. 1, p. 017002, 2021.
- [34] H. N. Rosly, K. S. Rahman, S. F. Abdullah et al., "The role of deposition temperature in the photovoltaic properties of RF-sputtered CdSe thin films," *Crystals*, vol. 11, no. 1, p. 73, 2021.
- [35] V. Singh, P. V. More, E. Hemmer, Y. K. Mishra, and P. K. Khanna, "Magic-sized CdSe nanoclusters: a review on synthesis, properties and white light potential," *Materials Advances*, vol. 2, no. 4, pp. 1204–1228, 2021.
- [36] S. Pokhriyal and S. Biswas, "Inducing ferromagnetism in surface stabilised intrinsic CdSe nanoparticles by a simple process," *Materials Science and Technology*, vol. 36, no. 13, pp. 1503–1506, 2020.
- [37] P. Maldonado-Altamirano, L. A. Martínez-Ara, M. de los Angeles Hernandez-Perez, J. R. Aguilar-Hernández, M. López-López, and J. Santoyo-Salazar, "Laser wavelength dependent size of CdSe nanoparticles synthesized by laser fragmentation in liquid medium," *Optical Materials*, vol. 111, p. 110637, 2021.
- [38] M. M. Abdullah, M. Faisal, J. Ahmed, F. A. Harraz, M. Jalalah, and S. A. Alsareii, "Sensitive detection of aqueous methanol by electrochemical route using mesoporous α -Fe₂O₃Doped CdSe nanostructures modified glassy carbon electrode," *Journal of the Electrochemical Society*, vol. 168, no. 5, p. 057525, 2021.
- [39] S. Abel, J. Leta Tesfaye, R. Kiran et al., "Studying the effect of metallic precursor concentration on the structural, optical, and morphological properties of zinc sulfide thin films in photovoltaic cell applications," *Advances in Materials Science and Engineering*, vol. 2021, 6 pages, 2021.
- [40] N. Arif and C. S. Fun, "Impact on development of ZnS nanoparticles thin film deposited by chemical bath deposition and spin coating," *International Journal of Advanced Engineering and Nano Technology*, vol. 4, no. 5, pp. 1–4, 2021.
- [41] N. I. M. Fauzi, Y. W. Fen, N. A. S. Omar et al., "Nanostructured chitosan/maghemite composites thin film for potential optical detection of mercury ion by surface plasmon resonance investigation," *Polymers*, vol. 12, no. 7, p. 1497, 2020.
- [42] T. Debele and F. Gashaw, "Effect of temperature on morphological structural and optical properties of cadmium selenide (CdSe) thin films deposited by chemical bath deposition method," *Advances in Life Science and Technology*, vol. 67, pp. 12–16, 2018.
- [43] S. Faisal, H. Jan, S. A. Shah et al., "Green synthesis of zinc oxide (ZnO) nanoparticles using aqueous fruit extracts of Myristica fragrans: their characterizations and biological and environmental applications," *ACS Omega*, vol. 6, no. 14, pp. 9709–9722, 2021.
- [44] A. Jayachandran, T. R. Aswathy, and A. S. Nair, "Green synthesis and characterization of zinc oxide nanoparticles using Cayratia pedata leaf extract," *Biochemistry and Biophysics Reports*, vol. 26, p. 100995, 2021.
- [45] R. A. Gonçalves, R. P. Toledo, N. Joshi, and O. M. Berengue, "Green synthesis and applications of ZnO and TiO₂ nanostructures," *Molecules*, vol. 26, no. 8, p. 2236, 2021.
- [46] M. C. Patino-Portela, P. A. Arciniegas-Grijalba, L. P. Mosquera-Sanchez et al., "Effect of method of synthesis on antifungal ability of ZnO nanoparticles: chemical route vs green route," *Advances in Nano Research*, vol. 10, no. 2, pp. 191–210, 2021.
- [47] S. Awan, K. Shahzadi, S. Javad, A. Tariq, A. Ahmad, and S. Ilyas, "A preliminary study of influence of zinc oxide nanoparticles on growth parameters of Brassica oleracea var italic," *Journal of the Saudi Society of Agricultural Sciences*, vol. 20, no. 1, pp. 18–24, 2021.
- [48] M. S. E. D. Salem, A. Y. Mahfouz, and R. M. Fathy, "The antibacterial and antihemolytic activities assessment of zinc oxide nanoparticles synthesized using plant extracts and gamma irradiation against the uro-pathogenic multidrug resistant Proteus vulgaris," *Bio Metals*, vol. 34, no. 1, pp. 175–196, 2021.
- [49] M. S. El-Ansary, R. A. Hamouda, and M. M. Elshamy, "Using biosynthesized zinc oxide nanoparticles as a pesticide to alleviate the toxicity on banana infested with parasitic-nematode," *Waste and Biomass Valorization*, vol. 13, no. 1, pp. 405–415, 2022.
- [50] M. Raafat, A. S. El-Sayed, and M. T. El-Sayed, "Biosynthesis and anti-mycotoxigenic activity of Zingiber officinale Roscoe-derived metal nanoparticles," *Molecules*, vol. 26, no. 8, p. 2290, 2021.

Research Article

Antibacterial Efficacy of Phytosynthesized Multi-Metal Oxide Nanoparticles against Drug-Resistant Foodborne Pathogens

Vijayalakshmi Selvakumar ^{1,2} Karnan Muthusamy,^{2,3} Amitava Mukherjee ⁴
Shahana Farheen S.,⁵ Ramachandran Chelliah ¹ Kaliyan Barathikannan ¹
Deog-Hwan Oh ¹ Ramamoorthy Ayyamperumal ⁶ and Shankar Karuppnanan ⁷

¹Food Science and Biotechnology, School of Agriculture and Life Sciences, Kangwon National University, Chuncheon, Republic of Korea

²Askoscen Probiotics (R&D), Tiruchirappalli, Tamil Nadu, India

³Grassland and Forage Division, National Institute of Animal Science, Republic of Korea

⁴Centre for Nanobiotechnology, Vellore Institute of Technology, Vellore, India

⁵Department of Microbiology, Shrimati Indira Gandhi College, Affiliated to Bharathidasan University, 620 002, Tamil Nadu, Tiruchirappalli, India

⁶MOE Key Laboratory of Western China's Environmental System, College of Earth and Environmental Sciences, Lanzhou University, Lanzhou 730000, China

⁷Department of Applied Geology, School of Applied Natural Sciences, Adama Science & Technology University, Adama, Ethiopia

Correspondence should be addressed to Vijayalakshmi Selvakumar; vijiselva10@gmail.com and Deog-Hwan Oh; deoghwa@kangwon.ac.kr

Received 5 April 2022; Revised 14 May 2022; Accepted 26 May 2022; Published 22 June 2022

Academic Editor: Pounsamy Maharaja

Copyright © 2022 Vijayalakshmi Selvakumar et al. This is an open access article distributed under the Creative Commons Attribution License, which permits unrestricted use, distribution, and reproduction in any medium, provided the original work is properly cited.

Human health is threatened worldwide by microbial infections. Antibiotic overuse and misuse have resulted in antimicrobial-resistant bacteria. To battle such resistant microbes, we are looking for safe and alternative antimicrobial treatments, and the advent of nanotechnology holds promise in this regard. Metal oxide nanoparticles have emerged as a promising alternative source for combating bacteria resistant to various antibiotics over the last two decades. Due to their diverse physicochemical characteristics, metal oxide nanoparticles can operate as antibacterial agents through various methods. In the present research, six types of metal oxide NPs were synthesized and characterized (XRD, FTIR, SEM with EDAX, and TEM) from different plants such as *Hydrangea paniculata* (for NiO NP synthesis), *Plectranthus amboinicus* (for ZnO-NP synthesis), and *Andrographis paniculata* (V_2O_5 NPs). On the other hand, drug-resistant pathogens were isolated from clinical samples, those who suffered from foodborne illness. V_2O_5 NPs produced from *Andrographis paniculata* plant extract have much higher bactericidal efficacy than other metal oxide NPs against all three bacterial strains. Sensitive bacteria included *S. aureus* and *E. coli*, followed by *K. pneumoniae*. As a result, structural characterization was used to further screen V_2O_5 NPs. The orthorhombic structure of the crystallites was confirmed by XRD, with an average crystallite size of 20 nm. The absorbance spectrum and functional groups were identified using UV-visible spectral analysis and FTIR. SEM and EDX identified spherical-shaped NPs, and particle size (58 nm) was confirmed by transmission electron microscopy (TEM). As a result, we hypothesized that bioinspired V_2O_5 -NPs could be employed as a possible antibacterial agent against drug-resistant pathogenic bacteria to replace currently existing inefficient antibacterial drugs.

1. Introduction

Foodborne infectious diseases caused by microbial pathogens are considered as a serious issue in developed as well as developing countries [1]. Diseases like hepatitis, typhoid, and cholera are often caused owing to the contamination in food materials by microbes such as *E.coli*, *Salmonella*, and *Shigella* and are easily transmitted through the unhygienic handling of food, contaminated water, and contact with animals [2]. Several researchers reported the emerging of pathogens resistant to currently available antimicrobial agents as a serious effect on human health [3]. Antibiotic resistance has reached epidemic proportions in the previous decade, according to the World Health Organization, posing a severe threat to world health [4]. Each year, antibiotic-resistant bacteria kill about 700,000 people worldwide [5]. Researchers from the public, private, academic, and food industries are all working hard to combat the growing epidemic of drug-resistant diseases [6]. As a result, progress is contingent on well-coordinated activities across sectors to address cross-cutting concerns in animal and human health, agriculture, food, and the environment [5]. The drug-resistant pathogens are developed by the changes in gene expression by environmental stress and overuse or misuse of antibiotics [7, 8]. In this scenario, potential antibacterial agents are highly required to treat infections caused by drug-resistant pathogens. Other than the medical field, antibacterial agents are crucially playing a role in the textile industry, paint industries, water purification system, food packaging, and preservation field [9].

Nanotechnology is booming as a fascinating branch of science and produces nanoscale (1-100 nm) materials for broad applications [10]. In science and technology, metal oxide NPs play a crucial role in many applications. In medical applications, the usage of nanomaterials and metal oxide NPs is rapidly mounting in cancer treatment, antimicrobial therapeutic agent, biosensing, chemotherapy, and imaging purposes due to its specific applications like surface to volume, size, and morphological features [11–13]. Various physical and chemical methods are adopted for the synthesis of metal oxide NPs [14]. Physical methods require more energy, and chemical approaches utilize a range of chemicals as a precursor and reducing agents that produce toxic by-products during the synthesis of nanoparticles, and yield percentage is also low [15, 16]. To overcome the limitations of conventional methods, green synthetic technologies are gaining a lot of traction in current materials science development and study. Green nanoparticle synthesis, as created by regulation, clean-up, and control and remediation methods, will primarily improve their eco-friendliness. As a result, several components such as pollution reduction, nontoxic solvent use, waste prevention, and renewable feedstock can be used to characterize certain basic principles of biosynthesis [17]. Biosynthesis is required to avoid the development of toxic by-products in a sustainable and environmentally responsible manner. Several biological entities, such as plant extracts, bacteria, and algae, have been accommodated by biosynthesis of metal and metal oxide nanoparticles. Using the plant is a quick, easy, and simple way to synthesis metal

and metal oxide nanoparticles among the available green ways to nanoparticle creation [18].

The diverse group of researchers reported the activity of green synthesized metal oxide NPs against drug-resistant pathogens. The metal oxide NPs developed by green route which include ZnO [19], CuO [20], NiO [21], MoO₃ [22], and V₂O₅ [23] showed efficient bactericidal activity against an extensive range of drug-resistant bacteria such as *E. coli*, *S. aureus*, *K. pneumoniae*, *B. cereus*, *L. monocytogenes*, and *S. typhi*. Gram-positive and Gram-negative bacteria, as well as spores resistant to high temperature and high pressure, were all killed by ZnO nanoparticles [24]. CuO nanoparticles demonstrated substantial antibacterial activity against a variety of bacterial strains (*E. coli*, *P. aeruginosa*, *K. pneumoniae*, *Enterococcus faecalis*, *Shigella flexneri*, *S. typhimurium*, *Proteus vulgaris*, and *S. aureus*) [25]. *E. coli* and *E. faecalis* were the pathogens with the highest sensitivity to CuO nanoparticles. The most vulnerable strains to NiO nanoparticles were *Bacillus licheniformis* and *Bacillus subtilis*, while *Klebsiella pneumoniae* was the least susceptible strain in the zone of inhibition [26]. V₂O₅ nanoparticles had good antibacterial efficacy against pathogens including *Escherichia coli* and *Staphylococcus aureus* [27]. An outstanding antimicrobial activity against *Staphylococcus aureus*, *Escherichia coli*, *Aspergillus flavus*, and *Candida albicans* was shown by MoO₃ nanoparticles [28].

Moreover, Hajipour et al. [29] reported the reusability of metal oxide NPs as an antibacterial agent. The present evaluation is aimed at exposing the antibacterial potency multi-type metal oxide NPs synthesized by plant extracts against drug-resistant pathogens. In this present study, the metal oxide NPs with higher potency have been selected for further characterization studies.

2. Materials and Methods

2.1. Isolation and Identification of ESBL Bacterial Strains.

The drug-resistant pathogens were isolated from clinical samples (stool) collected from patients infected with foodborne illness. The ESBL strains were screened based on the antibiotic sensitivity test and double-disk potentiation procedures suggested by the National Committee for Clinical Laboratory Standards (NCCLS) using two types of drugs, ceftazidime (30 µg) and ceftazidime+clavulanic acid (30 µg/10 µg). The isolated drug-resistant strains were cultured in nutrient agar medium composed of peptone (10 g), beef extract (1 g), sodium chloride (5 g), agar (10 g), and double-distilled (DD) water (1000 mL).

2.2. Phytosynthesis of Metal Oxide Nanoparticles

2.2.1. Preparation of Plant Extracts. The metal oxide NPs were synthesized using aqueous extracts obtained from three types of plants such as *Hydrangea paniculata* (for NiO NP synthesis), *Plectranthus amboinicus* (for ZnO-NP synthesis), and *Andrographis paniculata* collected from local areas of Tiruchirappalli District, Tamil Nadu. For the preparation of CuO, V₂O₅, and MoO₃ NPs, leaves of *A. paniculata* were cleaned thoroughly by distilled water and dried at 303 K.

TABLE 1: Bactericidal activity of metal oxide NPs against *S. aureus*.

Nanoparticles	Zone formation (mm) at different concentrations			
	Control (d.H ₂ O)	25 mg/50 μ L	25 mg/100 μ L	50 mg/50 μ L
MoO ₃	—	—	—	—
CuO	—	—	—	18 \pm 1.41
NiO	—	7 \pm 2.8	9 \pm 1.09	18 \pm 2.1
ZnO	—	—	—	—
V ₂ O ₅	—	11 \pm 1.4	16 \pm 0.7	17 \pm 0.4

Dried leaves were weighed (5 g), immersed in 100 mL of DD water, and boiled at 353 K for 1 h to obtain the extract. The extract was filtered twice to eliminate the residual solids. The green-colored boiled extract (reducing agent) was used for the synthesis of NPs.

2.2.2. Synthesis of NiO NPs. The nickel nitrate (1 mM) and *Hydrangea paniculata* flower extracts were used (1:1 v/v) and kept under the dark condition for 12 to 24 hrs of the incubation period. The resulting precipitate was centrifuged for 30 minutes at 6500 rpm, washed with double-distilled water to eliminate contaminants, and dried at 60°C for 6 hours. The powder that resulted was employed in subsequent research.

2.2.3. Synthesis of ZnO-NPs. In this protocol, 2 mL of *Plectranthus amboinicus* plant extract was added dropwise to 100 mL of zinc oxide (0.1%) solution (thoroughly mixed for 10 mins by magnetic stirrer). The ZnO-NPs were formed as white crystalline, which was washed several times with water, filtered, and dried at 333 K.

2.2.4. Synthesis of CuO, V₂O₅, and MoO₃ NPs. To synthesize, these metal oxide NPs, stoichiometric amounts of Cu (CH₃COO)₂·H₂O and ammonium metavanadate, and chloroethoxide (MoCl₅) were mixed with 30 mL DD water and mixed with 20 mL of *A. paniculata* plant extract without foam. Unreacted compounds were removed using DD water. The end products were dried at 453 K for 20 mins and calcinated at 673 K for 2 hrs. The obtained powders were used for the evaluation of bactericidal activity.

2.3. Assay of Bactericidal Activity of Green Synthesized Metal NPs. Metal oxide NPs were screened for their antibacterial activity against three drug-resistant foodborne pathogens *E. coli*, *Staphylococcus aureus*, and *Klebsiella pneumoniae* by well diffusion method. The pH of Muller Hinton agar media was adjusted to 7.3 \pm 0.2 at 25°C. Using gel puncture, form 6 mm diameter of well on the media. Using a sterile cotton swab, the bacterial cultures were spread all over the media separately. The concentration ranges from 25 mg/50 μ L, 25 mg/100 μ L, to 50 mg/50 μ L of water as control, liquid culture filtrate, and CuO, NiO, ZnO, MoO₃, and V₂O₅ were loaded into the well using a micropipette and then incubated at 35°C for 18 hrs, and inhibition zones were measured for different concentrations.

2.4. Structural Characterization of V₂O₅ Nanoparticles. The crystalline nature, functional groups, and morphological

with elemental composition features were analyzed by XRD, FTIR, SEM with EDAX, and TEM analysis.

3. Results and Discussion

For the assessment of the antibacterial efficacy of metal oxide NPs, β -lactamase-producing strains were isolated from the stool samples of diverse age groups of patients. 876 β -lactamase-producing bacterial strains were isolated for a period of 3 months from March 2019 to May 2019 [30]. The ESBL-producing *E. coli*, *Klebsiella pneumoniae*, and *Staphylococcus aureus* (MRSA) were screened and isolated based on the production of β -lactamases and picked for biocidal analysis. The inhibition zone of combination disk of ceftazidime+clavulanic acid was \geq 5 mm, when compared to ceftazidime disk alone, which confirmed the ESBL production [30].

3.1. Bactericidal Properties of Metal Oxide Nanoparticles. The bactericidal activity of green synthesized metal oxide NPs such as NiO, ZnO, CuO, MoO₃, and V₂O₅ was tested by the well diffusion method against three drug-resistant strains (*Escherichia coli*, *Staphylococcus aureus*, and *Klebsiella pneumoniae*) (Tables 1, 2, and 3; Figures 1–3). Among the NPs, V₂O₅-NP showed effective resistance against all three strains. NiO NP (50 mg/50 μ L) was found to be the most effective and exhibited maximum zone of inhibition against *S. aureus*. Seven and 9 mm sized inhibitory zones at 25 mg/50 μ L and 25 mg/100 μ L of concentration against *S. aureus*. But, no zone was found against the other two strains. Srihasam et al. [31] have described the antibacterial efficiency of NiO NPs synthesized using Stevia leaf extract as reducing agent and resulted inhibition zone against *E. coli* (16 mm), *B. subtilis* (15 mm), and *S. pneumoniae* (14 mm). Likewise, Abbasi et al. [32] also have reported the bactericidal potential of *Geranium wallichianum* plant-mediated NiO NPs against *E. coli* and *S. aureus*. Maximum inhibition zone was observed in the Gram-negative strains due to the easy penetration of NiO NPs to the cell membrane with the lack of (lipopolysaccharide) peptidoglycan layer [33]. There was no inhibition zone observed in the plates introduced with MoO₃-NP P.

CuO-NP explored its bactericidal action in contradiction of *E. coli* and *S. aureus* with 18 mm diameter sized inhibitory zone at the concentration 50 mg/50 μ L. No zone was observed against *K. pneumoniae* which indicates its resistant activity against CuO NPs. Ahamed et al. [25] have reported the antibacterial activity of CuO NPs against various

TABLE 2: Bactericidal activity of metal oxide NPs against *E.coli*.

Nanoparticles	Control	Zone formation (mm) at different concentrations		
		25 mg/50 μ L	25 mg/100 μ L	50 mg/50 μ L
MoO ₃	—	—	—	—
CuO	—	—	—	18 \pm 2.12
NiO	—	—	—	—
ZnO	—	—	—	—
V ₂ O ₅	—	8 \pm 0.7	12 \pm 1.06	14 \pm 1.7

TABLE 3: Bactericidal activity of metal oxide NPs against *K. pneumoniae*.

Nanoparticles	Control	Zone formation (mm) at different concentrations		
		25 mg/50 μ L	25 mg/100 μ L	50 mg/50 μ L
MoO ₃	—	—	—	—
CuO	—	—	—	—
NiO	—	—	—	—
ZnO	—	—	—	—
V ₂ O ₅	—	12 \pm 1.04	13 \pm 1.7	14 \pm 1.76

FIGURE 1: Bactericidal activity of CuO-NPs: (a) *E. coli*; (b) *S. aureus*; (c) *K. pneumoniae*.

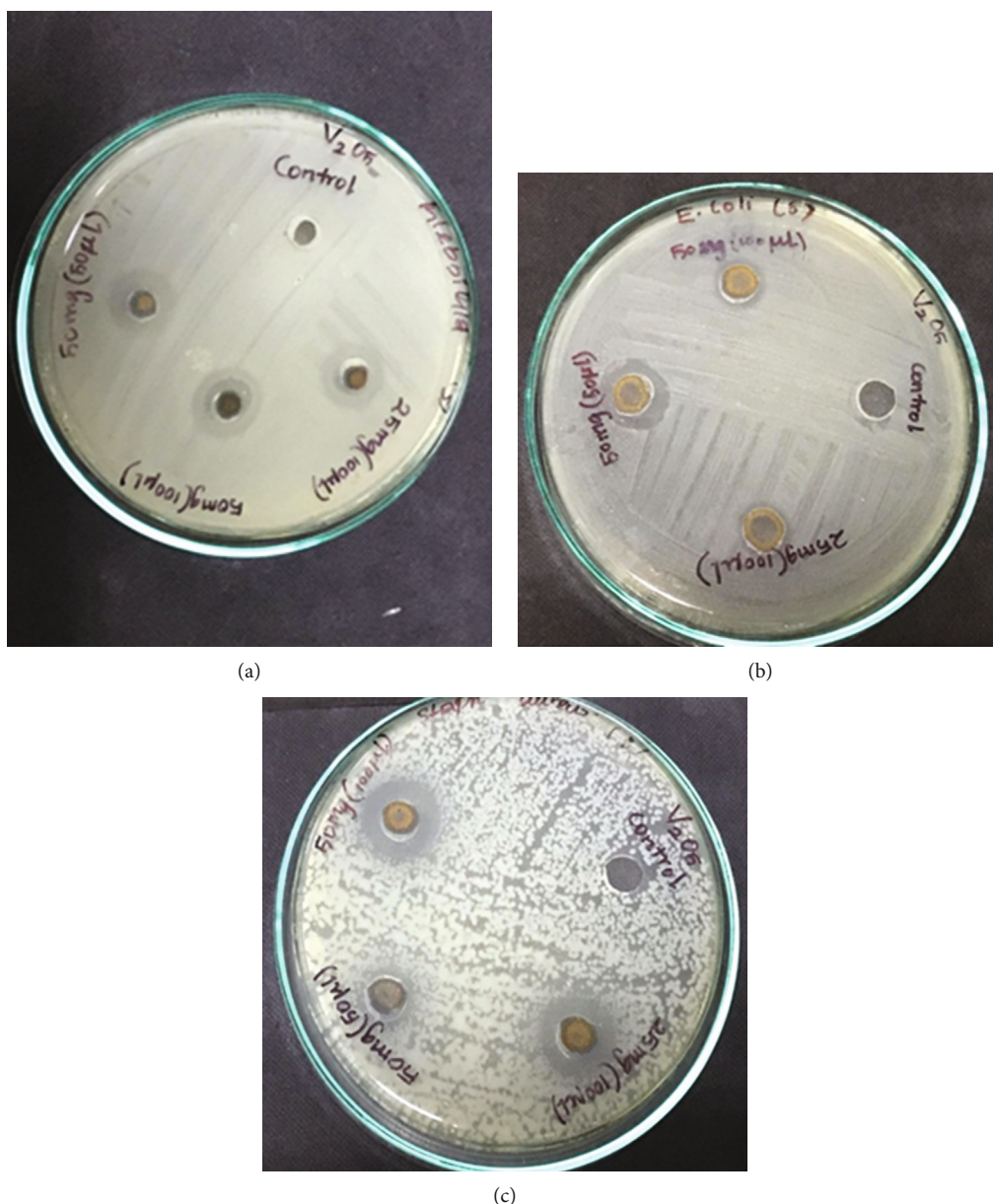


FIGURE 2: Bactericidal activity of V_2O_5 -NPs: (a) *K. pneumoniae*; (b) *E. coli*; (c) *S. aureus*.

bacterial strains and exhibited the highest inhibitory zone against *E. coli* and *E. faecalis*. Similarly, Sivaraj *et al.* [34] also proved the bactericidal efficiency of CuO NPs synthesized using the leaf extract of *Tabernaemontana divaricate*, and it produced 17 mm sized inhibitory zone against *E. coli* at 25 $\mu\text{g}/\text{mL}$ of concentration.

Vanadium pentoxide NPs inhibit the growth of all the strains which indicates the broad-spectrum toxic effect on the susceptible bacterial strains. It causes lethal effect observed with 11, 16, and 17 mm sized zone formation against *S. aureus*, and 12, 13, and 14 mm were found at the concentration 25 $\text{mg}/50 \mu\text{L}$, 25 $\text{mg}/50 \mu\text{L}$, and 50 $\text{mg}/50 \mu\text{L}$, respectively, against *K. pneumoniae*. For *E. coli*, inhibitory effect was observed as 8 mm at 25 $\text{mg}/50 \mu\text{L}$, 12 mm at 25 $\text{mg}/50 \mu\text{L}$, and 14 mm at 25 $\text{mg}/50 \mu\text{L}$. Kannan *et al.* [35] have demonstrated the antibacterial potency of V_2O_5 NPs

against *P. aeruginosa*. The inhibitory effect occurred through the attachment of a negatively charged cell membrane with positively charged V^{5+} that assisted in the penetration of NPs into the bacterial cell which causes DNA damage and lysis of the bacteria. Aliyu *et al.* [36] stated that green synthesized vanadium oxide NPs prepared using *Moringa oleifera* leaf extract inhibit the growth of bacteria. Kannan *et al.* [35] also utilized *Andrographis paniculata* (leaf extract) as a chelating agent for the synthesis of V_2O_5 NPs through microwave-assisted method. These potential metal oxide NPs can be promising antibacterial agents to treat illness caused by drug-resistant foodborne pathogens.

3.2. Structural Characterization of V_2O_5 Nanoparticles. Among all the synthesized NPs, V_2O_5 -NPs broadly showed bactericidal activity against all the selected pathogens. Thus,

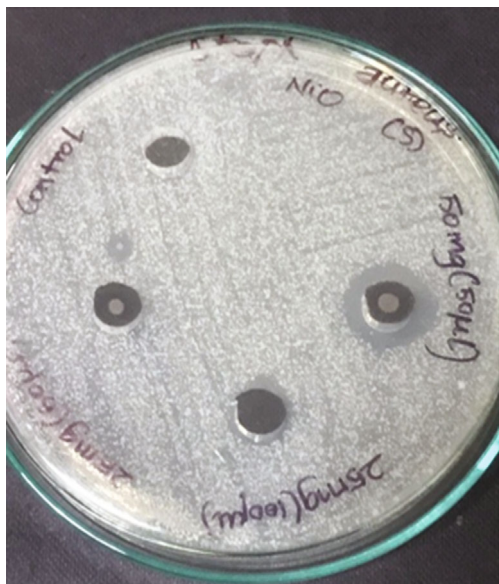


FIGURE 3: Bactericidal activity of NiO NPs against *S. aureus*.

further characterization studies were carried out for V_2O_5 -NPs. The crystalline nature, functional groups, and morphological with elemental composition features were analyzed by XRD, FTIR, SEM with EDAX, and TEM analysis.

3.2.1. XRD Analysis of V_2O_5 -NPs. XRD pattern of V_2O_5 -NPs synthesized using extract of *Andrographis paniculata* as reducing and stabilizing agent is shown in Figure 4. The spectra showed sharp peaks in the 2θ angle region, indexed to (2 0 2), (0 1 1), (1 0 3), (2 0 2), (4 1 0), (2 0 5), (4 0 4), (4 0 6), (1 2 5), and (2 0 2) Miller index planes matched with JCPDS card no. 85-2422. The crystalline NPs exhibit orthorhombic structure, and the average crystallite structure was determined by Debye-Scherrer's equation, $D = K\lambda/\beta \cos \theta$, where "D" referred to mean crystallite size, "K" is shape constant, angular FWHM (Full Width at Half Maximum) is denoted as " β ," and " θ " is the diffraction angle. The average crystallite size of V_2O_5 NPs was originated to be 20 nm. The lattice parameters a , b , and c were calculated by applying the specific formula for orthorhombic structure and the value for lattice constant $a = 9.946$, $b = 3.585$, and $c = 10.042$ Å. Similarly, Raj et al. [37] also stated the orthorhombic structure of V_2O_5 NPs synthesized by the chemical cum sonication method. The occurrence of sharp peaks in the XRD pattern indicated the excellent crystalline nature of the nanoparticle [38]. Alghool et al. [39] have recorded the orthorhombic structure of V_2O_5 NPs.

3.2.2. UV-Visible Spectral Analysis of V_2O_5 -NPs. The absorbance spectrum of V_2O_5 -NPs was observed between the wavelength 200 and 400 nm, and the result is shown in Figure 5. The colour changes from pale yellow to dark were owing to the phenomenon of Surface Plasmon Resonance (SPR), and the change in colour primarily confirmed the reduction of bulk materials to NPs by the plant extract [36]. Alghool et al. [39] reported the absorbance peaks at

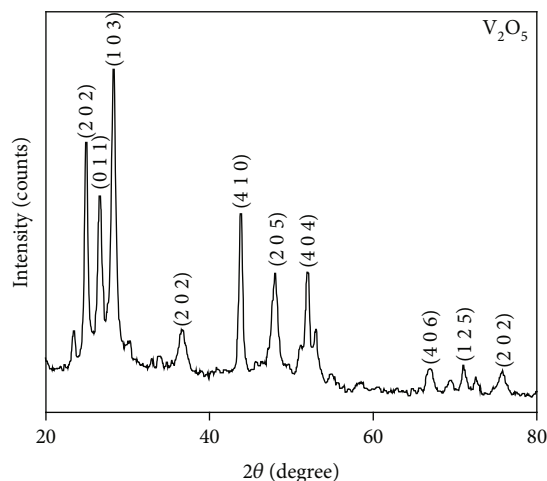


FIGURE 4: XRD pattern of V_2O_5 NPs

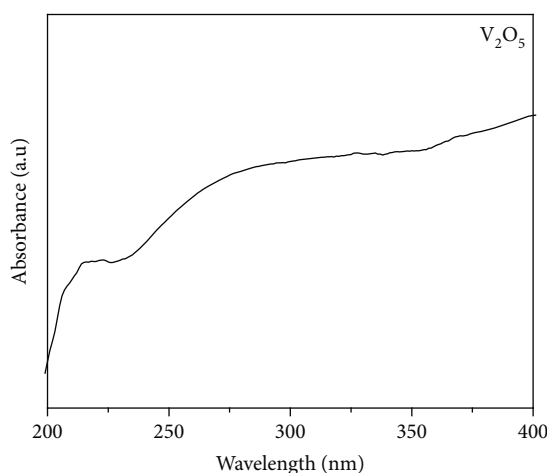


FIGURE 5: UV-Vis absorbance spectrum of V_2O_5 NPs.

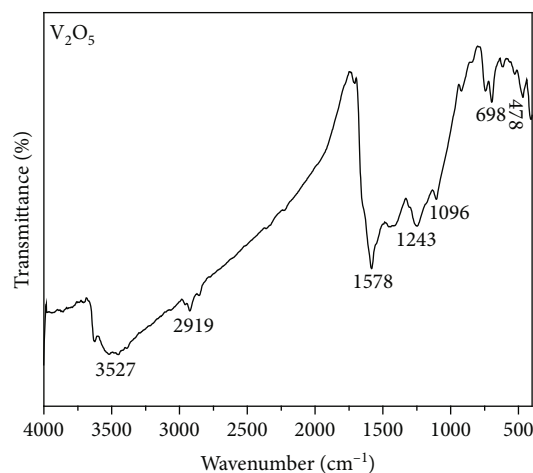


FIGURE 6: FTIR spectrum of V_2O_5 NPs.

234, 265, and 317 nm after band fitting by Gaussian functions using Origin 9.3 version software. Alghool et al. [39] have reported the existence of absorbance peak at 470 nm

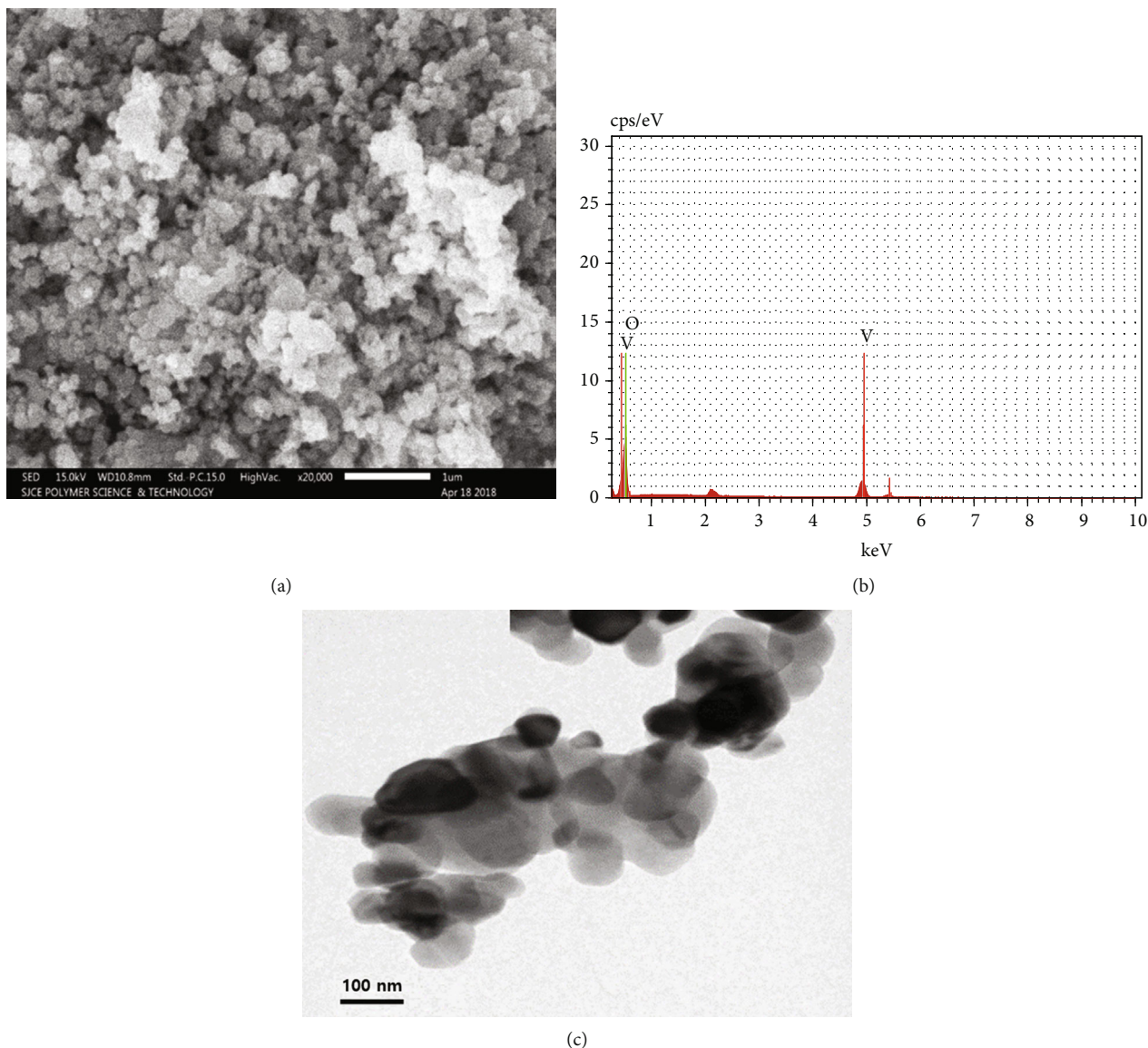


FIGURE 7: SEM (a) with EDX spectrum (b) and TEM (c) analysis of V_2O_5 -NPs.

assigned to the transition ($n \rightarrow \pi^*$) of the V=O group to V_2O_5 NPs.

3.2.3. FTIR Spectrum of V_2O_5 -NPs. The FTIR spectrum of V_2O_5 -NP is pictured in Figure 6. The functional groups found in the V_2O_5 -NP were identified by FTIR spectrum in the wavelength ranges from 4000 to 400 cm^{-1} . The absorption peaks 3527 cm^{-1} given to the hydroxyl group indicates presence of water molecules; 2919, 1578, and 1243 cm^{-1} band attributed to stretching of the CH_2 group, nitrogen containing group, and C-O stretched carboxylic acid which might be obtained from the plant extracts and acts as a reducing and capping agent of NP synthesis [36]. The band observed at 1096 cm^{-1} corresponds to other functional groups. The vanadium group presence was identified by the peaks observed in the ranges from 400 to 750 cm^{-1} [40]. This report assisted to confirm the presence of V_2O_5 NPs due to the presence of peaks at 698 and 478 cm^{-1} . The present result

agreed with the outcome of Kannan et al. [35]. The authors synthesized V_2O_5 NPs via ultrasound-assisted method and reported that the functional group V-O-V vibrational stretching bond at 478 cm^{-1} indicated the formation of V_2O_5 -NPs.

3.2.4. SEM and EDX Spectrum Analysis of V_2O_5 -NPs. SEM analysis proved the morphological features of vanadium oxide NPs, and the micrograph is shown in Figure 7(a). The results exposed the cluster of spherical-shaped NPs. A similar finding was stated for V_2O_5 NPs developed by *M. oleifera* leaf extract by Aliyu et al. [36]. The morphology of the NPs mostly depends on the fabricating process. Farahmandjou and Abaeiyan [41] also studied the surface morphology of V_2O_5 NPs. Alghool et al. [39] have reported the agglomerated spherical shape of V_2O_5 NPs in their SEM analysis. The EDX spectrum of V_2O_5 -NPs is given in Figure 7(b). The elemental analysis carried out by energy

dispersive X-ray spectroscopy examination confirmed the purity of green synthesized vanadium oxide NPs. The elemental composition of V_2O_5 NPs was found to be V (32.34%) and O (67.66%). The intense peaks for the vanadium compound were observed nearer to 0.15 keV and 4.9 keV.

3.2.5. TEM Analysis of V_2O_5 -NPs. TEM micrograph of prepared V_2O_5 NPs is presented in Figure 7(c). The images showed the aggregated spherical particles of V_2O_5 [35]. The average particle size of V_2O_5 NPs was determined by ImageJ software, and the size was found to be 58 nm. The particle size might depend on the reaction period taken for bioreduction bulk vanadium to nanoscale V_2O_5 [39]. The TEM analysis revealed the patterns and distribution of crystalline particles [41].

4. Conclusion

Foodborne pathogens are responsible for a wide range of diseases that have serious consequences for human health and the economy. Metal oxide NPs (NiO, CuO, ZnO, MoO₃, and V_2O_5) were produced employing extracts from *Hydrangea paniculata*, *Plectranthus amboinicus*, and *Andrographis paniculata* as reducing agents in the current study. The crystalline and morphological characteristics of V_2O_5 -NPs were demonstrated through characterization studies. Our study proved that the *E. coli*, *S. aureus*, and *K. pneumoniae* were more sensitive to V_2O_5 -NPs. As a result, we concluded that the biosynthesized metal oxide NPs (NiO, CuO, ZnO, MoO₃, and V_2O_5) were a promising antibacterial material against drug-resistant pathogenic bacteria, as a replacement for currently existing inefficient antibacterial drugs.

Data Availability

All data generated or analyzed during this study are included in the published article.

Conflicts of Interest

There is no conflict of interest.

References

- [1] J. A. Crump and E. D. Mintz, "Global trends in typhoid and paratyphoid fever," *Clinical Infectious Diseases*, vol. 50, no. 2, pp. 241–246, 2010.
- [2] I. Matle, K. R. Mbatha, and E. Madoroba, "A review of listeria monocytogenes from meat and meat products: epidemiology, virulence factors, antimicrobial resistance and diagnosis," *Onderstepoort Journal of Veterinary Research*, vol. 87, no. 1, pp. 1–20, 2020.
- [3] C. Malarkodi, S. Rajeshkumar, K. Paulkumar, M. Vanaja, G. Gnanajobitha, and G. Annadurai, "Biosynthesis and antimicrobial activity of semiconductor nanoparticles against oral pathogens," *Bioinorganic Chemistry and Applications*, vol. 2014, Article ID 347167, 10 pages, 2014.
- [4] WH Organization, *Antimicrobial Resistance: Global Report on Surveillance*, World Health Organization, 2014.
- [5] J. O'Neil, *Review on Antimicrobial Resistance. Antimicrobial Resistance: Tackling a Crisis for the Health and Wealth of Nations*, London, 2014, https://books.google.co.kr/books/about/Antimicrobial_Resistance.html?id=b1EOkAEACAAJ&redir_esc=y.
- [6] I. Roca, M. Akova, F. Baquero et al., "The global threat of antimicrobial resistance: science for intervention," *New Microbes and New Infections*, vol. 6, pp. 22–29, 2015.
- [7] N. Horn and A. K. Bhunia, "Food-associated stress primes foodborne pathogens for the gastrointestinal phase of infection," *Frontiers in Microbiology*, vol. 9, p. 1962, 2018.
- [8] F. C. Tenover, "Mechanisms of antimicrobial resistance in bacteria," *The American Journal of Medicine*, vol. 119, no. 6, pp. S3–S10, 2006.
- [9] F. Von Nussbaum, M. Brands, B. Hinzen, S. Weigand, and D. Häbich, "Antibacterial natural products in medicinal chemistry—exodus or revival?," *Angewandte Chemie International Edition*, vol. 45, no. 31, pp. 5072–5129, 2006.
- [10] S. Saif, A. Tahir, and Y. Chen, "Green synthesis of iron nanoparticles and their environmental applications and implications," *Nanomaterials*, vol. 6, no. 11, p. 209, 2016.
- [11] A. M. Allahverdiyev, E. S. Abamor, M. Bagirova, and M. Rafailovich, "Antimicrobial effects of TiO₂ and Ag₂O nanoparticles against drug-resistant bacteria and leishmania-parasites," *Future Microbiology*, vol. 6, no. 8, pp. 933–940, 2011.
- [12] X. Li, H. Xu, Z.-S. Chen, and G. Chen, "Biosynthesis of nanoparticles by microorganisms and their applications," *Journal of Nanomaterials*, vol. 2011, 16 pages, 2011.
- [13] S. Stankic, S. Suman, F. Haque, and J. Vidic, "Pure and multi metal oxide nanoparticles: synthesis, antibacterial and cytotoxic properties," *Journal of Nanobiotechnology*, vol. 14, no. 1, pp. 1–20, 2016.
- [14] E. Sánchez-López, D. Gomes, G. Esteruelas et al., "Metal-based nanoparticles as antimicrobial agents: an overview," *Nanomaterials*, vol. 10, no. 2, p. 292, 2020.
- [15] A. T. Khalil, M. Ayaz, M. Ovais et al., "In vitro cholinesterase enzymes inhibitory potential and in silico molecular docking studies of biogenic metal oxides nanoparticles," *Inorganic and Nano-Metal Chemistry*, vol. 48, no. 9, pp. 441–448, 2018.
- [16] H. E. A. Mohamed, S. Afridi, A. T. Khalil et al., "Phytosynthesis of BiVO₄ nanorods using Hyphaene thebaica for diverse biomedical applications," *AMB Express*, vol. 9, no. 1, pp. 1–14, 2019.
- [17] S. Tshoko, *Spectroelectrochemical graphene-silver/zinc oxide nanoparticulate phenotype biosensors for ethambutol and pyrazinamide*, University of the Western Cape, 2019.
- [18] A. M. El Shafey, "Green synthesis of metal and metal oxide nanoparticles from plant leaf extracts and their applications: a review," *Green Processing and Synthesis*, vol. 9, no. 1, pp. 304–339, 2020.
- [19] T. M. Osaili, B. A. Albiss, A. A. Al-Nabulsi et al., "Effects of metal oxide nanoparticles with plant extract on viability of foodborne pathogens," *Journal of Food Safety*, vol. 39, no. 5, article e12681, 2019.
- [20] K. Kannan, D. Radhika, S. Vijayalakshmi, K. K. Sadasivuni, A. A. Ojiaku, and U. Verma, "Facile fabrication of CuO nanoparticles via microwave-assisted method: photocatalytic, antimicrobial and anticancer enhancing performance,"

- International Journal of Environmental Analytical Chemistry*, vol. 102, pp. 1095–1108, 2022.
- [21] K. Kannan, D. Radhika, A. S. Nesaraj, K. Kumar Sadasivuni, and L. Sivarama Krishna, “Facile synthesis of NiO-CYSO nanocomposite for photocatalytic and antibacterial applications,” *Inorganic Chemistry Communications*, vol. 122, article 108307, 2020.
- [22] E. Lopes, S. Piçarra, P. L. Almeida, H. de Lencastre, and M. Aires-de-Sousa, “Bactericidal efficacy of molybdenum oxide nanoparticles against antimicrobial-resistant pathogens,” *Journal of Medical Microbiology*, vol. 67, no. 8, pp. 1042–1046, 2018.
- [23] K. Karthik, M. P. Nikolova, A. Phuruangrat, S. Pushpa, V. Revathi, and M. Subbulakshmi, “Ultrasound-assisted synthesis of V_2O_5 nanoparticles for photocatalytic and antibacterial studies,” *Materials Research Innovations*, vol. 24, no. 4, pp. 229–234, 2020.
- [24] A. Azam, A. S. Ahmed, M. Oves, Khan, Habib, and A. Memic, “Antimicrobial activity of metal oxide nanoparticles against Gram-positive and Gram-negative bacteria: a comparative study,” *International Journal of Nanomedicine*, vol. 7, p. 6003, 2012.
- [25] M. Ahamed, H. A. Alhadlaq, M. Khan, P. Karuppiyah, and N. A. al-Dhabi, “Synthesis, characterization, and antimicrobial activity of copper oxide nanoparticles,” *Journal of Nanomaterials*, vol. 2014, 4 pages, 2014.
- [26] S. U. Din, H. Iqbal, S. Haq et al., “Investigation of the biological applications of biosynthesized nickel oxide nanoparticles mediated by *Buxus wallichiana* extract,” *Crystals*, vol. 12, no. 2, p. 146, 2022.
- [27] S. K. Jayaraj, V. Sadishkumar, T. Arun, and P. Thangadurai, “Enhanced photocatalytic activity of V_2O_5 nanorods for the photodegradation of organic dyes: a detailed understanding of the mechanism and their antibacterial activity,” *Materials Science in Semiconductor Processing*, vol. 85, pp. 122–133, 2018.
- [28] R. Karthiga, B. Kavitha, M. Rajarajan, and A. Suganthi, “Synthesis of MoO_3 microrods via phytoconstituents of *Azadirachta indica* leaf to study the cationic dye degradation and antimicrobial properties,” *Journal of Alloys and Compounds*, vol. 753, pp. 300–307, 2018.
- [29] M. J. Hajipour, K. M. Fromm, A. A. Ashkarran et al., “Antibacterial properties of nanoparticles,” *Trends in Biotechnology*, vol. 30, no. 10, pp. 499–511, 2012.
- [30] V. Selvakumar, K. Kannan, A. Panneerselvam et al., “Molecular identification of extended spectrum β -lactamases (ESBLs)-producing strains in clinical specimens from Tiruchirappalli, India,” *Applied Nanoscience*, pp. 1–14, 2021.
- [31] S. Srihasam, K. Thyagarajan, M. Korivi, V. R. Lebaka, and S. P. R. Malleem, “Phytogenic generation of NiO nanoparticles using stevia leaf extract and evaluation of their in-vitro antioxidant and antimicrobial properties,” *Biomolecules*, vol. 10, no. 1, p. 89, 2020.
- [32] B. A. Abbasi, J. Iqbal, T. Mahmood, R. Ahmad, S. Kanwal, and S. Afridi, “Plant-mediated synthesis of nickel oxide nanoparticles (NiO) via *Geranium wallichianum*: characterization and different biological applications,” *Materials Research Express*, vol. 6, no. 8, 2019.
- [33] V. Helan, J. J. Prince, N. A. Al-Dhabi et al., “Neem leaves mediated preparation of NiO nanoparticles and its magnetization, coercivity and antibacterial analysis,” *Results in Physics*, vol. 6, pp. 712–718, 2016.
- [34] R. Sivaraj, P. K. Rahman, P. Rajiv, H. A. Salam, and R. Venckatesh, “Biogenic copper oxide nanoparticles synthesis using *Tabernaemontana divaricate* leaf extract and its antibacterial activity against urinary tract pathogen,” *Spectrochimica Acta Part A: Molecular and Biomolecular Spectroscopy*, vol. 133, pp. 178–181, 2014.
- [35] K. Kannan, D. Radhika, K. K. Sadasivuni, K. R. Reddy, and A. V. Raghu, “Nanostructured metal oxides and its hybrids for photocatalytic and biomedical applications,” *Advances in Colloid and Interface Science*, vol. 281, article 102178, 2020.
- [36] A. Aliyu, S. Garba, and O. Bognet, “Green synthesis, characterization and antimicrobial activity of vanadium nanoparticles using leaf extract of *Moringa oleifera*,” *International Journal of Chemical Sciences*, vol. 16, p. 231, 2017.
- [37] S. Raj, S. Kumar, and K. Chatterjee, “Facile synthesis of vanadia nanoparticles and assessment of antibacterial activity and cytotoxicity,” *Materials Technology*, vol. 31, no. 10, pp. 562–573, 2016.
- [38] C. Sridhar, N. Gunvanthrao Yernale, and M. Prasad, “Synthesis, spectral characterization, and antibacterial and antifungal studies of PANI/ V_2O_5 nanocomposites,” *International Journal of Chemical Engineering*, vol. 2016, Article ID 3479248, 6 pages, 2016.
- [39] S. Alghool, A. El-Halim, F. Hanan, and A. M. Mostafa, “An eco-friendly synthesis of V_2O_5 nanoparticles and their catalytic activity for the degradation of 4-nitrophenol,” *Journal of Inorganic and Organometallic Polymers and Materials*, vol. 29, no. 4, pp. 1324–1330, 2019.
- [40] Y. S. Kim, M. Y. Song, E. S. Park, S. Chin, G. N. Bae, and J. Jurng, “Visible-light-induced bactericidal activity of vanadium-pentoxide (V_2O_5)-loaded TiO_2 nanoparticles,” *Applied Biochemistry and Biotechnology*, vol. 168, no. 5, pp. 1143–1152, 2012.
- [41] M. Farahmandjou and N. Abaeiyan, “Chemical synthesis of vanadium oxide (V_2O_5) nanoparticles prepared by sodium metavanadate,” *Journal of Nano Research*, vol. 5, no. 1, article 00103, 2017.

Retraction

Retracted: Utilization of Eco-Friendly Waste Eggshell Catalysts for Enhancing Liquid Product Yields through Pyrolysis of Forestry Residues

Journal of Nanomaterials

Received 20 June 2023; Accepted 20 June 2023; Published 21 June 2023

Copyright © 2023 Journal of Nanomaterials. This is an open access article distributed under the Creative Commons Attribution License, which permits unrestricted use, distribution, and reproduction in any medium, provided the original work is properly cited.

This article has been retracted by Hindawi following an investigation undertaken by the publisher [1]. This investigation has uncovered evidence of one or more of the following indicators of systematic manipulation of the publication process:

1. Discrepancies in scope
2. Discrepancies in the description of the research reported
3. Discrepancies between the availability of data and the research described
4. Inappropriate citations
5. Incoherent, meaningless and/or irrelevant content included in the article
6. Peer-review manipulation

The presence of these indicators undermines our confidence in the integrity of the article's content and we cannot, therefore, vouch for its reliability. Please note that this notice is intended solely to alert readers that the content of this article is unreliable. We have not investigated whether authors were aware of or involved in the systematic manipulation of the publication process.

Wiley and Hindawi regrets that the usual quality checks did not identify these issues before publication and have since put additional measures in place to safeguard research integrity.

We wish to credit our own Research Integrity and Research Publishing teams and anonymous and named external researchers and research integrity experts for contributing to this investigation.

The corresponding author, as the representative of all authors, has been given the opportunity to register their agreement or disagreement to this retraction. We have kept a record of any response received.

References

- [1] S. Kaliappan, M. Karthick, P. P. Patil et al., "Utilization of Eco-Friendly Waste Eggshell Catalysts for Enhancing Liquid Product Yields through Pyrolysis of Forestry Residues," *Journal of Nanomaterials*, vol. 2022, Article ID 3445485, 10 pages, 2022.

Research Article

Utilization of Eco-Friendly Waste Eggshell Catalysts for Enhancing Liquid Product Yields through Pyrolysis of Forestry Residues

S. Kaliappan,¹ M. Karthick,² Pravin P. Patil,³ P. Madhu ,⁴ S. Sekar,⁵ Ravi Mani,⁶ D. Francisca Kalavathi,⁷ S. Mohanraj ,⁸ and Solomon Neway Jida ⁹

¹Department of Mechanical Engineering, Velammal Institute of Technology, Chennai, Tamil Nadu 601204, India

²Department of Mechanical Engineering, Velammal Engineering College, Chennai, Tamil Nadu 600066, India

³Department of Mechanical Engineering, Graphic Era Deemed to be University, Bell Road, Clement Town, Dehradun, Uttarakhand 248002, India

⁴Department of Mechanical Engineering, Karpagam College of Engineering, Coimbatore, Tamil Nadu 641032, India

⁵Department of Mechanical Engineering, Rajalakshmi Engineering College, Chennai, Tamil Nadu 602105, India

⁶Centre for Ocean Research, Sathyabama Institute of Science and Technology, Chennai, Tamil Nadu 600119, India

⁷PG Department of Environmental Science, Holy Cross College, Tiruchirappalli, Tamil Nadu 620002, India

⁸Department of Electronics and Communication Engineering, M.Kumarasamy College of Engineering, Karur, Tamil Nadu 639006, India

⁹Faculty of Mechanical Engineering, Arba Minch Institute of Technology, Arba Minch University, PO Box 21, Arba Minch, Ethiopia

Correspondence should be addressed to Solomon Neway Jida; solomon.neway@amu.edu.et

Received 25 April 2022; Revised 16 May 2022; Accepted 25 May 2022; Published 7 June 2022

Academic Editor: Pounsamy Maharaja

Copyright © 2022 S. Kaliappan et al. This is an open access article distributed under the Creative Commons Attribution License, which permits unrestricted use, distribution, and reproduction in any medium, provided the original work is properly cited.

In this study, catalytic and noncatalytic pyrolysis of *Prosopis juliflora* biomass was carried out in a fluidized bed reactor. This study highlights the potential use of forestry residues with waste eggshells under a nitrogen environment. The experiments were conducted to increase the yield of bio-oil by changing the parameters such as pyrolysis temperature, particle size, and catalyst ratio. Under noncatalytic pyrolysis, a maximum bio-oil yield of 40.9 wt% was obtained when the feedstock was pyrolysed at 500°C. During catalytic pyrolysis, the yield of bio-oil was increased by up to 16.95% compared to the noncatalytic process due to the influence of Ca-rich wastes on devolatilization behavior. In particular, the existence of alkali and alkaline-earth metals present in eggshells might have positive effects on the decomposition of biomass material. The bio-oil obtained through catalytic pyrolysis under maximum yield conditions was analyzed for its physical and chemical characterization by Fourier transform infrared (FT-IR) spectroscopy and gas chromatography mass spectroscopy (GC-MS).

1. Introduction

Due to an increased population and industrialization, the energy consumption of developed and developing countries has increased at a quicker rate in recent years [1]. The world's total power demand reached around 1640 billion units in 2020, and it is predicted to double in the year 2050. India's annual biomass availability is projected to be around 500 million tonnes, with 120-150 million tonnes

available for power production [2]. Direct combustion of any lignocellulosic biomass material has advantages since its heating value has been identified for a long time, but it is no longer recommended due to the presence of moisture in the samples, which makes it difficult during burning. Among this variety of techniques, pyrolysis is a simple, low-cost, and pollution-free method of extracting biofuel, especially bio-oil. Pyrolysis is the thermal degradation process of any organic materials to produce energy rich biofuel

in the absence of air [3]. Pyrolysis oil is the key element of pyrolysis which has properties nearer to diesel [4]. Investigations carried out on pyrolysis oil obtained from different types of materials such as biomass wastes, tyres, and rubber pyrolysis reported that the chemical composition and other properties were similar to diesel fuel. Hence, pyrolysis oil is considered as a potential alternate to diesel used for heating applications [5].

Pyrolysis oil is generally obtained from different raw materials such as plastics, rubber, and coal. Among these, biomass derived bio-oils are considered a good choice as they are renewable, nontoxic, biodegradable, and easily available. According to Bildirici [6], energy extracted from biomass contributes more to the development of the country than any other source of energy. It also contributes to poverty reduction. In addition to that, biomass is carbon-neutral and offers many environmental benefits [7]. Among slow pyrolysis, flash pyrolysis is the advanced method to produce maximum bio-oil yield [8]. However, some unsuitable characteristics such as poor volatility, acidity, and lower heating value significantly limit its application to use as a fuel [9]. Bio-oil is generally a combination of diverse classes of oxygenated components that cause its unfavourable properties. So the removal of oxygen is thus required and essential to transform bio-oil into a liquid fuel [10]. In recent years, many studies have concentrated on various pyrolysis techniques, such as microwave, solar, and stepwise pyrolysis [11–13]. Catalytic pyrolysis is the advanced technology that can convert low-quality pyrolysis vapours into high-quality bio-oils. This has the apparent advantages of a streamlined process and avoidance of condensation and reevaporation of obtained bio-oil [14]. The catalyst is intended to promote heavy molecular cracking processes, to yield maximum bio-oil [15]. In situ and ex situ are the two types of catalytic pyrolysis processes. This process has been extensively studied by various researchers in order to get higher bio-oil with decreased oxygenating elements [16]. During the in situ catalytic process, both feed materials and catalysts are mixed together while solid and vapour phases are upgraded in a reactor. On the other hand, ex situ requires the addition of feedstocks and catalysts separately, to improve the product yields [17]. The quantity and quality of the biofuel are generally affected by various parameters such as biomass type, catalyst type, operating temperature, amount of catalyst, reaction type, and size of the particles [18–20]. Previously, many researchers have performed pyrolysis processes by utilizing acidic zeolite, alumina, metals, bentonite clay, and red mud [21]. The catalyst used for pyrolysis significantly improves the production rate and number of aromatic hydrocarbons. The olive mill solid wastes were previously pyrolyzed by Christoforou et al. [22] with MgO catalyst. The catalytic process improved the production of bio-oil from 43.96 to 47.03 wt% compared to the noncatalytic process. Stefanidis et al. [23] investigated the outcome of ZSM-5 combined with biomass and showed improved bio-oil quality because of increased surface area of the catalyst. Hernando et al. [24] investigated pyrolysis reaction with h-ZSM-5 with MgO and ZnO as catalysts and found increased bio-oil production. The addition of catalyst in this study

showed a higher degree of deoxygenation with reduced char products.

The use of eco-friendly, inexpensive catalysts for the production of biofuel has been under attention in recent years. Eggshells have no commercial value and are discarded as solid waste. In 2018, global egg production reached 76.7 million metric tonnes [25]. China, US, Indonesia, India, and Mexico are the top five egg-producing countries, accounting for over 63% of world total egg production. In India, eggshell waste produced from poultry farm is huge. India has the 2nd largest poultry market in the world with annual growth of 14%. The majority of it is dumped in landfills without being pretreated. They are porous and contain a significant amount of calcium carbonate [26]. The eggshells are more efficient catalysts due to their higher reaction rates. According to Kim et al. [27], eggshell catalyst utilized for pyrolysis process accelerated various reaction processes such as cracking, deoxygenation, decarboxylation, and alkylation. Valizadeh et al. [28] utilized eggshells for catalytic pyrolysis of food wastes to produce clean and high quality gaseous products. This research suggests that a CO₂-assisted process over a Ni-eggshell catalyst might be an environmentally beneficial and long-term solution for food waste disposal. Another study conducted by Rohim et al. [29] showed higher bio-oil production through palm kernel pyrolysis with eggshell. The study showed maximum bio-oil production of 45.67 wt% compared to the noncatalytic process (19.69 wt%).

India is one of the world's top 10 forest-rich countries. Forestry is a significant rural sector and an important environmental resource in India, despite the fact that natural forests cover 21.34% of the country's total land area [30]. *Prosopis juliflora* is a spiny plant found in semiarid India. The plant produces about 2.5 tonnes of hard wood per hectare, and around 70% of the wood has hemicellulose [31]. In India, the occupancy of the tree is more in southern zone compared to other part of the country. It covers 79.4% invaded in this zone than western zone (46%). The higher hemicellulose fractions in the wood give a positive approach to produce maximum bio-oils. This plant is a nonfood plant, and it does not pose a risk to food security. Furthermore, the plant is suspected of depleting ground aquifers in its growing area, and the government of Tamil Nadu, India, decided to eradicate the plant completely in a particular region of the state. Chandran et al. [32] utilized the hard wood of the tree for high grade biofuel production. The pyrolysis oil produced in this study was characterized by various physical and chemical analysis and showed 6% water. The chemical analysis showed the presence of more than 20 organic elements in the bio-oil. Microwave pyrolysis of *Prosopis juliflora* for fuel intermediates was carried out by Suriapparao et al. [33]. The study used five different types of susceptors for the maximum bio-oil production. The study yielded 40 wt% of bio-oil by using fly ash as a susceptor. The produced bio-oil showed a maximum energy value of 26 MJ/kg with a majority of phenolic and aromatic hydrocarbons.

The current study examines the process and quality of the bio-oil acquired from *Prosopis juliflora* through the flash pyrolysis method. There was no study reported on the use of

waste eggshell as a catalyst along with the selected wood biomass for the pyrolysis process. The experiments were carried out through noncatalytic and catalytic environments with the addition of eggshell as a catalyst. The experiments were aimed at producing maximum bio-oil from biomass material combined with powdered eggshell as a catalyst by changing reaction temperature, particle size, and biomass to catalyst ratio. In addition to that, the produced bio-oil was characterized by various spectrochemical analysis in order to find its physical and chemical stability.

2. Materials and Methods

2.1. Material Preparation. Wood samples were collected from a village near Coimbatore, India. Initially, the wood pieces had a moisture content of up to 30%. A chopping machine was utilized to cut the wood into small pieces. After that, the wood pieces were ball milled to get four different particle sizes. The sieved feedstocks were dried in sunlight for 15 days. Furthermore, the materials were dried in a furnace for 2 hours at $\pm 90^\circ\text{C}$ in a controlled environment. The proximate and component analysis of the samples were found according to ASTM standards and are listed in Table 1. The material is having higher volatile matter and lower ash content. The higher amount of volatiles in the biomass is favour for the release for more condensable volatiles. During pyrolysis, the higher ash content in the biomass invariably reduces the production as well as the quality of the biofuel. The fixed carbon of the material was computed using the difference. Eggshells used for the catalytic process were collected from a local restaurant. The collected shells were cleaned well with fresh water to remove the dust particles and then dried in a furnace maintained at 100°C . The dried shells were ground to a homogenised size. In a tube furnace, raw eggshells were calcined for 1 hour under a nitrogen atmosphere at 800°C .

2.2. Material Characterization. The analysis of the biomass material and produced pyrolysis oil was done by using an Elementar Vario EL III CHNS analyzer (N2410650, Perkin Elmer Ltd., US). The physical analysis was done with a redwood viscometer (Swastik Scientific Instruments, MH, India), a Penske Martin closed cup apparatus (Ducom Instruments, India), and a Parr-6772 bomb calorimetric. The FT-IR spectra of the oil sample were recorded with the help of BRUKER Optik GmbH TENSOR-27 (Bruker Corporation) FT-IR spectroscopy. The spectra were recorded in the range of $400\text{--}4000\text{ cm}^{-1}$. For this analysis, 1 mg of the samples was mixed with 250 mg of KBr powder to form a pellet. The various chemical elements of bio-oil were analyzed and detected using Thermo GC-TRACE Ultra-5.0, THERMO MS DSQ-II.

2.3. Reactor Setup. A fluidized bed reactor used for this study has diameter of 150 mm and a height of 30 cm, which is operated by keeping the temperature between 350°C and 550°C . The reactor was designed to withstand temperatures of up to 900°C . Generally fluidized bed reactors are well suitable one for pyrolysis process than other type of reactors.

They offer higher efficiency in heat transfer. They are very easy to control and higher gas velocities do not cause any pressure drop. This leads to reduced heat exchange area, simple construction, and lower gas compression costs. Nitrogen was supplied to fluidize the feed material along with the sand particle of 0.5 mm. For all the experiments, the flow rate of the nitrogen was maintained at $1.75\text{ m}^3/\text{hr}$ which is more than the minimum fluidization velocity of the particle. The reactor was heated electrically, and the heat input was controlled by a PID controller. In order to measure the temperature of the reactor, five K-type thermocouples were attached at five different points. The exit of the reactor tube was connected with two cyclone separators and further connected to the condenser. The cooling water circulated to the condenser was maintained at $\pm 5^\circ\text{C}$. The condensed liquid fractions were collected separately. The char was collected from the cyclone separator. Both the components were weighed using an electronic weighing machine. The weight of the gas components was found by remaining material balance. The following is the formula used for the determination of the desired output products:

$$\text{Yield of the desired products in wt\%} = \frac{\text{Yield of gas or oil or char}}{\text{Amount of biomass}} \times 100. \quad (1)$$

2.4. Experimental Scheme. The experimental work for this study was conducted in three different phases. The first two phases of the work were described with a noncatalytic process of biomass material to optimize the operating parameters such as reactor temperature and particle size. The third phase of the work is associated with the effect of eggshell on bio-oil yield. In this phase, the reactor was kept at 500°C and the particle size of 1.0 mm. The readings in this phase were taken by adding eggshell blended with the biomass material at 5, 10, 15, and 20 wt%. The experiments in all these phases were conducted at the heating rate of $20^\circ\text{C}/\text{min}$.

3. Results and Discussion

3.1. Thermogravimetric Analysis. The stability of the biomass materials with regard to heat was analyzed from the data acquired from TGA analysis done with the help of TGA701 (LECO Corporation, Michigan, US) thermogravimetric analyzer shown in Figure 1. This analysis can also be used to find the temperature at which pyrolysis can take place. According to this analysis, the breakdown of the biomass material occurred in four different stages. For this analysis, the biomass materials were heated to 600°C at $10^\circ\text{C}/\text{min}$. In the first zone, the moisture content associated with the biomass was removed from the material between 40°C and 125°C . The second zone of the process was related to the breakdown of hemicellulose between 150°C and 275°C . This process was confirmed with the peak obtained at 275°C . The third zone is the active pyrolysis zone whereas the degradation of hemicelluloses, cellulose, and lignin happen. This process was continued till it reaches to 500°C . The breakdown of hemicellulose and cellulose at this stage is also

TABLE 1: Biomass characterization.

Analysis	Parameter	Value in wt%	Standard
Proximate	Moisture	5.1	ASTM D3173
	Volatile matter	69.1	ASTM D3175
	Fixed carbon ^a	22.7	By difference
	Ash	3.1	ASTM D3174
Ultimate (ash free basis)	C	48.2	ASTM D5373
	H	5.9	ASTM D5373
	N	0.7	ASTM D5373
	S	0.2	ASTM D5373
	O ^a	45.0	By difference
	H/C molar ratio	1.4585	—
	O/C molar ratio	0.7008	—
Empirical formula	$\text{CH}_{1.458}\text{N}_{0.012}\text{O}_{0.7}$	—	
	Heating value in MJ/kg	17.21	ASTM D240

^aBy difference.

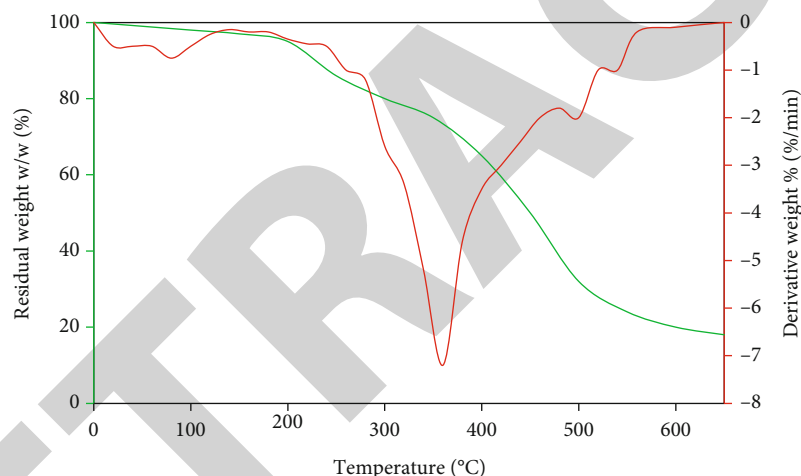


FIGURE 1: TGA and DTG curve of the biomass.

associated with the literature [34, 35]. Due to lower molecular weight, the decomposition of the hemicellulose started more quickly than other components. Here, the decomposition of cellulose began 250°C. Generally, the cellulose in the biomass material started to decompose at 250°C and end around 375°C [36]. The peak of cellulose degradation at 360°C in DTG curve confirmed highly ordered structure of the polymer. The degradation of lignin was stated at 150°C in the fourth zone, but it occurred slowly due to the complex polymeric structure. Lignin is a higher molecular weight component and more thermally stable than hemicellulose and cellulose.

3.2. Pyrolysis Experiment

3.2.1. Effect of Reactor Temperature. Pyrolysis of wood was conducted by changing the reactor temperature as shown in Figure 2. The temperature of pyrolysis has a considerable impact on product yield and properties [37, 38]. The yield of

bio-oil generally reach maximum at the temperatures between 400 and 550°C and then begin to fall with further increment [39, 40]. In this case, the yield of char reached its maximum at 350°C and declined with increased temperature. The production of char is lower at 550°C (30.3 wt%) due to the cracking reaction of the volatile matter. According to Sakhiya et al. [41], thermal cracking is the key factor for the production of light hydrocarbons, resulting in substantial proportions of bio-oil and gas yields. The bio-oil yield increased as the reactor temperature increased from 350 to 500°C, with decreased char and gas products. At 350°C, the bio-oil yield was 27.2 wt%, and at 500°C, it reached to the maximum value of 40.9 wt%. The yield of bio-oil is decreased when the temperature is reached 500°C. The increased bio-oil at 450 C is due to the maximum decomposition of condensable volatile matters. The TGA analysis also confirmed the complete decomposition of the biomass at 500°C with least volatiles remaining. Baghel et al. [35] conducted pyrolysis experiments on *Prosopis juliflora* and

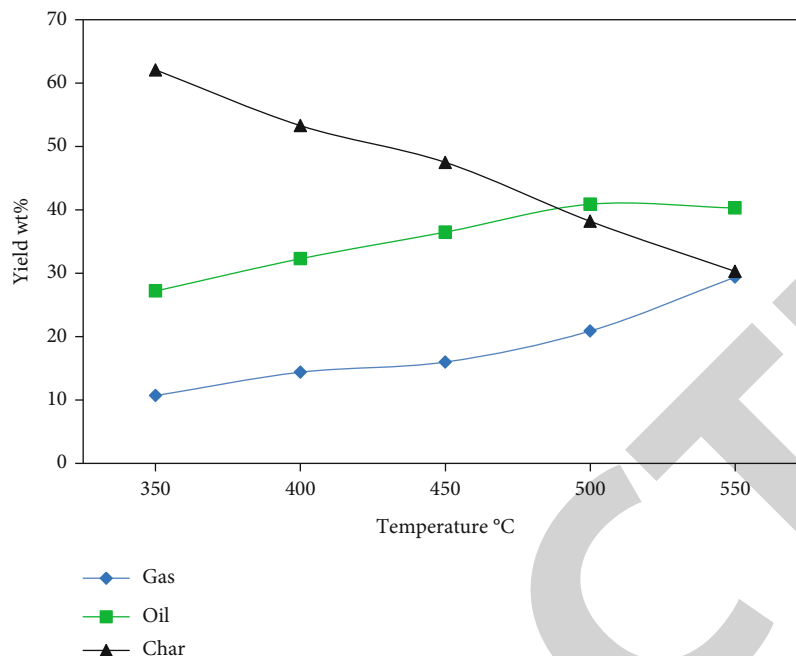


FIGURE 2: Effect of temperature on pyrolysis yield.

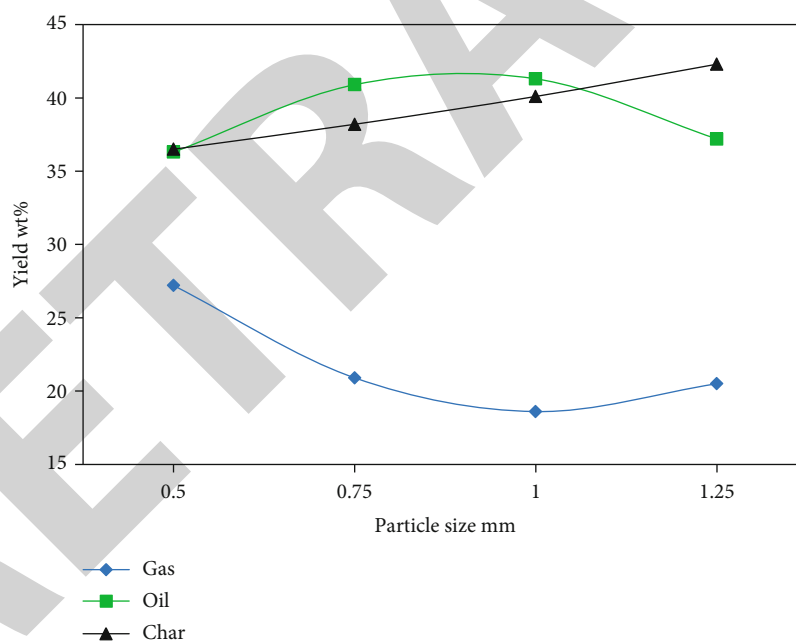


FIGURE 3: Effect of particle size on pyrolysis yield.

obtained maximum bio-oil at 500°C. The gas yield is steadily improved with increased temperature. The gas yield is changed from 10.7 wt% to 29.4 wt% when the reactor is changed from 350 to 550°C. The increased gas yield can be described by the cracking process and the formation of light hydrocarbons [42].

3.2.2. Effect of Particle Size. Particle size is another factor that influences the yields of biofuels. The yield of pyrolysis oil will be maximum at which the maximum heat transfer and

complete decomposition will occur [43]. Figure 3 depicts the effect of particle size on different biofuel yields. The figure demonstrates that as particle size decreases, liquid yield also decreases. The yield of pyrolysis oil was 36.3 wt% when a 0.5 mm particle was utilized for the experiment. The yield of char increased steadily with increasing particle size. The yield of char was 36.5 wt% at 0.5 mm particle size, and the yield was changed to 42.3 wt% at 1.25 mm. The yield of gas fractions has a tendency to decrease with increasing particle size up to 1.0 mm. The decreased increased pattern of the gas

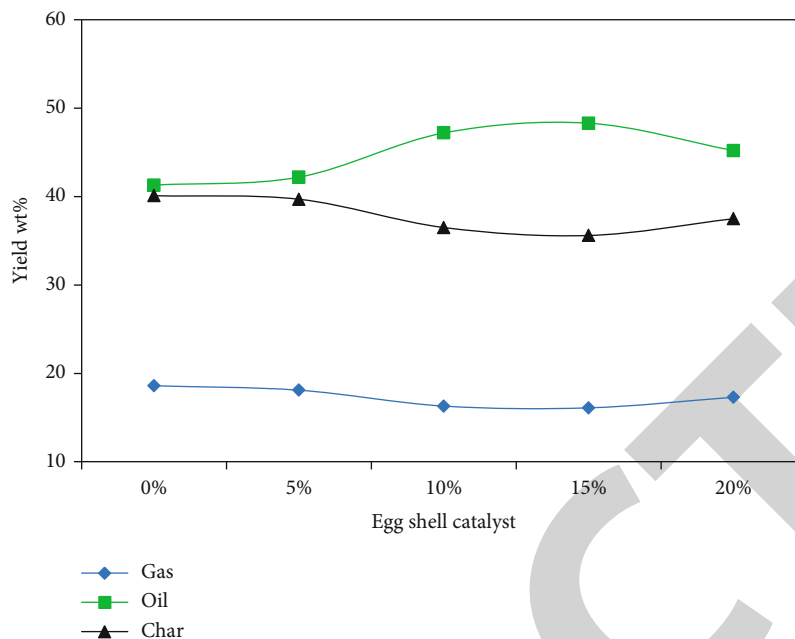


FIGURE 4: Effect of catalyst on pyrolysis yield.

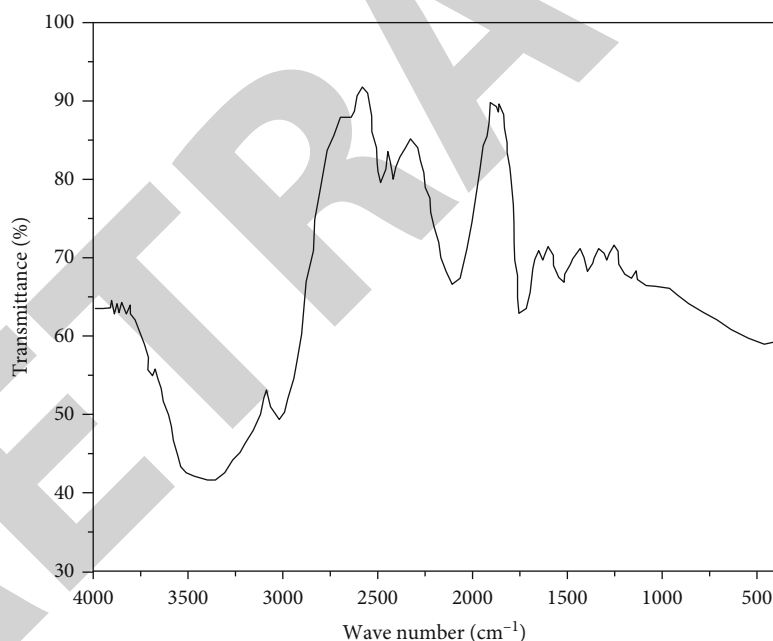


FIGURE 5: FT-IR analysis of the bio-oil.

yield can be explained by two perspectives. The smaller particles inside the reactor are subjected to maximum heat transfer due to increased surface area. The maximum heat transfer produces light gases and less char [43]. When the particle exceeds 1.0 mm, the residence time of the particle is prolonged, which leads to secondary cracking reactions [44]. With an increased particle size of 1.25 mm, the yield of gas improved from 18.6 wt% to 20.5 wt%. Since the smaller particles produced a maximum gas of 27.2 wt% than the larger particles, it can be concluded that the maximum

heat transfer with smaller particles is more pronounced than the secondary cracking reactions.

3.2.3. Effect of Catalyst. The effect of eggshell catalysts on the pyrolysis of *Prosopis juliflora* conducted at 500°C is shown in Figure 4. The conversion of biomass into oil increased from 41.3 to 48.3 wt% with the addition of 15% catalyst. With further increase of catalyst, the yield is reduced to 45.2 wt%. The primary aim of using catalysts for the pyrolysis process is to increase the reaction rate at lower temperatures. The

TABLE 2: GC-MS analysis of the bio-oil.

RT/min	Compound name	Molecular formula	Area %
3.41	2-Cyclopenten-1-one	C ₅ H ₆ O	2.24
3.78	Pyrogallol 1,3-dimethyl ether	C ₈ H ₁₀ O ₃	2.97
4.04	Formic acid	CH ₂ O ₂	3.33
6.12	4-Hydroxy-3-methoxy benzaldehyde	C ₈ H ₈ O ₃	2.47
9.44	1,2-Cyclopentanedione, 3-methyl	C ₆ H ₈ O ₂	4.04
9.52	Acetic acid	CH ₃ COOH	3.11
10.01	Butyrolactone	C ₄ H ₆ O ₂	3.97
12.22	Phenol	C ₆ H ₅ OH	8.76
14.52	Dibenzo[a,e]cyclooctene	C ₁₆ H ₁₂	0.84
14.69	1,4-Dimethoxybenzene	C ₈ H ₁₀ O ₂	2.67
16.87	Butyrolactone	C ₄ H ₈ O ₄	4.38
16.91	4-Methyl phenol (p-cresol)	C ₇ H ₈ O	0.91
18.08	Phenol, 2-methoxy-	C ₇ H ₈ O ₂	12.33
18.83	Phenol, 3,4-dimethyl-	C ₈ H ₁₀ O	3.41
20.15	Benzenemethanol, 4-hydroxy	C ₇ H ₈ O ₂	1.72
20.26	9-Octadecenoic acid (Z)-,methyl ester	C ₁₉ H ₃₆ O ₂	7.55
20.84	4-Ethyl-2-methoxy phenol	C ₉ H ₁₂ O ₂	2.74
22.51	1-Propyne, 3-iodo-	C ₃ H ₃ I	1.42
22.89	2-Methoxyphenol	C ₇ H ₈ O ₂	5.11
23.58	Cyclohexanol,3,3,5-trimethyl	C ₉ H ₁₈ O	4.12
23.80	Triamcinolone	C ₂₁ H ₂₇ FO ₆	0.95
24.04	9-Octadecenamide	C ₁₈ H ₃₅ NO	1.14
24.15	Phenol, 3-amino	C ₆ H ₇ NO	5.07
24.58	2H-Pyran, 2-(2 heptadecyloxy)tetrahydro-	C ₂₂ H ₄₀ O ₂	4.74
24.99	1-Methyl-1,3,3-triphenylindan-2-one	C ₂₈ H ₂₂ O	1.52
25.04	4-(2'-Methyl-3'-butenyl)azulene	C ₁₅ H ₁₆	0.21
26.57	Pyridine, 2-propyl-	C ₈ H ₁₁ N	2.74
26.91	2,4-Methanoprolin	C ₆ H ₉ NO ₂	0.62
27.09	Methyl 4-T-butyl-2-furoate	C ₁₀ H ₁₄ O ₃	3.98

yield of bio-oil was higher at 15% addition of catalyst than other percentages due to catalytic contact of the higher vapours produced during the pyrolysis reaction [45]. Considering char and gas yield, both decreased with the addition of the catalyst. The char and gas yields were 40.1 wt% and 18.6 wt% at noncatalytic pyrolysis, respectively. But the yield was decreased to 35.6 wt% and 16.1 wt% with 15% addition of eggshell. In this case, the yield of gas fractions was not affected much due to catalytic reaction. Rohim et al. [19] conducted pyrolysis experiments on palm kernel shells using eggshell catalyst and found maximum bio-oil production of 45.67 wt% by adding 20% catalyst with the biomass. In another study conducted by Ahmad et al. [46] 65.67 wt% of bio-oil was produced by utilizing 20% of eggshell and palm shell under 450°C.

3.3. Characterization

3.3.1. Analysis of Functional Groups. The FT-IR spectra displayed in Figure 5 help to detect the various functional groups of the catalytic pyrolysis oil. The test was carried

out on the sample obtained at maximum yield conditions. The existence of broad -OH stretching vibrations indicates the occurrence of phenols and alcohols. The presence of the water components in the oil sample is indicated by the peak that appears at 3200-3600 cm⁻¹ [47]. The C≡C stretch at 2000-2200 cm⁻¹ shows the appearance of alkynes. The C-H stretching vibrations of alkenes and aromatics match the peak found at 1650-1750 cm⁻¹. The peak obtained at 1400-1600 cm⁻¹ confirms the presence of mono, polycyclic, and aromatic components. The C-H stretching vibration that appeared at 1350-1450 cm⁻¹ shows the existence of alkanes. The existence of alcohols and phenols is confirmed by peaks that appear between 800 and 1250 cm⁻¹ [48].

3.3.2. Composition of Bio-oil. The various chemical components present in the bio-oil derived from the catalytic process were analyzed using GC-MS. Bio-oil is a complex mixture of several elements. Around 30 compounds were identified through mass spectra and are listed in Table 2. The oil has large quantities of acids, phenols, ketones, furfural, and alcohols. Similar components have been found in

bio-oil derived from wood chips, pressed oil cake, and red pine [49–51]. Phenols and their constituents are the key elements of bio-oil, which are ascribed to the oxidation of cellulose and lignin [52]. The breakdown of carbohydrates in the biomass material may result in the formation of acids and alkanes. The presence of furfural suggests that it has a possible potential for usage as a biofuel for burners and biomedical applications. The total percentage of phenol and its derivatives is greater than the other components. These components are important industrial feedstock used for the production of plastics and other products. In addition to that, pharmaceutical medications require phenol and its chemical derivatives.

4. Conclusion

In this study, the flash pyrolysis characteristics of *Prosopis juliflora* biomass with Ca-rich eggshell wastes were investigated. Eggshell waste collected from restaurants can be repurposed as a catalytic material for this study. According to the experimental findings, a maximum of 48.3 wt% bio-oil was achieved at 500°C, 1.0 mm particle size, with the addition of 15% waste eggshell. The reuse of waste based environmental friendly eggshell components can reduce the risk of microbiological activities and the disposal cost into the environment as well as provide raw materials. Compared to thermal pyrolysis processes, the catalytic pyrolysis improved the bio-oil output by 16.95% due to higher lignin decomposition influenced by the calcium-based catalyst. The addition of eggshell potentially reduces the production costs due to the increased reaction rate. The analysis of bio-oil with FT-IR and GC-MS analysis showed the existence of acids, phenols, ketones, furfural, and alcohols. The chromatographic study showed that the bio-oil can be used as a potential source for industrial chemicals. The current research can be expanded in the future to include blending bio-oil with diesel to make biodiesel and testing its efficiency in IC engines.

Data Availability

The data used to support the findings of this study are included within the article.

Conflicts of Interest

The authors declare that there is no conflict of interest regarding the publication of this article.

References

- [1] K. V. Shivaprasad, R. Rajesh, W. A. Wogasso, B. Nigatu, and F. Addisu, "Usage of hydrogen as a fuel in spark ignition engine," *IOP Conference Series: Materials Science and Engineering*, vol. 376, article 012037, 2018.
- [2] R. Prakash, R. K. Singh, and S. Murugan, "Experimental studies on combustion, performance and emission characteristics of diesel engine using different biodiesel bio oil emulsions," *Journal of the Energy Institute*, vol. 88, no. 1, pp. 64–75, 2015.
- [3] C. S. Dhanalakshmi and P. Madhu, "Recycling of wood bark of *Azadirachta indica* for bio-oil and chemicals by flash pyrolysis," *Indian Journal of Ecology*, vol. 46, no. 2, pp. 347–353, 2019.
- [4] P. Das and A. Ganesh, "Bio-oil from pyrolysis of cashew nut shell—a near fuel," *Biomass and Bioenergy*, vol. 25, no. 1, pp. 113–117, 2003.
- [5] P. Madhu, M. Sasireka, R. Samikannu et al., "Production and characterization of maximum liquid oil products through individual and copyrolysis of pressed neem oil cake and waste thermocol mixture," *Advances in Polymer Technology*, vol. 2022, 11 pages, 2022.
- [6] M. E. Bildirici, "Economic growth and biomass energy," *Biomass and Bioenergy*, vol. 50, pp. 19–24, 2013.
- [7] F. Abnisa and W. M. A. W. Daud, "A review on co-pyrolysis of biomass: an optional technique to obtain a high-grade pyrolysis oil," *Energy Conversion and Management*, vol. 87, pp. 71–85, 2014.
- [8] R. O. Arazo, D. A. D. Genuino, M. D. G. de Luna, and S. C. Capareda, "Bio-oil production from dry sewage sludge by fast pyrolysis in an electrically-heated fluidized bed reactor," *Sustainable Environment Research*, vol. 27, no. 1, pp. 7–14, 2017.
- [9] M. Parthasarathy, S. Ramkumar, and J. I. J. R. Lalvani, "Influence of various flow rates of CNG in CI engine with blend of tamanu methyl ether and ethanol," *International Journal of Vehicle Structures & Systems*, vol. 11, no. 2, pp. 144–148, 2019.
- [10] J. I. J. Lalvani, M. Parthasarathy, B. Dhinesh, and K. Annamalai, "Pooled effect of injection pressure and turbulence inducer piston on performance, combustion, and emission characteristics of a DI diesel engine powered with biodiesel blend," *Ecotoxicology and Environmental Safety*, vol. 134, Part 2, pp. 336–343, 2016.
- [11] S. Jiang, X. Hu, X. Shao, Y. Song, D. Xia, and C. Z. Li, "Effects of thermal pretreatment and ex-situ grinding on the pyrolysis of mallee wood cylinders," *Fuel Processing Technology*, vol. 159, pp. 211–221, 2017.
- [12] J. Asomaning, S. Haupt, M. Chae, and D. C. Bressler, "Recent developments in microwave-assisted thermal conversion of biomass for fuels and chemicals," *Renewable and Sustainable Energy Reviews*, vol. 92, pp. 642–657, 2018.
- [13] X. Chen, Q. Che, S. Li et al., "Recent developments in lignocellulosic biomass catalytic fast pyrolysis: strategies for the optimization of bio-oil quality and yield," *Fuel Processing Technology*, vol. 196, article 106180, 2019.
- [14] B. Valle, A. Remiro, N. García-Gómez, A. G. Gayubo, and J. Bilbao, "Recent research progress on bio-oil conversion into bio-fuels and raw chemicals: a review," *Journal of Chemical Technology & Biotechnology*, vol. 94, no. 3, pp. 670–689, 2019.
- [15] A. V. L. N. Sujith, R. Swathi, R. Venkatasubramanian et al., "Integrating nanomaterial and high-performance fuzzy-based machine learning approach for green energy conversion," *Journal of Nanomaterials*, vol. 2022, Article ID 5793978, 2022.
- [16] Y. Wang, A. Akbarzadeh, L. Chong, J. Du, N. Tahir, and M. K. Awasthi, "Catalytic pyrolysis of lignocellulosic biomass for bio-oil production: a review," *Chemosphere*, vol. 297, pp. 134181, 2022.
- [17] R. Liu, M. Sarker, M. M. Rahman et al., "Multi-scale complexities of solid acid catalysts in the catalytic fast pyrolysis of biomass for bio-oil production - a review," *Progress in Energy and Combustion Science*, vol. 80, article 100852, 2020.

- [18] C. Vibhakar, R. S. Sabeenian, S. Kaliappan et al., "Production and optimization of energy rich biofuel through co-pyrolysis by utilizing mixed agricultural residues and mixed waste plastics," *Advances in Materials Science and Engineering*, vol. 2022, 9 pages, 2022.
- [19] M. Sharifzadeh, M. Sadeqzadeh, M. Guo et al., "The multi-scale challenges of biomass fast pyrolysis and bio-oil upgrading: review of the state of art and future research directions," *Progress in Energy and Combustion Science*, vol. 71, pp. 1–80, 2019.
- [20] D. Raguraman, A. Kumar, S. Prasanna Raj Yadav et al., "Performance and emission characteristics of pyrolysis oil obtained from neem de Oiled cake and waste polystyrene in a compression ignition engine," *Advances in Materials Science and Engineering*, vol. 2021, pp. 1–10, 2021.
- [21] R. Liu, M. M. Rahman, M. Sarker, M. Chai, C. Li, and J. Cai, "A review on the catalytic pyrolysis of biomass for the bio-oil production with ZSM-5: focus on structure," *Fuel Processing Technology*, vol. 199, article 106301, 2020.
- [22] E. A. Christoforou, P. A. Fokaides, S. W. Banks et al., "Comparative study on catalytic and non-catalytic pyrolysis of olive mill solid wastes," *Waste and Biomass Valorization*, vol. 9, no. 2, pp. 301–313, 2018.
- [23] S. D. Stefanidis, K. G. Kalogiannis, E. F. Iliopoulou, A. A. Lappas, and P. A. Pilavachi, "In-situ upgrading of biomass pyrolysis vapors: catalyst screening on a fixed bed reactor," *Bioresource Technology*, vol. 102, no. 17, pp. 8261–8267, 2011.
- [24] H. Hernando, I. Moreno, J. Feroso et al., "Biomass catalytic fast pyrolysis over hierarchical ZSM-5 and beta zeolites modified with Mg and Zn oxides," *Biomass Conversion and Biorefinery*, vol. 7, no. 3, pp. 289–304, 2017.
- [25] T. A. Ahmed, L. Wu, M. Younes, and M. Hincke, "Biotechnological applications of eggshell: recent advances," *Frontiers in Bioengineering and Biotechnology*, vol. 9, p. 548, 2021.
- [26] Y. Gao and C. Xu, "Synthesis of dimethyl carbonate over waste eggshell catalyst," *Catalysis Today*, vol. 190, no. 1, pp. 107–111, 2012.
- [27] S. Kim, C. G. Lee, Y. T. Kim, K. H. Kim, and J. Lee, "Effect of Pt catalyst on the condensable hydrocarbon content generated via food waste pyrolysis," *Chemosphere*, vol. 248, article 126043, 2020.
- [28] S. Valizadeh, C. H. Ko, J. Lee et al., "Effect of eggshell- and homo-type Ni/Al₂O₃ catalysts on the pyrolysis of food waste under CO₂ atmosphere," *Journal of Environmental Management*, vol. 294, article 112959, 2021.
- [29] R. O. H. A. Rohim, R. Ahmad, N. Ibrahim, N. Hamidin, and C. Z. A. Abidin, "Potential of eggshell waste for pyrolysis process," *Advanced Materials Research*, vol. 1087, pp. 77–80, 2015.
- [30] D. K. Davis and P. Robbins, "Ecologies of the colonial present: pathological forestry from the taux de boisement to civilized plantations," *Environment and Planning E: Nature and Space*, vol. 1, no. 4, pp. 447–469, 2018.
- [31] A. Demirbas, "Biofuels securing the planet's future energy needs," *Energy Conversion and Management*, vol. 50, no. 9, pp. 2239–2249, 2009.
- [32] R. Chandran, R. Kaliaperumal, S. Balakrishnan, A. J. Britten, J. MacInnis, and M. Mkandawire, "Characteristics of bio-oil from continuous fast pyrolysis of Prosopis juliflora," *Energy*, vol. 190, article 116387, 2020.
- [33] D. V. Suriapparao, N. Pradeep, and R. Vinu, "Bio-oil production from Prosopisjuliflora via microwave pyrolysis," *Energy & Fuels*, vol. 29, no. 4, pp. 2571–2581, 2015.
- [34] A. Sahoo, S. Kumar, J. Kumar, and T. Bhaskar, "A detailed assessment of pyrolysis kinetics of invasive lignocellulosic biomasses (Prosopisjuliflora and Lantana camara) by thermogravimetric analysis," *Bioresource Technology*, vol. 319, article 124060, 2021.
- [35] P. Baghel, A. K. Sakhiya, and P. Kaushal, "Influence of temperature on slow pyrolysis of Prosopis Juliflora: an experimental and thermodynamic approach," *Renewable Energy*, vol. 185, pp. 538–551, 2022.
- [36] A. Chandrasekaran, S. Subbiah, S. Ramachandran, S. Narayanasamy, P. Bartocci, and F. Fantozzi, "Natural draft-improved carbonization retort system for biocarbon production from Prosopis juliflora biomass," *Energy & Fuels*, vol. 33, no. 11, pp. 11113–11124, 2019.
- [37] P. Madhu, L. Vidhya, S. Vinodha et al., "Co-pyrolysis of Hardwood Combined with Industrial Pressed Oil Cake and Agricultural Residues for Enhanced Bio-Oil Production," *Journal of Chemistry*, vol. 2022, pp. 1–12, 2022.
- [38] P. Madhu, M. M. Matheswaran, and G. Periyanyagi, "Optimization and characterization of bio-oil produced from cotton shell by flash pyrolysis using artificial neural network," *Energy Sources, Part A: Recovery, Utilization, and Environmental Effects*, vol. 39, no. 23, pp. 2173–2180, 2017.
- [39] I. Kathir, K. Haribabu, A. Kumar et al., "Utilization of tea industrial waste for low-grade energy recovery: optimization of liquid oil production and its characterization," *Advances in Materials Science and Engineering*, vol. 2022, 9 pages, 2022.
- [40] Y. K. Park, M. L. Yoo, H. W. Lee et al., "Effects of operation conditions on pyrolysis characteristics of agricultural residues," *Renewable Energy*, vol. 42, pp. 125–130, 2012.
- [41] A. K. Sakhiya, I. Aier, S. Pathak et al., "Copper (II) removal from aqua solution using rice straw derived biochar," *Materials Today: Proceedings*, vol. 43, pp. 740–745, 2021.
- [42] J. Park, Y. Lee, C. Ryu, and Y. K. Park, "Slow pyrolysis of rice straw: analysis of products properties, carbon and energy yields," *Bioresource Technology*, vol. 155, pp. 63–70, 2014.
- [43] L. J. Cui, W. G. Lin, and J. Z. Yao, "Influences of temperature and coal particle size on the flash pyrolysis of coal in a fast-entrained bed¹," *Chemical Research in Chinese Universities*, vol. 22, no. 1, pp. 103–110, 2006.
- [44] S. Luo, B. Xiao, Z. Hu, and S. Liu, "Effect of particle size on pyrolysis of single-component municipal solid waste in fixed bed reactor," *International Journal of Hydrogen Energy*, vol. 35, no. 1, pp. 93–97, 2010.
- [45] B. B. Krishna, R. Singh, and T. Bhaskar, "Effect of catalyst contact on the pyrolysis of wheat straw and wheat husk," *Fuel*, vol. 160, pp. 64–70, 2015.
- [46] R. Ahmad, N. Kasmuri, S. Ramasamy, R. Santiagoo, and N. A. Mahadi, "Catalytic pyrolysis of agricultural waste using waste egg shell," *AIP Conference Proceedings*, vol. 2347, no. 1, article 020013, 2021AIP Publishing LLC.
- [47] E. R. Kenawy, A. A. Ghfar, S. M. Wabaidur et al., "Cetyltrimethylammonium bromide intercalated and branchedpolyhydroxystyrene functionalized montmorillonite clay to sequester cationic dyes," *Journal of Environmental Management*, vol. 219, pp. 285–293, 2018.
- [48] A. Aboulkas, H. Hammani, M. El Achaby, E. Bilal, and A. Barakat, "Valorization of algal waste via pyrolysis in a